NONLINEAR DYNAMICS OF MULTI-MESH GEAR SYSTEMS

DISSERTATION

Presented in Partial Fulfillment of the Requirements of the Degree Doctor of Philosophy
in the Graduate School of The Ohio State University

By
Gang Liu, B.S., M.S.

*****

The Ohio State University
2007

Dissertation Committee:

Prof. Robert G. Parker, Advisor

Prof. Donald R. Houser

Prof. Ahmet Kahraman

Prof. Herman Shen

Approved by

____
Advisor
Graduate Program in Mechanical Engineering

ABSTRACT

Multi-mesh gear systems are used in a variety of industrial machinery, where noise, quality, and reliability lie in gear vibration. The complicated dynamic forces at the gear meshes are the source of vibration and result from parametric excitation and tooth contact nonlinearity. The primary goal of this work is to develop mathematical models for multi-mesh gearsets with nonlinear, time-varying elements, to conduct numerical and analytical studies to understand parametric and nonlinear gear dynamic behaviors, such as parametric instabilities, frequency response, contact loss, and profile modification, and to provide guidelines for practical design and troubleshooting.

First, a nonlinear analytical model considering dynamic load distribution between individual gear teeth is proposed, including the influence of variable mesh stiffnesses, profile modifications, and contact loss. This model captures the total and partial contact loss and yields better agreement than two existing models when compared against nonlinear gear dynamics from a validated finite element benchmark. Perturbation analysis finds approximate frequency response solutions for the system operating in the absence of contact loss due to the optimized system parameters. The closed-form solution is validated by numerical integration and provides guidance for optimizing mesh phasing, contact ratios, and profile modification magnitude and length.

Second, the nonlinear, parametrically excited dynamics of idler and counter-shaft gear systems are examined. The periodic steady state solutions are obtained using analytical and numerical approaches. With proper stipulations, the non-smooth tooth separation function that determines contact loss and the variable mesh stiffness are reformulated into a form suitable for perturbation. The closed-form solutions from perturbation analysis expose the impact of key parameters on the nonlinear response. The analysis for this strongly nonlinear system compares well to separate harmonic balance/continuation and numerical integration solutions. The expressions in terms of fundamental design quantities have natural practical application.

Finally, this work studies the influences of tooth friction on parametric instabilities and dynamic response of a single-mesh gear pair. A mechanism whereby tooth friction causes gear tooth bending is shown to significantly impact the dynamic response. A dynamic translational-rotational model is developed to consider this mechanism together with the other contributions of tooth friction and mesh stiffness fluctuation. An iterative integration method to analyze parametric instabilities is proposed and compared with an established numerical method. Perturbation analysis is conducted to find approximate solutions that predict and explain the numerical parametric instabilities. The effects of time-varying friction moments about the gear centers and friction-induced tooth bending are critical to parametric instabilities and dynamic response. The impacts of friction coefficient, bending effect, contact ratio, and modal damping on the stability boundaries are revealed. The friction bending effect on the nonlinear dynamic response is examined and validated by finite element results.

Dedicated to my wife, Farong Zhu

to my son, Elvin Liu

and to my parents

ACKNOWLEDGMENTS

I would like to thank Dr. Robert G. Parker for his guidance and continuous support on this research. Without these, this dissertation would not be possible. It was with Dr. Parker that I learned how to do research and how to write. I am also grateful to Dr. Sandeep M. Vijayakar for his generous help on finite element analysis and being patient with my questions. His amazing sharpness and dedication on gear dynamics software blows me away. I thank Dr. Avinash Singh for his valuable feedback on my research. I especially thank General Motors Corporation for staying supportive of my work and providing continuous funding for the research projects. I also thank Dr. Donald R. Houser, Dr. Ahmet Kahraman, and Dr. Herman Shen, for being members of my dissertation committee. This research also benefited from friends in the dynamics and vibration laboratory. Thanks to them for hours of discussion and cooperation on the gear testing. Lastly, but not least, I am indebted to my wife and my parents. Thanks to them for staying supportive and their warming encouragement through the years.

VITA

1997……………………………B.S., Tsinghua University, Beijing, China

2000……………………………M.S., Tsinghua University, Beijing, China

2000 – 2006 …………………Graduate Research Associate, The Ohio State University

PUBLICATIONS

1. Gang Liu and Shiliang Dai, 2000, "Design and Experiment of Measuring Equipments for Dynamics of Military Helmet Suspension System," Journal (Natural Science) of Tsinghua University (In Chinese).

FIELDS OF STUDY

Major Field: Mechanical Engineering

TABLE OF CONTENTS

LIST OF FIGURES

Figure Page

LIST OF TABLES

Table Page

NOMENCLATURE

b_j	Backlash	K_m	Mesh stiffness matrix
c_j	Contact ratio	L	Friciton matrix
f	Mesh frequency	M	Mass matrix
g_j	Profile modification	R	Iteration residual
h_j	Tooth separation	T_i	Applied torque
i	Gear index	U	Response vector
j	Mesh index	V	Modal matrix
k_{si}	Shaft stiffness	X	DTE vector
k_{xi}, k_{yi}	Bearing stiffness	α	Response amplitude
k_j	Mesh stiffness	β	Response phase
$\bar{k}_j$	Average mesh stiffness	γ	Response phase
l	Friction moment arm	ε	Stiffness variation
m_i	Gear mass	ϕ	Mesh phasing
q_i	Modal coordinate	κ,η	Mesh stiffness harmonic

r_i	Base radii	λ	Eigenvalue
s	Harmonic number	ρ	Tip relief magnitude
t	Time	μ	Friction coeffient
u, v	Displacement	θ	Gear rotation
w	Gear tooth bending	σ	Detuning parameter
x_j	DTE	τ	Dimensionless time
y_j	Dimensionless DTE	ω	Mesh frequency
C	Damping matrix	ω_i	Natural frequency
E	Excitation matrix	Φ	Transition matrix
F_j	Mesh forces	Λ	Complex amplitude
G	Profile modification	Θ	Mesh stiffness harmonic
I_i, J	Gear inertia	Ω	Response frequency
K_b	Bearing stiffness matrix		

CHAPTER 1

INTRODUCTION

1.1 Motivation and Objectives

High speed, multi-mesh gear systems have numerous applications in a variety of industrial machinery including helicopters, automotive transmissions, aircraft engines, etc. For example, multi-stage parallel-axis gears (Figure 1.1) transmit power from engines to drivelines in passenger vehicles and heavy duty trucks. Despite their compactness, high power density and efficiency, gear systems generate considerable vibration and noise that impact customer perceptions of quality, noise, and reliability. The sources of vibration are the complicated dynamic forces at the gear meshes, which come primarily from parametric excitations, geometric errors, and tooth micro-geometry design. Parametric excitation results from periodically-varying gear tooth flexibility (mesh stiffness). Geometric errors in the tooth surface and gear position deviations from the prototype result from manufacturing and assembly tolerance. The translational-rotational coupling between gears and bearings excites dynamic bearing forces as well as the axial and tilting motions of gears. Furthermore, the tilting motions caused by flexible bearings introduce gyroscopic effects that make the system stability depend on the gear spin speed. Two types of strong nonlinearities are identified for gear meshes. The first is tooth backlash that is intentionally introduced to allow tolerance, lubrication, and thermal expansion. It admits the contact loss and backside contact during gear vibrations. The second is sliding velocities of the mating tooth surfaces that fluctuate in both amplitude and direction. Most gear teeth, even well lubricated ones, are subject to complicated friction forces and moments that significantly impact the vibro-acoustic behavior [1].

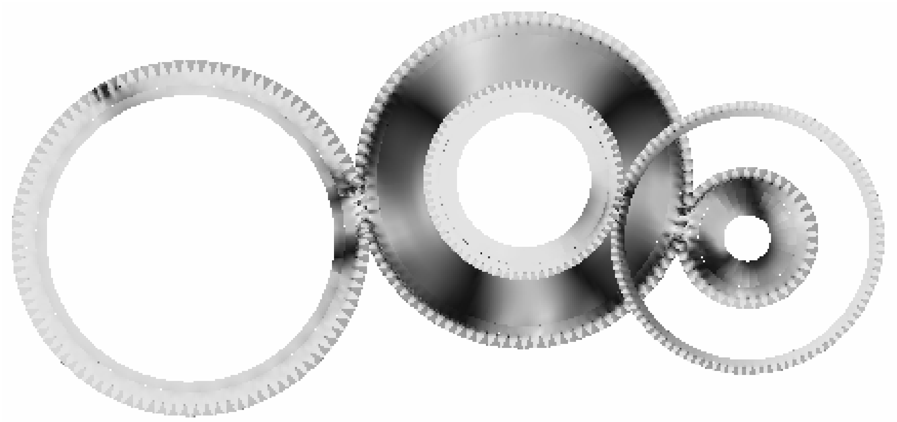

Figure 1.1: A typical multi-mesh gear system (finite element model).

Most research has focused on the study of dynamic responses of a gear pair with single mesh [2-5]. Recently, considerable progress has been made in the modeling and analysis of planetary gears [6-9]. Studies on multi-mesh gear systems, however, are quite limited. Many complicated factors, such as the coupling between components, bearing interactions, contact loss, and sliding friction can dramatically impact system behavior but have not been fully investigated. They constitute the main obstacles in analytical determination of the system frequency response. The static interaction between tooth surface deviations and tooth flexibility is included in the static transmission error (STE) by dynamic models in [10-12]. To accurately predict gear dynamic behavior, the dynamic interaction between tooth surface deviations and tooth flexibility should be considered. A new model is desired to examine the effect of friction on system vibration. The goal of this proposed research is to build accurate analytical models incorporating the above mentioned factors and to give closed-form, approximate solutions for the dynamic response. Especially, the analytical models aim to reveal the effects of the interaction between tooth surface deviations and tooth flexibility. The proposed research seeks to address problems of practical importance. Prediction of the dynamic behavior, and so the noise potential, in the design stage is crucial because changes are difficult to accomplish once prototypes are built.

In summary, there are five main objectives in this study:

1) Build analytical multi-mesh models to incorporate contact loss, periodically-varying mesh stiffnesses, and surface deviations. Use these models to predict the diverse nonlinear dynamic behaviors under different operating conditions.

2) Develop effective methods, both theoretical and numerical, to address the steady state nonlinear dynamic response problems arising from the above models. Study the influence of key design parameters on system dynamics.

3) Capture new mechanisms (like friction-induced tooth bending vibration and dynamic load division between multiple gear tooth pairs) and investigate their influences on the gear dynamics.

4) Provide practical design guidance to designers of multi-mesh gear systems.

5) Develop comprehensive simulation tools for the dynamic analysis of gear systems.

1.2 Literature Review

Extensive research has been conducted on single mesh and planetary (or epicyclica) gears. The studied topics include parametric instabilities, friction-induced instabilities, dynamic response, and bifurcations [13-20]. Many different mathematical models have been established, as reviewed by Blankenship and Singh [21], Ozguven and Houser [22], and Velex and Maatar [9]. Dynamic modeling and analysis of multi-mesh gear systems, however, only receive attention recently [11, 19, 23-26] and need to be further investigated.

Experimental efforts have been made to identify the major sources of gear noise. Oswald et al. [27] test the noise radiation from the top of a gearbox. Jacobson et al. [28] measure the acoustic intensity of a simple gear transmission. These experiments disclose that noise energy concentrates on the spectral lines of mesh frequency and its harmonics, implying the gear mesh is the dominant noise source. Kahraman and Blankenship [29, 30] conduct a number of experiments on a specially designed gear pair and capture several nonlinear phenomena subject to parametric excitation. The noise source is shown to be the gear tooth deflections (mesh stiffness) and geometric deviations that vary periodically at the mesh frequency (product of tooth number and gear rotation speed).

Dynamic problems related to gear parametric excitations have been intensively examined [19, 20, 31-34]. The geometric errors on tooth surfaces, however, are excluded in most studies, and mesh stiffness variation is the only excitation source. Two types of dynamic models are established: linear time-varying (LTV) and nonlinear time-varying (NTV). LTV models are applied to study parametric instabilities, rotational vibrations, and bearing forces. Bollinger et al. [31, 33, 34] investigate parametric instability of single-pair gears using a Mathieu equation. Lin and Parker [19, 20] examine two-stage and planetary gears and obtain boundaries separating stable and unstable conditions. Vinayak and Singh [35] extend the multi-body dynamics strategy to include gear body elasticity as well as rigid body modes. Lin and Parker [36] analytically study the unique characteristics of natural frequencies and vibration modes of planetary gears.

Parametric instabilities are bounded by tooth separations due to the clearance between gear teeth. The contact loss is a softening nonlinearity that causes complicated phenomena such as jump, period-doubling, bifurcation, and chaos. Numerical integration and harmonic balance methods are employed in previous studies to attack such strongly nonlinear problems. Parker et al. [5, 8] adopt a finite element/contact mechanics method to analyze dynamic responses of single mesh and planetary gears. The frequency responses of single mesh gears are compared with the experimental results in [29]. Kahraman and Singh [4] explore the interactions between time-varying mesh stiffness and contact loss nonlinearity of single-mesh gears. Al-shyyab and Kahraman [24] use harmonic balance and continuation methods to investigate subharmonic and chaotic motions of a multi-mesh gear train. Long subharmonic motions and period-doubling phenomenon leading to chaotic behavior are observed. Theodossiades and Natisiavas [37] predict periodic steady state responses by using a piecewise linear technique and perturbation analysis.

Gear tooth surface error is another important vibration source. It refers to any deviation from the perfect involute tooth shape, including manufacturing or assembly error and intentional tooth modifications. The gear error significantly affects the operating contact behaviors and is widely used by gear engineers (in the form of tooth modifications) to reduce gear vibrations and control undesirable corner contact. Harris and Gregory et. al [2, 3] first observe the influences of surface errors on dynamic transmission error (DTE). STE is frequently regarded as a design metric for the dynamic response of single-pair gears. Later, Kahraman and Blankenship [30, 38] conduct several experiments to study the effect of involute tip relief on the dynamic performance of a spur gear pair. Oswald and Townsend's experiments [39] show that well designed tooth profile modification can significantly reduce dynamic loads in spur gears. Some effort has been made to seek efficient dynamic models including surface errors. STE are considered as displacement excitations to include the effect of tooth errors, but it is only applicable under certain circumstances [10-12, 16]. This treatment ignores the interaction between tooth errors and mesh stiffness that is prominent in most cases. Velex and Maatar [23] develop a mathematical model to investigate the contributions of tooth errors. The contact plane is discretized into a number of slices and a discrete normal deviation is used to simulate the tooth error, but this leads to complicated contact analysis and, in some cases, convergence problems.

Sliding friction has received less attention because the friction force is small compared to the normal load. Both analytical and experimental studies on the dynamic impact of sliding frictions are limited. Recent studies [40, 41] show that gears with minimized STE do not necessarily lead to the expected noise reduction. This implies that sliding friction could excite the dynamic bearing forces. The strong influence of tooth friction on the vibro-acoustic behavior has been demonstrated by Vaishya and Houser [42]. Relatively new models [43-47] have been established to study sliding friction. A Coulomb friction law is used. The load sharing between contacting gear tooth pairs and the reversal of sliding friction are discussed in these works. Nevertheless, estimation of the normal load, load sharing, or sliding velocity come mainly from quasi-static analysis. The conclusions from different works are not consistent [40, 42, 44, 45].

1.3 Scope of Investigation

The current research addresses analytical modeling and analysis of nonlinear, parametrically excited dynamics for multi-mesh gear systems. It aims to establish validated analytical models, examine the rich nonlinear dynamic behaviors occurring in practical multi-mesh gear systems, and consequently provide guidance for practical design by examining the impact of the design parameters on the system vibrations. The problems studied in this work are of practical importance in industrial power transmission use. The work helps to advance the understanding of the broader field of nonlinear dynamics in multi-mesh gear systems.

Chapter 2 studies the dynamic effects of tooth profile modification on multi-mesh gearset vibration. An analytical nonlinear model is established to include the influence of variable mesh stiffnesses, profile modifications, and contact loss. The special feature of this model is to consider dynamic load distribution between individual gear teeth, which allows this model to capture the total and partial contact loss demonstrated by finite element analysis. The model is compared against two existing models by a validated finite element benchmark for nonlinear gear dynamics. These comparisons are made for different load, profile modification, and bearing deflection conditions. Approximate frequency response solutions are found by perturbation analysis for the system with the optimal system parameters that prevent contact loss. The closed-form solution is validated by numerical integration and used to examine influences on system vibration from mesh phasing, contact ratios, and profile modification magnitude and length.

Chapter 3 discusses the nonlinear, parametrically excited dynamics of idler gearsets. The two gear tooth meshes provide two interacting time-varying mesh stiffnesses (parametric excitations) and two tooth separations with the same period. The ratio of mesh stiffness variation to its mean value is a small parameter. The time of tooth separation is assumed to be a small fraction of the mesh period. The non-smooth separation function that determines contact loss and the variable mesh stiffness are reformulated into a form suitable for perturbation analysis that gives the periodic steady state solution branches and their stabilities near fundamental, secondary, and subharmonic resonances. The perturbation analysis for this strongly nonlinear system compares well to a harmonic balance/arclength continuation approach that provides accurate semi-analytical solutions for both stable and unstable branches. The impacts of key parameters on the nonlinear response are investigated by the analytical closed-form expressions.

Chapter 4 studies the nonlinear, parametrically excited dynamics of counter-shaft gear systems. A nonlinear dynamic model is established for counter-shaft gears to include parametric excitation and contact loss with two different periodicities. In a similar spirit to Chapter 3, the periodic steady state solutions for frequency response are obtained by perturbation analysis and compared against semi-analytical harmonic balance and numerical integration methods for fundamental, subharmonic and second harmonic resonances with varied system parameters. The interaction of the two meshes is found to depend on the relation of the two mesh periods. The dynamic influences of design parameters, such as shaft stiffness, mesh stiffness variation, contact ratio, and mesh phasing, are discussed via analytical and numerical solutions.

Chapter 5 examines the influences of tooth friction on parametric instabilities and dynamic response of a single-mesh gear pair. A dynamic translational-rotational model is developed to consider a mechanism whereby tooth friction causes gear tooth bending together with the other contributions of tooth friction and mesh stiffness fluctuation. Parametric instabilities resulting from tooth friction and mesh stiffness are studies by iterative integration and perturbation methods. The proposed iterative method is compared with an established numerical method and validates perturbation solutions that expose the impacts of friction coefficient, bending effect, contact ratio, and modal damping on the stability boundaries. The friction bending effect on the nonlinear dynamic response is examined and validated by finite element results. The included effects of time-varying friction moments about the gear centers and friction-induced tooth bending are critical to parametric instabilities and dynamic response.

The contributions of the current research are summarized as follows.

1. Established analytical multi-mesh models to incorporate contact loss, periodically-varying mesh stiffnesses, surface deviations, and sliding friction effects. The effectiveness and efficiency of the proposed models are compared against existing models. The proposed models are validated by finite element analysis and cast into forms suitable for theoretical and numerical analysis.

2. Developed effective methods, both theoretical and numerical, to address the steady state dynamic response problems arising from the above models for two types of multi-mesh gear systems: idler and counter-shaft gears. Perturbation analysis yields closed-form solutions for the periodic steady state response, exposes the influence of key design parameters on system dynamics, and consequently provides design guidance for practical applications.

3. Examined dynamic analysis of the system transmission error. The tooth surface deviation is incorporated with careful modeling, in addition to most other factors considered in former models. This research gives insight and more accurate prediction of the reduction of DTE through surface modifications.

4. Investigated the impact of tooth friction and its bending effect on gear dynamics. The study includes not only the dynamic interactions between the normal load and the moments about the gear center from tooth friction forces but also the coupling interaction

from the gear tooth bending effect from friction forces. The analytical study and finite element analysis confirms that tooth friction bending effect affects parametric instability.

5. Implemented the above analysis into industry application by devising a comprehensive dynamic simulation code. This brings the findings and methods of the analysis within reach of practicing engineers working on gear systems. Practical design advice to reduce noise and vibrations will also emerge.

CHAPTER 2

DYNAMIC MODELING AND ANALYSIS OF TOOTH PROFILE MODIFICATION FOR MULTI-MESH GEAR VIBRATION

This chapter studies the dynamic effects of tooth profile modification on multi-mesh gearset vibration. An analytical nonlinear model is established to include the influence of variable mesh stiffnesses, profile modifications, and contact loss. Dynamic load distribution between individual gear teeth is considered to capture the total and partial contact loss. Comparison and contrast on gear dynamics are made for the proposed model and two existing models against a validated finite element/contact mechanics benchmark. Perturbation analysis based on the proposed model finds approximate frequency response solutions for the system parameters preventing contact loss. The closed-form solution is validated by numerical integration and provides guidance for optimizing mesh phasing, contact ratios, and profile modification magnitude and length.

2.1 Introduction

Large amplitude gear tooth forces and bearing loads are created at dynamic resonances, which are the root cause of gear durability and noise problems. This necessitates prediction of dynamic behavior at the design stage. Researchers have developed a variety of mathematical models to investigate gear vibration and noise [21-23]. In practice there are numerous models because of the great variety of specific systems and applications. The nucleus of all models, however, is the modeling of the gear tooth contact actions.

One category of tooth mesh model involves parametrically excited models with periodically-varying mesh stiffnesses and shape deviations of gear teeth [19, 20, 37, 48-53]. These lumped-parameter models consider the gear bodies as rigid disks and the gear teeth as elastic elements with periodically varying stiffness due to the changing contact action and number of gear teeth in contact. The gear tooth elasticity is usually calculated by finite element (FE), boundary element, or continuous beam models at multiple points in a mesh cycle [23, 51, 54, 55]. The shape deviations of gear teeth occur because of manufacturing tolerances, wear, and deliberate profile modification to reduce abnormal tooth contact and vibrations. Many models, however, exclude the shape deviation by assuming perfect involute gear teeth.

A second group of tooth mesh models consists of lumped-parameter models with external excitation from static transmission error (STE) that models the effects of gear tooth elasticity and shape deviation. Constant mesh stiffness is usually assumed. This modeling idea is used in complex systems, where simplification is necessary, or systems with relatively small mesh stiffness variation [10, 11, 56]. The action of mesh stiffness parametric excitations can not be examined. The load sharing between individual gear pairs of teeth is assumed to be the same as the static state, which may not represent the dynamic state.

A third category includes detailed computational models built by the FE method. The moving contact point along a gear tooth surface requires extremely refined meshes for commercial FE programs, and this typically precludes dynamic response analysis. Some specialized FE models have been developed to efficiently treat the gear tooth contact and permit dynamic response analysis [5, 8, 57, 58].

Gear tooth profile modification is introduced to optimize contact patterns and stresses, compensate for manufacturing errors, and reduce gear dynamics. Micro-geometry modification of the involute gear teeth dramatically affects static and dynamic performance of the gear system [48, 59]. The peak-peak value of STE is sensitive to gear load, the magnitude and length of profile modification, and contact ratio. The impact of tip relief on rotational vibration of a gear pair is investigated experimentally in [30]. Mathematical modeling and analysis of gear dynamics including tooth modification are found in [10, 23, 60].

Despite a variety of existing models, what is the most effective and efficient lumped-parameter model with profile modifications for gear dynamics remains unsettled. In addition, the comparison and validation of analytical models for *multi-mesh* gearsets are quite limited in the literature. For multi-mesh gearsets, the dynamic impact of profile modification is commonly correlated with STE for isolated individual meshes. In practice, however, the profile modifications of individual meshes interact with each other and with other parameters such as mesh stiffness variations and contact ratios. Furthermore, tooth contact patterns are strongly affected by profile modification and dynamic response. The total mesh stiffness from all tooth pairs nominally in contact is no longer sufficient to analyze dynamic mesh forces. Instead, the dynamic load distributions for individual tooth pairs are required.

This work proposes a nonlinear, time-varying model of a multi-mesh idler system that analyzes dynamic forces of individual tooth pairs in terms of their variable mesh stiffnesses and profile modifications. Interactions between the multiple meshes are impacted by mesh phasing, that is, the phase difference between mesh stiffnesses or profile modifications for the multiple meshes. This model is compared against two existing models and a FE benchmark for different load, profile modifications, and bearing conditions. The proposed model agrees well with the benchmark for all selected conditions, in contrast to the two existing models, and it reveals the partial and total contact losses due to profile modifications. The approximation of optimal profile modification for vibration reduction is obtained by perturbation analysis and compared to numerical integration. The interactions of the two meshes with different magnitudes and lengths of profile modification, contact ratios, and mesh phasing are discussed.

2.2 Discussion of System and Parameters

2.2.1 Physical System and Assumptions

Idler gearsets as shown in Figure 2.1 are a basic sub-system in multi-mesh gear systems. Studies on this system can be extended to more complicated ones. The middle gear (idler) engages with the input gear (pinion) and the output gear (follower) that are connected to input and output devices.

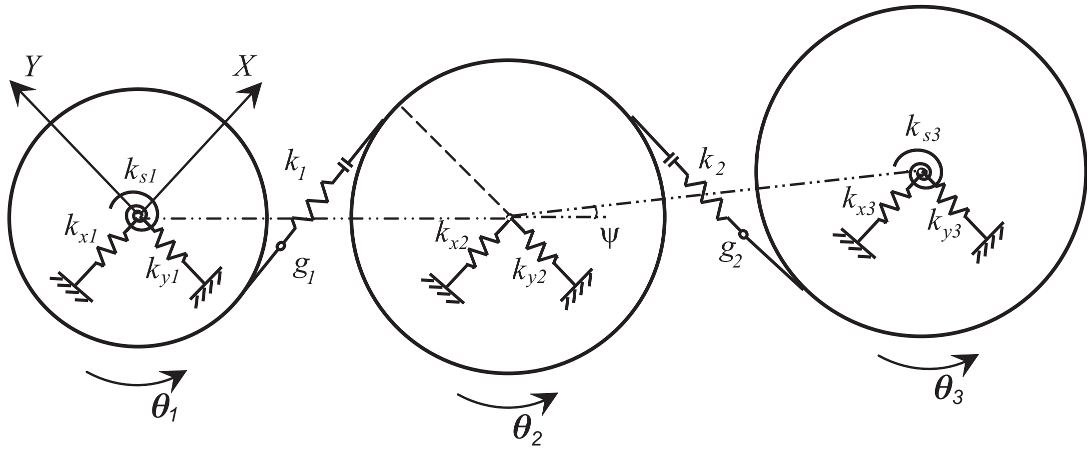

Figure 2.1: Translational-rotational model of idler gearsets.

The flexibilities of the gear blank and teeth are lumped into mesh stiffnesses that vary periodically over a tooth mesh cycle. The tooth shape deviation varies periodically as well. Contact loss and backside contact of the gear teeth due to gear backlash are considered. With these stipulations, three nonlinear models are established to simulate the spur idler gearset in Figure 2.1.

The pinion, idler and follower are labeled as gears 1, 2 and 3, respectively. The mass, polar moment of inertia, and base circle radius of gear i are m_i, I_i, and r_i. The resultant mesh stiffnesses of the two meshes are $k_{1,2}$. The bearing and coupling stiffnesses are k_{xi}, k_{yi}, and k_{si}, with $k_{s2}=0$. T_1 and T_3 are the constant external torques exerted on the pinion and follower. The three gear centers are not necessarily aligned; an orientation angle ψ is defined between the pinion-idler and idler-follower center lines (Figure 2.1). The gear mesh contact ratios, operating pressure angles, and backlashes are $c_{1,2}$, $\alpha_{1,2}$, and $b_{1,2}$, respectively. To define gear vibratory translations x_i and y_i, a fixed reference frame is established based on the line of action of the first mesh (pinion-idler) such that the pinion translation y_1 is decoupled from the remaining degrees of freedom (DOF). θ_i are vibratory angular displacements superimposed on the nominal rigid body rotations where the gear teeth have no elastic deflection and surface shape deviation. The parameters of an example idler system are listed in Table 2.1.

GEAR I	1	2	3	MESH J	1	2
$r_i\,(m)$	0.04535	0.06564	0.11218	α_n	21.22°	21.02°
$m_i\,(kg)$	2.2325	4.4380	16.9419	c_n	1.504	1.510
$I_i\,(kg\text{-}m^2)$	0.002621	0.01091	0.1193	$\hat{k}_n\,(N/m)$	2.9831	3.2108
$k_{si}\,(N\text{-}m/rad)$	3389.6	0	11297.9	$\rho_n\ (\mu m)$	10	10
$k_{xi}, k_{yi}(N/m)$	1.27E8	1.4732E8	1.6637E8	ς_n	0.504	0.510
$T_i\,(N\text{-}m)$	100	0	-247	ε_n	0.35	0.4
FACEWIDTH	0.0127	0.0127	0.0127	$\phi(rad)$	0	

Table 2.1 Parameters of the example idler system

2.2.2 Discussion of Individual Mesh Stiffness

Mesh stiffness defines the compliance of the flexible gear teeth due to variations in the number of teeth in contact. In principle, the mesh stiffnesses $k_{1,2}$ fluctuate with the dynamic load. Although dynamic load deviates from the static load near resonances, the effect on mesh stiffness is modest and not considered here. Quasi-static mesh stiffness fluctuations over a mesh cycle can be obtained by FE, boundary element, experiment, and analytical approximation.

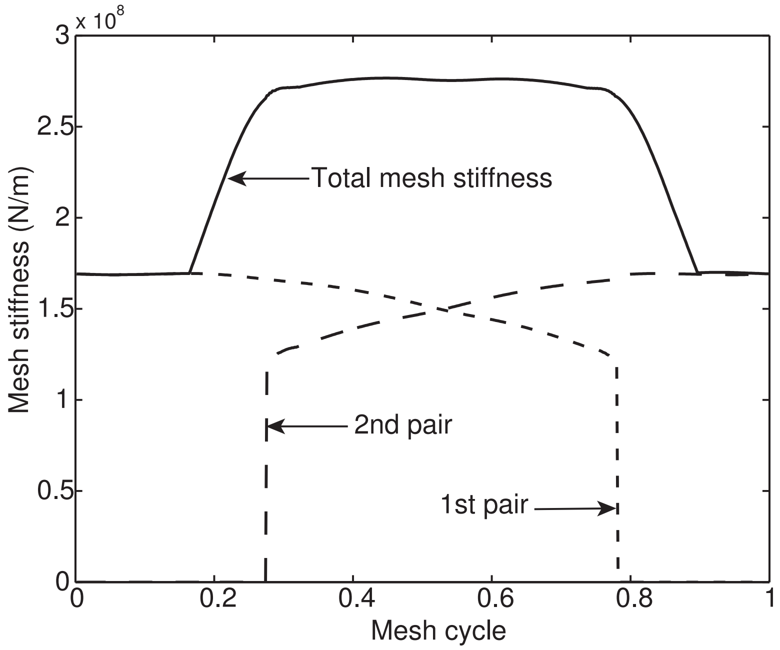

Figure 2.2: Mesh stiffnesses of the pinion-idler mesh for system parameters in Table 2.1 and no profile modifications.

When there are P_n tooth pairs in contact for gear mesh n, the total mesh stiffness is $k_n = \sum_{p=1}^{P_n} k_{n,p}$, where $k_{n,p}$ are the mesh stiffnesses of tooth pair p. For instance, the mesh stiffnesses of two tooth pairs are calculated by FE static analysis and shown in Figure 2.2. The first pair engages from 0 (pitch point) to 0.78 in a mesh period. The stiffness slightly decreases during the recess. The second pair engages from 0.26 to 1, and the stiffness slightly increases during the approach. The two pairs of teeth share the load from 0.26 to 0.78, known as double-tooth contact, where the load gradually switches from the first pair to the second pair. Note that the first pair is also in contact from -0.74 to 0 in a previous mesh cycle (not shown in Figure 2.2), which is similar to the contact for the second pair from 0.26 to 1. In practice, the corner contact effect is significantly reduced by profile modification. Thus, this effect is neglected in the individual mesh stiffnesses, which have sharp changes at the beginning and end of contact as shown in Figure 2.2.

2.2.3 Modeling of Tooth Profile Modifications

Micro-scale profile modifications of the same order (μm) as transmission errors have negligible impact on the tooth surface curvature and the mesh stiffness of the tooth pair. On the other hand, profile modifications change the dynamic load distribution between multiple tooth pairs and provide variable displacement excitation for dynamic and static analyses. There are several methods to modify gear tooth surfaces, including crowning, tip relief, and root relief having linear or parabolic variations with roll angle. Without loss of generality, linear tip relief is applied in this study. Only two parameters are needed to define tip relief: the magnitude of the relief ρ_n (at the tooth tip) and the modification length ς_n that is the ratio of the roll angle difference between the starting point and tooth tip to the pitch angle (2π divided by the number of gear teeth).

Several key reference points along a gear tooth surface are defined for low contact ratio gears. Contact on the involute curve is bounded by the start of active profile (SAP) and the tip, i.e., the lowest and highest roll angles among all contact points. HPSTC is the highest point of single-tooth contact. LPSTC is the lowest point of single-tooth contact. For the first tooth pair in Figure 2.2 and Figure 2.3, the tip of the driving gear and the

SAP of the driven gear are in contact at 0.78. The HPSTC of the driver and the LPSTC of the driven gear are in contact at 0.26.

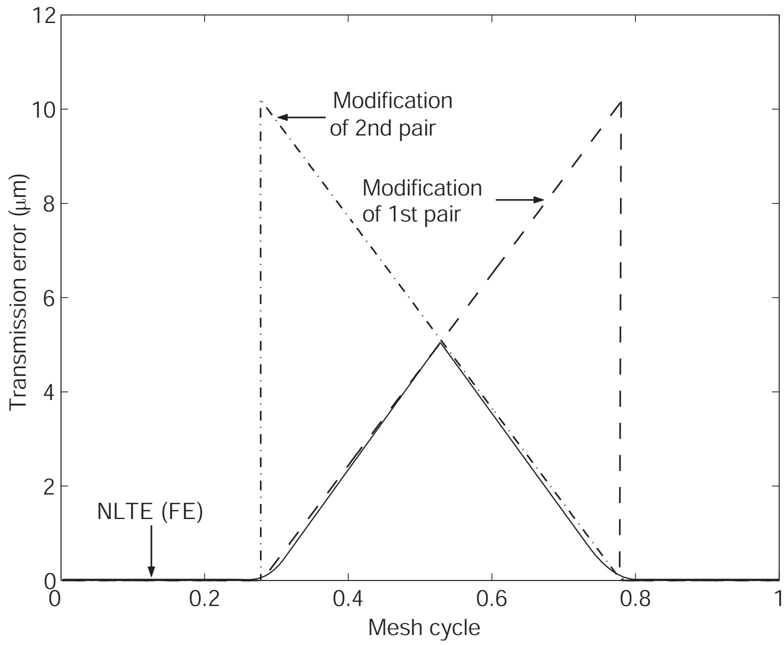

Figure 2.3: Gap constraints and no-load transmission error (NLTE) of the pinion-idler mesh along the line of action for system parameters and tooth modifications in Table 2.1.

Tooth profile modifications are applied using gap constraints for the elastic elements (mesh stiffnesses) along the line of action. The gap of a tooth pair for an instantaneous position in a mesh cycle is the sum of the profile modification amounts at the two nominally contacting points. The elastic element is not engaged unless the relative motion of the mating gears along the line of action exceeds this gap. Figure 2.3 shows gap functions of the pinion-idler mesh for the example system in Table 2.1 with $\varsigma_n = c_n - 1$ and $\rho_n = 10\ \mu m$. Each gap function forms a saw-tooth shape. The gaps of the first and second pairs are due to the idler and pinion tooth modifications ranging from HPSTC to tip, which increase and decrease from 0.26 to 0.78, respectively. For the no-load condition, there is always a single tooth pair in contact because the tooth pair with the smaller gap takes over the contact. This is verified by the no-load transmission error (NLTE) calculated from FE that shows a triangular wave; the gear load switches from the first tooth pair to the second pair at the vertex. Above a certain load, the elastic deflection overcomes the gap and creates contact between multiple pairs.

2.2.4 Mesh Interactions for Multiple Meshes

One of the most important characteristics of multi-mesh gear systems is the mesh phasing ϕ defined as the phase difference between the periodically-varying parameters (mesh stiffnesses and profile modifications) of the two meshes. Variations in these parameters have the same periodicity for the two gear meshes, but they are not necessarily in phase. There can be a time difference ϕT between them, where T is the mesh period and the time difference is between two corresponding points in the meshes (e.g., the pitch points). The mesh phasing is governed by gear geometry [61]. It strongly affects gear dynamics [62].

Expanded as Fourier series, the periodic total mesh stiffnesses for each mesh are

$$\begin{aligned} k_1 &= \bar{k}_1 + \left(\sum_{s=1}^{\infty} k_{1s} e^{is\omega t} + c.c. \right) \\ k_2 &= \bar{k}_2 + \left(\sum_{s=1}^{\infty} k_{2s} e^{is\omega (t-\phi T)} + c.c. \right) \end{aligned} \tag{2.1}$$

where ω is the mesh frequency, k_{1s} and k_{2s} are complex Fourier amplitudes that include contact ratio differences between the two meshes, and *c.c.* denotes the complex conjugate of previous terms. k_{1s} and k_{2s} are calculated such that a reference point (e.g., the pitch point) of the two meshes occur at the same instant; the mesh phasing ϕ then accounts for the phase shift. The Fourier expansion can be applied to the mesh stiffness and profile modification of an individual tooth pair as well.

2.3 Dynamic Models of Multiple Meshes

A nonlinear, time-varying model (Model-1) is proposed to investigate gear dynamics with profile modifications. This model is compared with two existing models (Model-2 and Model-3).

2.3.1 Time Varying Mesh Stiffness Model (Model-1)

The resultant dynamic force at mesh n is calculated from the individual loads of each tooth pair as

$$F_n = \sum_{p=1}^{P_n} h_{n,p} k_{n,p} (S_n - g_{n,p}) \tag{2.2}$$

$$S_1 = u_1 + u_2 + x_1 - x_2 \qquad S_2 = -u_2 - u_3 - (x_2 - x_3)\cos\chi - (y_2 - y_3)\sin\chi \tag{2.3}$$

$$h_{n,p} = \left[sgn(S_n - g_{n,p}) + sgn(S_n - g_{n,p} + b_n) \right] / 2 \tag{2.4}$$

where $u_i = r_i \theta_i$ and $\chi = \alpha_1 + \alpha_2 + \psi$, the subscripts n and p are mesh number and tooth pair index, respectively, P_n is the smallest integer greater than the contact ratio for mesh n, S_n are mesh deflections, $S_n - g_{n,p}$ are elastic mesh deflections, $g_{n,p}$ are the gap functions (for instance, $g_{1,1}$ is the gap constraint of the first tooth pair shown in Figure 2.3), and $h_{n,p} \in \{1, 0, -1\}$ are tooth contact functions that determine drive-side contact (1), contact loss (0), or back-side contact (-1). Total contact loss is defined as all $h_{n,p} = 0$ for a given mesh n, i.e., all tooth pairs lose contact. Partial contact loss is when one (or more for high contact ratios) but not all tooth pairs nominally in contact lose contact.

The component and matrix equations of motion are

$$
\begin{aligned}
& m_1\ddot{x}_1 + k_{x1}x_1 + F_1 = 0 \quad I_1\ddot{\theta}_1 + k_{s1}\theta_1 + r_1F_1 = T_1 \\
& m_2\ddot{x}_2 + k_{x2}x_2 - F_1 - F_2\cos\chi = 0 \quad m_2\ddot{y}_2 + k_{y2}y_2 + F_2\sin\chi = 0 \quad I_2\ddot{\theta}_2 + r_2F_1 - r_2F_2 = 0 \\
& m_3\ddot{x}_3 + k_{x3}x_3 + F_2\cos\chi = 0 \quad m_3\ddot{y}_3 + k_{y3}y_3 + F_2\sin\chi = 0 \quad I_3\ddot{\theta}_3 + k_{s3}\theta_3 - r_3F_2 = T_3
\end{aligned}
\tag{2.5}
$$

$$
\begin{aligned}
& \mathbf{M}\ddot{\mathbf{U}} + \mathbf{C}\dot{\mathbf{U}} + [\mathbf{K}_b + \mathbf{K}(\omega t, \mathbf{U})]\mathbf{U} - \mathbf{E}_1(\omega t, \mathbf{U}) = \mathbf{F}_T \\
& \mathbf{U} = [x_1, u_1, x_2, y_2, u_2, x_3, y_3, u_3]^T
\end{aligned}
\tag{2.6}
$$

where $\mathbf{C}$ is the damping matrix calculated from a modal damping ratio ζ, $\mathbf{K}_b$ is the constant bearing stiffness matrix, $\mathbf{K}$ is the time-varying mesh stiffness matrix, $\mathbf{F}_T$ is the external load vector, and $\mathbf{E}_1$ includes excitations from mesh stiffnesses and profile modifications. The matrices for a purely rotational model are

$$
\begin{aligned}
& \mathbf{U}=[u_1, u_2, u_3]^T; \quad \mathbf{M} = diag(I_1/r_1^2, I_2/r_2^2, I_3/r_3^2) \\
& \mathbf{K}_b = diag(k_{s1}/r_1^2, 0, k_{s3}/r_3^2); \quad \mathbf{F}_T = [F, 0, -F]^T \\
& \mathbf{K}(\omega t, \mathbf{U}) = \begin{bmatrix} \sum_{p=1}^{P_1} h_{1,p}k_{1,p} & \sum_{p=1}^{P_1} h_{1,p}k_{1,p} & 0 \\ & \sum_{p=1}^{P_1} h_{1,p}k_{1,p} + \sum_{p=1}^{P_2} h_{2,p}k_{2,p} & \sum_{p=1}^{P_2} h_{2,p}k_{2,p} \\ symmetric & & \sum_{p=1}^{P_2} h_{2,p}k_{2,p} \end{bmatrix} \\
& \mathbf{E}_1(\omega t, \mathbf{U}) = \begin{bmatrix} \sum_{p=1}^{P_1} h_{1,p}k_{1,p}g_{1,p} \\ \sum_{p=1}^{P_1} h_{1,p}k_{1,p}g_{1,p} - \sum_{p=1}^{P_2} h_{2,p}k_{2,p}g_{2,p} \\ -\sum_{p=1}^{P_2} h_{2,p}k_{2,p}g_{2,p} \end{bmatrix}
\end{aligned}
\tag{2.7}
$$

where $F = T_1 / r_1$ is the nominal mesh force. Static analysis of (2.7) yields the analytical STE

$$\tilde{\delta}_n = \left(F + \sum_{p=1}^{P_n} h_{n,p} g_{n,p} k_{n,p} \right) / \sum_{p=1}^{P_n} h_{n,p} k_{n,p} \tag{2.8}$$

This includes contributions from elastic deflections and profile modifications. Without profile modification ($g_{n,p} = 0$), $\mathbf{E}_1 = \mathbf{0}$ and all tooth pairs for a given mesh lose contact at the same time, implying

$$\sum_{p=1}^{P_n} h_{n,p} k_{n,p} = h_n k_n, \quad h_n = \left[sgn(s_n) + sgn(s_n + b_n) \right] / 2 \tag{2.9}$$

Overall, Model-1 includes parametric excitation, profile modifications, dynamic load division among the individual gear teeth in mesh at each instant, and partial contact loss.

2.3.2 Static Transmission Error Model (Model-2)

Studies on single mesh gears [48, 59] show that the effect of profile modification on dynamic transmission error (DTE) is related to its effect on the STE. This correlation between STE and DTE suggests Model-2, in which the periodic STE are regarded as displacement excitations applied at the gear mesh. Because the fluctuation of tooth elasticity is included in the STE, only the average mesh stiffnesses $\hat{k}_n$ are used. Multiple teeth in contact is treated as a single stiffness element with no division into individual tooth contributions. Let δ_n be the loaded STE of mesh n with the mean value excluded.

Substitution of the dynamic mesh forces $F_n = h_n \hat{k}_n (s_n - \delta_n)$ into (2.5) gives the STE model in matrix form as

$$\mathbf{M\ddot{U}} + \mathbf{C\dot{U}} + [\mathbf{K}_b + \hat{\mathbf{K}}(\mathbf{U})]\mathbf{U} - \mathbf{E}_2(\omega t, \mathbf{U}) = \mathbf{F}_T \tag{2.10}$$

where $\hat{\mathbf{K}}$ is obtained by replacing $\sum_{p=1}^{P_n} h_n k_{n,p}$ with $h_n \hat{k}_n$ in $\mathbf{K}$ of (2.6). For a purely rotational model, $\mathbf{E}_2 = [h_1 k_1 \delta_1, h_1 k_1 \delta_1 - h_2 k_2 \delta_2, -h_2 k_2 \delta_2]^T$.

Although Model-2 neglects parametric excitation, dynamic tooth load division between individual teeth and partial contact loss, it simplifies the problem and provides reasonable estimates of gear dynamics under certain conditions [10].

2.3.3 No-Load Transmission Error Model (Model-3)

Model-3 incorporates the fluctuating mesh stiffnesses as parametric excitation. Profile modifications are modeled using the no-load STE $\hat{\delta}_n$ as a displacement excitation [63]. The dynamic mesh forces are $F_n = h_n k_n (s_n - \hat{\delta}_n)$. The equation of motion is

$$\mathbf{M\ddot{U}} + \mathbf{C\dot{U}} + [\mathbf{K}_b + \tilde{\mathbf{K}}(\omega t, \mathbf{U})]\mathbf{U} - \mathbf{E}_3(\omega t, \mathbf{U}) = \mathbf{F}_T \tag{2.11}$$

where the matrix $\tilde{\mathbf{K}}$ is obtained by replacing $\hat{k}_n$ with k_n in the $\hat{\mathbf{K}}$ of (2.10). For a purely rotational model, $\mathbf{E}_3 = [h_1 k_1 \hat{\delta}_1, h_1 k_1 \hat{\delta}_1 - h_2 k_2 \hat{\delta}_2, -h_2 k_2 \hat{\delta}_2]^T$.

2.3.4 Finite Element Benchmark

Conventional finite element can calculate tooth deflection, mesh stiffness, and stress with highly refined meshes, but it is impractical for dynamic analysis. The finite element formulation employed in this work, however, treats the tooth contact mechanics with sufficient accuracy and computational efficiency that dynamic analyses are possible. A full gear mesh is used (Figure 2.4) rather than a gear with one or two representative teeth. Past efforts [5, 8, 55] show the fidelity and efficiency of this method for multi-mesh gear systems.

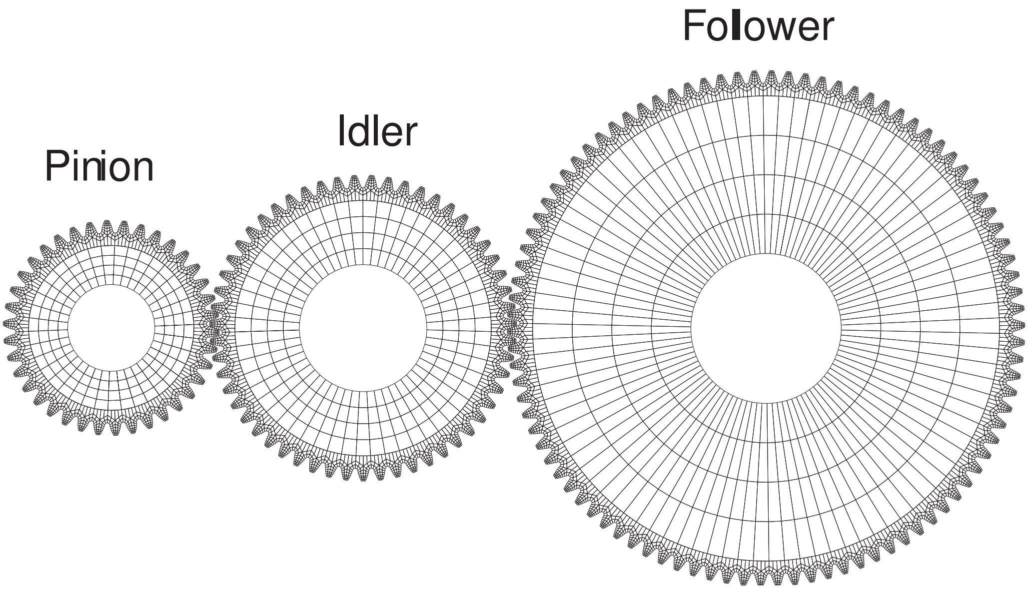

Figure 2.4: Finite element model of the example idler gearset in Table 2.1.

Numerical integration is used in the FE dynamic analysis. Steady state responses over a range of input speeds with a proper speed step, known as speed sweep, are obtained, from which the frequency response is calculated. Gradual switches between two speeds are necessary because abrupt speed changes cause numerical instability. Uniform acceleration (linear speed ramp) of the gears is enforced during the speed-switching period.

For accuracy of the solution and computational efficiency, the numerical parameters must be selected carefully. First, the speed step determines the mesh frequency resolution. Small speed step gives high resolution with high computational consumption. The ramp rate affects the transition time in switching from one speed to another. A high ramp rate causes larger transient response for the next speed, but a low one extends the time needed to switch speeds. The time step controls the accuracy of numerical integration, maximum frequency in the response spectra, and computation cost. Multiple mesh frequency harmonics participate in the response at a given mesh frequency. The time step should be selected based on the highest significant harmonic. Finally, the span of integration time should allow the transient response to decay, which depends on damping, natural frequencies, and the initial conditions. The time spans are integer numbers of mesh periods to prevent leakage.

Runge-Kutta integration is employed for numerical simulations with the analytical models. The discussion of speed step, time step, and integration time span are similar, but a ramp rate is no longer required. The initial condition of the current speed is the final condition of the previous speed instead.

2.4 Evaluation of Analytical Models Against Finite Element

The proposed model (Model-1) is benchmarked against FE and compared to the two existing models (Model-2 and Model-3). Comparisons are made for different torques, profile modifications, and bearing conditions using the example system in Table 2.1. Realistic mesh stiffness functions (Figure 2.2) with smooth load transition between tooth pairs are used for the analytical models. Dynamic speed sweep analyses are conducted for increasing and decreasing speeds to find all stable solution branches. Root-mean-square (RMS) values of the steady state DTE $z_1 = u_1 + u_2$ and $z_2 = -u_2 - u_3$ are calculated near resonances. The mean values of DTE are subtracted prior to all RMS calculations

2.4.1 Comparisons of Frequency Response

2.4.1.1 Rigid bearing condition

The example system in Table 2.1 is examined without profile modifications for three different input torques (50, 100, and 150 *N-m*) and rigid bearings (no translation).

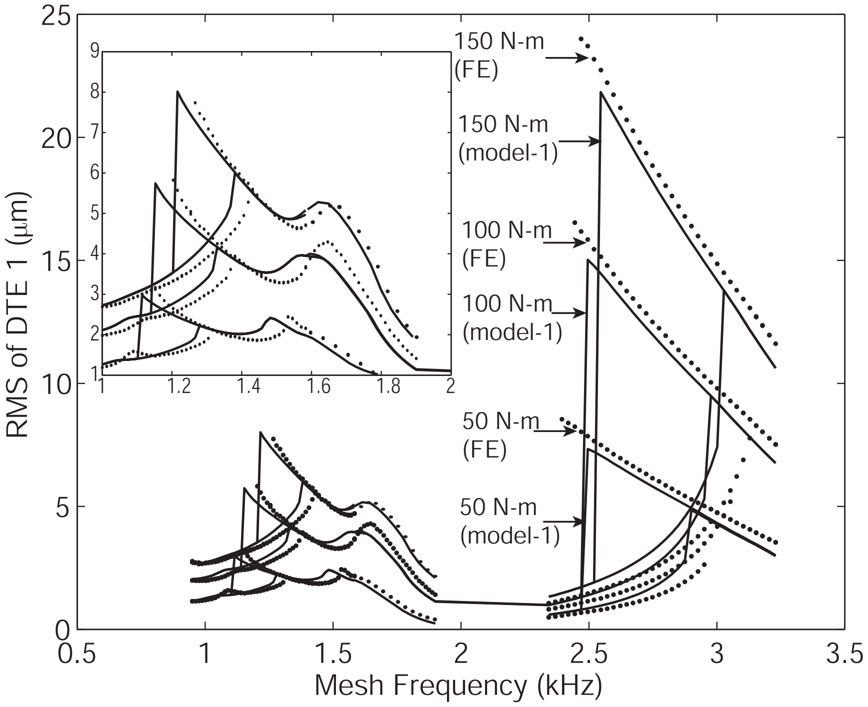

Figure 2.5: Comparison of dynamic transmission error (with mean removed) from Model-1 and finite element for multiple torques, no tooth modification, and other system parameters in Table 2.1.

The system natural frequencies for average mesh stiffnesses are $f_0 = 60$ *Hz* (the "rigid body" mode, i.e., a mode with minimal mesh deflections), $f_1 = 1600$ *Hz* (idler-follower mesh mode), and $f_2 = 3230$ Hz (pinion-idler mesh mode). f_1 and f_2 are referred to as the first and second natural frequencies.

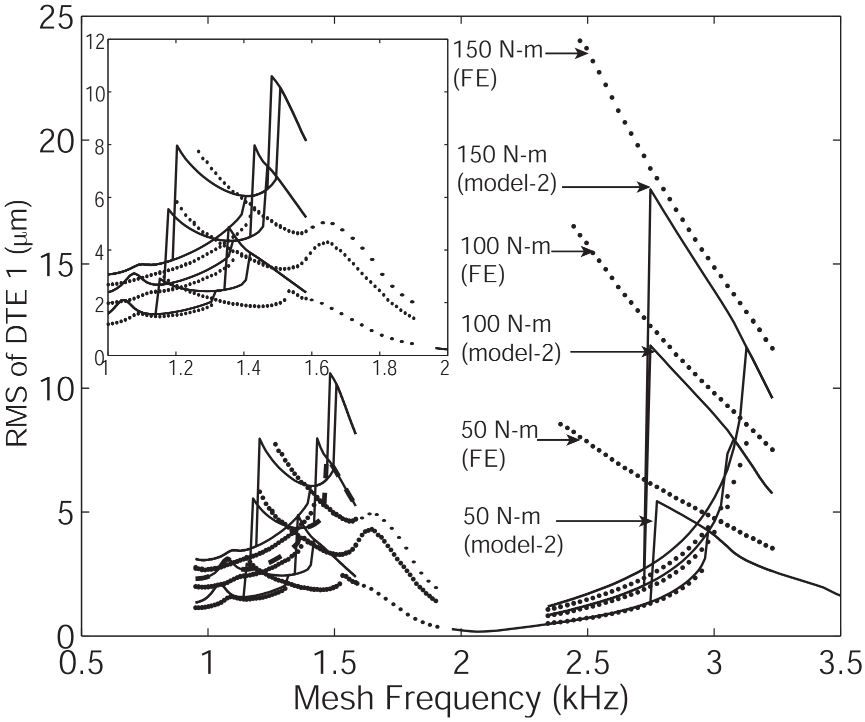

Figure 2.6: Comparison of dynamic transmission error (with mean removed) from Model-2 and finite element for multiple torques, no tooth modification, and other system parameters in Table 2.1.

Comparisons between Model-1 and FE are shown in Figure 2.5 with good agreement for all three torques. Fundamental resonances near f_1 and f_2 show strong nonlinearity with classical jump phenomena because of contact loss. The fundamental resonances of f_1 and f_2 have jump-down frequencies near 1.2 kHz and 2.5 kHz. The higher amplitude of z_1 near f_2 compared to f_1 is due to the vibration mode. Jump-up and jump-down are associated with up-sweep and down-sweep, respectively, and result from the softening nonlinearity. Two stable branches exist in the range bounded by the jump-up and jump-down frequencies. The peak amplitudes increase nearly linearly with torque, but the jump-up and jump-down frequencies are almost invariant, which is consistent with the perturbation analysis in [62]. Peaks around $f_2/2 \approx 1.6$ kHz are the second harmonic excitation resonances of the second mode; the 50 *N-m* torque peak is at 1.5 kHz because the lower torque decreases the average mesh stiffness. Nonlinearity is not found near these peaks because of the low amplitude from higher harmonic excitation. The frequencies from FE are higher than from Model-1 because the dynamic mesh stiffness is slightly stiffer than the quasi-static mesh stiffness used in Model-1.

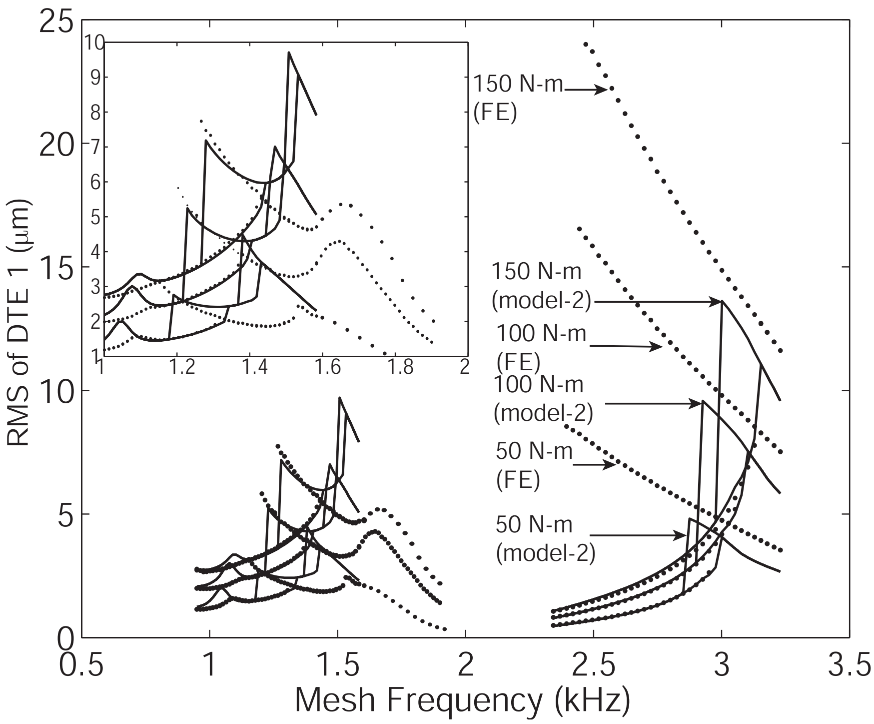

Figure 2.7: Comparison of dynamic transmission error (with mean removed) from Model-3 and finite element for multiple torques, no tooth modification, and other system parameters in Table 2.1.

Figure 2.6 shows the comparison of Model-2 and the FE model. The agreement is poorer than for Model-1. The amplitude of fundamental resonance of the second mode is much lower than FE. The RMS for off-resonant frequencies and the jump-up frequencies agree well with the benchmark though. The amplitude of the second harmonic resonance is much higher than for FE because the STE harmonics act as forced excitation compared to the parametric excitation of Model-1. The second harmonic resonance even shows nonlinear jumps from total tooth contact loss compared to the linear response of FE. The comparison of Model-3 and FE model in Figure 2.7 is poorer than Model-1 and similar to that of Model-2. The amplitudes of the fundamental resonances for Model-3 are even lower compared to FE than for Model-2.

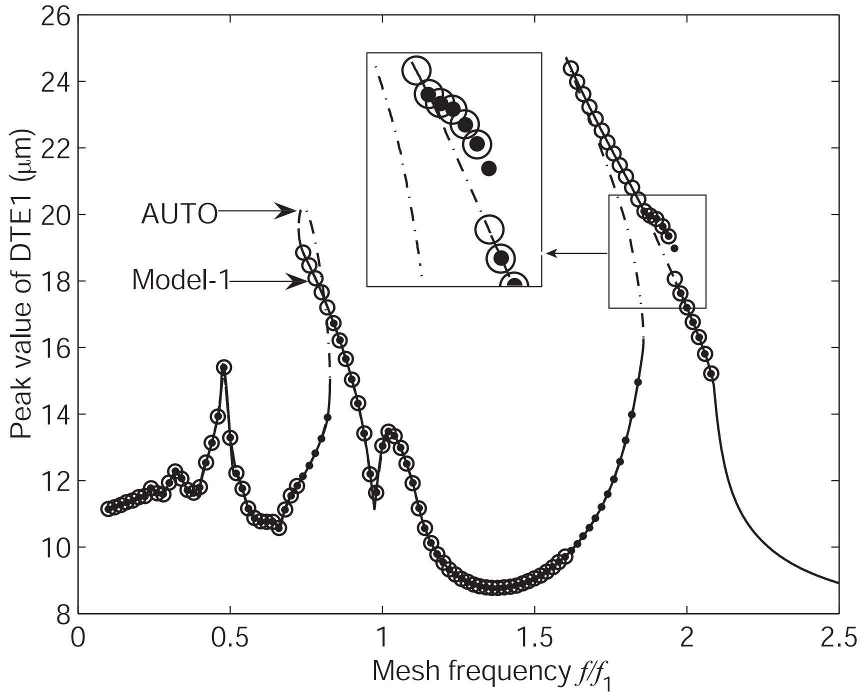

Figure 2.8: Comparison of dynamic transmission error from Model-1 and AUTO for input torque 100 *N-m*, no tooth modification, and other system parameters in Table 2.1 (—— stable AUTO solution; -.- unstable AUTO solution; • numerical up-sweep; ○ numerical down-sweep).

More comparisons with Model-1 are made using the established nonlinear solver AUTO [64]. Figure 2.8 depicts peak values of DTE over a speed range. The numerical integration results exactly match the stable solution branches of AUTO. The unstable solution branches of AUTO explain the jump phenomena in numerical integration. Bifurcations occur at the stability transition points associated with jump-up and jump-down frequencies. The small hump below $f / f_1 = 2$ from numerical integration results from primary parametric instability of the first mode superposed with fundamental resonance of the second mode because $\omega_2 \approx 2\omega_1$. The instability boundaries of AUTO match well with the frequency span of the hump from numerical integration.

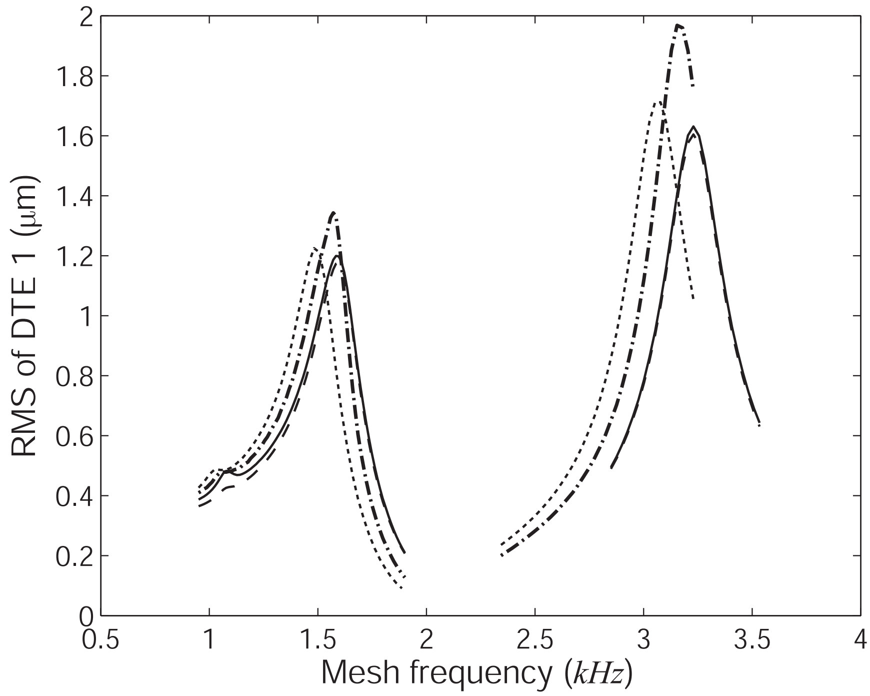

Figure 2.9: Comparison of dynamic transmission error (with mean removed) from the three analytical models and FE for modification A, input torque 100 *N-m*, and other system parameters in Table 2.1 (_ . . _ FE; ...... Model-1; ___ Model-2; _ _ _ Model-3).

We now consider the analytical models with profile modification for two linear tip relief conditions A and B. The profile modifications both start at HPSTC but have 10 μm and 25 μm relief magnitudes, respectively. Modification A reduces the peak-peak value of STE for 100 N-m input torque, and modification B increases it. The impact of profile modification A on DTE for the three models is compared with FE in Figure 2.9. No nonlinear jumps are observed. The predictions of the three analytical models agree well with the benchmark because of the absence of partial or total contact loss. The DTE amplitude is dramatically reduced at the fundamental and the second harmonic excitation resonances compared to that without profile modification.

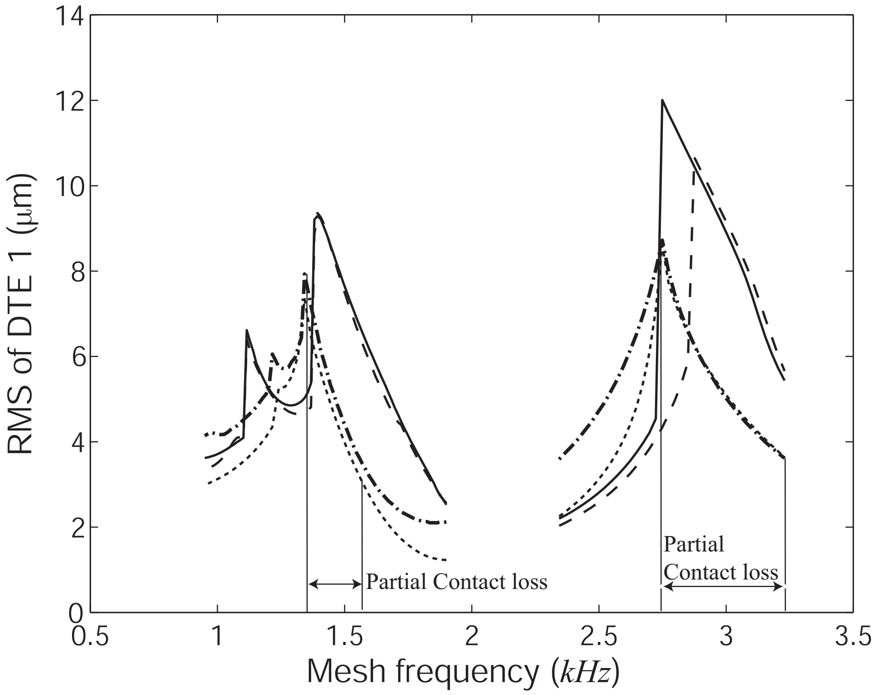

Figure 2.10: Comparison of dynamic transmission error (with mean removed) from the three analytical models and FE with modification B, input torque 100 N-m, and other system parameters in Table 2.1 (_ . . _ FE; ...... Model-1; ___ Model-2; _ _ _ Model-3).

The model comparisons with modification B are depicted in Figure 2.10. Model-1 agrees well with FE. The shapes and the peak amplitudes of the solution branches of Model-2 and Model-3, however, match poorly with the benchmark, including significant qualitative differences. FE and Model-1 show peculiar sharp peaks around the fundamental resonances. No jump phenomena occur despite the presence of partial contact loss as indicated in Figure 2.10. The frequencies of the resonance peaks drop from 1.6 *kHz* to 1.3 *kHz* and from 3.2 *kHz* to 2.7 *kHz* compared to the eigenvalue analysis because of the contact loss. These frequencies are higher than for the unmodified case of Figure 2.5 (1.2 *kHz* and 2.5 *kHz*) because the amount of contact loss (and so the reduction in average mesh stiffness over a response period) is reduced due to the profile modification. Although the peak-peak value of STE is increased by modification B, the amplitudes at the two fundamental resonances are reduced compared to those without modifications. The amplitude of the second harmonic excitation resonance ($f = 1.4$ *kHz*) increases from 4.5 μm to 8 μm, however, due to the profile modification. Thus, static and dynamic transmission errors do not always increase or decrease together.

Mode #	Mode type	ω_l (Hz)
1	Rigid body	69
2	Coupled lateral-rotational	446
3	Follower offline lateral	499
4	Coupled lateral-rotational	640
5	Coupled lateral-rotational	890
6	Coupled lateral-rotational	1076
7	Coupled lateral-rotational	2530
8	Coupled lateral-rotational	3850

Table 2.2: Natural frequencies for average mesh stiffnesses and bearing stiffness in Table 2.1.

2.4.1.2 Compliant bearing condition

The natural frequencies of Model-1 with compliant bearings are shown in Table 2.2. Mode 1 is the "rigid body" mode noted earlier. Mode 3 is decoupled follower translation along the off-line-of-action direction. The other modes involve coupled line-of-action-translation and rotation motions. Modes 6 and 7 involve mostly line-of-action translations of the idler.

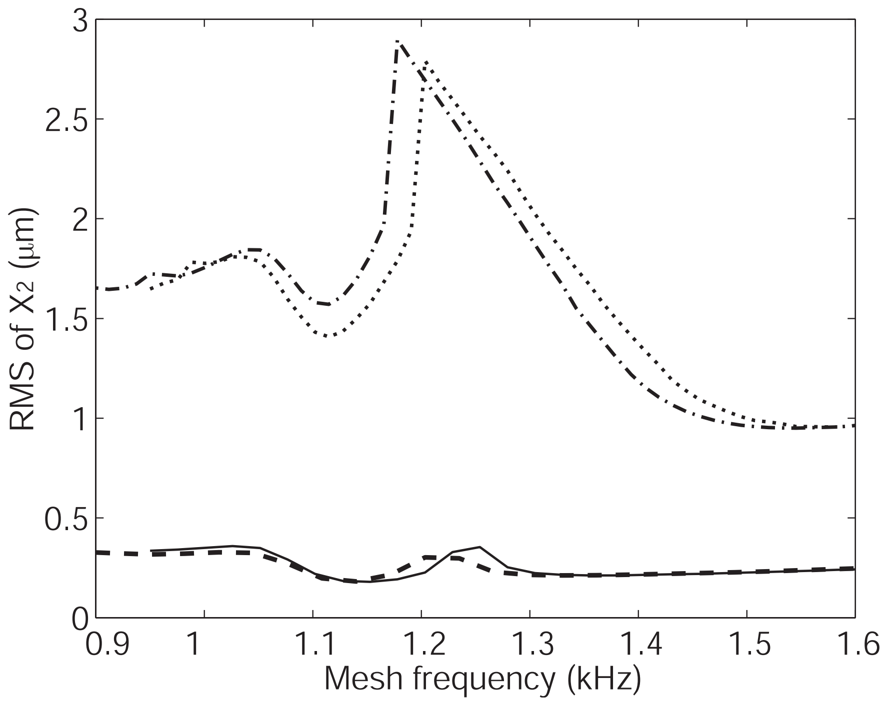

Figure 2.11: Comparison of idler line-of-action translation from Model-1 and FE with system parameters in Table 2.1 and input torque 100 *N-m* (_._ FE no profile modification; ...... Model-1 no profile modification; _ _ _ FE profile modification A; ___ Model-1 profile modification A).

Figure 2.11 shows good comparisons between Model-1 and FE for steady state idler line-of-action translation with no profile modification and with profile modification A. The two resonances near 1.08 *kHz* and 1.26 *kHz* are the first harmonic exciting mode 6 and the second harmonic exciting mode 7, respectively. The resonance amplitudes are significantly reduced and nonlinearity disappears for profile modification A, compared to the case with no profile modification. Note that the amplitudes for off-resonant frequencies are also reduced by the profile modification.

Summarizing, Model-1 provides good predictions of dynamic response for different torques, profile modifications, and bearing compliances. The peak amplitudes and frequency range with contact loss match well with FE. Although Model-2 and Model-3 yield acceptable predictions for strictly linear response, they work poorly when nonlinear partial or total contact loss occur and for higher harmonic resonances. The profile modification has significantly different impact on various resonances, which cannot be inferred from the STE.

2.4.2 Discussions on Nonlinear Dynamic Forces

2.4.2.1 Absence of profile modification

Mesh forces are a more challenging comparison with FE than DTE. As shown in Figure 2.5, mesh frequency $f = 2490$ *Hz* corresponds to the peak for the second mode resonance. The stable solution jumps down to the lower branch when mesh frequency is decreased to 2470 *Hz*. Figure 2.12 compares the Model-1 and FE resultant dynamic mesh forces (summation of the individual tooth pairs) for 2470 *Hz* and 2490 *Hz* without profile modification. The results agree well for both cases. No contact loss is observed for the lower branch frequency 2470 *Hz*, and the average mesh force is close to the static force $F = T_1 / r_1 = 2205$ *N*. Total contact loss at the first mesh occurs during 46% of a mesh cycle at the upper branch frequency 2490 *Hz*; the peak magnitude of dynamic force is over three times the static force.

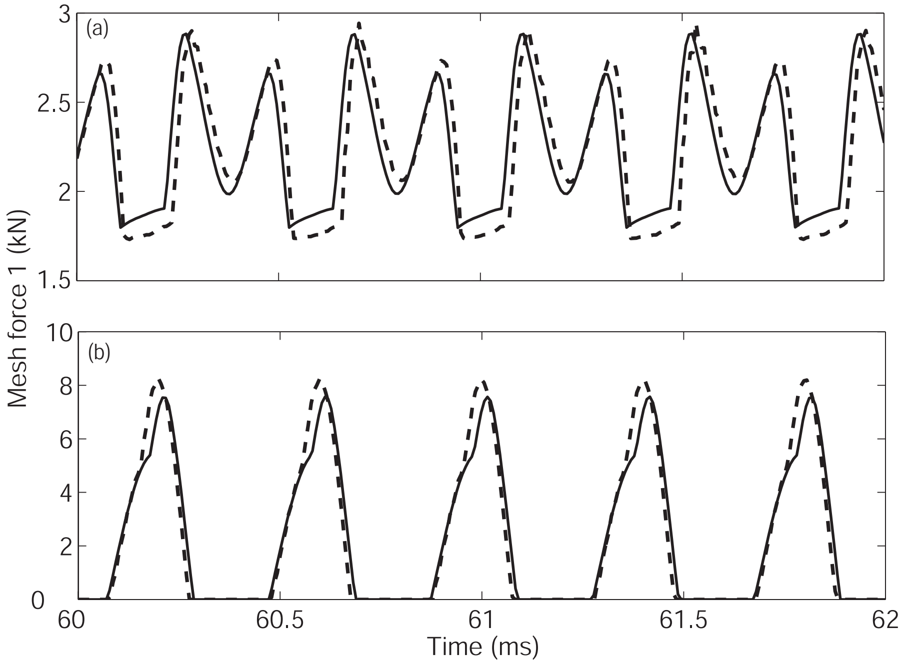

Figure 2.12: Dynamic mesh forces for mesh 1 for two mesh frequencies near jump-down for input torque 100 *N-m*, no tooth modification, and other system parameters in Table 2.1 (—— Model-1; – – FE); (a) Mesh frequency $f = 2470$ *Hz* for lower branch; (b) Mesh frequency $f = 2490$ *Hz* for upper branch.

2.4.2.2 Presence of profile modification

We now consider the dynamic forces for profile modifications A and B. Figure 2.13a with modification B shows that the peak mesh force of the second mode resonance peak (2750 *Hz*) reduces to 5.5 *kN* compared to 7.6 *kN* for the second mode resonance and unmodified gears in Figure 2.12b. The tooth pair separates when the DTE is less than the profile modification. In the nominal double tooth contact region, partial and total contact loss both occur. The second tooth pair is the first to lose contact; then, the first pair separates also; finally, the second pair regains contact. The span of total contact loss in a period decreases to 25% compared to 46% in Figure 2.12b.

The complicated tooth separation sequence for modification A and first mode resonance ($f = 1400\,Hz$) are illustrated in Figure 2.13b for 50 N-m. Contact loss occurs when the torque changes from 100 N-m (Figure 2.9) to 50 N-m, which is consistent with the well-known torque dependence of optimal profile modification. To better understand the separation, the figure includes the profile modification, DTE from Model-1, and number of engaged tooth pairs in a mesh period obtained by FE simulation. In the nominal double-tooth contact region marked by the dashed butterfly shape, the FE analysis shows four contact conditions: I) total contact loss; II) the second tooth pair loses contact; III) no contact loss and all gear teeth remain in nominal contact status; and IV) the first tooth pair loses contact. Model-1 determines the contact status of a tooth pair by comparing dynamic mesh deflection (DTE) and profile modification as shown in (2.4): I) $s_1 < g_{1,1} < g_{1,2}$ such that $h_{1,1} = h_{1,2} = 0$; II) $g_{1,1} < s_1 < g_{1,2}$ such that $h_{1,1} = 1$, $h_{1,2} = 0$; III) $g_{1,2} < g_{1,1} < s_1$ such that $h_{1,1} = h_{1,2} = 1$; IV) $g_{1,2} < s_1 < g_{1,1}$ such that $h_{1,1} = 0$, $h_{1,2} = 1$. Contact conditions from these criteria applied to the Model-1 DTE and modification agree well with the number of engaged tooth pairs from FE in Figure 2.13b. Partial contact loss (patterns II and IV) occurs between individual gear teeth and causes the sharp nonlinear solution branches at $f = 1.3\ kHz$ and $f = 2.7\ kHz$ in Figure 2.10. Partial contact loss is not included in Model-2 and Model-3.

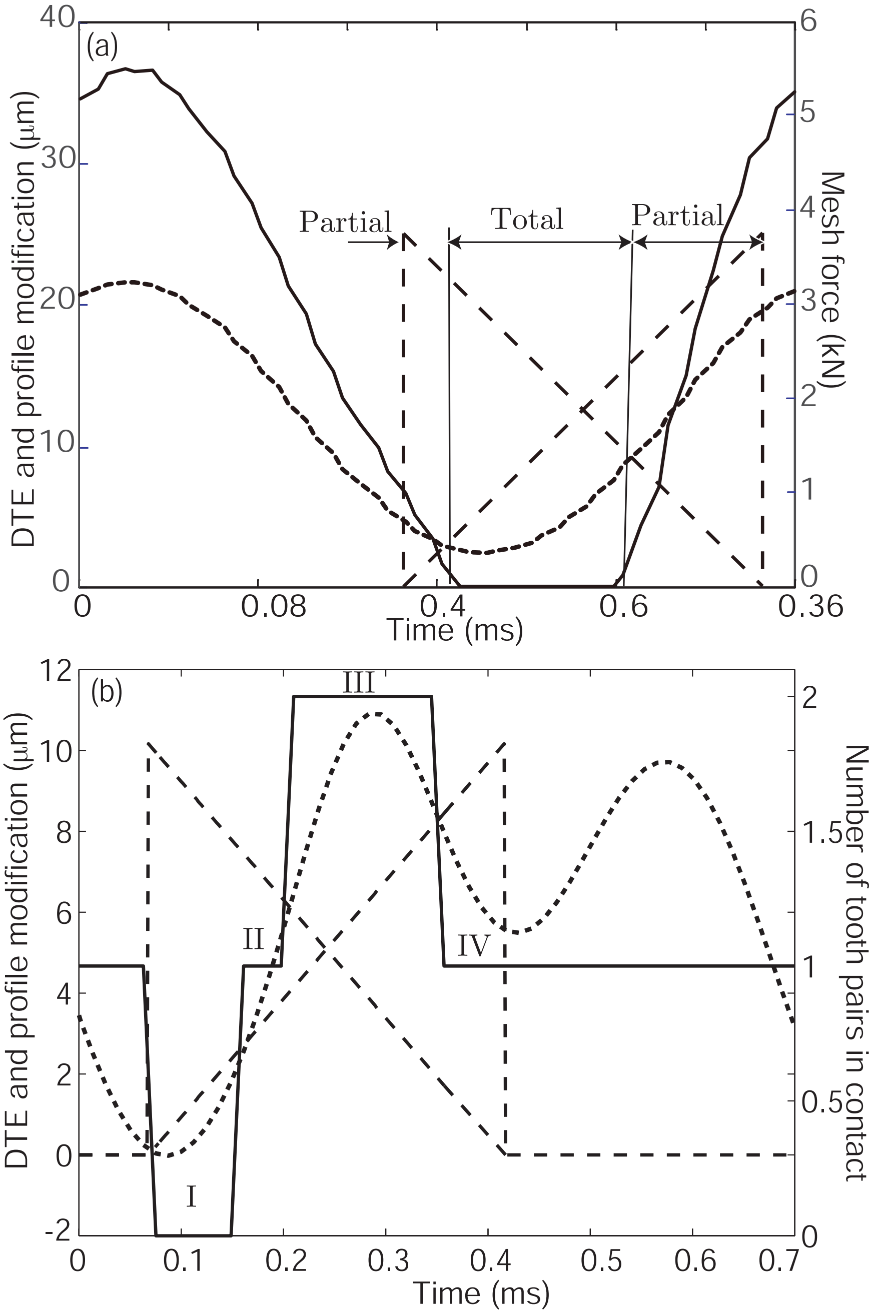

Figure 2.13: Profile modification, DTE from Model-1, and tooth contact from FE over one mesh cycle for system parameters in Table 2.1; (a) Mesh frequency 2750 *Hz* for torque 100 *N-m* and tooth modification B (_ _ _ profile modification; ...... DTE; ___ Mesh force); (b) Mesh frequency 1400 *Hz* for 50 *N-m* torque and tooth modification A (_ _ _ profile modification; ...... DTE; ___ tooth number).

2.5 Analytical Study on Optimal Profile Modification

2.5.1 Perturbation Analysis

With optimized profile modifications, the amplitude of parametrically excited responses can be drastically decreased and tooth separation can be avoided. In other words, the system operates in the linear dynamics range.

For the rotational model, there is one "rigid body" mode and two elastic modes. The two transmission errors $z_{1,2}$ describe the elastic motions of interest. The transformation between $\mathbf{u}=[u_1,u_2,u_3]^T$ and $\mathbf{x}=[z_1,z_2]^T$ is found from orthogonality of the "rigid body" mode to the elastic modes [65].

The linear, time-varying governing equations of Model-1 are recast as

$$\begin{aligned}
&\tilde{\mathbf{M}}\ddot{\mathbf{x}}(t)+\tilde{\mathbf{K}}(t)\mathbf{x}(t)=\tilde{\mathbf{E}}(t)\\
&\tilde{\mathbf{M}}=\frac{1}{(m_1+m_2+m_3)}\begin{bmatrix} m_1(m_2+m_3) & m_1m_3\\ m_1m_3 & m_3(m_1+m_2)\end{bmatrix}\\
&\tilde{\mathbf{K}}=\begin{bmatrix} k_1 & 0\\ 0 & k_2\end{bmatrix},\quad \tilde{\mathbf{E}}=\begin{bmatrix} F+L_1\\ F+L_2\end{bmatrix}
\end{aligned} \tag{2.12}$$

where $k_n=\sum_{p=1}^{P_n}k_{n,p}$ and $L_n=\sum_{p=1}^{P_n}k_{n,p}g_{n,p}$ are known. This has the form of a forced, parametrically excited system. Fourier expansion gives

$$\begin{aligned}
k_n&=\hat{k}_n+\varepsilon\left(\sum_{s=1}^{\infty}\kappa_{ns}e^{is\omega t}+c.c.\right)\\
L_n&=\hat{L}_n+\varepsilon\left(\sum_{s=1}^{\infty}\lambda_{ns}e^{is\omega t}+c.c.\right)
\end{aligned} \tag{2.13}$$

where $n=1,2$ is the mesh index, $\varepsilon=[\max(k_1)-\min(k_1)]/\hat{k}_1$ is the stiffness variation ratio of k_1, $\hat{L}_n$ is the mean value of L_n, and $\kappa_{ns} = O(1)$ and $\lambda_{ns} = O(1)$ are known complex Fourier amplitudes because $k_{n,p}$ and $g_{n,p}$ are specified. The eigenvalue problem of (2.12) using the average mesh stiffnesses is $\left(\omega_m^2 \mathbf{M} - \mathbf{K}\right)\mathbf{v}_m = 0$ ($m = 1, 2$). The modal matrix $\mathbf{V} = [\mathbf{v}_1\ \mathbf{v}_2]$ is such that $\mathbf{V}^T\mathbf{M}\mathbf{V} = \mathbf{I}$.

Substituting $\mathbf{x} = \mathbf{V}\mathbf{q}$ and pre-multiplying by $\mathbf{V}^T$, (2.12) is cast into the modal form

$$\begin{aligned} &\frac{d^2 q_m}{dt^2} + \varepsilon\mu\omega_m \frac{dq_m}{dt} + \omega_m^2 q_m + \varepsilon \sum_{n=1}^{2}\sum_{l=1}^{2} v_{nm} v_{nl} \left(\sum_{s=1}^{\infty} \kappa_{ns} e^{is\omega t} + c.c.\right) q_l = \\ &\sum_{n=1}^{2} v_{nm}(F + \hat{L}_n) + \varepsilon \sum_{n=1}^{2} v_{nm} \left(\sum_{s=1}^{\infty} \lambda_{ns} e^{is\omega t} + c.c.\right) \quad m = 1, 2 \end{aligned} \tag{2.14}$$

where v_{nm}, v_{nl} are elements of $\mathbf{V}$ and the modal damping is $\zeta = \varepsilon\mu / 2$.

In practice, $\varepsilon \ll 1$. The excitations (k_n and L_n) are separated into unperturbed ($\hat{k}_n$ and $\hat{L}_n$) and perturbed parts (κ_{ns} and λ_{ns}). The dynamic responses are approximated by asymptotic power series, and t is expanded into multiple time scales $t_r = \varepsilon^r t_0$ [66]

$$q_m = u_{m0}(t_0, t_1 \ldots) + \varepsilon u_{m1}(t_0, t_1 \ldots) + O(\varepsilon^2) \tag{2.15}$$

Substitution of (2.15) into (2.12) yields the ε^0 and ε^1 order differential equations

$$\frac{\partial^2 u_{m0}}{\partial t_0^2} + \omega_m^2 u_{m0} = \sum_{n=1}^{2} v_{nm}(F + \hat{L}_n) \quad m = 1,\ 2 \tag{2.16}$$

$$\begin{aligned} &\frac{\partial^2 u_{m1}}{\partial t_0^2} + \omega_m^2 u_{m1} = -2\frac{\partial^2 u_{m0}}{\partial t_0 \partial t_1} - \mu\omega_m \frac{\partial u_{m0}}{\partial t_0} - \\ &\sum_{n=1}^{2}\sum_{l=1}^{2} v_{nm} v_{nl} \left(\sum_{s=1}^{\infty} \kappa_{ns} e^{is\omega t_0} + c.c.\right) u_{l0} + \sum_{n=1}^{2} v_{nm} \left(\sum_{s=1}^{\infty} \lambda_{ns} e^{is\omega t_0} + c.c.\right) \quad m = 1,\ 2 \end{aligned} \tag{2.17}$$

The leading order solutions for (2.16) are

$$u_{m0} = C_m + \left[A_m(t_1) e^{i\omega_m t_0} + c.c. \right] \qquad C_m = \sum_{n=1}^{2} v_{nm} (F + \hat{L}_n) / \omega_m^2 \tag{2.18}$$

When the mesh frequency is near a natural frequency, i.e., $\omega = \omega_m + \varepsilon\sigma$ (σ is the detuning parameter), parametric instability occurs. Substituting this ω into the right-hand-side (RHS) of (2.17) yields

$$\begin{aligned} RHS = &-(2i\omega_m \frac{\partial A_m}{\partial t_1} + \mu i\omega_m A_m) e^{i\omega_m t_0} + \sum_{n=1}^{2} v_{nm} \left[\sum_{s=1}^{\infty} \lambda_{ns} e^{is(\omega_m + \varepsilon\sigma)t_0} + c.c. \right] \\ &-\sum_{s=1}^{\infty} \sum_{l=1}^{2} \sum_{n=1}^{2} v_{nm} v_{nl} \kappa_{ns} e^{is(\omega_m + \varepsilon\sigma)t_0} \left[C_l + (A_l e^{i\omega_l t_0} + c.c.) \right] \qquad m = 1,\ 2 \end{aligned} \tag{2.19}$$

For $\omega_2 \neq 2\omega_1$, elimination of secular terms causing unbounded, aperiodic response requires

$$2i\omega_m \frac{\partial A_m}{\partial t_1} + \mu i\omega_m^2 A_m + \Lambda e^{i\sigma t_1} + \Theta \bar{A}_m e^{i2\sigma t_1} = 0 \tag{2.20}$$

$$\Lambda = \sum_{l=1}^{2} \sum_{n=1}^{2} v_{nm} v_{nl} \kappa_{n1} C_l - \sum_{n=1}^{2} v_{nm} \lambda_{n1} \qquad \Theta = \sum_{n=1}^{2} v_{nm}^2 \kappa_{n2} \tag{2.21}$$

where $\bar{A}_m$ denotes the complex conjugate of A_m. Substitution of $A_m = \alpha e^{i\beta}$ and $\beta = \sigma t_1 - \gamma$ into (2.21) gives

$$2\omega_m (i\frac{\partial \alpha}{\partial t_1} + \alpha \frac{\partial \gamma}{\partial t_1} - \sigma\alpha) + i\mu\omega_m^2 \alpha + \Lambda e^{i\gamma} + \Theta \alpha e^{i2\gamma} = 0 \tag{2.22}$$

Considering the steady state response with $\partial\alpha / \partial t_1 = \partial\gamma / \partial t_1 = 0$, (2.22) separates into real and imaginary parts as

$$\begin{aligned} (\Theta_R - 2\sigma\omega_m)\cos\gamma + (\mu\omega_m^2 - \Theta_I)\sin\gamma + \Lambda_R / \alpha = 0 \\ (\mu\omega_m^2 + \Theta_I)\cos\gamma + (\Theta_R + 2\sigma\omega_m)\sin\gamma + \Lambda_I / \alpha = 0 \end{aligned} \tag{2.23}$$

This gives the frequency response approximation for $\omega \approx \omega_m$ as

$$\alpha = \frac{\varepsilon}{|\Delta|}\Big\{|\Lambda|^2\Big[|\varepsilon\Theta|^2 + 4\omega_m^2(\omega-\omega_m)^2 + 4\zeta^2\omega_m^4\Big] + 4\left(\Lambda_R^2 - \Lambda_I^2\right)\Big[\omega_m\Theta_R(\omega-\omega_m) + \zeta\omega_m^2\Theta_I\Big]$$
$$-8\Lambda_R\Lambda_I\Big[\zeta\omega_m^2\Theta_R - \omega_m\Theta_I(\omega-\omega_m)\Big]\Big\}^{1/2} \tag{2.24}$$
$$\Delta = |\varepsilon\Theta|^2 - 4(\omega-\omega_m)^2\omega_m^2 - \zeta^2\omega_m^4$$

where Λ_R, Λ_I and Θ_R, Θ_I are real and imaginary parts of Λ and Θ.

The complex quantity Λ includes the contributions of the first harmonics of the individual mesh stiffnesses and profile modifications, and Θ includes only the second harmonics of the two mesh stiffnesses. Parametric instability analysis shows that, in the absence of profile modification ($\lambda_{ns} = 0$), the second harmonics of mesh stiffness in Θ cause (theoretically) unbounded linear response when $\omega \approx \omega_m$ [19, 20, 67]; the instability boundaries are $\omega = \omega_m \pm \frac{1}{2}\sqrt{|\varepsilon\Theta|^2/\omega_m^2 - 4\zeta^2\omega_m^2}$. In practice, large response for mesh frequencies in this range cause contact loss that bounds the associated nonlinear response. In the presence of profile modification, however, the response remains bounded even without contact loss; the frequency response has the character of a low-amplitude resonance as given by (2.24) and confirmed by numerical integration in results to follow. The amplitude of the resonant response depends on both Λ and Θ, and tuning the profile modification included in Λ allows one to minimize the amplitude according to (2.21) and (2.24). If $|\kappa_{n2}| \ll |\kappa_{n1}|$ (e.g., $c_n \approx 1.5$), (2.24) simplifies to

$$\alpha = \frac{\varepsilon|\Lambda|}{\omega_m\sqrt{4(\omega-\omega_m)^2 + \zeta^2\omega_m^2}} \tag{2.25}$$

Equations (2.25) and (2.21) show the interaction between mesh stiffness harmonics κ_{n1} and profile modification harmonics λ_{n1}. Optimizing the modifications λ_{n1} to minimize α for the mth mode depends on mesh phasing and contact ratio (which control κ_{n1}) as well as the vibration modes. Equations (2.25) and (2.21) also show that profile modification can reduce or increase response amplitude, and the signs of quantities in Λ are important in this regard.

Similarly, the frequency response for resonance driven by the second-harmonic of mesh stiffness variation and profile modification ($\omega \approx \omega_m / 2$) has the same form as (2.24) except Λ and Θ in (2.21) become

$$\Lambda = \sum_{l=1}^{2} \sum_{n=1}^{2} v_{nm} v_{nl} \kappa_{n2} C_l - \sum_{n=1}^{2} v_{nm} \lambda_{n2} \qquad \Theta = \sum_{n=1}^{2} v_{nm}^2 \kappa_{n4} \tag{2.26}$$

For the case where $\omega \approx 2\omega_m$, perturbation yields the frequency bounds for instability as

$$\omega = 2\omega_m \pm \frac{1}{2\omega_m} \sqrt{\left| \sum_{n=1}^{2} v_{nm}^2 \varepsilon \kappa_{n1} \right|^2 - \zeta^2 \omega_m^4} \tag{2.27}$$

and the linear system amplitude is unbounded in this mesh frequency range. The primary parametric instability boundaries depend only on the first harmonic of mesh stiffness, vibration modes, and modal damping. Unlike the instabilities captured in (2.21), (2.24) and (2.26), profile modifications have no influence on the primary instability boundaries and do not prevent the large amplitude response that initiates contact loss. The nonlinear response resulting from the instability, however, is affected by profile modifications but not analyzed here.

2.5.2 Optimal Profile Modifications

2.5.2.1 Optimal profile modification for minimum static transmission error

Considering each tooth pair carrying half the load during double-tooth contact, the mesh stiffnesses of double-tooth contact and single-tooth contact for mesh n are chosen as $\hat{k}_n[1+\varepsilon_n(1-c_n)]$ and $\hat{k}_n[1+\varepsilon_n(2-c_n)]/2$, respectively, where $\varepsilon_n = [\max(k_n)-\min(k_n)]/\hat{k}_n$. From (2.8), excluding corner contact and misalignment, the STE with minimal peak-peak value is obtained when HPSTC is the starting roll angle (i.e., $\varsigma_n = c_n - 1$) and the tip relief magnitudes satisfy

$$\rho_n = \frac{2F\varepsilon_n}{\hat{k}_n[1+\varepsilon_n(1-c_n)][1+\varepsilon_n(2-c_n)]} \tag{2.28}$$

The relief magnitude ρ_n is twice the peak-peak value of the STE without profile modification, which is confirmed by FE analysis. Indeed, the magnitude that minimizes STE depends only on the parameters from its own single mesh (load, average mesh stiffness, mesh stiffness variation, and contact ratio).

2.5.2.2 Numerical validation of perturbation analysis

The perturbation solutions for dynamic response with optimal profile modification are compared to numerical integration of the nonlinear time-varying model. A profile modification for minimum STE is chosen from (2.28) with the default parameters in Table 2.1 and $T_1 = 100\ N\text{-}m$ (HPSTC as the starting roll angle, $\rho_1 = 10\,\mu m$, and

$\rho_2 = 12\,\mu m$). The first vibration mode is dominated by the second mesh motion with $\mathbf{v}_1 = [-0.30 \ \ -0.55]^T$. The second mode is $\mathbf{v}_2 = [-1.1 \ \ 0.53]^T$.

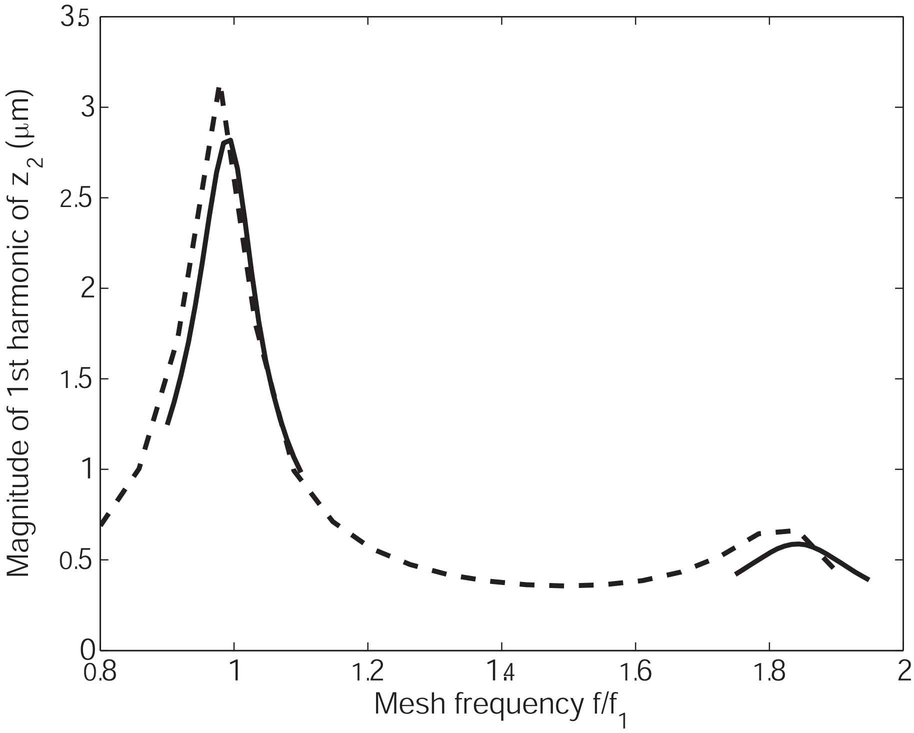

Figure 2.14: Comparison of DTE between perturbation and numerical simulation for $c_1 = 1.4$, $c_2 = 1.6$, $\phi = 0$, $\rho_1 = 10\,\mu m$, $\rho_2 = 12\,\mu m$, and gear 1 torque 100 *N-m* (___ perturbation; _ _ _ numerical integration).

Figure 2.14 shows that the perturbation frequency response agrees well with the numerical results near the two fundamental resonances. The linear resonant response from the numerical result of the nonlinear model indicates the selected profile modification reduces amplitude and eliminates contact loss. This also indicates that the perturbation solution captures the response due to optimized profile modification applied to this nonlinear, time-varying gear system.

2.5.2.3 Impact of profile modification magnitude

The analytical expressions (2.24) and (2.25) show the interactions between profile modifications (ρ_n and ς_n) and mesh stiffnesses (ε_n, ϕ, and c_n). For rectangular wave mesh stiffness approximations and profile modifications starting from HPSTC, the complex Fourier amplitudes for k_n and L_n in (2.13) are

$$\begin{aligned}
\kappa_{1s} &= \frac{\bar{k}_1}{s\pi}\sin s\pi(c_1-1)e^{is\pi(c_1-1)}, \quad \lambda_{1s} = \frac{\tilde{\varepsilon}_1(F+\bar{L}_1)}{\varepsilon s\pi}\sin s\pi(c_1-1)e^{is\pi(c_1-1)} \\
\kappa_{2s} &= \frac{\varepsilon_2\bar{k}_2}{\varepsilon s\pi}\sin s\pi(c_2-1)e^{is\pi(c_2-1+\phi)}, \quad \lambda_{2s} = \frac{\tilde{\varepsilon}_2(F+\bar{L}_2)}{2\varepsilon s\pi}\sin s\pi(c_2-1)e^{is\pi(c_2-1+\phi)}
\end{aligned} \tag{2.29}$$

where B_n is the STE of mesh *n* for average mesh stiffness. Substitution of (2.29) into Λ of (2.21) gives

$$\begin{aligned}
\Lambda &= \Delta_1 e^{i\pi(c_1-1)} + \Delta_2 e^{i\pi(c_2-1+\phi)} \\
\Delta_n &= \frac{v_{nm}\hat{k}_n \sin\pi(c_n-1)}{\pi}\left[\sum_{l=1}^{2} v_{nl}C_l - \left(B_n+\eta_n\right)\right] \quad n=1,2
\end{aligned} \tag{2.30}$$

Λ includes the mean and the first harmonic excitation of mesh stiffness and profile modification from each mesh. These excitations are coupled through the mesh phasing, contact ratio, and vibration modes.

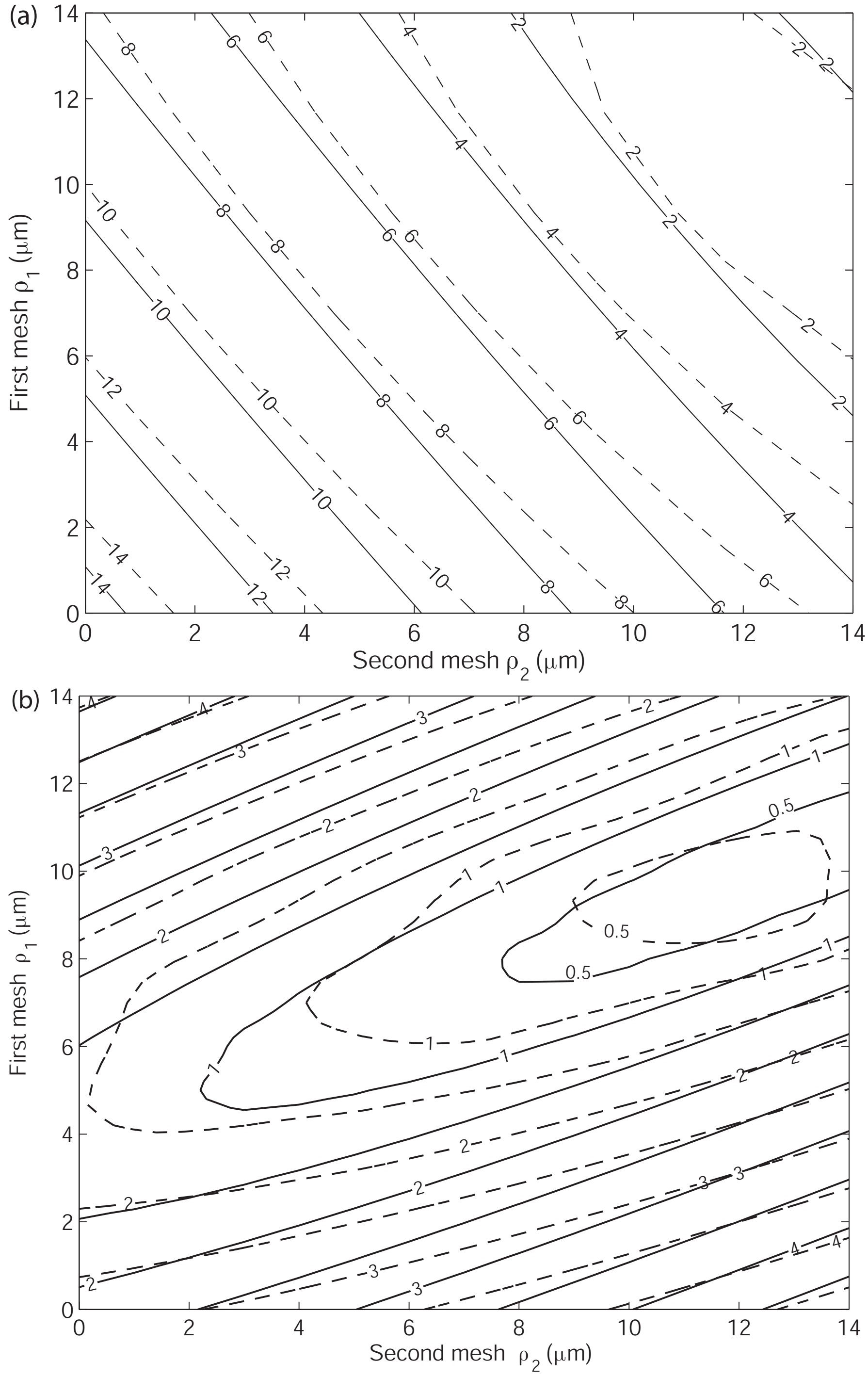

Figure 2.15: Contour plot of the DTE amplitudes varying with the two tip relief magnitudes for $\omega = \omega_1$, $c_1 = 1.4$, $c_2 = 1.6$, $\varsigma_n = c_n - 1$, and $\phi = 0$ (—— analytical solution; - - - numerical integration) (a) z_1 (b) z_2.

The influence of the two relief magnitudes on the DTE amplitudes z_1 and z_2 at the first-mode fundamental resonance is studied in Figure 2.15. The analytical and numerical solutions agree well and show a set of elliptical contours formed by the two relief magnitudes. From (2.25) and (2.30), the analytical solution shows that the square of the amplitude is

$$\alpha^2 = \frac{\Delta_1^2 + \Delta_2^2 + 2\Delta_1\Delta_2 \cos\pi\left(c_2 - c_1 + \phi\right)}{\omega_m\sqrt{4\left(\omega-\omega_m\right)^2 + \zeta^2\omega_m^2}} = \frac{\chi_1\rho_1^2 + \chi_2\rho_1\rho_2 + \chi_3\rho_2^2 + \chi_4\rho_1 + \chi_5\rho_2 + \chi_6}{\omega_m\sqrt{4\left(\omega-\omega_m\right)^2 + \zeta^2\omega_m^2}} \quad (2.31)$$

where χ_{1-6} are real coefficients. When $\chi_2^2 < 4\chi_1\chi_3$, (2.31) describes an ellipse in the $\rho_1 - \rho_2$ plane. The center and axes of the ellipse are independent of α. The elliptical contours have the same center and the same directions for the two axes whose orientation and magnitude depend on c_n, ε_n, ϕ, $\bar{k}_n$, F, and modal properties. The response amplitude is most sensitive to relief magnitudes along the minor axis of the elliptical contours, and it is least sensitive to relief magnitudes along the major axis. The optimal profile modifications are bounded by an elliptical contour, e.g., the contour with amplitude 0.5 in Figure 2.15b. The two DTE for the same resonance have different modifications yielding the minimum DTE and different orientations for the elliptical axes, which means the modification optimized for one DTE can be non-optimal for the other DTE.

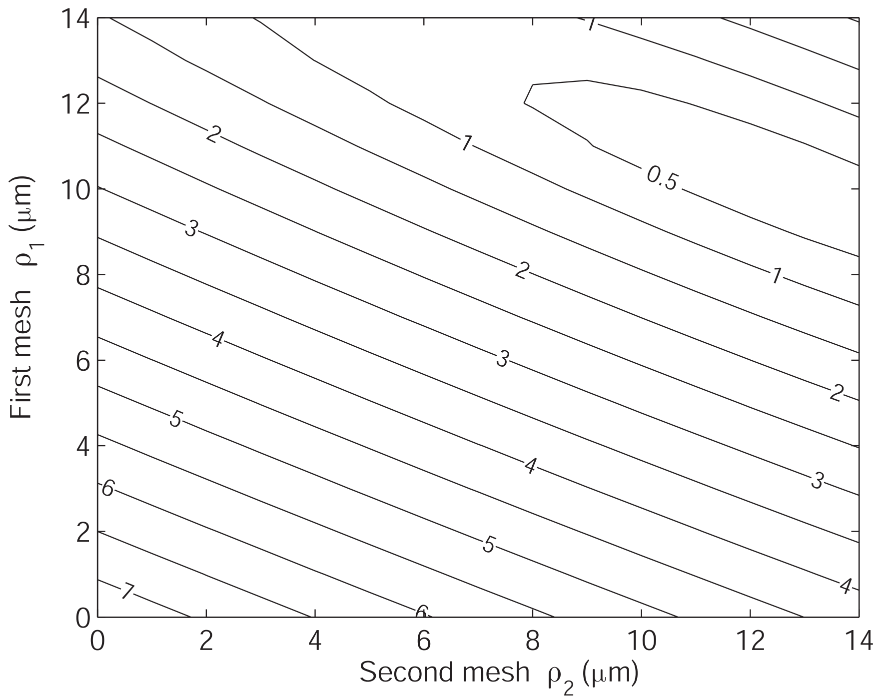

Figure 2.16: Contour plot of the response amplitude z_2 varying with two tip relief magnitudes for $\omega = \omega_1$, $c_1 = 1.4$, $c_2 = 1.6$, $\varsigma_n = c_n - 1$, and $\phi = \pi$.

The impact of tip relief magnitudes is re-examined with the mesh phasing changed from 0 to π in Figure 2.16. The directions of the elliptical axes are rotated clockwise about 40 degrees due to the change of mesh phasing. The center of the contours is only slightly changed. $\Delta_{1,2} = 0$ in (2.30) corresponds to the center point, and this is independent of mesh phasing. From (2.31) and as shown in Figure 2.16, however, mesh phasing affects the orientation of the major and minor axes of the elliptical contours. This is important as it changes the sensitivity to parameters, which dictates the robustness of the selected modification to uncertainties in model parameters. For instance, mesh phasing variation rotates the optimal elliptical zone so that the profile modification optimized for a previous mesh phasing can fall out of the optimal zone. This significant effect of mesh phase demonstrates the need to consider interactions between the two meshes in optimizing the modifications, as opposed to the common practice of optimizing modifications for each mesh individually based on static TE.

2.5.2.4 Impact of contact ratio

The impact of the contact ratios c_n on the amplitude of z_2 near ω_1 is depicted in Figure 2.17. The analytical and numerical solutions show peaks near $c_1 = 1.2$, $c_2 = 1.25$ and $c_1 = 1.7$, $c_2 = 1.75$. Both solutions also indicate valleys for integer c_n and around $c_1 = c_2 = 1.5$. According to (2.25), (2.30), the given system parameters, and the resulting vibration modes, the amplitude α for $\omega \approx \omega_1$ ($m = 1$) is determined by

$$|\Lambda| = \left| \begin{array}{l} \hat{k}_1 \dfrac{8.6\times10^{-7} - 0.30(B_1 + \eta_1)}{\pi} \sin \pi (c_1 - 1) \\ + \hat{k}_2 \dfrac{2.0\times10^{-6} - 0.55(B_2 + \eta_2)}{\pi} \sin \pi (c_2 - 1) e^{i\pi(c_2 - c_1)} \end{array} \right| \qquad (2.32)$$

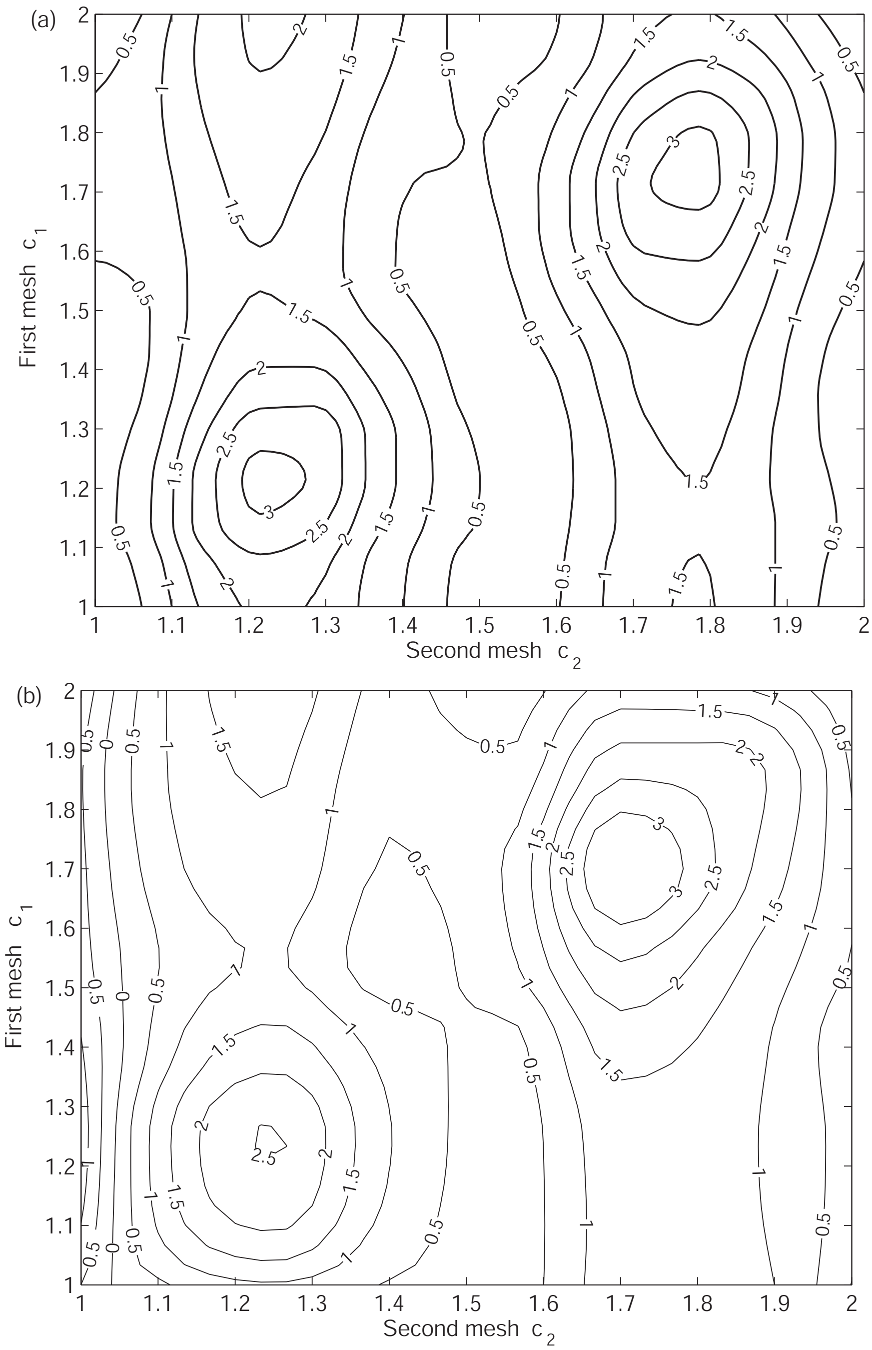

Figure 2.17: Contour plot of z_1 amplitude varying with two contact ratios for $\omega = \omega_2$, $\rho_1 = 10\ \ \mu m$, $\rho_2 = 12\mu m$, $\varsigma_n = c_n - 1$, and $\phi = 0$ (a) analytical solution (b) numerical integration.

The first term captures the interplay between mesh stiffness excitation (first term of the numerator) and profile modification η_1 (second term of the numerator) at the first mesh; the second term captures this for the second mesh. Note $\hat{k}_{1,2}$, $B_{1,2}$, and $\eta_{1,2}$ are always positive. For the current parameter set, the two numerators are positive, and, considering the complex exponential, the two terms in (2.32) are additive to $|\Lambda|$ for the entire $c_1 - c_2$ plane except near the two corners $c_1 \approx 1, c_2 \approx 2$ and $c_1 \approx 2, c_2 \approx 1$ (where response amplitude is small for nearly integer contact ratios). Examining each numerator, the terms involving profile modification $(B_n + \eta_n) > 0$ have opposite sign as the first terms from mesh stiffness excitation $\hat{k}_n$. This analytically shows the counteraction of mesh stiffness excitations from profile modification. η_n in (2.29) is maximized for $c_1 = c_2 = 1.5$ and, because the numerators remain positive, this maximizes the counteraction of mesh stiffness excitation and minimizes the response amplitude, thus explaining the valley in Figure 2.17. The amplitude of z_2 is more sensitive to c_2 because the second mesh strain energy dominates for this mode. For $c_1 = c_2 = 1.25$ and $c_1 = c_2 = 1.75$, despite the counteraction from profile modification, the contributions of $|\Theta|$ from the second harmonics of mesh stiffnesses are maximized, which correlates to the two peaks in the contour plots. The valleys near integer contact ratios are because $|\Lambda| = |\Theta| = 0$ for $c_1 = c_2 = \text{integer}$.

2.5.2.5 Impact of profile modification length

The impact of modification length ς_n on the amplitude of z_2 near ω_2 is depicted in Figure 2.18. A valley is shown around profile modification starting at HPSTC ($\varsigma_1 = 0.4$, $\varsigma_2 = 0.6$). Two peaks occur near $\varsigma_1 = 0$, $\varsigma_2 = 0.7$ and $\varsigma_1 = 0.55$, $\varsigma_2 = 0.08$. Substitution of $c_1 = 1.4$ and $c_2 = 1.6$ into (2.30) with $\omega \approx \omega_2$ ($m = 2$), which governs response amplitude α in (2.25), yields

$$|\Lambda| = \left| \hat{k}_1 \frac{2.9\times 10^{-6} + (B_1 + \eta_1)}{\pi} - \hat{k}_2 \frac{1.8\times 10^{-6} + 0.50(B_2 + \eta_2)}{\pi} e^{i\pi/5} \right| \tag{2.33}$$

Because of the vibration mode $\mathbf{v}_2$, the contribution from mesh stiffness variation of the first mesh (2.9×10^{-6}) has the same sign as the profile modification $(B_1 + \eta_1) > 0$ (and similarly for the second mesh stiffness variation and $(B_2 + \eta_2) > 0$). This means mesh stiffness and profile modification excitations do not counteract each other for the same mesh. On the other hand, the two terms in (2.33) have opposite sign, so the two meshes counteract each other (after accounting for the complex exponential). $\eta_n = 0$ when there is no profile modification for mesh n, in which case the other mesh excitation dominates in (2.33) and the minimized counteraction from mesh n to the other mesh yields the peaks in Figure 2.18. The profile modification near the valley achieves the best mesh counteraction. The results indicate the need to consider interactions between the profile modifications for the multiple meshes in multi-mesh gearsets. Note that the interaction between the two meshes (as in (2.33)) or between mesh stiffness and profile modification excitations at the same mesh (as in (2.32)) is sharply affected by mesh phasing and contact ratios.

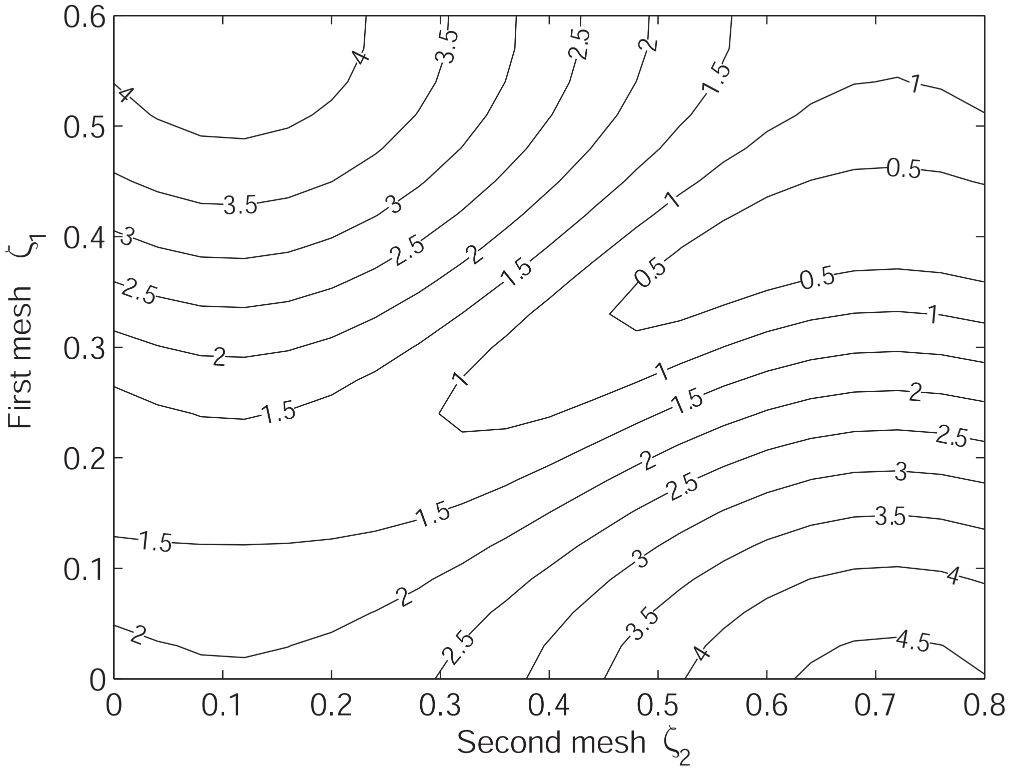

Figure 2.18: Contour plot of z_2 amplitude varying with two modification lengths for $\omega = \omega_2$, $c_1 = 1.4$, $c_2 = 1.6$, $\rho_1 = 10\mu m$, $\rho_2 = 12\mu m$, and $\phi = 0$.

CHAPTER 3

NONLINEAR DYNAMICS OF IDLER GEAR SYSTEMS

This chapter exmaines the nonlinear, parametrically excited dynamics of idler gearsets having two interacting parametric excitation sources and two tooth separations. The ratio of mesh stiffness variation to its mean value and the time of tooth separation compared to mesh period are assumed to be small parameters. The non-smooth tooth separation function describing contact loss and the variable mesh stiffness are reformulated into a form suitable for perturbation analysis to obtain periodic steady state solutions near primary, secondary, and subharmonic resonances. The perturbation analysis for this strongly nonlinear system compares well to harmonic balance/arclength continuation and numerical integration solutions. The impact of key parameters on the nonlinear response is discussed using the analytical closed-form expressions.

3.1 Introduction

Multi-mesh gear systems are widely used in a variety of industrial machinery, where they can generate vibration that negatively impacts noise, product quality, and reliability (gear tooth failure and bearing damage). The complicated dynamic forces at the gear meshes are the source of vibration. Parametric excitation results from the periodically-varying gear tooth flexibility (mesh stiffness). Tooth backlash is intentionally introduced to accommodate tolerances, lubrication, and thermal expansion. It admits the contact loss and backside contact that can occur during gear vibrations.

Extensive research has focused on the study of single mesh gear pair dynamics [2-5]. Recently, considerable progress has been made in the modeling and analysis of planetary (or epicyclic) gears [6-9]. Studies on multi-mesh gear systems, however, are limited. The studied topics on single mesh and planetary gears include parametric instabilities [19, 20], friction-induced vibration [18], dynamic response [13, 14], and bifurcations [15-17]. Many different mathematical models have been established, as reviewed by Blankenship and Singh [21], Ozguven and Houser [22], and Velex and Maatar [9]. Dynamic modeling and analysis of multi-mesh gear systems includes the works in [11, 19, 23-26, 68-70].

Parametrically excited gear dynamics problems have been examined, where mesh stiffness variation is the excitation source [19, 20, 31-33, 71]. Two types of dynamic models are established: linear time-varying (LTV) and nonlinear time-varying (NTV). LTV models identify operating conditions that cause parametric instabilities. The works [31, 33, 71] investigate parametric instability of a single pair of gears using a Mathieu equation. Lin and Parker [19, 20] examine two-stage systems and planetary gears and obtain boundaries separating stable and unstable conditions.

Under conditions of parametric instabilities, tooth separation can occur due to the clearance between gear teeth. The contact loss is a softening nonlinearity that causes phenomena such as jumps, period-doubling, and chaos [29]. Numerical integration and harmonic balance methods are employed in previous studies to attack such strongly nonlinear problems. The papers [5, 8, 72] adopt a finite element/contact mechanics method to analyze the nonlinear dynamic response of single-mesh and planetary gears. Kahraman and Singh [4] explore the interactions between time-varying mesh stiffness and contact loss nonlinearity of single-mesh gears. Al-shyyab and Kahraman [24] use harmonic balance and continuation methods to investigate subharmonic and chaotic motions of a multi-mesh gear train. Long subharmonic motions and period-doubling phenomenon leading to chaotic behavior are observed. Theodossiades and Natisiavas [37] predict periodic steady state responses by using a piecewise linear technique and perturbation analysis.

The parametric excitation and contact loss lead to nonlinear, time-varying differential equations with multiple degrees of freedom. This typically necessitates numerical simulation. The computational results, however, provide limited physical understanding, and the conclusions are often valid for only a certain group of parameters. With appropriate assumptions, the present work seeks analytical approximations for the periodic steady state solutions. Perturbation yields closed-form expressions that expose the impact of key parameters on the nonlinear dynamic response. The expressions in terms of fundamental design quantities have natural practical applications. One of the most important distinctions in multi-mesh systems is the interaction between mesh parameters such as the phasing between the multiple mesh stiffness fluctuations and contact ratios. The significance of the phase of mesh stiffnesses on dynamic responses has been discussed recently in [61, 72-74]. This work discusses the interplay of the phases with contact ratios, and their significant impact on nonlinear response for fundamental, secondary, and subharmonic resonances. The impact of system parameters on the instability and the amplitude of the nonlinear resonance are studied analytically and confirmed with numerical integration, harmonic balance, and finite element.

3.2 Dynamic Model and Method

3.2.1 Dynamic Model

Lumped-parameter models such as that in Figure 3.1 for an idler gearset are used to study gear dynamics because the gear teeth are usually much more compliant than the gear bodies. By focusing on the tooth contact and bearing forces, lumped-parameter models capture the primary dynamics while providing computational efficiency and opportunity for analytical study, in contrast to finite element and comparable models. In this study, the dynamic model is confined to spur gear systems. To focus on the interactions between the two gear meshes, geometric errors, sliding friction, bearing compliance and gear tilting motions are not considered. Backside tooth contact is not normally observed in practice due to the gear preload and backlash and it is neglected.

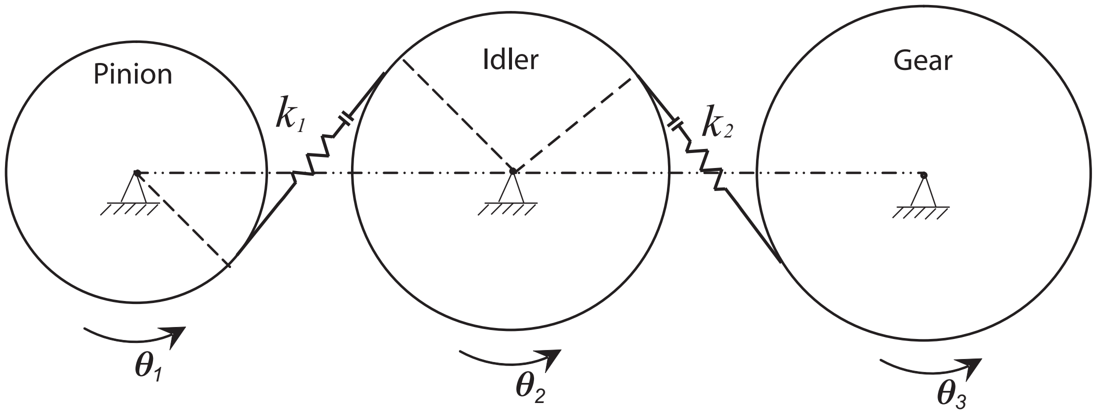

Figure 3.1: Rotational vibration model of idler gearsets.

In a purely rotational degree-of-freedom model, the angle between gear centerlines only affects the phase relation (mesh phase) between the two mesh excitations. To avoid an unnecessary system parameter, mesh phase is considered instead of the angle of gear centers, so without loss of generality the centers of the three gears are aligned. The pinion, idler, and gear are labeled as gears 1, 2, and 3, respectively, with rotations θ_i (i=1, 2, 3). These motions are converted to linear displacements $u_i = r_i\theta_i$ along the line of action where r_i are the base radii. The equivalent masses are $m_i = I_i / r_i^2$ where I_i are the polar moments of inertia. The dynamic mesh forces are $F_j = H_j(x_j)k_j(t)x_j$, where j =1, 2 is the mesh index, $k_j(t)$ are the time-varying mesh stiffnesses, x_j are the dynamic transmission errors ($x_1 = u_1 + u_2$ and $x_2 = -u_2 - u_3$), and $H_j(x_j) = [1 + sgn(x_j)]/2$ are the tooth separation functions that incorporate contact loss. All teeth at a particular mesh are presumed to lose contact at the same time when a dynamic transmission error (DTE) is negative.

For idler gearsets, there is one rigid body mode and two elastic modes. Only the two transmission errors x_j are needed to describe the elastic motions of interest. The 3×2 matrix $\mathbf{Q}$ in the transformation $\mathbf{u}=\mathbf{Qx}$ is found from the orthogonality of the rigid body mode to the elastic modes [65] where $\mathbf{u}=[u_1,u_2,u_3]^T$ and $\mathbf{x}=[x_1,x_2]^T$. The governing equation for the idler gearset in Figure 3.1 is formulated into

$$\mathbf{M}\ddot{\mathbf{x}}+\mathbf{K}(\tilde{\omega}t,\mathbf{x})\mathbf{x}=\mathbf{F} \tag{3.1}$$

$$\begin{aligned}
&\mathbf{Q}=\frac{1}{\sum_{i=1}^{3}m_i}\begin{bmatrix} m_2+m_3 & m_3 \\ m_1 & -m_3 \\ -m_1 & -m_1-m_2 \end{bmatrix};\quad \mathbf{F}=[T,T]^T \\
&\mathbf{M}=\frac{1}{\sum_{i=1}^{3}m_i}\begin{bmatrix} (m_2+m_3)m_1 & m_1m_3 \\ m_1m_3 & (m_1+m_2)m_3 \end{bmatrix};\quad \mathbf{K}=\begin{bmatrix} H_1(\mathbf{x})k_1(t) & 0 \\ 0 & H_2(\mathbf{x})k_2(t) \end{bmatrix}
\end{aligned} \tag{3.2}$$

where $\tilde{\omega}$ is the mesh frequency, $\mathbf{K}(\tilde{\omega}t,\mathbf{x})$ is the nonlinear, time-varying mesh stiffness matrix, and T denotes the nominal mesh force.

3.2.2 Harmonic Balance/Continuation Method

Finite element analysis, piecewise linear techniques, Galerkin schemes, and direct numerical integration are common techniques to find the frequency response of nonlinear systems. Some of these cannot predict certain characteristics such as unstable or quasi-periodic solutions. To provide numerical comparisons for the analytical approximation, this work combines the harmonic balance method with an arclength continuation path following technique [24, 64, 75]. Multiple solutions, even loops or knots, in the parameter space are possible, and the continuation method can trace these solutions.

The periodic steady state dynamic response x_j is expanded in a Fourier series and discretized in the time domain as

$$x_j(t_z) = u_{j,1} + \sum_{r=1}^{R} \left(u_{j,2r} \cos r\tilde{\Omega} t_z + u_{j,2r+1} \sin r\tilde{\Omega} t_z \right) \quad j = 1,2 \quad z = 1,2,\cdots,Z \tag{3.3}$$

where $\tilde{\Omega}$ is the fundamental frequency of dynamic response, $\mathbf{u}_j = \{u_{j,1},\cdots,u_{j,2R},u_{j,2R+1}\}^T$ are Fourier coefficients, and the response in one period $T_r = 2\pi / \tilde{\Omega}$ is discretized into Z points ($t_z = \frac{z}{Z} T_r$). Aliasing is avoided by setting the discrete sampling frequency well above the Nyquist frequency, $Z \gg 2R$. The matrix form of (3.3) is $\mathbf{x}_j = \mathbf{L}_j \mathbf{u}_j$ where $\mathbf{L}_j$ is the discrete inverse Fourier transform matrix and $\mathbf{x}_j = \{x_j(t_1) \cdots x_j(t_Z)\}^T$. Similarly, the periodic mesh stiffnesses are expanded in Fourier series and discretized in one mesh period $T_m = 2\pi / \tilde{\omega}$ as

$$k_j(t_z) = k_{j,1} + \sum_{r=1}^{R} \left(k_{j,2r} \cos r\tilde{\omega} t_z + k_{j,2r+1} \sin r\tilde{\omega} t_z \right) \quad j = 1,2 \quad z = 1,2,\cdots,Z \tag{3.4}$$

where $\boldsymbol{\kappa}_j = \{k_{j,1},\cdots,k_{j,2R},k_{j,2R+1}\}^T$ are known Fourier coefficients of the mesh stiffnesses, *i.e.*, $\mathbf{k}_j = \mathbf{L}_j \boldsymbol{\kappa}_j$. The mesh period T_m is not necessarily the same as the response period T_r.

The global vectors $\mathbf{X} = [\mathbf{x}_1^T \ \mathbf{x}_2^T]^T$ and $\mathbf{U} = [\mathbf{u}_1^T \ \mathbf{u}_2^T]^T$ satisfy $\mathbf{X} = \mathbf{LU}$ or $\mathbf{U} = \mathbf{GX}$ where $\mathbf{L} = diag(\mathbf{L}_j)$ and the discrete Fourier transformation $\mathbf{G}$ is the left inverse of $\mathbf{L}$. Similarly, the discrete Fourier expansions of $\ddot{\mathbf{x}}$, $\dot{\mathbf{x}}$, $\mathbf{M}$, $\mathbf{C}$ and H_j are

$$\ddot{\mathbf{X}} = \tilde{\Omega}^2 \mathbf{LAU}, \ \dot{\mathbf{X}} = \tilde{\Omega} \mathbf{LBU}, \ \tilde{\mathbf{M}} = [m_{ij} \mathbf{I}_Z], \ \tilde{\mathbf{C}} = [c_{ij} \mathbf{I}_Z], \ \mathbf{H}_j = \tfrac{1}{2}\left[1 + \tanh(\rho \mathbf{x}_j)\right] \tag{3.5}$$

where $\mathbf{A}$ and $\mathbf{B}$ are constant matrices [16, 64, 76] and $\mathbf{I}_Z$ is the identity matrix of dimension *Z*. The separation function is smoothed by a hyperbolic tangent function [64, 77]. The value $\rho = 200$ in this study accurately approximates the *sgn*() function. Therefore, the nonlinear, time-varying matrix $\mathbf{K}(H_j, k_j)$ in (3.2) is discretized into

$$\tilde{\mathbf{K}} = \begin{bmatrix} diag\left(\left\langle \tfrac{1}{2}[1+\tanh(\rho\mathbf{L}_1\mathbf{u}_1)],\, \mathbf{L}_1\boldsymbol{\kappa}_1 \right\rangle\right) & \mathbf{0} \\ \mathbf{0} & diag\left(\left\langle \tfrac{1}{2}[1+\tanh(\rho\mathbf{L}_2\mathbf{u}_2)],\, \mathbf{L}_2\boldsymbol{\kappa}_2 \right\rangle\right) \end{bmatrix} \tag{3.6}$$

where $\langle \Psi, \Theta \rangle = \Psi^T \Theta$ denotes the inner product.

Substituting these discretized matrices and vectors into (3.1) and applying the Fourier transformation $\mathbf{G}$ yield a nonlinear algebraic equation in the frequency domain that can be solved by Newton-Raphson iteration. The residual form for iteration is

$$\Re(\mathbf{U}, \tilde{\Omega}) = \left(\tilde{\Omega}^2 \hat{\mathbf{M}}\mathbf{A} + \tilde{\Omega}\hat{\mathbf{C}}\mathbf{B}\right)\mathbf{U} + \mathbf{G}\tilde{\mathbf{K}}\mathbf{U} - \mathbf{f} \tag{3.7}$$

where the matrices $\hat{\mathbf{M}}$ and $\hat{\mathbf{C}}$ satisfy $\mathbf{L}\hat{\mathbf{M}} = \tilde{\mathbf{M}}\mathbf{L}$ and $\mathbf{L}\hat{\mathbf{C}} = \tilde{\mathbf{C}}\mathbf{L}$. The load vector $\mathbf{f}$ includes the Fourier coefficients of $\mathbf{F}$. Note that $\tilde{\mathbf{K}}\mathbf{U}$ is a nonlinear function of $\mathbf{U}$. The spectral vector solution $\mathbf{U}$ is obtained when the norm of $\Re$ is less than a specified tolerance.

To follow periodic solution branches as the parameter $\tilde{\Omega}$ varies, the continuation method treats $\tilde{\Omega}$ as an unknown parameter. This expands the unknown vector to be $\mathbf{a} = \{\mathbf{U}^T\ \tilde{\Omega}\}^T$. The Newton-Raphson iteration is

$$\mathbf{a}_{q+1}^p = \mathbf{a}_q^p + \mathbf{J}^{-1}(\mathbf{a}_q^p)\Re(\mathbf{a}_q^p);\ \ \mathbf{J} = \begin{bmatrix} \dfrac{\partial \Re}{\partial \mathbf{U}} & \dfrac{\partial \Re}{\partial \tilde{\Omega}} \end{bmatrix} \tag{3.8}$$

where $\mathbf{J}$ denotes the Jacobian matrix of the residual, $\mathbf{J}^{-1}$ denotes pseudo-inverse, and superscript p and subscript q are the frequency index and iteration number, respectively. The iteration reaches the steady state periodic solution $\mathbf{a}^p$ when $\left\|\mathbf{a}_{q+1}^p - \mathbf{a}_q^p\right\|$ is less than a specified tolerance.

The selection of initial guess affects the speed of convergence and solution itself. The continuation method is applied to get the first guess of the next iteration. The first guess of a new solution along the equilibrium path is given in terms of the previous solution $\mathbf{a}^p$ plus an arclength $d\mathbf{s}$ ($\mathbf{a}_0^{p+1} = \mathbf{a}^p + d\mathbf{s}$). The direction of arclength is along the tangent plane of the current solution. Special care is taken to control the arclength step size [16, 64, 76]. Although the smoothed nonlinear function $\mathbf{H}_j$ is a better approximation of the true tooth separation function for higher values of ρ, higher ρ can cause an ill-conditioned Jacobian matrix.

The Floquet-Liapunov theorem is applied to determine the stability of solution branches. The eigenvalues of the state transition (monodromy) matrix over one period determines the solution stability. If the magnitude of any eigenvalue is greater than unity, the solution is unstable; otherwise, it is stable. Hsu [78, 79] develops a method using a series of step functions to approximate the monodromy matrix of one period. Friedmann et al. [80] present a numerical integration method that is adopted in this study.

The advantages of the harmonic balance method lie not only in the capture of unstable solution branches but also the computational efficiency. The disadvantages are that it can diverge with an ill-conditioned Jacobian matrix and the computation cost increases significantly with the number of harmonics and discretized points.

3.2.3 Perturbation Analysis

Harmonic balance/continuation provides only numerical solutions. Multiple scale perturbation analysis is conducted in this study to give closed-form approximations that explicitly show the impact of key parameters on the nonlinear dynamic response.

Two quantities are chosen to non-dimensionalize the governing equation (3.1): the first natural frequency ω_1 and the mean value of the first mesh static transmission error (STE) $\bar{x}_1 = T/\bar{k}_1$. The dimensionless quantities are

$$\tau = \omega_1 t,\ \omega = \frac{\tilde{\omega}}{\omega_1},\ \Omega = \frac{\tilde{\Omega}}{\omega_1},\ y_j = \frac{x_j}{\bar{x}_1},\ c = \frac{\omega_2}{\omega_1},\ \lambda = \frac{\bar{k}_2}{\bar{k}_1} \tag{3.9}$$

where the dimensionless DTE y_j represent the dynamic factors and $\bar{k}_j$ are the average mesh stiffnesses over one mesh cycle. The dimensionless governing equation is

$$\hat{\mathbf{M}}\ddot{\mathbf{y}} + \hat{\mathbf{K}}(\omega\tau, \mathbf{y})\mathbf{y} = \hat{\mathbf{F}} \tag{3.10}$$

where $\hat{\mathbf{M}} = \omega_1^2 \bar{x}_1 \mathbf{M}/T$, $\hat{\mathbf{K}} = \bar{x}_1 \mathbf{K}/T$, $\hat{\mathbf{F}} = \mathbf{F}/T$, and $\mathbf{y} = [y_1, y_2]^T$. The eigenvalue problem of (3.10) for the case of average mesh stiffnesses is $\left(c_l^2 \hat{\mathbf{M}} - \hat{\mathbf{K}}\right)\mathbf{s}_l = \mathbf{0}$. Due to the normalization, $c_1 = 1$ and $c_2 = c > 1$. The normalized modal matrix is $\mathbf{S} = [\mathbf{s}_1\, \mathbf{s}_2]$.

Substituting $\mathbf{y} = \mathbf{S}\mathbf{q}$ and pre-multiplying by $\mathbf{S}^T$, (3.10) is recast into the modal form

$$\ddot{q}_l + 2\Gamma c_l \dot{q}_l + \frac{1}{\bar{k}_1} \sum_{n=1}^{2} \sum_{j=1}^{2} s_{jl} s_{jn} H_j k_j q_n = c_l^2 F_l \quad l = 1, 2 \tag{3.11}$$

where s_{jl} (mode l, mesh j), s_{jn} are elements of $\mathbf{S}$, the modal forces $F_l = \sum_{n=1}^{2} s_{nl} / c_l^2$ are independent of the nominal mesh force T, and modal damping Γ is introduced. The mesh stiffnesses $k_j(t)$ vary periodically with gear tooth contact and are expanded as

$$
\begin{aligned}
k_1 &= \bar{k}_1 + \sum_{m=1}^{\infty}\left(\tilde{\kappa}_m e^{im\omega\tau} + c.c.\right) = \bar{k}_1\left[1 + \varepsilon\sum_{m=1}^{\infty}\left(\kappa_m e^{im\omega\tau} + c.c.\right)\right] \\
k_2 &= \bar{k}_2 + \sum_{m=1}^{\infty}\left(\tilde{\eta}_m e^{im\omega\tau} + c.c.\right) = \bar{k}_2\left[1 + \varepsilon\sum_{m=1}^{\infty}\left(\eta_m e^{im\omega\tau} + c.c.\right)\right]
\end{aligned}
\tag{3.12}
$$

where $\varepsilon = \dfrac{2|\tilde{\kappa}_1|}{\bar{k}_1}$, $\kappa_m = \dfrac{\tilde{\kappa}_m}{2|\tilde{\kappa}_1|}$, $\eta_m = \dfrac{\bar{k}_1}{\bar{k}_2}\dfrac{\tilde{\eta}_m}{2|\tilde{\kappa}_1|}$, and the abbreviation *c.c.* denotes complex conjugate of previous terms.

The ratio ε of the first harmonic of mesh stiffness to mean mesh stiffness for the first mesh is adopted as the perturbation parameter and assumed to be small compared to unity. For low contact ratio gears, if the stiffness is presumed to double when single-tooth contact switches to double-tooth contact, then $\varepsilon = 1/\varsigma_1$, where ς_1 is the first mesh contact ratio. Such doubling does not occur, however, and $\varepsilon < 1/\varsigma_1$ in practice. For high contact ratio spur gears or helical gears, ε is much less. In practice, $\varepsilon < 0.5$ according to prior approximations [19, 38].

A fixed phase relation exists between the contact actions (i.e., the mesh stiffness variations) of the two meshes in an idler gear system. If the only difference between the two mesh stiffness variations is a time shift Δt while both variations have the same periodic waveform, the mesh phase is defined naturally as $2\pi\Delta t / T_m$. When the mesh stiffness variations also differ in shape, which they likely will in practice from a difference in contact ratios, a reference condition is needed to define the mesh phase. Without loss of generality, the transition point where the number of teeth in contact switches to a lower number is selected as the reference condition. For instance, two simplified mesh stiffness functions (rectangular waves) are shown in Figure 3.2, and the mesh phase between the reference conditions is ϕ. The mesh phase is determined by the angle of gear centerlines and gear tooth geometry [61]. The complex Fourier coefficients of the mesh stiffnesses in Figure 3.2 are

$$\begin{aligned}\tilde{\kappa}_m &= -\frac{\Lambda_1}{m\pi}\sin\left(m\pi\varsigma_1\right)e^{-im\pi\varsigma_1} = \hat{\kappa}_m e^{-im\pi\varsigma_1}\\ \tilde{\eta}_m &= -\frac{\Lambda_2}{m\pi}\sin\left(m\pi\varsigma_2\right)e^{-im(\pi\varsigma_2-\phi)} = \hat{\eta}_m e^{-im(\pi\varsigma_2-\phi)}\end{aligned} \tag{3.13}$$

where $\Lambda_1 = b - a$ and Λ_2 are peak-peak values. The total phase difference between the Fourier coefficients $\tilde{\kappa}_m$ and $\tilde{\eta}_m$ of the two mesh stiffnesses are functions of the stiffness function shape (contact ratio) and the geometric relations between the two contacts that causes a time shift between the reference contact condition (captured by ϕ in Figure 3.2). The selection of reference condition for mesh phase does not affect the phase difference between the two complex amplitudes. Although idealized rectangular wave mesh stiffness functions are used here, the conclusion holds for general mesh stiffness variations.

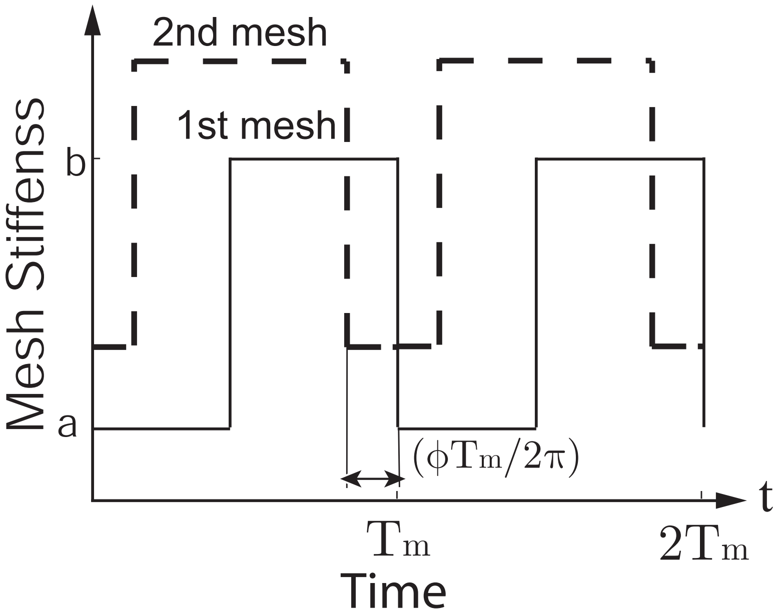

Figure 3.2: Mesh phase between the two meshes.

Large vibration occurs when the varying mesh stiffnesses cause parametric instability in a particular mode, which can be predicted by the linear system. The ensuing large response triggers nonlinear contact loss that bounds the vibration. With this action, the unstable mode dominates the response, implying nearly harmonic response [5, 37, 72, 81, 82]. Numerical experiments confirm this. Thus, the response has the form

$$y_j = \bar{y}_j + \tilde{y}_j \cos(\Omega\tau - \gamma_j) \qquad j = 1, 2 \tag{3.14}$$

where $\Omega \approx c_1$ or c_2. The relation between the response frequency Ω and the mesh frequency ω depends on the type of parametric instability.

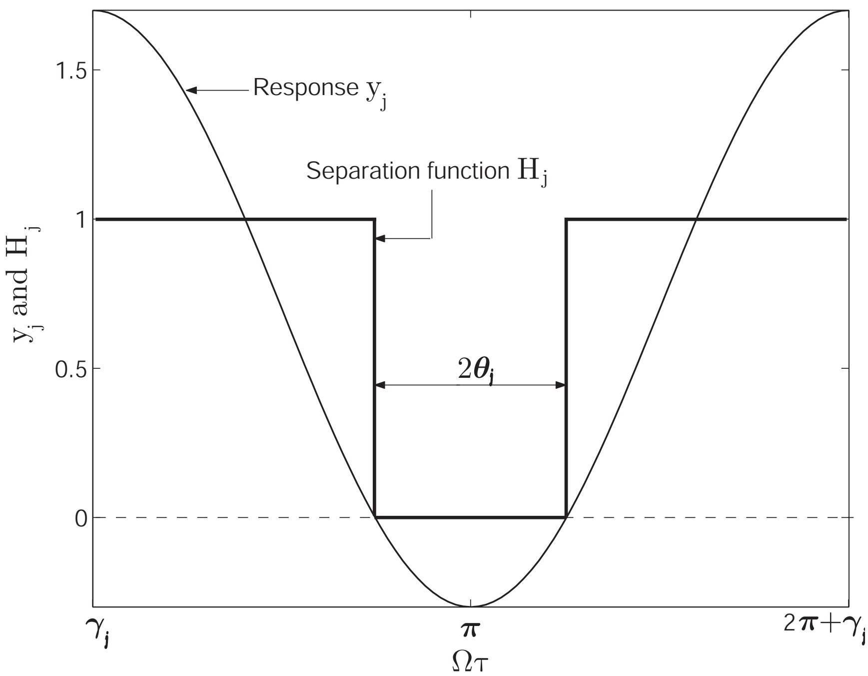

Figure 3.3: Relation of separation function and dynamic response.

Figure 3.3 sketches a dynamic transmission error y_j and tooth separation function H_j in a period. The separation angle $2\theta_j$ represents the time of separation during one period of response. In practice and from numerical simulations, the separation time is a small fraction of the response period, that is, $\theta_j / \pi = O(\varepsilon)$. With this stipulation, the periodic separation functions are reformulated into a form suitable for perturbation

$$H_1 = 1 + \varepsilon \sum_{n=0}^{\infty} \left(h_n e^{-in\gamma_1} e^{in\Omega\tau} + c.c. \right); \quad H_2 = 1 + \varepsilon \sum_{n=0}^{\infty} \left(g_n e^{-in\gamma_2} e^{in\Omega\tau} + c.c. \right) \tag{3.15}$$

$$\begin{aligned}
& h_0 = -\frac{\theta_1}{\pi\varepsilon}, \; g_0 = -\frac{\theta_2}{\pi\varepsilon}, \\
& h_n = \frac{\sin n(\pi - \theta_1)}{n\pi\varepsilon}, \quad g_n = \frac{\sin n(\pi - \theta_2)}{n\pi\varepsilon} \quad n = 1, 2, \cdots \quad if \; \tilde{y}_j > 0 \\
& h_n = -\frac{\sin n\theta_1}{n\pi\varepsilon}, \quad g_n = -\frac{\sin n\theta_2}{n\pi\varepsilon} \quad n = 1, 2, \cdots \quad if \; \tilde{y}_j < 0
\end{aligned} \tag{3.16}$$

The separation angles θ_j and phase angles γ_j are implicit functions of the (unknown at this stage) amplitudes and mean values of the DTE. The unknown Fourier coefficients h_0, g_0, h_n and g_n are $O(1)$.

Substituting (3.12) and (3.15) into (3.11) yields the governing equations in a form suitable for perturbation analysis

$$\ddot{q}_l + \varepsilon\mu c_l \dot{q}_l + c_l^2 q_l + \varepsilon(f_{l1}q_1 + f_{l2}q_2) = F_l \quad l = 1,2 \tag{3.17}$$

$$\begin{aligned} f_{lj} &= \sum_{m=1}^{M}\left(s_{1l}s_{1j}\kappa_m + \lambda s_{2l}s_{2j}\eta_m\right)e^{im\omega\tau} \\ &\quad + \sum_{n=0}^{N}\left(s_{1l}s_{1j}h_n e^{-in\gamma_1} + \lambda s_{2l}s_{2j}g_n e^{-in\gamma_2}\right)e^{in\Omega\tau} + c.c. \quad j = 1,2 \end{aligned} \tag{3.18}$$

where $\mu = 2\Gamma/\varepsilon = O(1)$ is the reformulated modal damping. The functions f_{lj} involve the mesh stiffness parametric excitations and contact loss separation functions of both meshes.

The dynamic responses are approximated by asymptotic power series in ε, and τ is expanded into multiple time scales $T_n = \varepsilon^n T_0$ in the conventional way [66]

$$\begin{aligned} q_1 &= u_0(T_0, T_1 ...) + \varepsilon u_1(T_0, T_1 ...) + O(\varepsilon^2) \\ q_2 &= v_0(T_0, T_1 ...) + \varepsilon v_1(T_0, T_1 ...) + O(\varepsilon^2) \end{aligned} \tag{3.19}$$

Substitution of (2.15) into (3.17) yields the ε^0 and ε^1 order differential equations (where $D_n = \partial / \partial T_n$)

$$\begin{aligned} D_0^2 u_0 + u_0 &= F_1 \\ D_0^2 v_0 + c^2 v_0 &= c^2 F_2 \end{aligned} \tag{3.20}$$

$$
\begin{aligned}
D_0^2 u_1 + u_1 &= -2D_0 D_1 u_0 - \mu D_0 u_0 - f_{11} u_0 - f_{12} v_0 \\
D_0^2 v_1 + c^2 v_1 &= -2D_0 D_1 v_0 - \mu c D_0 v_0 - f_{21} u_0 - f_{22} v_0
\end{aligned} \tag{3.21}
$$

From (3.20) , the leading order solutions are

$$
\begin{aligned}
u_0 &= F_1 + \left[A_1(T_1) e^{iT_0} + c.c. \right] \\
v_0 &= F_2 + \left[A_2(T_1) e^{icT_0} + c.c. \right]
\end{aligned} \tag{3.22}
$$

When the mesh frequency is close to a natural frequency $\omega = c_r + \varepsilon\sigma$ ($r =$ 1 or 2 and σ is the detuning parameter), fundamental resonance ($\Omega = \omega$) is excited. To avoid simultaneous parametric, or internal, resonances $c_2 = c \neq 2$. Substitution of (3.22) into (3.21) exposes the solvability conditions to prevent secular terms that cause unbounded, aperiodic response

$$
2ic_l A_l' + \mu i c_l^2 A_l + (s_{1l}^2 h_0 + \lambda s_{2l}^2 g_0) A_l = 0 \quad l \neq r \tag{3.23}
$$

$$
\begin{aligned}
&2ic_r A_r' + (\mu i c_r^2 + s_{1r}^2 h_0 + \lambda s_{2r}^2 g_0) A_r + \left[s_{1r}^2 (\kappa_2 + h_2 e^{-i2\gamma_1}) + \lambda s_{2r}^2 (\eta_2 + g_2 e^{-i2\gamma_2}) \right] \bar{A}_r e^{i2\sigma T_1} \\
&+ \left[s_{1r} (s_{11} F_1 + s_{12} F_2)(\kappa_1 + h_1 e^{-i\gamma_1}) + \lambda s_{2r} (s_{21} F_1 + s_{22} F_2)(\eta_1 + g_1 e^{-i\gamma_2}) \right] e^{i\sigma T_1} = 0
\end{aligned} \tag{3.24}
$$

where $A_l' = dA_l / dT_1$ and $\bar{A}_r$ denotes the complex conjugate of A_r. From (3.23), $A_l = 0$ ($l \neq r$). Substituting $A_r = \alpha e^{i\beta}$ into the leading order approximation of the two DTE $y_j = s_{j1} u_0 + s_{j2} v_0$ gives

$$
y_j = s_{j1} F_1 + s_{j2} F_2 + 2\alpha s_{jr} \cos(c_r T_0 + \beta) \tag{3.25}
$$

Comparing (3.14) and (3.25), the phase angles $\gamma_j = \gamma = (\Omega - c_r) T_0 - \beta = \sigma T_1 - \beta$ are identical for the two DTE. Substituting A_r and γ into (3.24) casts the solvability condition in terms of real quantities as

$$
\begin{aligned}
2c_r\alpha'/\alpha &= \left[\operatorname{Re}(\hat{R}_4) - 2c_r\sigma + (\hat{R}_1 + \hat{R}_2/\alpha)\right]\cos\gamma + \left[\mu c_r^2 - \operatorname{Im}(\hat{R}_4)\right]\sin\gamma + \operatorname{Re}(\hat{R}_3)/\alpha \\
2c_r\gamma' &= \left[\mu c_r^2 + \operatorname{Im}(\hat{R}_4)\right]\cos\gamma + \left[\operatorname{Re}(\hat{R}_4) + 2c_r\sigma - (\hat{R}_1 + \hat{R}_2/\alpha)\right]\sin\gamma + \operatorname{Im}(\hat{R}_3)/\alpha
\end{aligned} \tag{3.26}
$$

$$
\begin{aligned}
\hat{R}_1 &= s_{1r}^2(h_0 + h_2) + \lambda s_{2r}^2(g_0 + g_2) \\
\hat{R}_2 &= s_{1r}(s_{11}F_1 + s_{12}F_2)h_1 + \lambda s_{2r}(s_{21}F_1 + s_{22}F_2)g_1 \\
\hat{R}_3 &= s_{1r}(s_{11}F_1 + s_{12}F_2)\kappa_1 + \lambda s_{2r}(s_{21}F_1 + s_{22}F_2)\eta_1 \\
\hat{R}_4 &= s_{1r}(s_{11}F_1 + s_{12}F_2)\kappa_2 + \lambda s_{2r}(s_{21}F_1 + s_{22}F_2)\eta_2
\end{aligned} \tag{3.27}
$$

The fixed points ($\alpha' = \gamma' = 0$) of (3.26) give the steady state leading order response and the frequency response relation

$$
\begin{aligned}
\alpha = &\left| |\hat{R}_4|^2 - (2c_r - \hat{R}_1 - \hat{R}_2/\alpha)^2 - \mu^2 c_r^4 \right|^{-1} \Big\{ |\hat{R}_3|^2 \left[|\hat{R}_4|^2 + (2c_r - \hat{R}_1 - \hat{R}_2/\alpha)^2 + \mu^2 c_r^4 \right] \\
&+ 2\left[\operatorname{Re}(\hat{R}_3)^2 - \operatorname{Im}(\hat{R}_3)^2\right]\left[(2c_r - \hat{R}_1 - \hat{R}_2/\alpha)\operatorname{Re}(\hat{R}_4) + \mu c_r^2 \operatorname{Im}(\hat{R}_4)\right] \\
&- 4\operatorname{Re}(\hat{R}_3)\operatorname{Im}(\hat{R}_3)\left[\mu c_r^2 \operatorname{Re}(\hat{R}_4) - (2c_r - \hat{R}_1 - \hat{R}_2/\alpha)\operatorname{Im}(\hat{R}_4)\right]\Big\}
\end{aligned} \tag{3.28}
$$

The complicated closed-form expression in (3.28) yields limited analytical insight. This result includes contributions from the first and second harmonics of the mesh stiffnesses and separation functions. For non-integer contact ratios, however, $\kappa_1 \gg \kappa_2$, and $\eta_1 \gg \eta_2$. Neglecting the contribution of the second harmonics ($\kappa_2 = \eta_2 \approx 0$), the simplified solvability conditions are

$$
\begin{aligned}
\alpha' &= -\frac{1}{2c_r}\left[\mu c_r^2 \alpha + |\hat{R}_3| \sin(\gamma + \psi)\right] \\
\gamma' &= \sigma - \frac{1}{2\alpha c_r}\left[\hat{R}_1\alpha + \hat{R}_2 + |\hat{R}_3|\cos(\gamma + \psi)\right]
\end{aligned} \tag{3.29}
$$

where ψ is the phase angle of the complex $\hat{R}_3$. While $\hat{R}_1$ and $\hat{R}_2$ depend on the unknown amplitude α, $\hat{R}_3$ depends only on known input quantities, including the mesh stiffness variations and modal deflections. This is significant in subsequent analysis. Note that h_n and g_n depend on the separation angle given by

$$\theta_j = \begin{cases} \pi - \cos^{-1}\left(-\dfrac{s_{j1}F_1 + s_{j2}F_2}{2s_{jr}\alpha} \right) & if\ s_{jr} > 0 \\ \cos^{-1}\left(-\dfrac{s_{j1}F_1 + s_{j2}F_2}{2s_{jr}\alpha} \right) & if\ s_{jr} < 0 \end{cases} \tag{3.30}$$

The fixed points ($\alpha' = \gamma' = 0$) of (3.29) give the steady state leading order response and the frequency response relation

$$\omega = c_r + \varepsilon\sigma = c_r + \frac{1}{2\alpha c_r}\left[R_1\alpha + R_2 \pm \sqrt{|R_3|^2 - 4\Gamma^2\alpha^2 c_r^4} \right] \tag{3.31}$$

$$\begin{aligned} R_1 &= \varepsilon\hat{R}_1 = -s_{1r}^2(\sin\theta_1\cos\theta_1 + \theta_1)/\pi - \lambda s_{2r}^2(\sin\theta_2\cos\theta_2 + \theta_2)/\pi \\ R_2 &= \varepsilon\hat{R}_2 = s_{1r}(s_{11}F_1 + s_{12}F_2)\sin\theta_1/\pi + \lambda s_{2r}(s_{21}F_1 + s_{22}F_2)\sin\theta_2/\pi \\ R_3 &= \varepsilon\hat{R}_3 = s_{1r}(s_{11}F_1 + s_{12}F_2)\tilde{\kappa}_1/\bar{k}_1 + \lambda s_{2r}(s_{21}F_1 + s_{22}F_2)\tilde{\eta}_1/\bar{k}_2 \end{aligned} \tag{3.32}$$

The stability of the steady state solutions in (3.31) is determined by the real parts of the eigenvalues of the Jacobian matrix linearized from the solvability conditions (3.29).

	Pinion	Idler	Gear
Number of teeth	38	55	94
Modulus (mm)	2.54	2.54	2.54
Base radius (mm)	45.35	65.64	112.2
Inertias I_i ($kg \cdot m^2$)	2.62e-3	3.27e-3	1.19e-2
Default values for the variable parameters			
ϕ	0	Γ	0.04
ς_1	1.5	ς_2	1.5
c	2.76		

Table 3.1: Parameters of the example idler gearset.

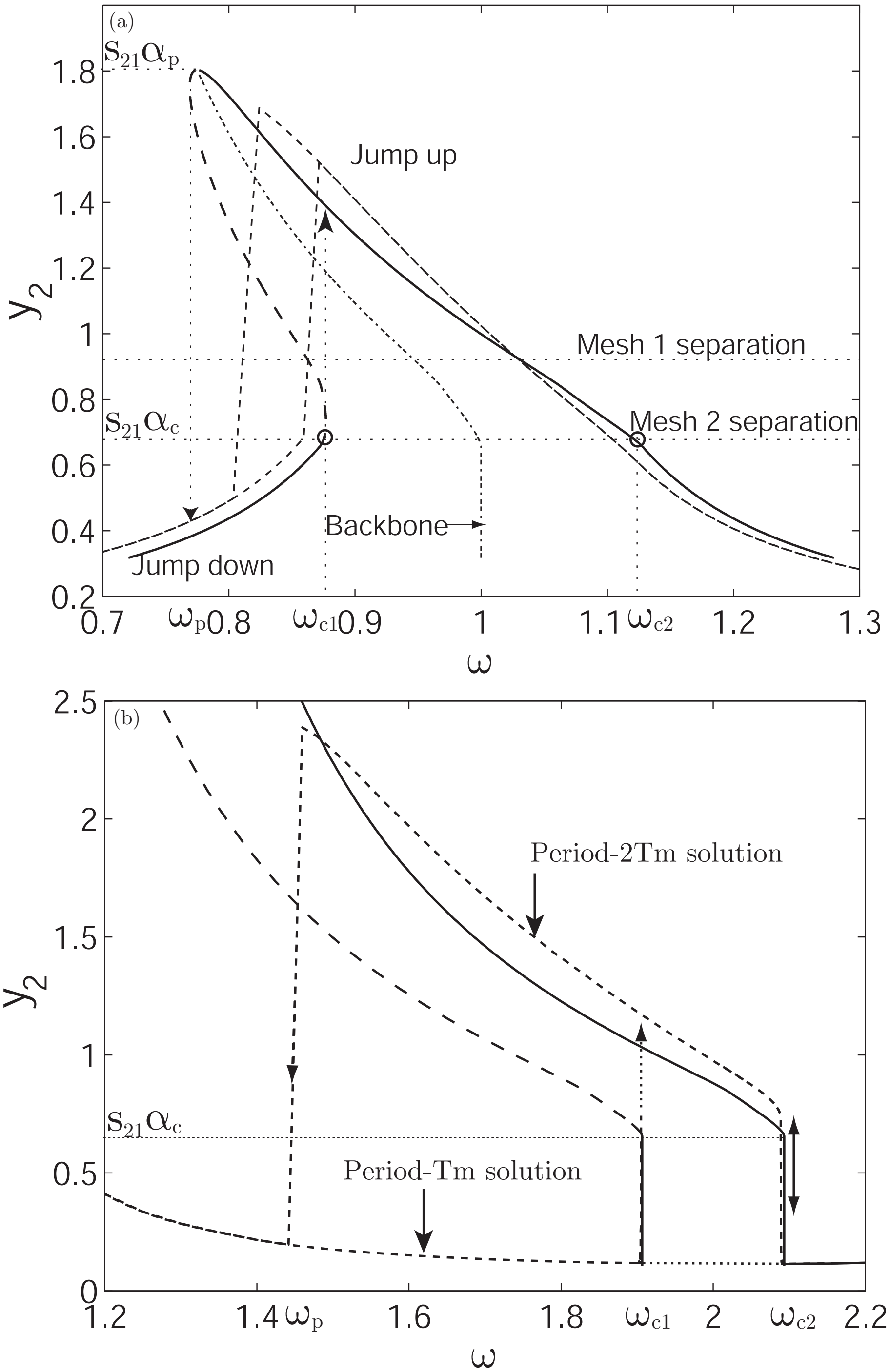

Figure 3.4: Frequency response near resonances for the system in Table 3.1 and one harmonic of FE mesh stiffnesses (a) Fundamental resonance $\omega \approx 1$ (b) Subharmonic resonance $\omega \approx 2$ (—— stable perturbation solution; — — unstable perturbation solution; - - - numerical integration; .... unstable period-Tm solution).

The nonlinear characteristics emerge qualitatively and quantitatively from (3.31). Figure 3.4a depicts the frequency response of (3.31) near the fundamental resonance $\omega \approx c_1$ for the system in Table 3.1. The solution branch shows softening nonlinearity determined by the backbone curve $\omega = c_r + (R_1\alpha + R_2)/(2\alpha c_r)$ for $\alpha > \alpha_c$, where α_c corresponds to the response amplitude at the onset of contact loss. The softening nonlinearity is from the contact loss captured in $R_{1,2}$ where the separation angles θ_1 and θ_2 depend on the amplitude. The frequencies ω_{c1} and ω_{c2} are the transition points from linearity to nonlinearity when the parametric instability causes tooth separation to arise. Stability analysis shows the middle solution between ω_p and ω_{c1} is unstable while all others are stable, which causes jump phenomena at ω_p and ω_{c1}. The transition at ω_{c2} gives rise to a kink in the frequency response curve. The condition $\theta_j = 0$ gives the transition amplitude and frequencies as

$$\alpha_c = \min\left(\left|\frac{s_{11}F_1 + s_{12}F_2}{2s_{1r}}\right|, \left|\frac{s_{21}F_1 + s_{22}F_2}{2s_{2r}}\right|\right), \quad \omega_{c1,c2} = c_r \pm \frac{1}{2\alpha_c c_r}\sqrt{|R_3|^2 - 4\Gamma^2\alpha_c^2 c_r^4} \quad (3.33)$$

From (3.33), which mesh first loses contact is determined entirely by the modal forces and vibration modes. The transition frequencies are affected by these quantities as well as the modal damping and the interaction of the two mesh stiffness variations in R_3.

An especially important quantity is the peak amplitude at resonance. This and its associated frequency are

$$\alpha_p = \frac{|R_3|}{2\Gamma c_r^2}, \quad \omega_p = c_r + \frac{R_1}{2c_r} + \frac{\Gamma c_r R_2}{|R_3|} \quad (3.34)$$

A key point is that all of the factors that govern α_p are known explicitly, so one of the most important quantities is given by a relatively simple closed-form expression. With α_p determined, all values needed to calculate ω_p are known, but the influence of design parameters on this less important quantity are not as easily visible because of the dependence on R_1 and R_2 and so the Fourier coefficients of the separation functions.

When the mesh frequency is nearly twice a natural frequency, $\omega = 2c_r + \varepsilon\sigma$, a period-$2T_m$ subharmonic resonance ($\Omega = \omega/2$) is excited. Similar procedures yield the steady state frequency response relation

$$\omega = 2c_r + \frac{1}{c_r\alpha}\left(Q_1\alpha + Q_2\right) \pm \frac{1}{c_r}\sqrt{\left|Q_3\right|^2 - 4\Gamma^2 c_r^4} \tag{3.35}$$

$$\begin{aligned} Q_1 &= -s_{1r}^2(\sin\theta_1\cos\theta_1 + \theta_1)/\pi - \lambda s_{2r}^2(\sin\theta_2\cos\theta_2 + \theta_2)/\pi \\ Q_2 &= s_{1r}(s_{11}F_1 + s_{12}F_2)\sin\theta_1/\pi + \lambda s_{2r}(s_{21}F_1 + s_{22}F_2)\sin\theta_2/\pi \\ Q_3 &= s_{1r}^2\tilde{\kappa}_1/\bar{k}_1 + \lambda s_{2r}^2\tilde{\eta}_1/\bar{k}_2 \end{aligned} \tag{3.36}$$

Figure 3.4b shows the frequency response (3.35) near the subharmonic resonance $\omega \approx 2c_1$ for the system in Table 3.1. The softening nonlinearity is more severe than at fundamental resonance because the frequencies on the backbone curve satisfy $\left(Q_1\alpha + Q_2\right)/(c_r\alpha) > \left(R_1\alpha + R_2\right)/\left(2\alpha c_r\right)$. This means a wider range of excitation frequency where contact loss occurs. When there is no contact loss ($Q_1 = Q_2 = 0$), the two vertical period-$2T_m$ solution branches bifurcate at the frequencies $\omega_{c1,c2} = c_r \pm \sqrt{\left|Q_3\right|^2 - 4\Gamma^2 c_r^4}/c_r$, which are the linear system primary parametric instability boundaries. When the excitation frequency reaches the boundaries, large period-$2T_m$ response (theoretically unbounded for the linear model) triggers the nonlinear tooth separation for $\alpha > \alpha_c$. The contact loss suppresses the instability and yields the nonlinear period- $2T_m$ solution branches that are two open curves similar to the resonance of a parametrically excited Duffing equation [66]. The frequency interval $\omega_{c2} - \omega_{c1}$ is a key practical concern. Because Q_3 is a simple expression involving known quantities, the parameter dependence of $\omega_{c2} - \omega_{c1}$ is clearly evident.

Two types of resonance could be excited near the mesh frequency $\omega = \Omega / 2 = c_r / 2 + \varepsilon\sigma$. The first one (called second-harmonic excitation resonance) is like the prior fundamental resonance case except it is excited by the second harmonic of a mesh stiffness. The second is nonlinear super-harmonic resonance resulting from the first harmonic of a mesh stiffness. It is difficult to distinguish from numerical results which one contributes more to the resonant response. The differences can be studied by perturbation analysis, which yields the frequency response function of the second-harmonic resonance as

$$\omega = c_r / 2 + \frac{1}{4\alpha c_r}\left(R_1\alpha + R_2 \pm \sqrt{\left|\tilde{R}_3\right|^2 - 4\Gamma^2\alpha^2 c_r^4} \right) \tag{3.37}$$

$$\tilde{R}_3 = s_{1r}(s_{11}F_1 + s_{12}F_2)\tilde{\kappa}_2 / \bar{k}_1 + \lambda s_{2r}(s_{21}F_1 + s_{22}F_2)\tilde{\eta}_2 / \bar{k}_2 \tag{3.38}$$

This expression is identical to the fundamental resonance solution (3.31) except that $\tilde{R}_3$ is a function of the second mesh stiffness harmonics $\tilde{\kappa}_2$ and $\tilde{\eta}_2$ that drive this resonance.

To obtain the frequency response of the super-harmonic resonance $\omega = \Omega / 2 = c_r / 2 + \varepsilon\sigma$, a second order perturbation is conducted with mesh stiffnesses only including the first harmonic. Substituting (3.22) into (3.21) gives $A_1 = A_2 = 0$ similar to (3.23) due to $c \neq 2$. This implies $u_0 = F_1,\ v_0 = F_2$. From (3.21) the second order terms of (2.15) are

$$\begin{aligned} u_1 &= B_1 e^{i\omega T_0} + A_3\left(T_1\right) e^{iT_0} + c.c. \\ v_1 &= B_2 e^{i\omega T_0} + A_4\left(T_1\right) e^{icT_0} + c.c. \\ B_l &= \frac{s_{1l}(s_{11}F_1 + s_{12}F_2)\kappa_1 + \lambda s_{2l}(s_{21}F_1 + s_{22}F_2)\eta_1}{\omega^2 - c_l^2} \quad l = 1,2 \end{aligned} \tag{3.39}$$

$$\begin{aligned} D_0^2 u_2 + u_2 &= -\left(D_1^2 + 2D_0 D_1\right) u_0 - \mu D_1 u_0 - 2D_0 D_1 u_1 - \mu D_0 u_1 - f_{11} u_1 - f_{12} v_1 \\ D_0^2 v_2 + c^2 v_2 &= -\left(D_1^2 + 2D_0 D_1\right) v_0 - \mu c D_1 v_0 - 2D_0 D_1 v_1 - \mu c D_0 v_1 - f_{21} u_1 - f_{22} v_1 \end{aligned} \tag{3.40}$$

where A_3 and A_4 are unknown. With (3.39), analysis of the solvability conditions for the equations governing u_2 and v_2 yields the super-harmonic frequency response relation

$$\omega = c_r / 2 + \frac{1}{2\alpha c_r}\left[R_1 \alpha \pm \sqrt{\left|W\right|^2 - 4\Gamma^2 \alpha^2 c_r^4} \right] \tag{3.41}$$

$$W = s_{1r}(s_{11}B_1 + s_{12}B_2)\tilde{\kappa}_1 / \bar{k}_1 + \lambda s_{2r}(s_{21}B_1 + s_{22}B_2)\tilde{\eta}_1 / \bar{k}_2 \tag{3.42}$$

Unlike the second-harmonic resonant response that is $O(1)$, the super-harmonic resonant response is $O(\varepsilon)$. In general, the response of the second-harmonic excitation is dominant for $\omega = c_r / 2 + \varepsilon\sigma$. On the other hand, by tuning system parameters such as mesh phase and contact ratio to reduce $\left|\tilde{R}_3\right|$, the second-harmonic excitation can be reduced, in which case the super-harmonic response dominates.

3.3 Results and Discussion

The following sections compare frequency response predictions from the analytical expressions with numerical simulations. The impacts of system parameters on the dynamic response are investigated based on the closed-form expressions. The nominal parameters are in Table 3.1. The non-rectangular periodic mesh stiffnesses in Figure 3.5 over a mesh cycle are obtained by static analysis using a specialized finite element model [5, 8]. They include tooth and gear body flexibility. The mesh stiffnesses are smooth and include corner contact effects. Adopting a common approximation, the rectangular-wave mesh stiffnesses in Figure 3.5 with the same average mesh stiffness, contact ratio and peak-peak value as the finite element mesh stiffnesses are examined in some circumstances.

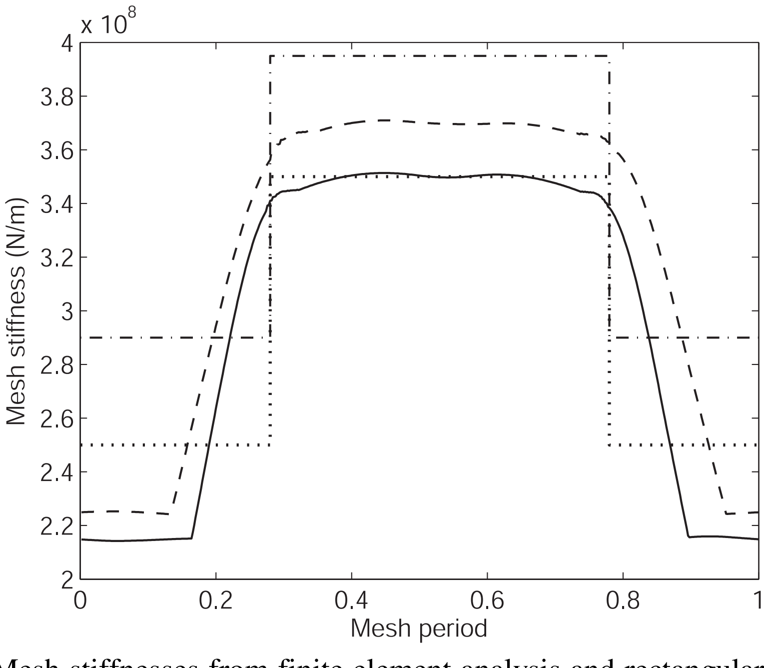

Figure 3.5: Mesh stiffnesses from finite element analysis and rectangular waves (___ FE mesh 1; _ _ FE mesh 2; _ . . rectangular wave mesh 1; ……… rectangular wave mesh 2).

3.3.1 Comparison of Numerical and Analytical Results

The dynamic response of the idler gearset computed from perturbation, numerical integration, and harmonic balance methods are compared in Figure 3.6 using the finite element mesh stiffnesses and system parameters in Table 3.1. Root-mean-square (RMS) values of DTE y_j are shown; in all results the mean values are subtracted prior to computing the RMS. Fundamental resonances of the two modes ($\omega \approx 1, c$) and the subharmonic resonance ($\omega \approx 2$) of the first mode are pronounced. Contact loss occurs at the first mode. Stable branches of the harmonic balance solutions match numerical integration results exactly. Perturbation solutions are evaluated against two numerical integration results that take one and ten mesh stiffness harmonics, respectively. The major features of the fundamental resonance, such as the backbone curve, amplitude, and onset of nonlinearity, are captured by the perturbation analysis. The two solution branches of harmonic balance at the first mesh form a loop, which is not captured by the perturbation approximations. Considering higher order perturbation and more modes might improve the analysis at the cost of increased complexity. The subharmonic perturbation solution agrees well with the numerical results for identifying the vertical branches and the stable nonlinear branches. The subharmonic from harmonic balance shows closed solution branches with a jump phenomenon resonance peak, which is not captured by the perturbation at first order. The amplitude of jump-down, however, is proportional to the instability interval $\omega_{c2} - \omega_{c1}$ and can be qualitatively inferred from the perturbation solution. The frequency range with contact loss at subharmonic is wider than at fundamental resonance.

Another comparison (Figure 3.7) is made by adopting rectangular mesh stiffnesses that retain the mean and peak-peak values but change the contact ratios to 1.3, which affects the mesh stiffness harmonics. Two perturbation solutions are presented for $\omega \approx 1$ with one and two harmonics as given by (3.31) and (3.28), respectively. Both solutions agree well with ten-harmonic numerical and harmonic balance results. The two-harmonic solution provides only slightly better prediction than the one-harmonic perturbation, while its analytical expressions are much more complicated.

In summary, the perturbation analysis effectively approximates the solutions near resonances where one mode is dominant. With careful selection of the number of harmonics and time steps, the harmonic balance method yields the complete solution branches with high accuracy.

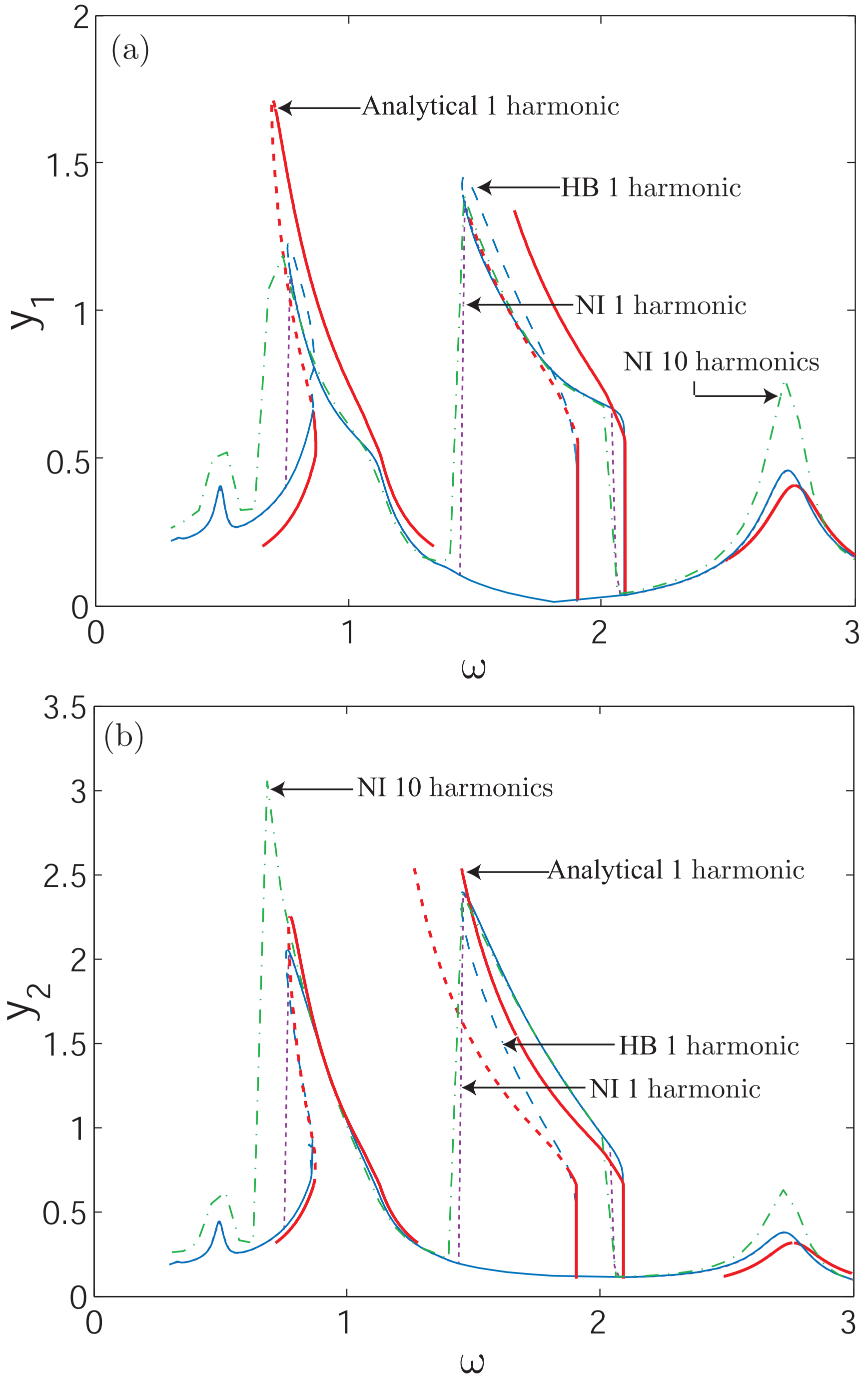

Figure 3.6: Comparisons of DTE of the idler gear in Table 3.1 with FE mesh stiffnesses and the number of retained Fourier harmonics indicated (HB-harmonic balance, NI-numerical integration) (a) The first mesh (b) The second mesh (dashed data are unstable).

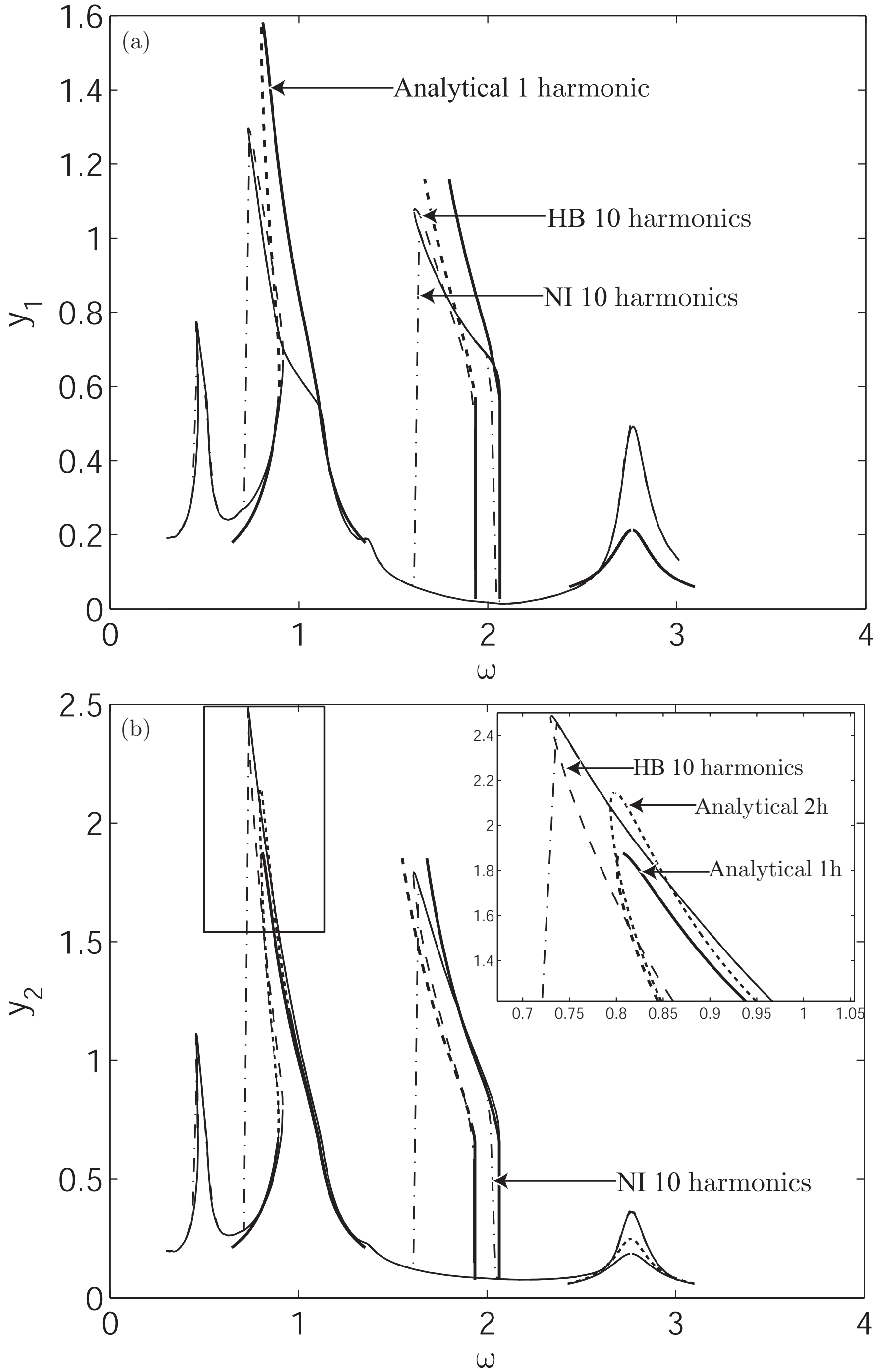

Figure 3.7: Comparisons of DTE of the idler gear in Table 3.1 ($\varsigma_1 = \varsigma_2 = 1.3$) with rectangular mesh stiffnesses and the number of retained Fourier harmonics indicated (a) The first mesh (b) The second mesh (dashed data are unstable).

3.3.2 Onset of Tooth Separation (Nonlinearity)

Prediction of the transition points between linearity and nonlinearity identifies the onset of tooth separation. At the transition points, the separation angle $\theta_j = 0$. From (3.33), the amplitude of response at the onset of nonlinearity is determined entirely by modal forces and modal deflections s_{jr}. The two meshes usually separate at different stages. The mesh having maximum modal strain energy separates first. While this slows the rate of amplitude growth, the other mesh separates if the amplitude reaches the critical value. The transition frequencies of mesh j separation at the fundamental resonance of mode r are

$$\omega = c_r \pm \left[\left(\frac{s_{jr}}{s_{j1}F_1 + s_{j2}F_2} \right)^2 \left| s_{1r}(s_{11}F_1 + s_{12}F_2)\frac{\tilde{\kappa}_1}{\bar{k}_1} + \lambda s_{2r}(s_{21}F_1 + s_{22}F_2)\frac{\tilde{\eta}_1}{\bar{k}_2} \right|^2 - \Gamma^2 c_r^2 \right]^{\frac{1}{2}} \quad (3.43)$$

All quantities in (3.43) are readily known. Figure 3.4a shows the fundamental resonance of mode 1 with the two meshes losing contact at different stages. The response of the second mesh is dominant in this first mode. When $\alpha_c = 0.69/s_{21}$ the second mesh loses contact while the first mesh separates at $\alpha_c = 0.92/s_{21}$. There is no tooth separation below the dashed line of the second mesh separation. The second mesh separates between the two dashed lines. Both meshes separate above the upper dashed line. The corresponding separation angles are shown in Figure 3.8. The maximum separation angles θ_j are less than 1.3, *i.e.*, $\theta_j / \pi < 0.41$. The transition frequencies of the second mesh are $\omega = 0.870$ and 1.130, which are symmetric about $\omega = 1$. The transition frequencies of the first mesh are $\omega = 0.875$ and 1.073, where the second mesh already loses contact. These transition frequencies are not symmetric about $\omega = 1$ due to contact loss of the second mesh.

For contact loss at both meshes, the separation angle of the second mesh is bigger than the first mesh when $\omega \approx 1$. The situation is reversed when $\omega \approx c$. The time spans of tooth separations for the two meshes either overlap (in-phase) or do not overlap (out-of-phase). From (3.30), the phase of the tooth separation functions between the two meshes are decided by the vibration mode. For instance, at the first mode resonance ($\omega \approx 1$), the two separation functions are in-phase due to $s_{11}s_{21} > 0$. At the second mode resonance ($\omega \approx c$), the two separation functions are out-of-phase due to $s_{12}s_{22} < 0$.

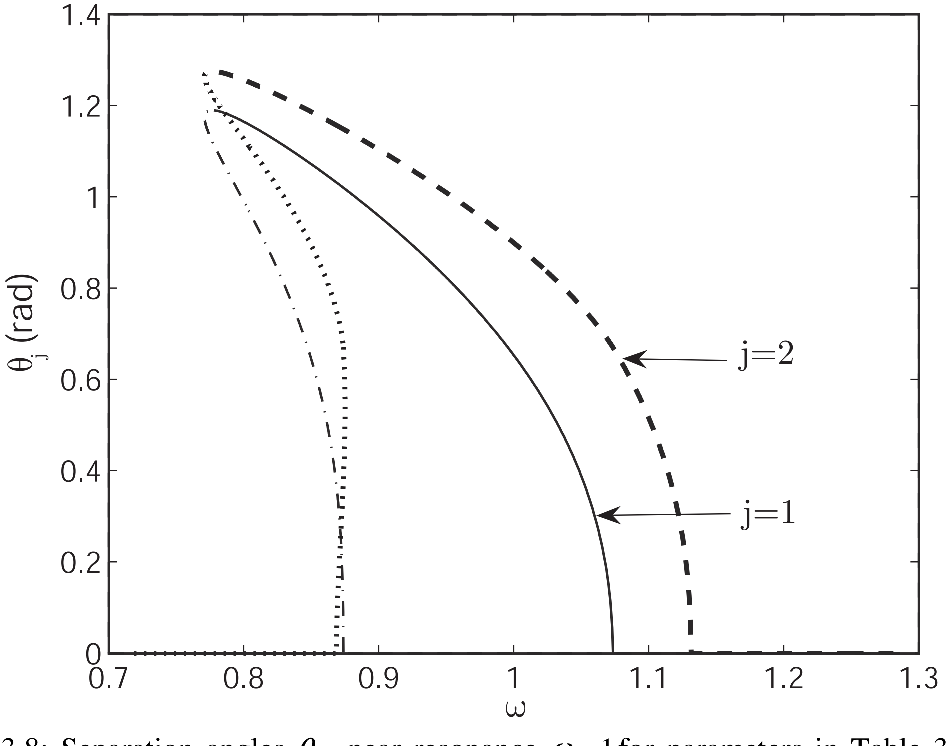

Figure 3.8: Separation angles $\theta_{1,2}$ near resonance $\omega \approx 1$ for parameters in Table 3.1 and FE mesh stiffnesses (dash-dot and dotted data are unstable).

3.3.3 Subharmonic Resonance

Figure 3.4b shows the nonlinear period- $2T_m$ solutions from perturbation and numerical integration at the subharmonic resonance $\omega \approx 2c_1 = 2$ with FE mesh stiffnesses. The perturbation analysis gives two parallel vertical branches implying primary parametric instability boundaries at the frequencies $\omega_{c1,c2}$. Two open curves (unstable dashed line and stable solid line) emerge after contact loss occurs. Numerical integration with fine frequency resolution converges to the two vertical perturbation solution branches. The system suffers from harmful sudden status changes at both sides of the resonant frequency. With increasing mesh frequency the numerical result first follows the linear period-T_m solution branch and jumps up at ω_{c1}. It then follows the stable, nonlinear period-$2T_m$ branch and jumps down to the period-T_m solution at ω_{c2}. With decreasing frequency, the numerical result jumps up at ω_{c2}, follows the stable, nonlinear period-$2T_m$ solution past ω_{c1}, and jumps down to the period-T_m branch at the resonance peak. The harmonic balance analysis reveals that the nonlinear solution branches are closed at the resonance peak, which is a bifurcation point causing jump-down. First order perturbation does not capture the closure of the branches and resulting jump. The instability interval $\omega_{\text{int}} = \omega_{c2} - \omega_{c1}$, however, is found to be proportional to the peak amplitude of the jump-down. The perturbation solution naturally predicts ω_{c1} and ω_{c2} . Thus, it provides qualitative understanding of the amplitude of subharmonic resonance, the most important factor affecting vibration and noise.

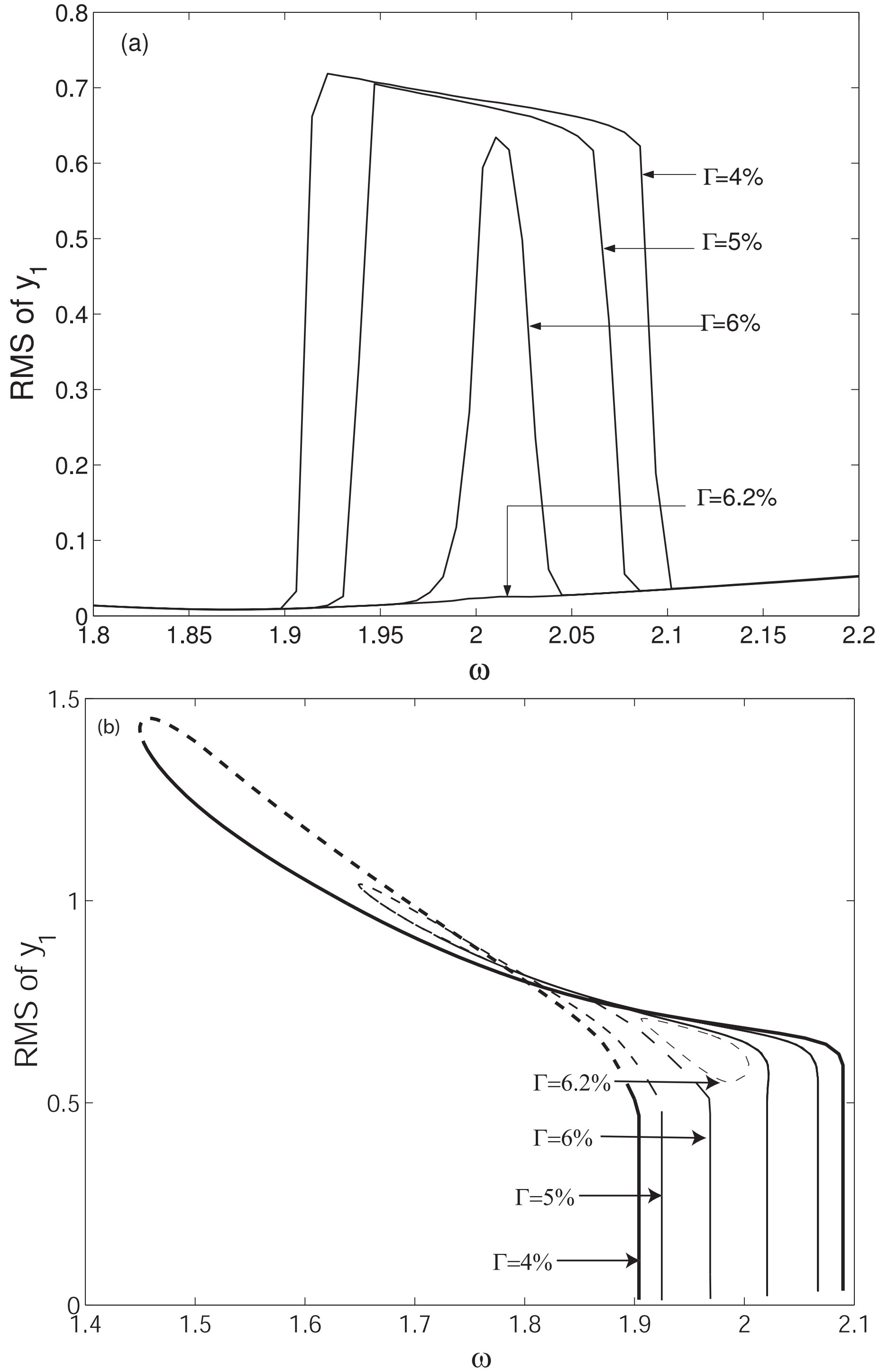

Figure 3.9: Damping effect on the subharmonic resonance $\omega \approx 2$ with parameters in Table 3.1 and FE mesh stiffnesses (a) Numerical integration with increased frequency (b) Harmonic balance.

By tuning the instability interval ω_{int}, one can reduce or even eliminate the subharmonic resonance. For instance, the instability interval sensitivity with respect to damping is

$$\omega_{\text{int}} = 2\sqrt{|Q_3|^2 - 4\Gamma^2 c_r^4} / c_r, \quad \frac{d\omega_{\text{int}}}{d\Gamma} = -\frac{8c_r^3\Gamma}{\sqrt{|Q_3|^2 - 4\Gamma^2 c_r^4}} \tag{3.44}$$

Equation (3.44) shows that the instability region, and correspondingly the amplitude of subharmonic resonance, are highly sensitive to the damping, and the instability disappears when $\Gamma \geq |Q_3|/(2c_r^2)$. Figure 3.9a depicts the effect of damping on subharmonic response for increasing frequency calculated by numerical integration. Damping substantially narrows the instability region and decreases the maximum stable amplitude. The resonance is eliminated when $\Gamma = |Q_3|/2 = 0.062$. Figure 3.9b confirms these details and adds the unstable branches using the harmonic balance method. When $\Gamma = 0.062$, the period-2 T_m solution is an unstable loop, and the primary instability interval disappears.

3.3.4 Interactions between Multiple Meshes

A major difference between single mesh and multi-mesh systems is the interactions between the meshes. The key parameter is the phase difference between the two mesh stiffnesses. The mesh phase and contact ratios strongly affect the dynamic response amplitude and presence/absence of certain resonances. According to (3.31), (3.35), and (3.37), R_3, $\tilde{R}_3$ and Q_3 are considered as indicators of the resonant peak amplitudes.

For the fundamental resonance of the r-th mode, this indicator is

$$\left|R_3\right| = \left|s_{1r}C_1\hat{\kappa}_1 + s_{2r}C_2\hat{\eta}_1 e^{i\left[\phi+\pi(\varsigma_1-\varsigma_2)\right]}\right| / \bar{k}_1, \quad C_j = s_{j1}F_1 + s_{j2}F_2 \tag{3.45}$$

where $\hat{\kappa}_1$, $\hat{\eta}_1$ are the magnitudes of $\tilde{\kappa}_1$, $\tilde{\eta}_1$, respectively. C_j are the constant static transmission errors of mesh j for average mesh stiffnesses. The C_j are positive (compressed tooth) with proper external loads. Both mesh stiffness variations contribute to resonant excitation. The phase angle between the harmonics of two mesh stiffnesses includes the contact ratios and mesh phase. To isolate the effect of mesh phase, the two contact ratios and the amplitudes of the two mesh stiffness harmonics are assumed identical. With these stipulations, (3.45) simplifies to

$$\left|R_3\right| = \hat{\kappa}_1\left(s_{1r}^2C_1^2 + 2C_1C_2s_{1r}s_{2r}\cos\phi + s_{2r}^2C_2^2\right)^{1/2} / \bar{k}_1 \tag{3.46}$$

The periodicity of mesh phase ϕ is 2π. The indicator is symmetric about π so that only the range from 0 to π is considered. The impact of mesh phase on peak amplitude depends on the vibration modes. For the idler system, $s_{11}s_{21} > 0$ for the first mode ($r = 1$), and $s_{12}s_{22} < 0$ for the second mode ($r = 2$). Therefore, if $\phi = 0$, the first mode resonance is maximized while the second mode resonance is minimized due to the cancellation or addition of the two mesh variations. The effects are reversed if $\phi = \pi$.

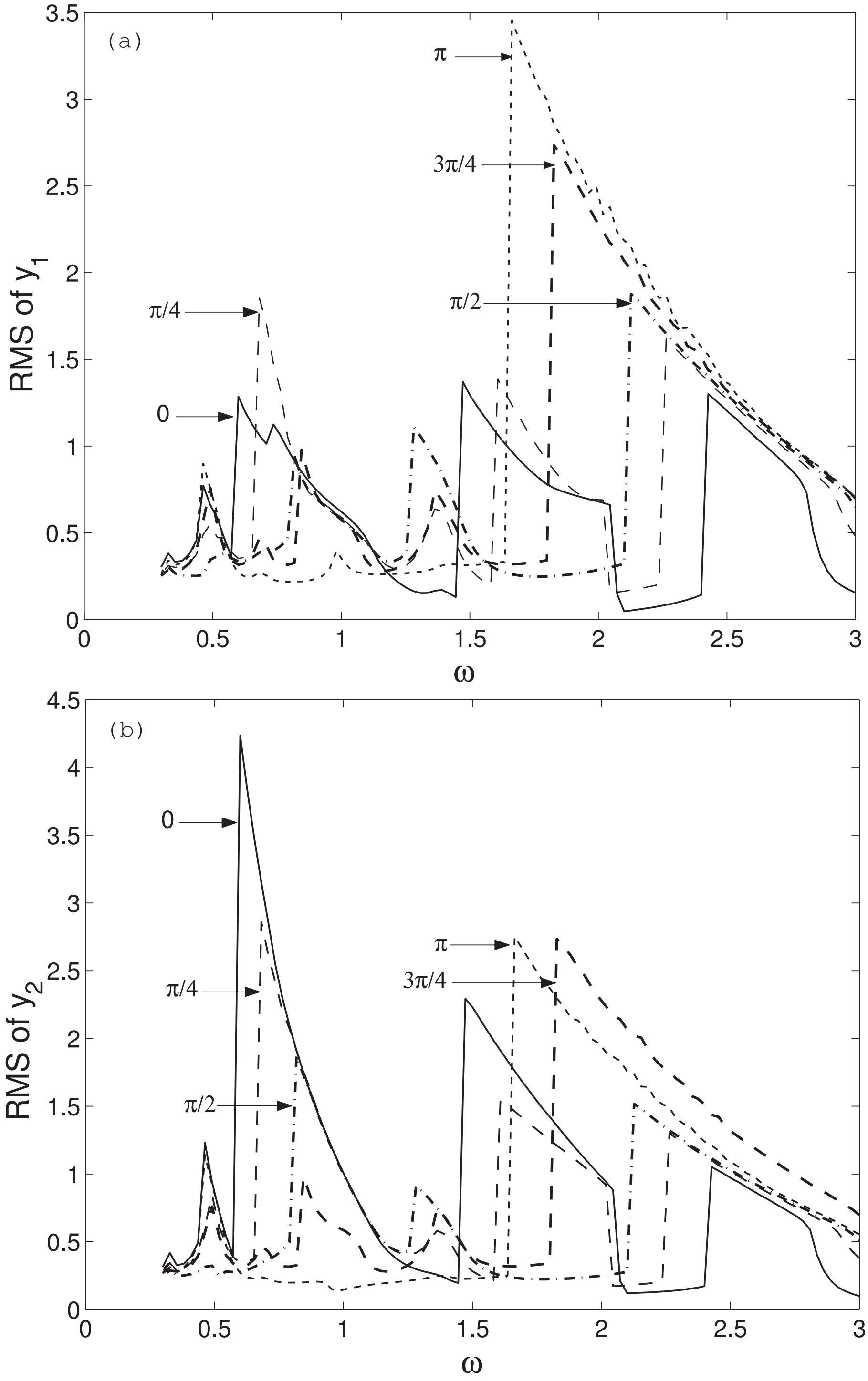

Figure 3.10: Influence of mesh phase on DTE calculated by numerical integration with parameters in Table 3.1 and FE mesh stiffnesses (a) The first mesh; (b) The second mesh.

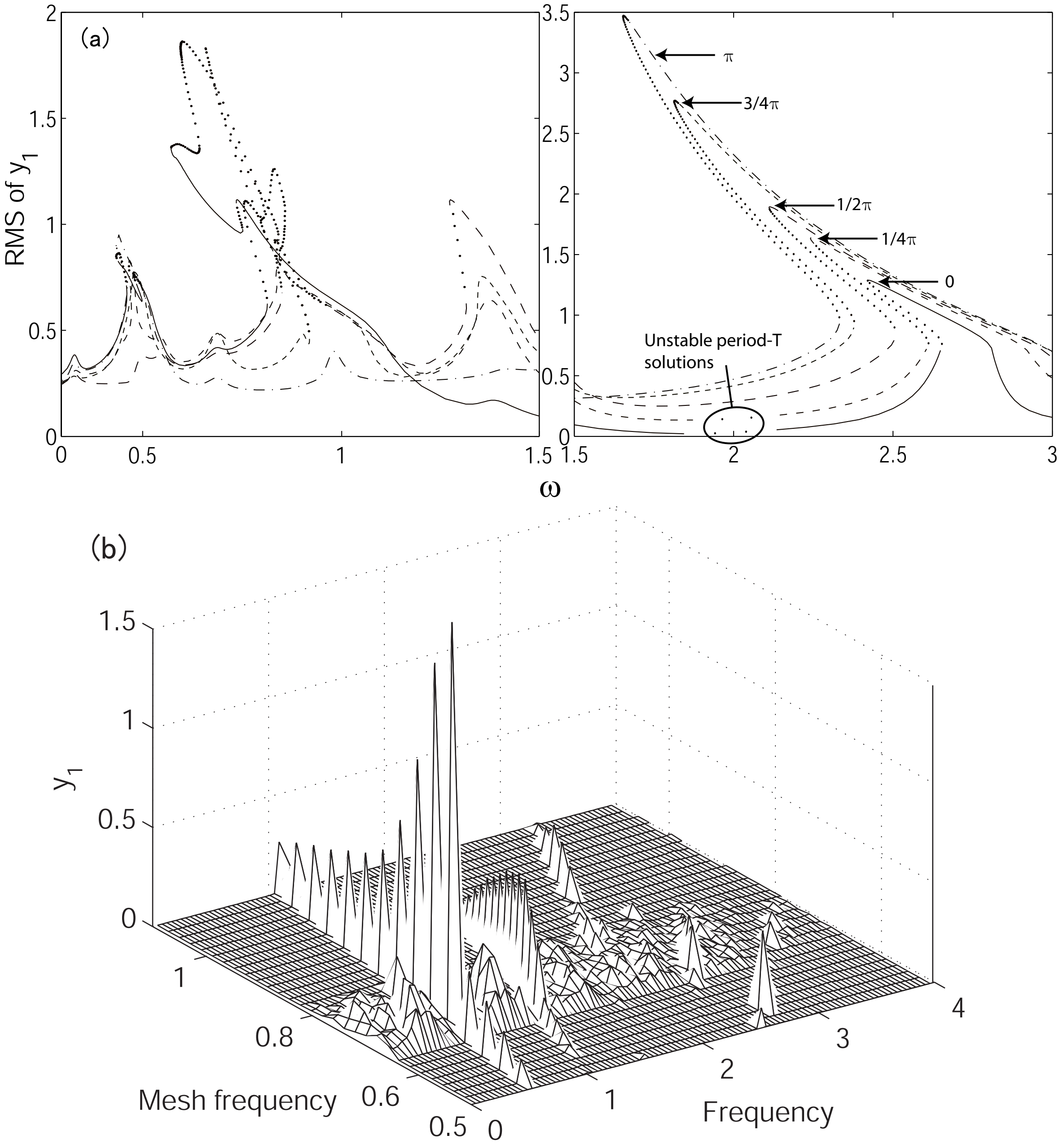

Figure 3.11: Influence of mesh phase on DTE with parameters in Table 3.1 ($\varsigma_1 = \varsigma_2 = 1.5$) and FE mesh stiffnesses (a) Harmonic balance results (dotted data is unstable); (b) Spectra of $\phi = \pi / 4$.

Similarly, the indicators of the subharmonic and second-harmonic resonance for equal contact ratios and mesh stiffness harmonics are

$$
\begin{aligned}
|Q_3| &= \hat{\kappa}_1 \left(s_{1r}^4 + 2 s_{1r}^2 s_{2r}^2 \cos\phi + s_{2r}^4 \right)^{1/2} / \overline{k}_1 \\
|\tilde{R}_3| &= \hat{\kappa}_2 \left(s_{1r}^2 C_1^2 + 2 C_1 C_2 s_{1r} s_{2r} \cos 2\phi + s_{2r}^2 C_2^2 \right)^{1/2} / \overline{k}_1
\end{aligned}
\tag{3.47}
$$

Unlike fundamental resonance, the influence of mesh phase on subharmonic resonance is independent of the sign of $s_{1r}s_{2r}$, which implies the peak amplitude of subharmonic decreases from $\phi = 0$ to $\phi = \pi$ regardless of the excited vibration mode. For the second-harmonic resonance, $\phi = \pi / 2$ minimizes the first mode resonance and maximizes the second mode resonance. When $\phi = 0$ (or π), the impact is reversed for both modes.

The significant effects of mesh phase on dynamic response are shown in Figure 3.10. The y_2 at the first mode fundamental resonance ($\omega \approx 1$) decreases monotonically with mesh phase because of the cancellation of the two excitations, as predicted. The y_1 for $\phi = \pi / 4$ at $\omega \approx 1$, however, is higher than the y_1 for $\phi = 0$ due to the aperiodic solution evolving from a two-mode combination instability not captured by the single-mode perturbation solution. As shown in Figure 3.11a, complicated solution loops occur for $\phi = 0$, $\pi / 4$, and $\pi / 2$. When the mesh phase increases from 0 to $\pi / 4$, the solutions for $\omega \approx 1$ change from period-T_m to period-$2T_m$ and then to chaos. Chaos occurs from $\omega = 0.65$ to $\omega = 0.84$ for $\phi = \pi / 4$ as shown in Figure 3.11b where the peaks at $\omega \approx 1$ and $\omega \approx 2.76$ indicate two-mode instability. The solution for $\omega = 0.845$ is period-T_m, and that for $\omega = 0.840$ changes to period-$2T_m$. A further slight change to $\omega = 0.800$ yields chaos, as shown by the broadband spectrum in Figure 3.11b and the Poincare maps in Figure 3.12.

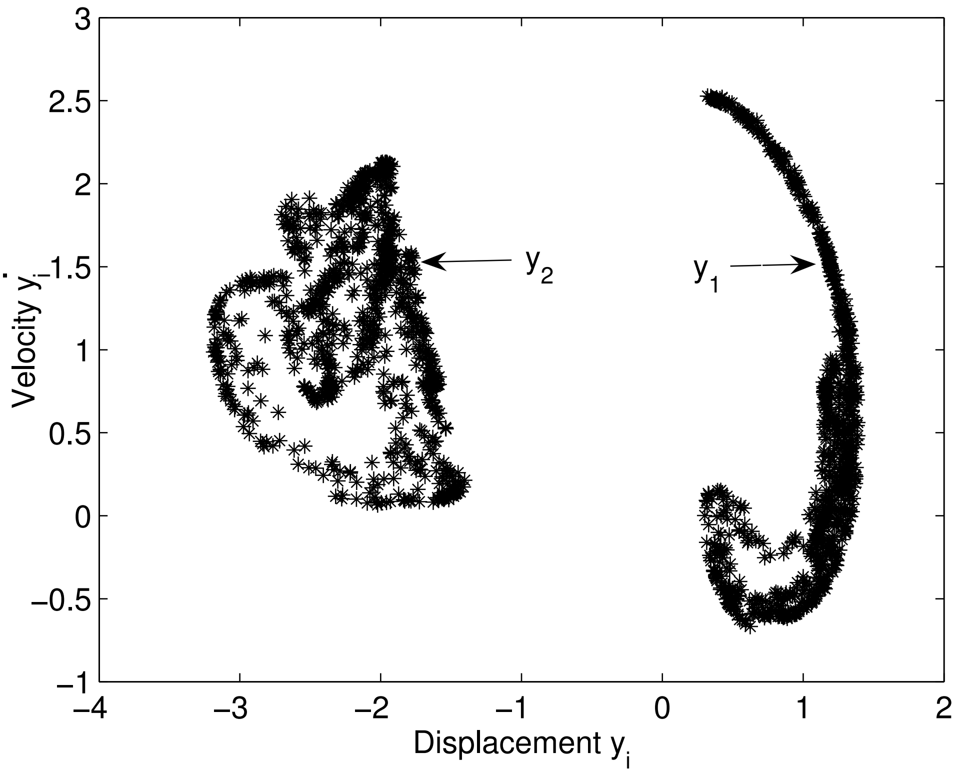

Figure 3.12: Poincare map of $\phi = \pi/4$ and $\omega = 0.800$ extracted from Figure 3.11b.

Figure 3.10 and Figure 3.11a both show the amplitude of the second-mode fundamental resonance ($\omega \approx 2.76$) increases with mesh phase due to the addition of the two mesh excitations. The second-harmonic resonance at $\omega \approx 0.5$ shows the highest amplitude at $\phi = 0$ (and π) and the lowest amplitude at $\phi = \pi/2$, while the one at $\omega \approx 1.38$ shows the highest amplitude at $\phi = \pi/2$ and the lowest amplitude at $\phi = 0$ (and π). The resonant amplitude indicators from perturbation (Figure 3.13a) predict amplitude changes with mesh phase variation as given by the numerical results. While the curves in Figure 3.13a are independent of Γ, subharmonic resonance occurs only when $|Q_3| \geq 2\Gamma$. For the present system, $2\Gamma = 0.08$ and subharmonic resonance occurs only for $\phi < 0.4\pi$.

Consistent with this prediction, the subharmonic resonances ($\omega \approx 2$) in Figure 3.10 occur only when $\phi = 0$ and $\pi/4$. The primary instability ($\omega \approx 2$) in Figure 3.11a emerge when $\phi = 0$ and $\pi/4$.

In practice the two contact ratios are not the same and the difference of contact ratio interacts with mesh phase. Assuming identical amplitude of stiffness harmonics, the indicator of the peak amplitudes of the fundamental resonances are

$$\left|R_3\right| = \hat{\kappa}_1 \left\{ s_{1r}^2 C_1^2 + 2C_1 C_2 s_{1r} s_{2r} \cos\left[\phi + \pi\left(\varsigma_1 - \varsigma_2\right)\right] + s_{2r}^2 C_2^2 \right\}^{1/2} / \bar{k}_1 \tag{3.48}$$

The range of mesh phase ϕ increases to 2π. The critical mesh phases for the extrema of the fundamental resonance are $(\varsigma_2 - \varsigma_1)\pi$ and $(\varsigma_2 - \varsigma_1 + 1)\pi$. Similar analysis of $\left|\tilde{R}_3\right|$ yields the critical mesh phase for the extrema of the second-harmonic resonances as $(\varsigma_2 - \varsigma_1)\pi$, $(\varsigma_2 - \varsigma_1 + 1)\pi$ and $(\varsigma_2 - \varsigma_1 \pm 1/2)\pi$. Figure 3.13b shows the influence of mesh phase with different contact ratios predicted by the perturbation analysis. The mesh phases leading to extrema of peak amplitudes are changed by the differing contact ratios. The impacts of mesh phase on the fundamental and subharmonic resonances are shifted by $\pi/2$ compared to the case $\varsigma_1 = \varsigma_2 = 1.5$. The impact of mesh phase on the second-harmonic resonances is the same as the case $\varsigma_1 = \varsigma_2 = 1.5$ because the difference of contact ratio causes a shift of π.

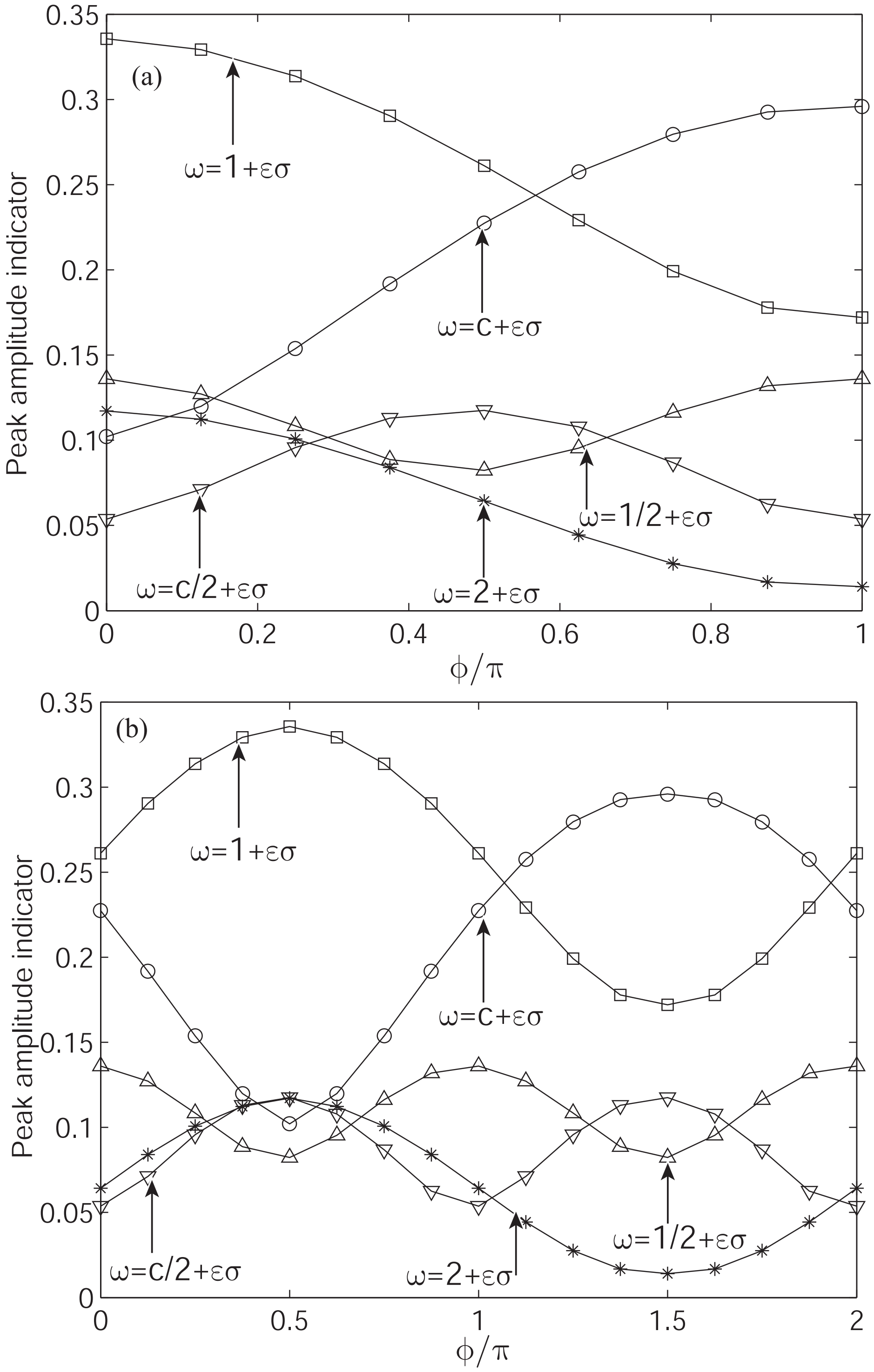

Figure 3.13: Influence of mesh phase on DTE by perturbation analysis with parameters in Table 3.1 and FE mesh stiffnesses (a) $\varsigma_1 = \varsigma_2 = 1.5$; (b) $\varsigma_1 = 1.2$ and $\varsigma_2 = 1.7$.

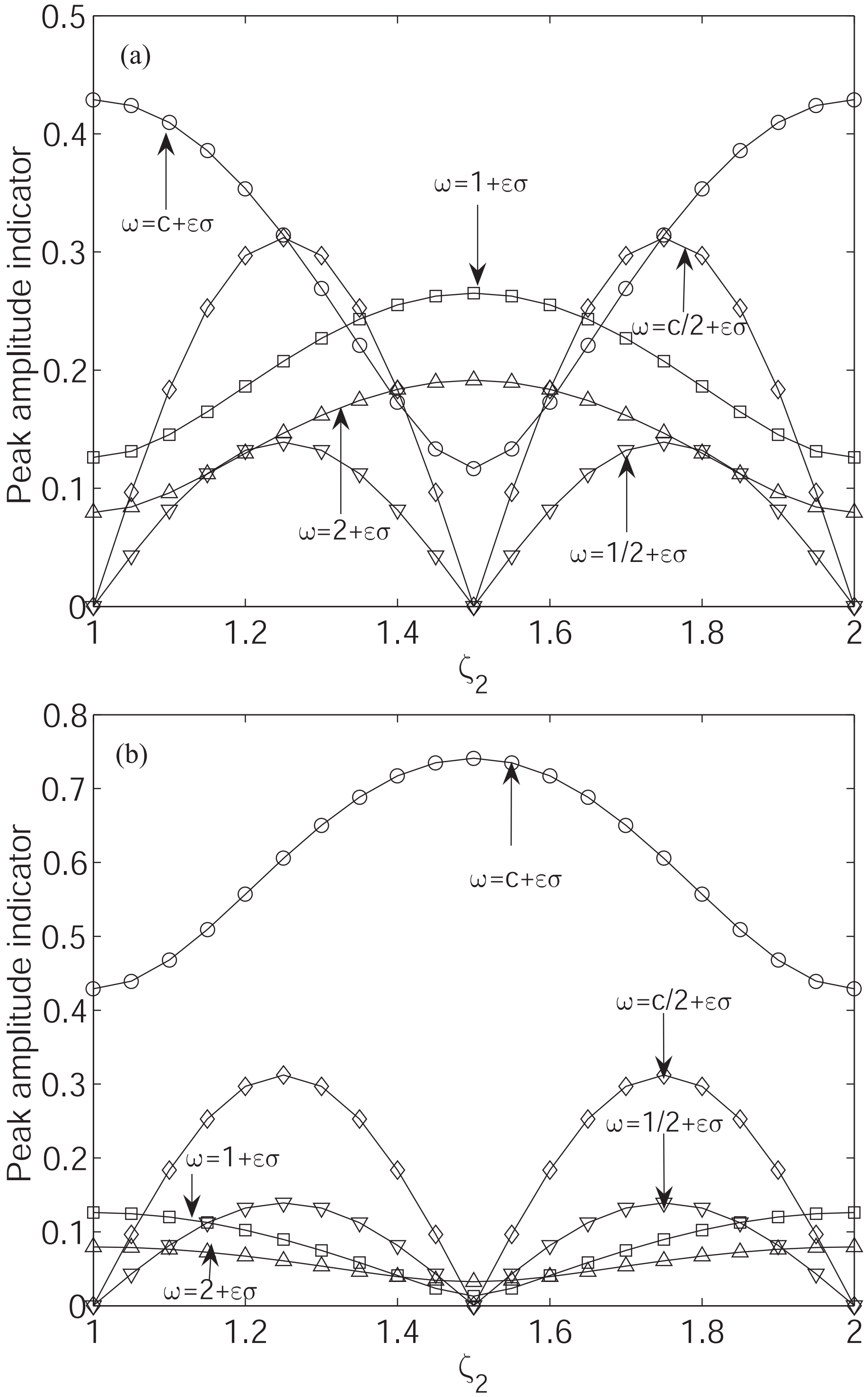

Figure 3.14: Influence of the second mesh contact ratio on DTE with parameters in Table 3.1 ($\phi = 0$) and rectangular-wave mesh stiffnesses by perturbation (a) $\phi = 0$; (b) $\phi = \pi$.

The different contact ratios not only contribute to the phase difference but also affect the amplitudes of the mesh stiffness harmonics. To set aside the complexity from corner contact the rectangular wave mesh stiffnesses are used here. Firstly, $\phi = 0$ and $\varsigma_1 = 1.5$ are fixed while ς_2 varies between 1 and 2. In view of (3.13) and (3.45), the influence of ς_2 on the fundamental resonance is

$$|R_3| = \left[s_{1r}^2 C_1^2 + \frac{\Lambda_2}{\Lambda_1} s_{2r} C_2 (2 s_{1r} C_1 + \frac{\Lambda_2}{\Lambda_1} s_{2r} C_2) \sin^2(\pi \varsigma_2) \right]^{1/2} / 2 \qquad (3.49)$$

The indicator is symmetric about $\varsigma_2 = 1.5$. For the first mode, $\frac{\Lambda_2}{\Lambda_1} s_{2r} C_2 (2 s_{1r} C_1 + \frac{\Lambda_2}{\Lambda_1} s_{2r} C_2)$ is positive. It is negative and the magnitude is less than $s_{1r}^2 C_1^2$ for the second mode. Thus, the first fundamental resonance is maximized at $\varsigma_2 = 1.5$ and minimized at $\varsigma_2 = 1$ or 2, while the second fundamental resonance is minimized at $\varsigma_2 = 1.5$ and maximized at $\varsigma_2 = 1$ or 2. Similar analysis can be applied to the second-harmonic and subharmonic resonances. The analytical prediction in Figure 3.14a shows the sensitivity of contact ratio on the resonant indicators; these predictions have been validated against numerical results. Surprisingly, high contact ratio does not always reduce the resonant amplitude. For example, at the second fundamental resonance, the amplitude of contact ratio 2.0 is higher than contact ratio 1.5. This is because the two mesh variations cancel each other for $\varsigma_2 = 1.5$, while the second mesh variation is zero and no cancellation is provided for $\varsigma_2 = 2$. Subharmonic resonance occurs for the whole range of ς_2 because $|Q_3| > 2\Gamma$.

For a second example, the mesh phase is set as π and $\varsigma_1 = 1.5$. The influence of ς_2 simplifies to

$$|R_3| = \left[s_{1r}^2 C_1^2 - \frac{\Lambda_2}{\Lambda_1} s_{2r} C_2 (2 s_{1r} C_1 - \frac{\Lambda_2}{\Lambda_1} s_{2r} C_2) \sin^2(\pi \varsigma_2) \right]^{1/2} / 2 \tag{3.50}$$

For the first mode, $\frac{\Lambda_2}{\Lambda_1} s_{2r} C_2 (2 s_{1r} C_1 - \frac{\Lambda_2}{\Lambda_1} s_{2r} C_2) > 0$ and its magnitude is less than $s_{1r}^2 C_1^2$. It is negative for the second mode. Therefore, the first fundamental resonance is cancelled by the two mesh excitations while the second fundamental resonance is strengthened by the two mesh excitations. As shown in Figure 3.14b, the first one is maximized at $\varsigma_2 = 1$ or 2 and minimized at $\varsigma_2 = 1.5$. Contrarily, the second one is minimized at $\varsigma_2 = 1$ or 2 and maximized at $\varsigma_2 = 1.5$. Similar analysis can be applied to the second-harmonic and subharmonic resonances. The sensitivity of the second-harmonic resonance on ς_2 is the same as $\phi = 0$ because the mesh phase π leads to a 2π phase shift. Note the important fact that the subharmonic resonance disappears for the whole range of ς_2 because $|Q_3| \le 2\Gamma$.

3.3.5 Torque Impact

With the assumption that changes in the applied torque within a reasonable range do not change the mesh stiffness peak-peak value or the operating contact ratio, the dimensionless dynamic responses near resonances are

$$y_j = s_{j1} F_1 + s_{j2} F_2 + 2 s_{jr} \alpha \cos(c_r \tau - \gamma) \quad r = 1 \; or \; 2 \tag{3.51}$$

where α satisfies the frequency response expressions (3.31), (3.35), and (3.37), which are independent of the external torque. Therefore, most dimensionless nonlinear characteristics, such as the transition frequencies, peak frequency, peak amplitude, and stability boundaries, are invariant for different torques. The physical dynamic responses $x_j = \bar{x}_1 y_j = T y_j / \bar{k}_1$, however, depend linearly on the external torque. This implies that the dimensional frequency response curves scale proportionally with torque. As an important and counter-intuitive consequence, contact loss persists even at high torques.

CHAPTER 4

NONLINEAR DYNAMICS OF COUNTER-SHAFT GEARSETS

This chapter studies the nonlinear, parametrically excited dynamics of counter-shaft gear systems. A nonlinear dynamic model is established for counter-shaft gears including parametric excitation and contact loss. The periodic steady state solutions are obtained by perturbation analysis and compared against a semi-analytical harmonic balance method as well as numerical integration for fundamental, subharmonic and second harmonic resonances with varied system parameters. The interaction of the two meshes is found to depend on the relation of the two mesh periods. The dynamic influences of design parameters, such as shaft stiffness, mesh stiffness variation, contact ratio, and mesh phasing, are discussed based on the closed-form solutions.

4.1 Introduction

Prior research of gear dynamics yields a variety of mathematical gear models which are reviewed in [21-23]. Three different lumped-parameter models are evaluated against finite element (FE) analysis in [83]. A model with time-varying mesh stiffness is used in [62] to analytically study nonlinear idler gear dynamics. Interaction between the two meshes is found to be critical to nonlinear gear dynamics. Analytical models with periodically-varying mesh stiffnesses for two-stage (counter-shaft) gear systems are found in [19, 26, 49]. A model with periodic static transmission error (STE) excitation is adopted for two-stage helical gear systems in [11]. Only the mean value of mesh stiffness is considered in the stiffness matrix, and the mesh stiffness variation is implicitly included in the STE. Special finite element (FE) gear models combined with contact mechanics are developed and gain success on dynamic analysis in the past [5, 8, 55, 84].

The studies on counter-shaft gear systems (Figure 4.1) are much fewer than for single gear pair systems. The complexity of counter-shaft systems lies not only in the increased number of gear bodies but, more importantly, the interactions between the multiple gear meshes compared to single mesh gear systems. Parametric instability analyses are discussed in [19, 32]. The mesh phasing (phase between the fluctuating mesh stiffnesses of the two meshes) and contact ratio interaction are claimed to be influential to instability boundary when the ratio of the two mesh frequencies are close to an integer multiple. Dynamic coupling in two-stage gear systems are studied in [23, 49, 85], where the impact of shaft flexibility between the two middle gears is focused. The work in [86] discusses coupled lateral-torsional vibration of a two-stage gear train system.

The analytical solution of linear response is obtained when the multiples of mesh frequency equals to natural frequency. It is concluded that adopting an adequate phase or contact ratio can avoid some resonances of the system. The nonlinear dynamics of idler and counter-shaft gearsets is investigated in [26]. Mesh phasing and contact ratio are found to impact gear dynamics for both types of gearsets.

The past studies on counter-shaft gearsets rely primarily on numerical integration solutions. The numerical solutions, however, provide limited physical understanding, and the conclusions are often valid for a certain group of parameters. The harmonic balance method and perturbation analysis on a gear pair are discussed in [37, 87]. To get closed-form expressions, only the first harmonic of mesh stiffness is included in the harmonic balance method. The piece-wise linear solution in the perturbation analysis leads to the semi-analytical solution. Complex nonlinear, time-varying problems of counter-shaft gear systems make analytical methods difficult. There is no readily useful closed-form solution available for counter-shaft gearsets to predict nonlinear dynamics and conduct parametric studies. Furthermore, the interactions between counter-shaft gear meshes and how to utilize the interactions for vibration reduction have not been explored.

In this study, the nonlinear and time-varying analytical model includes key design parameters such as mesh stiffness variation, mesh phasing, and contact ratios. The dynamic model is compared to a finite element/contact mechanics benchmark. With appropriate assumptions, the present work seeks analytical approximations for the periodic steady state solutions. Perturbation yields closed-form expressions that connect the important design parameters to the characteristics of the nonlinear resonances (e.g., bifurcation frequencies and peak amplitude). Based on these expressions, this work discusses the interplay between the two meshes with different mesh periods, mesh stiffness variations, and contact ratios, examining their impact on nonlinear response for fundamental, secondary, and subharmonic resonances. The effects of system parameters on the amplitude and characteristic features of the nonlinear resonances are studied analytically and confirmed with numerical integration, harmonic balance, and finite element solutions. The closed-form expressions provide guidelines for vibration reduction by tuning design parameters.

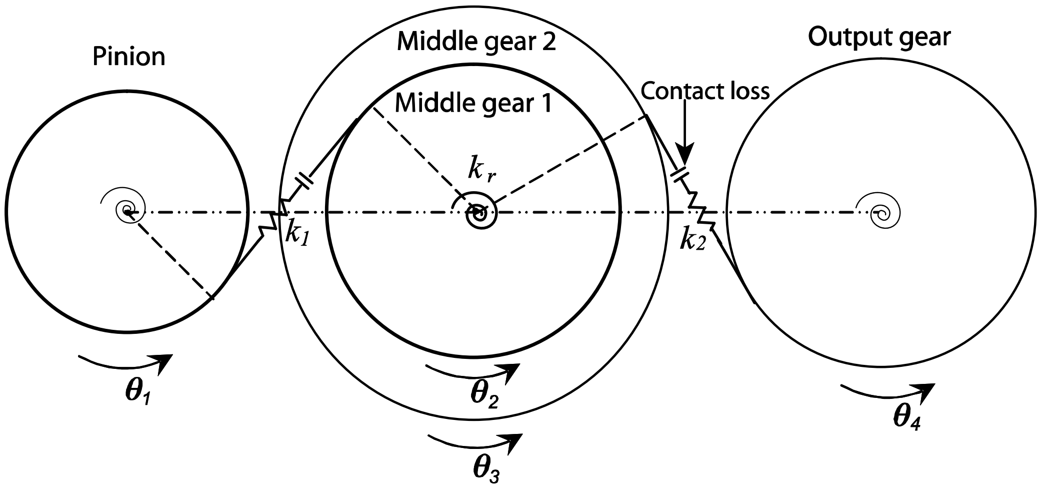

Figure 4.1: Translational-rotational model of counter-shaft gear systems.

4.2 Modeling and methodology

A two-stage counter-shaft gearset is shown in Figure 4.1. The input gear (pinion) meshes with a middle gear coaxially connected with another middle gear that transmits power to the output gear. The two middle gears are either connected by a shaft or made from one part. The mesh frequencies of the two gear meshes are different. The fluctuating stiffnesses of the tooth meshes as contact conditions change lead to parametric excitations, and clearances of the gear meshes create contact loss nonlinearity.

4.2.1 Physical System Model and Assumptions

4.2.1.1 Assumptions and nomenclature

The number of gear teeth and base radii are z_{1-4} and r_{1-4}, where gears 1, 2, 3, and 4 are the pinion, the two middle gears, and the output gear, respectively. Only gear rotational vibrations ψ_{1-4} are considered. Mesh phasing is considered instead of the angular orientation of the gear centers, so the gear centers are aligned without loss of generality.

Parametric excitation is introduced by the time-varying mesh stiffness k_j (mesh index $j = 1, 2$) that includes the flexibility of the gear bodies and teeth. The periodic mesh stiffness is calculated by a finite element/contact mechanics method, whose effectiveness and efficiency for multi-mesh gear dynamics are discussed in [5, 8, 55, 88]. The gear teeth separate (i.e., contact loss) when the mesh deflection is negative due to backlash. Backside tooth contact is not included because it is rare for systems with proper gear load and backlash. Gear tooth profile deviations are not included in this study. Constant external torques Q_{1-4} are applied to each gear with $Q_2 = Q_3 = 0$, in general. k_r is the rotational stiffness of the middle shaft. Rotational stiffnesses of the input and output shafts are not considered, but they can readily be included if appropriate. To remove the rigid body mode, elastic motions are introduced as

$$x_1 = r_1\psi_1 + r_2\psi_2 \qquad x_2 = -(r_2\psi_2 + r_3\psi_3) \qquad x_3 = r_2(\psi_2 - \psi_3) \tag{4.1}$$

where $x_{1,2}$ are dynamic transmission errors (DTE) and x_3 is the relative rotation between the two middle gears.

4.2.1.2 Mathematical model

A three-DOF nonlinear dynamic model is derived in terms of the elastic motions as

$$\hat{\mathbf{M}}\ddot{\mathbf{X}} + \hat{\mathbf{K}}(\tilde{\omega}_j t, \mathbf{X})\mathbf{X} = \hat{\mathbf{F}} \tag{4.2}$$

$$\mathbf{X}=[x_1, x_2, x_3]^T; \;\; \hat{\mathbf{K}} = Diag(H_1 k_1, H_2 k_2, k_s); \;\; \hat{\mathbf{F}} = F[1, r_2 / r_3, -1] \tag{4.3}$$

where $\mathbf{K}$ is the stiffness matrix with contact loss nonlinearity and mesh stiffness parametric excitations; the tooth separation functions are $H_j\left(x_j\right)=\begin{cases}1 & x_j \geq 0 \\ 0 & x_j < 0\end{cases}$; $F = Q_1 / r_1$ is the contact force of the first mesh; and the mesh frequency $\tilde{\omega}_j$ denotes passing frequency of gear teeth for mesh j. The two mesh frequencies satisfy $\tilde{\omega}_2 / \tilde{\omega}_1 = \rho = z_3 / z_2$.

Letting $\bar{k}_j$ and $\bar{\mathbf{K}}$ be the mean values of k_j and $\mathbf{K}$, respectively, the eigenvalue problem of Eq. (4.2) is $\left(\bar{\mathbf{K}} - \lambda_{\tilde{s}}^2 \hat{\mathbf{M}}\right)\mathbf{v}_{\tilde{s}} = \mathbf{0}$. The modal matrix is $\mathbf{V} = \left[\mathbf{v}_1 \vdots \mathbf{v}_2 \vdots \mathbf{v}_3\right]$ normalized such that $\mathbf{V}^T\mathbf{M}\mathbf{V} = \mathbf{I}$. The average static transmission errors (STE) are $\bar{x}_1 = F / \bar{k}_1$ and $\bar{x}_2 = F r_2 / (r_3 \bar{k}_2)$.

Let Γ_j ($j = 1, 2$) be the peak-peak values of the mesh stiffnesses. The dimensionless mesh stiffness variations are $\varepsilon_j = \Gamma_j / \bar{k}_j$. $\varepsilon_j < 1$ and this yields the small perturbation parameters. $\varepsilon < 0.5$ according to prior studies [19, 89].

The periodic mesh stiffnesses $k_j(t)$ are expanded as

$$\begin{aligned} k_1 &= \bar{k}_1 + \sum_{m=1}^{\infty}\left(\tilde{\kappa}_{1m}e^{im\tilde{\omega}_1 t} + c.c.\right) = \bar{k}_1\left[1+\varepsilon\sum_{m=1}^{\infty}\left(\kappa_{1m}e^{im\tilde{\omega}_1 t} + c.c.\right)\right] \\ k_2 &= \bar{k}_2 + \sum_{m=1}^{\infty}\left(\tilde{\kappa}_{2m}e^{im\tilde{\omega}_2 t} + c.c.\right) = \bar{k}_2\left[1+\varepsilon\sum_{m=1}^{\infty}\left(\xi\kappa_{2m}e^{im\tilde{\omega}_2 t} + c.c.\right)\right] \end{aligned} \tag{4.4}$$

where $\varepsilon = \varepsilon_1$, $\xi = \varepsilon_2 / \varepsilon_1 = O(1)$, $\kappa_{1m} = \dfrac{\tilde{\kappa}_{1m}}{\Gamma_1} = O(1)$, $\kappa_{2m} = \dfrac{\tilde{\kappa}_{2m}}{\Gamma_2} = O(1)$, and *c.c.* denotes complex conjugate of previous terms.

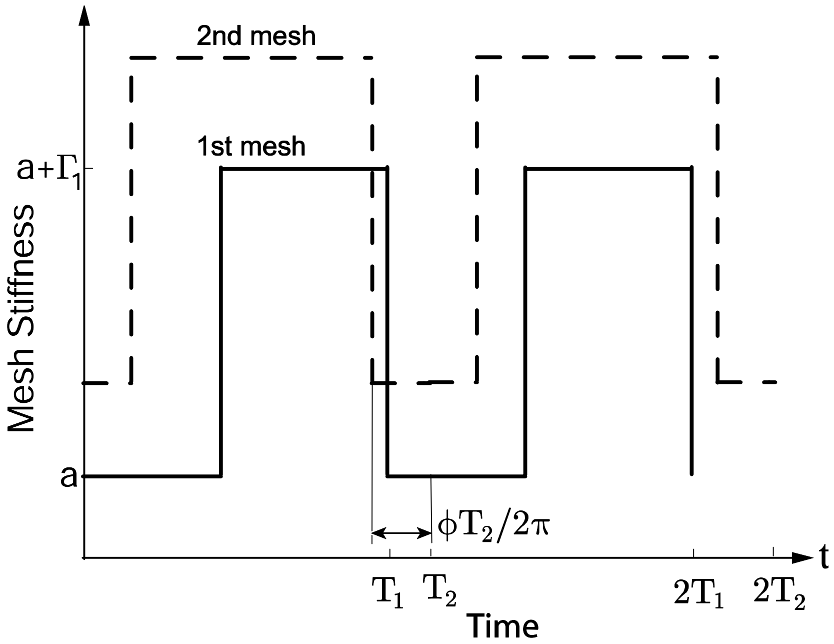

Figure 4.2: Mesh phasing for two rectangular-wave mesh stiffnesses of counter-shaft gear systems.

A phase relation exists between the same contact reference state for the two mesh stiffnesses of a counter-shaft gearset. Without loss of generality, consider two rectangular-wave mesh stiffness approximations as in Figure 4.2. The number of gear teeth in contact at mesh 1 changes from N_1+1 to N_1 at the end of mesh period T_1, where

N_j is the largest integer smaller than the contact ratio ς_j. The tooth number of the second mesh decreases from N_2+1 to N_2 at an instant $\phi T_2/(2\pi)$ before the end of mesh period T_2, where ϕ is the mesh phasing determined by the angle of gear centerlines and gear tooth geometry [61]. The selection of the reference state (e.g., reduction from N_j+1 to N_j contacting teeth) does not affect the phase. For example, the pitch points could also be used.

The complex Fourier coefficients of the mesh stiffnesses in Figure 4.2 are

$$\left.\begin{aligned}\tilde{\kappa}_{1m} &= -\frac{\Gamma_1}{m\pi}\sin\left(m\pi\varsigma_1\right)e^{-im\pi\varsigma_1}\\ \tilde{\kappa}_{2m} &= -\frac{\Gamma_2}{m\pi}\sin\left(m\pi\varsigma_2\right)e^{-im\left(\pi\varsigma_2-\phi\right)}\end{aligned}\right\} \Rightarrow \left\{\begin{aligned}\kappa_{1m} &= -\frac{1}{m\pi}\sin\left(m\pi\varsigma_1\right)e^{-im\pi\varsigma_1}\\ \kappa_{2m} &= -\frac{1}{m\pi}\sin\left(m\pi\varsigma_1\right)e^{-im\left(\pi\varsigma_2-\phi\right)}\end{aligned}\right. \tag{4.5}$$

where m is the harmonic order. The total phase difference between the Fourier coefficients $\tilde{\kappa}_{1m}$ and $\tilde{\kappa}_{2m}$ includes the stiffness shape difference (as captured by the contact ratio) and the time difference for the same contact state (i.e., the mesh phasing).

Gear resonance with nearly harmonic response [5, 8, 48, 55, 90] occurs when a mesh frequency or integer multiple of mesh frequency is close to a natural frequency or a particular multiple of natural frequency. The large amplitude response due to parametric instability causes nonlinear contact loss that bounds the vibration. In practice and from numerical simulations for most parametric resonances, one contact loss occurs in each response cycle. Thus, the tooth separation functions H_j are rectangular waves in a cycle. The separation times q_j (where H_j=0) are assumed to be small fractions of the response period ($q_j \ll 2\pi/\tilde{\Omega}$, where $\tilde{\Omega}$ is fundamental frequency of response), and this is borne out in finite element simulations and numerical integration. Consequently,

$$H_j = 1 + \varepsilon \hat{H}_j \qquad j = 1,2 \tag{4.6}$$

The tooth separation angles are defined as $\theta_j = q_j \tilde{\Omega}/2$ ($\theta_j / \pi < 1$).

4.2.1.3 Dimensionless model formulation

Two quantities are chosen to non-dimensionalize the equations: the first natural frequency λ_1 and the average first mesh STE $\bar{x}_1$. The dimensionless quantities are

$$\tau = \lambda_1 t,\ \omega_j = \frac{\tilde{\omega}_j}{\lambda_1},\ \Omega = \frac{\tilde{\Omega}}{\lambda_1},\ y_{\tilde{s}} = \frac{x_{\tilde{s}}}{\bar{x}_1},\ c_{\tilde{s}} = \frac{\lambda_{\tilde{s}}}{\lambda_1},\ \eta = \frac{\bar{k}_2}{\bar{k}_1},\ \tilde{\mathbf{F}} = \mathbf{F}/(Fc_{\tilde{s}}^2) \qquad \tilde{s} = 1,2,3 \tag{4.7}$$

The dimensionless governing equations in modal form (with the transformation $\mathbf{y = Vu}$) are

$$\ddot{u}_{\tilde{s}} + \varepsilon \mu c_{\tilde{s}} \dot{u}_{\tilde{s}} + c_{\tilde{s}}^2 u_{\tilde{s}} + \varepsilon \sum_{p=1}^{3} f_{\tilde{s}p} u_p = c_{\tilde{s}}^2 F_{\tilde{s}} \qquad \tilde{s} = 1,2,3 \tag{4.8}$$

$$f_{\tilde{s}p} = \sum_{m=1}^{M} \left(v_{1\tilde{s}} v_{1p} \kappa_{1m} e^{im\omega_1 \tau} + \eta v_{2\tilde{s}} v_{2p} \kappa_{2m} e^{im\omega_2 \tau} + c.c. \right) + v_{1\tilde{s}} v_{1p} \hat{H}_1(\mathbf{u}) + \eta v_{2\tilde{s}} v_{2p} \hat{H}_2(\mathbf{u}) \tag{4.9}$$

where $\mu = 2\zeta/\varepsilon$ captures the small modal damping ζ and $F_{\tilde{s}}$ is the component of $\mathbf{V}^T \tilde{\mathbf{F}}$. The functions $f_{\tilde{s}p}$ include the mesh stiffness parametric excitations and nonlinear tooth separation of the two meshes.

4.2.2 Perturbation Analysis

The method of multiple scales [66] is adopted to seek approximate analytical solutions for (4.8). The unknown dynamic responses $u_{\tilde{s}}$ are approximated by asymptotic power series $u_{\tilde{s}}^{(n)}$ in ε, and τ is expanded into multiple time scales $\tau_n = \varepsilon^n \tau$. The ε^0 and ε^1 order differential equations (where $D_n = \partial / \partial \tau_n$) are

$$D_0^2 u_{\tilde{s}}^{(0)} + c_{\tilde{s}}^2 u_{\tilde{s}}^{(0)} = c_{\tilde{s}}^2 F_{\tilde{s}} \qquad \tilde{s} = 1,2,3 \tag{4.10}$$

$$D_0^2 u_{\tilde{s}}^{(1)} + c_{\tilde{s}}^2 u_{\tilde{s}}^{(1)} = -2D_0 D_1 u_{\tilde{s}}^{(0)} - \mu c_{\tilde{s}} D_0 u_{\tilde{s}}^{(0)} - \sum_{p=1}^{3} f_{\tilde{s}p} u_p^{(0)} \tag{4.11}$$

4.2.2.1 Frequency response of fundamental resonances

Case 1: $\omega_j \approx c_s$, and $\rho \neq z$ or $1/z$ (z is an integer)

In this case, one of the two mesh frequencies is near a natural frequency. From (4.10), the leading order solutions for $\Omega = \omega_j = c_s + \varepsilon\sigma$ (σ is the detuning) are

$$u_{\tilde{s}}^{(0)} = F_{\tilde{s}} + \left[A_{\tilde{s}}\left(\tau_1\right)e^{ic_{\tilde{s}}\tau_0} + c.c.\right] = F_{\tilde{s}} + \left[B_{\tilde{s}}\left(\tau_1\right)e^{i\Omega\tau_0} + c.c.\right] \quad B_{\tilde{s}} = A_{\tilde{s}}e^{-i\sigma\tau_1} \quad \tilde{s} = 1,2,3 \tag{4.12}$$

where the complex amplitude $A_s = \alpha(\tau_1)e^{i\beta(\tau_1)}$. To avoid simultaneous parametric, or internal, resonances $c_2 \neq 2c_1$, $c_3 \neq 2c_2$, and $c_3 \neq 2c_1$.

Substitution of (4.12) into the right hand side of (4.11) yields the solvability conditions to prevent secular terms causing unbounded, aperiodic response

$$i2c_{\tilde{s}}\frac{\partial A_{\tilde{s}}}{\partial \tau_1} + \mu c_{\tilde{s}}^2 A_{\tilde{s}} + (v_{1\tilde{s}}^2 \hat{H}_1 + \eta v_{2\tilde{s}}^2 \hat{H}_2)A_{\tilde{s}} = 0 \qquad \tilde{s} \neq s \tag{4.13}$$

$$2ic_s\frac{\partial A_s}{\partial \tau_1} + (\mu i c_s^2 + v_{1s}^2 \hat{H}_1 + \eta v_{2s}^2 \hat{H}_2)A_s = -v_{js}\sum_{p=1}^{3}\left(v_{jp}F_p\right)\kappa_{j1}\bar{k}_j e^{i\sigma\tau_1} / \bar{k}_1 \tag{4.14}$$

where only the first harmonic of k_j is retained. While (4.13) is nonlinear because $\hat{H}_{1,2}$ depend on $A_{\tilde{s}}$, $A_{\tilde{s}} = 0$ is an asymptotically stable fixed point. The steady state

($\alpha' = \beta' = 0$) response of (4.14) yields $A_s \neq 0$. From **y = Vu** and (4.12), the first order solutions for the DTE are

$$y_j = \sum_{p=1}^{3} v_{jp} u_p^{(0)} = \sum_{p=1}^{3} v_{jp} F_p + 2 v_{js} \alpha \cos(\Omega \tau_0 - \gamma) \tag{4.15}$$

where $\gamma = \sigma \tau_1 - \beta$ is the response phase. Vanishing of the DTE delineates tooth contact and tooth separation. Thus, the condition $y_j = 0$ defines the period of tooth separation, and this yields the separation angles as

$$\theta_j = \begin{cases} \pi - \cos^{-1}\left(-\sum_{p=1}^{3} \left(v_{jp} F_p \right) / \left(2 v_{js} \alpha \right) \right) & if\ v_{js} > 0 \\ \cos^{-1}\left(-\sum_{p=1}^{3} \left(v_{jp} F_p \right) / \left(2 v_{js} \alpha \right) \right) & if\ v_{js} < 0 \end{cases} \tag{4.16}$$

y_j and $\hat{H}_j$ are in phase and have the same periodicity, so the periodic $\hat{H}_j$ in (4.6) are expanded as

$$\begin{aligned} \hat{H}_1 &= \sum_{n=0}^{\infty} \left(h_n e^{-in\gamma} e^{in\Omega\tau} + c.c. \right) \\ \hat{H}_2 &= \sum_{n=0}^{\infty} \left(g_n e^{-in\gamma} e^{in\Omega\tau} + c.c. \right) \end{aligned} \tag{4.17}$$

$$\begin{aligned} & h_0 = -\frac{\theta_1}{\pi\varepsilon},\ \ g_0 = -\frac{\theta_2}{\pi\varepsilon}, \\ & h_n = \frac{\sin n(\pi - \theta_1)}{n\pi\varepsilon},\ \ g_n = \frac{\sin n(\pi - \theta_2)}{n\pi\varepsilon} \quad n = 1, 2, \cdots \quad if\ v_{js} > 0 \\ & h_n = -\frac{\sin n\theta_1}{n\pi\varepsilon},\ \ g_n = -\frac{\sin n\theta_2}{n\pi\varepsilon} \quad n = 1, 2, \cdots \quad if\ v_{js} < 0 \end{aligned} \tag{4.18}$$

where the Fourier coefficients h_0, g_0, h_n and g_n are $O(1)$ and depend implicitly on the as yet undetermined amplitude.

Substitution of (4.17) and (4.18) into (4.14) for steady A_s ($\alpha' = \gamma' = 0$) yields the solvability condition

$$\begin{aligned} \alpha' &= 0 = -\frac{1}{2}\left[c_s^2 \mu\alpha + R_3 \sin\left(\gamma + \Theta\right)\right] \\ \gamma' &= 0 = c_s \sigma - \frac{R_1}{2} - \frac{R_2}{2\alpha} - \frac{R_3 \cos\left(\gamma + \Theta\right)}{2\alpha} \end{aligned} \tag{4.19}$$

$$\begin{aligned} R_1 &= -v_{1s}^2(\sin\theta_1 \cos\theta_1 + \theta_1)/\pi - \eta v_{2s}^2(\sin\theta_2 \cos\theta_2 + \theta_2)/\pi \\ R_2 &= v_{1s}\sum_{p=1}^{3}\left(v_{1p}F_p\right)\sin\theta_1/\pi + \eta v_{2s}\sum_{p=1}^{3}\left(v_{2p}F_p\right)\sin\theta_2/\pi \\ R_3 &= v_{js}\sum_{p=1}^{3}\left(v_{jp}F_p\right)\tilde{\kappa}_{j1}/\bar{k}_j \end{aligned} \tag{4.20}$$

After eliminating $\gamma + \Theta$ (Θ is the phase angle of the comples κ_{j1} in (4.4)) from (4.19) and using $\omega_j = c_s + \varepsilon\sigma$ and $\mu = 2\zeta/\varepsilon$, the perturbation solutions for the frequency response are

$$\omega_j = c_s + \frac{1}{2c_s\alpha}\left[R_1\alpha + R_2 \pm \sqrt{\left|R_3\right|^2 - 4\zeta^2\alpha^2 c_s^4}\right] \quad j = 1, 2 \tag{4.21}$$

$R_{1,2}$ are functions of θ_j and determine the backbone curves of the softening nonlinearity solution branches. The solution branches with $\theta_j = 0$ (i.e., $R_{1,2} = 0$) have no contact loss and represent linear, parametrically excited response. Nonlinear solutions emerge when tooth separation starts and one of the $\theta_j \neq 0$.

The initiation of contact loss is indicated by $y_j = 0$ in (4.15), from which the amplitude at which contact loss occurs at mesh *j* is computed. The corresponding mesh frequency is given by (4.21) with $\alpha = \alpha_j^{(CL)}$. Thus, for the resonance $\omega_j \approx c_s$

$$\alpha_j^{(CL)} = \left| \sum_{p=1}^{3} v_{jp} F_p / 2 v_{js} \right|$$
$$\omega_j^{(CL)} = c_s \pm \left[\left(\frac{|R_3|}{2 c_s \alpha_j^{(CL)}} \right)^2 - \zeta^2 c_s^2 \right]^{1/2} \tag{4.22}$$

The maximum resonance amplitude occurs when the square root term in (4.21) vanishes, i.e.,

$$\alpha^{(P)} = |R_3| / (2\zeta c_s) \tag{4.23}$$

All quantities in (4.22) and (4.23) are known explicitly because R_3 depends on mesh stiffness variations and vibration modes.

For $\rho \neq z$ or $1/z$, the peak amplitude and contact loss initiation frequencies depend only on the mesh stiffness variation of the mesh driving the resonance (mesh j). The other mesh stiffness excitation does not affect these features. This does not mean, however, that the system can be studied by two single mesh gear pairs because of three reasons. First, the DTE of the mesh not driving the resonance is strongly excited by the resonant mesh j, according to (4.15). Secondly, the mean and amplitude of the DTE of mesh j in (4.15) are affected by vibration modes that are not captured in the single mesh pair systems. Finally the important backbone curves of the softening nonlinearity solution branches determined by $R_{1,2}$ in (4.20) include tooth separations from both meshes.

The steady state solutions are the equilibria for the solvability conditions (4.19). The stabilities are determined by the eigenvalues χ of (4.19) linearized about the equilibria. The eigenvalues satisfy

$$\chi^2+\mu\chi+\Gamma=0 \tag{4.24}$$

where Λ is a continuous function of α and σ whose projection on the $\alpha-\sigma$ plane is the frequency response function. The solutions are unstable for $\Lambda<0$, i.e., there exists a $\mathrm{Re}(\chi)>0$, and stable for $\Lambda<0$. Thus, the roots of Λ are bifurcation points, and one can prove that these roots are the points of the frequency response curve with vertical tangents in the $\alpha-\sigma$ plane ($\frac{d\sigma}{d\alpha}=0$). Accordingly, $\Lambda<0$ (unstable) between the two tangent points, and $\Lambda>0$ (stable) otherwise. This results in jump or hysteresis phenomena at the bifurcation points.

Case 2: $\omega_j \approx c_s$, and $\rho = z$ or $1/z$

When $\omega_j = c_s+\varepsilon\sigma$, the other mesh frequency satisfies $\omega_l=\omega_j/z$ or $\omega_l = z\omega_j$. The perturbation solutions from a procedure similar to that above are given by (4.21) with

$$R_3=\begin{cases} v_{js}\sum_{p=1}^{3}\left(v_{jp}F_p\right)\tilde{\kappa}_{j1}/\bar{k}_j+v_{ls}\sum_{p=1}^{3}\left(v_{lp}F_p\right)\tilde{\kappa}_{lz}/\bar{k}_l, & \omega_l=\omega_j/z \\ v_{js}\sum_{p=1}^{3}\left(v_{jp}F_p\right)\tilde{\kappa}_{j1}/\bar{k}_j, & \omega_l=z\omega_j,\quad z>2 \end{cases} \tag{4.25}$$

where $R_{1,2}$ are given in (4.20) and $z=2$ is considered later. The peak resonant amplitude and mesh frequencies at which contact loss starts are still given by (4.23) and (4.22).

From (4.25), mesh interaction, as captured in the important quantity $|R_3|$, occurs if the non-resonant mesh frequency ω_l satisfies $\omega_l=\omega_j/z$. The first harmonic of mesh j and the z^{th} harmonic of the other (l^{th}) mesh jointly drive the resonance; this alters the resonance peak shape, peak amplitude, and contact loss initiation frequencies through

$|R_3|$. The two terms in $|R_3|$ for this case give the separate contributions from mesh *j* and mesh *l* excitations. Depending on the contact ratios and mesh phasing between complex-valued $\tilde{\kappa}_{j1}$ and $\tilde{\kappa}_{lz}$ as well as the vibration modes, these two mesh excitations can counteract or reinforce to each other to affect $|R_3|$. The coefficient weighting of these two terms is impacted heavily by the modal deflections of the two meshes. Although it is typical that $|\tilde{\kappa}_{j1}| > |\tilde{\kappa}_{lz}|$, the influence from the non-resonant mesh can be significant for resonance in modes where mesh l dominates.

4.2.2.2 Frequency response for subharmonic resonances

Case 1: $\omega_j \approx 2c_s$, and $\rho \neq z$ or $1/z$

When $\omega_j = 2c_s + \varepsilon\sigma$, subharmonic resonance with dominant response frequency $\Omega = \omega_j / 2 \approx c_s$ is excited. The amplitude-frequency relationship for these period $-2T_j$ solutions are

$$\begin{aligned} \omega_j &= 2c_s + \frac{1}{c_s \alpha}\left(R_1 \alpha + R_2\right) \pm \frac{1}{c_s}\sqrt{|R_4|^2 - 4\zeta^2 c_s^4} \\ R_4 &= v_{js}^2 \tilde{\kappa}_{j1} / \bar{k}_j \end{aligned} \tag{4.26}$$

From (4.26), the two frequencies $\omega_j = 2c_s \pm \sqrt{|R_4|^2 - 4\zeta^2 c_s^4} / c_s$ for no contact loss ($\theta_1 = \theta_2 = R_1 = R_2 = 0$) are the boundaries of primary parametric instability; they can be calculated from linear system analysis that predicts theoretically unbounded period-$2T_j$ response for mesh frequencies in this interval [19, 62]. Eqn. (4.26), however, gives the bounded nonlinear amplitude in this region as a result of contact loss. The instability interval $2\sqrt{|R_4|^2 - 4\zeta^2 c_s^4}\,/\,c_s$ depends on mesh stiffness variation of mesh j, the vibration modes and damping; note that it is independent of the torque, so high loads do not reduce the mesh frequency range where large amplitude response occurs. Unlike the fundamental resonance, the two nonlinear solution branches do not converge to form a peak at this order of perturbation (occurs when square root in R_4 vanishes).

Case 2: $\omega_j \approx 2c_s$, and $\rho = z$ or $1/z$

When $\omega_j = 2c_s + \varepsilon\sigma$, the other mesh frequency satisfies $\omega_l = \omega_j / z$ or $\omega_l = z\omega_j$. The frequency response solutions are given by (4.26) with

$$R_4 = \begin{cases} v_{js}^2 \tilde{\kappa}_{j1} / \bar{k}_j + v_{ls}^2 \tilde{\kappa}_{lz} / \bar{k}_l, & \omega_l = \omega_j / z,\ z \text{ is odd integer} \\ v_{js}^2 \tilde{\kappa}_{j1} / \bar{k}_j, & \omega_l = z\omega_j,\ z > 2 \end{cases} \tag{4.27}$$

where even z in the first of (4.27) and z=2 in the second are discussed later. For $\omega_l = z\omega_j$ ($z > 2$), there is no interaction from the non-resonant mesh. For $\omega_l = \omega_j / z$ the two meshes interact for subharmonic resonance. The first harmonic of mesh j and the z^{th} harmonic of the other (l^{th}) mesh jointly drive the resonance, and the two terms in R_4 indicate the strength of contribution from these two resonant sources. The contact ratios and mesh phasing significantly affect if theses sources counteract or reinforce each other. The coefficient weightings have different character than for fundamental resonance in (4.25); the fundamental resonance coefficient depends on applied torque through F_p, but the subharmonic resonance contribution from mesh l is independent of torque.

4.2.2.3 Frequency response for combined fundamental and subharmonic resonances

For $z\omega_j \approx c_s$ and $\omega_l \approx 2c_s$ (giving $\omega_l = 2z\omega_j$), mesh l parametrically excites a subharmonic resonance of the s^{th} mode simultaneously with the fundamental resonance of the same mode from the z^{th} harmonic of mesh *j*. The frequency response relations are

$$
\begin{aligned}
\omega_j &= c_s + \frac{1}{2c_s\alpha}\left(R_1\alpha + R_2\right) \pm \sqrt{\frac{|R_5|^2}{4c_s^2} - \zeta^2 c_s^2} \\
\omega_l &= 2c_s + \frac{1}{c_s\alpha}\left(R_1\alpha + R_2\right) \pm \sqrt{\frac{|R_5|^2}{c_s^2} - 4\zeta^2 c_s^2} \\
R_5 &= v_{js}\left[\sum_{p=1}^{3}\left(v_{jp}F_p\right)\tilde{\kappa}_{jz} / \alpha + v_{js}\tilde{\kappa}_{j(2z)}\right] / \bar{k}_j + v_{ls}^2\tilde{\kappa}_{l1} / \bar{k}_l
\end{aligned}
\tag{4.28}
$$

Compared to (4.25) and (4.27), combined fundamental and subharmonic resonances occurs in (4.28). There are three excitations driving the resonances in R_5 of (4.28): the z^{th} harmonic of mesh *j* driving fundamental resonance; the $(2z)^{\text{th}}$ harmonic of mesh *j* and the 1^{st} harmonic of mesh l jointly driving subharmonic resonance. Note that R_5 depends on α because of the combined effects. For linear (no contact loss) response with small amplitude ($1/\alpha \gg 1$), the solution is dominated by the fundamental resonance component. Compared to discontinuous increase in the linear response of subharmonic resonance of (4.27), the amplitude of response in (4.28) increases continuously when mesh frequency gets close to the resonant frequency, and the ensuing amplitude leads to tooth separation and nonlinear solution. The nonlinear solution is dominated by the subharmonic component ($1/\alpha \ll 1$), and $R_5 \approx v_{js}^2\tilde{\kappa}_{j(2z)} / \bar{k}_j + v_{ls}^2\tilde{\kappa}_{l1} / \bar{k}_l$ that is similar to that of (4.27). Thus, the two nonlinear solution branches do not converge to form a peak at this order of perturbation. The contact loss initiation amplitude is the same as in (4.22), and $\omega_j^{(CL)}$ is changed according to (4.28).

4.2.3 Harmonic Balance Method with Arc-Length Continuation

To provide numerical comparisons for the perturbation solutions, the harmonic balance method combined with arc-length continuation is used to identify complete solution branches near the nonlinear resonances. This method is applicable to both weak and strong nonlinearities, although it can experience numerical convergence problems.

The periodic solutions are expanded in Fourier series and the sinusoidal functions are discretized by N points in a period $T = 2\pi / \Omega$. The unknown $\mathbf{U} = [\mathbf{u}_s]$ is the Fourier coefficients of y_s. $\mathbf{G}$ is the discrete Fourier series transformation matrix; $\mathbf{L}$ is the right inverse of $\mathbf{G}$; $\hat{\mathbf{M}}$, $\hat{\mathbf{C}}$, and $\mathbf{f}$ are the discrete Fourier expansions of mass, damping matrix, and load vector; and $\tilde{\mathbf{K}}$ is the discretization of nonlinear, time-varying mesh stiffness matrix. Following [62], the dimensionless governing equation is formulated into the algebraic equation ready for the Newton-Raphson iteration followed as.

$$\Re(\mathbf{U},\Omega) = \left(\Omega^2\hat{\mathbf{M}}\mathbf{A} + \Omega\hat{\mathbf{C}}\mathbf{B}\right)\mathbf{U} + \mathbf{G}\tilde{\mathbf{K}}\mathbf{L}\mathbf{U} - \mathbf{f} \tag{4.29}$$

For period $-pT$ (p is an integer) response, Ω satisfies $p\Omega = \omega_1 / z_2 = \omega_2 / z_3$, where $\rho = z_3 / z_2$. This implies the response period is pz_2 times the first mesh period and pz_3 times the second mesh period. The number of harmonics of $\mathbf{U}$ should be no less than $\max(z_2, z_3)$ to include both mesh frequencies. Smooth hyperbolic tangent functions $\left[1+\tanh(y_j)\right]/2$ are used to approximate the tooth separation functions H_j. The mesh stiffnesses $k_{1,2}$ are expanded by Fourier series in pT time span and discretized into the vector $\boldsymbol{\kappa}_{1,2}$. The elements for $\boldsymbol{\kappa}_{1,2}$ are

$$
\begin{aligned}
\boldsymbol{\kappa}_{1,n} &= \bar{k}_1 + \sum_{m=1}^{\infty}\left[a_{1,m}\cos\left(m\frac{2\pi n}{N} z_2 p \right) + b_{1,m}\sin\left(m\frac{2\pi n}{N} z_2 p \right)\right] \\
\boldsymbol{\kappa}_{2,n} &= \bar{k}_2 + \sum_{m=1}^{\infty}\left[a_{2,m}\cos\left(m\rho(\frac{2\pi n}{N} z_2 p + \phi) \right) + b_{2,m}\sin\left(m\rho(\frac{2\pi n}{N} z_2 p + \phi) \right)\right]
\end{aligned}
\tag{4.30}
$$

where $a_{j,m}$ and $b_{j,m}$ are known Fourier coefficients.

To follow periodic solution branches as Ω varies, the continuation method expands the unknown vector to be $\mathbf{a} = \{\mathbf{U}^T\ \Omega\}^T$. The Newton-Raphson iteration is

$$
\begin{aligned}
&\mathbf{a}_{q+1}^{p} = \mathbf{a}_{q}^{p} + \mathbf{J}^{-1}(\mathbf{a}_{q}^{p})\Re(\mathbf{a}_{q}^{p}) \qquad \mathbf{J} = \left[\frac{\partial\Re}{\partial\mathbf{U}}\ \frac{\partial\Re}{\partial\Omega}\right] \\
&\frac{\partial\Re}{\partial\mathbf{U}} = \Omega^2\widehat{\mathbf{M}}\mathbf{A} + \Omega\widehat{\mathbf{C}}\mathbf{B} + \mathbf{G}\frac{\partial(\tilde{\mathbf{K}}\mathbf{X})}{\partial\mathbf{X}}\mathbf{L} \qquad \mathbf{X} = \mathbf{L}\mathbf{U} \\
&\frac{\partial\Re}{\partial\Omega} = 2\Omega\widehat{\mathbf{M}}\mathbf{A}\mathbf{U} + \widehat{\mathbf{C}}\mathbf{B}\mathbf{U} \\
&\frac{\partial(\tilde{\mathbf{K}}\mathbf{X})}{\partial\mathbf{X}} = \begin{bmatrix} \mathbf{D}_1 & \mathbf{0} & \mathbf{0} \\ \mathbf{0} & \mathbf{D}_2 & \mathbf{0} \\ \mathbf{0} & \mathbf{0} & k_r\mathbf{I} \end{bmatrix} \\
&D_j = diag\left(\frac{1}{2}\left\langle \mathbf{L}\mathbf{u}_j \ ./\ \cosh^2(\mathbf{L}\mathbf{u}_j) + \left[1 + \tanh(\mathbf{L}\mathbf{u}_j)\right], \boldsymbol{\kappa}_j \right\rangle\right)
\end{aligned}
\tag{4.31}
$$

where ./ is the element-by-element dividing operation; $<\bullet,\bullet>$ is inner product; $\mathbf{J}$ denotes the Jacobian matrix of the residual $\Re$ in (4.29); $\mathbf{J}^{-1}$ is the pseudo-inverse; superscript p and subscript q are the frequency and iteration number. The iteration reaches the steady state periodic solution when $\left\|\mathbf{a}_{q+1}^{p} - \mathbf{a}_{q}^{p}\right\|$ is less than a specified tolerance.

The continuation method is applied to get the first guess of the next iteration. The first guess of a new solution along the equilibrium path is given as $\mathbf{a}_0^{p+1} = \mathbf{a}^p + d\mathbf{s}$ ($d\mathbf{s}$ is an arclength). The direction of arclength is along the tangent plane of the current solution.

4.3 Results and Discussion

4.3.1 Evaluation of the Mathematical Model Against Finite Element Benchmark

An example counter-shaft system is listed in Table 4.1.

	Pinion	Middle 1	Middle 2	Gear
Number of teeth	51	72	19	73
Modulus (*mm*)	1.405	1.405	2.2175	2.2175
Face width (*mm*)	22.5	29	20	20
Inertias J_z ($kg \cdot m^2$)	0.01837	0.03531	0.00071	0.1740
Contact ratio	1.60		1.70	
Mean mesh stiffness (*N/m*)	4.24×10^9		3.45×10^9	
Mesh phasing ϕ	0.257			
Torque T_z ($N \cdot m$)	100	0	0	-258.4

Table 4.1: Parameters of the example countershaft gearset for FE model validation.

A FE model is built for this gearset to compare with the analytical model. The shaft connecting the middle gears is assumed rigid. The mesh stiffnesses used by the analytical model are obtained from static analysis of the FE model. Root-mean-square (RMS) values of DTE are shown in Figure 4.3; in all results the mean values are subtracted prior to computing the RMS. The RMS of DTE representing frequency response function agrees well with the analytical model solved by numerical integration. Nonlinear jump phenomena from contact loss occur in certain resonances. Different mesh stiffness, contact ratios, shaft stiffness, and mesh phasing are used in the following analysis.

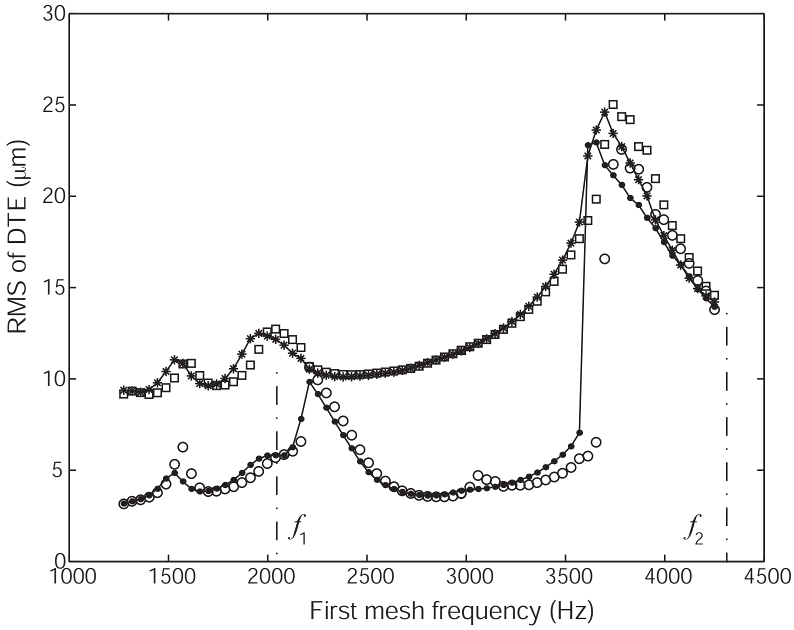

Figure 4.3: Comparisons of RMS dynamic transmission errors between the analytical and finite element models for the counter-shaft gear system in Table 4.1 (○ FE dynamic transmission error of the first mesh; − Analytical dynamic transmission error of the first mesh; □ FE dynamic transmission error of the second mesh; -*- Analytical dynamic transmission error of the second mesh).

4.3.2 Comparisons of Analytical and Numerical Solutions

The second example counter-shaft system is chosen for the analytical studies with rectangular mesh stiffnesses defined by $\bar{k}_j$, ε_j, ς_j, and ϕ. The default system parameters are $k_r = 6.35\times10^5$ *N-m/rad*, $\bar{k}_1 = 2.98\times10^8$ *N/m*, $\eta = 1.08$, $\varepsilon_{1,2}$ =0.3, $\varsigma_1 = \varsigma_2 = 1.5$, $\phi = 0$, $\rho = 3/5$, and ζ =0.04. The dimensionless natural frequencies c_s are 1, 2.34, and 3.29. The three modes have the dominant modal energy in y_3 (middle shaft), y_2 (mesh 2), and y_1 (mesh 1), respectively. Frequency response of the system is analyzed by perturbation, harmonic balance, and numerical integration methods.

4.3.2.1 Comparisons of frequency response for $\rho = 3/5$

The RMS of y_1 calculated by the three methods are compared in Figure 4.4a. Two numerical methods (integration and harmonic balance) are in good agreement, benchmarking perturbation analysis. From (4.23) and R_3 in (4.20), the resonances at mode 3 (mesh 1 dominates) tends to be excited by mesh 1. As shown in frequency-response of y_1 in Figure 4.4a and spectra in Figure 4.4b, the fundamental and subharmonic nonlinear resonances of mode 3 occur near $\omega_1 = c_3 = 3.29$ and $\omega_1 = 2c_3 = 6.58$. The perturbation solution agrees well with numerical results at the fundamental resonance that shows classic jump phenomena at the bifurcation points.

For fundamental resonance, minimum frequency component of the response is the least common factor of two mesh frequencies because the response frequency includes the components $\omega = M\omega_1 \pm N\omega_2$ (M, N are arbitrary integers). The fundamental frequency is $\omega_f = \omega_1/5 = \omega_2/3$ in Figure 4.4b for ρ=3/5. If z_2 and z_3 ($\rho = z_2/z_3$) have no common factors, ω_f is the shaft frequency. For subharmonic resonance, the fundamental frequency is a half of the least common factor of two mesh frequencies. $\omega_f = \omega_1/10$ is for the subharmonic resonance in Figure 4.4b, for example. The dominant spectral component is 3.29 that is a half of ω_1.

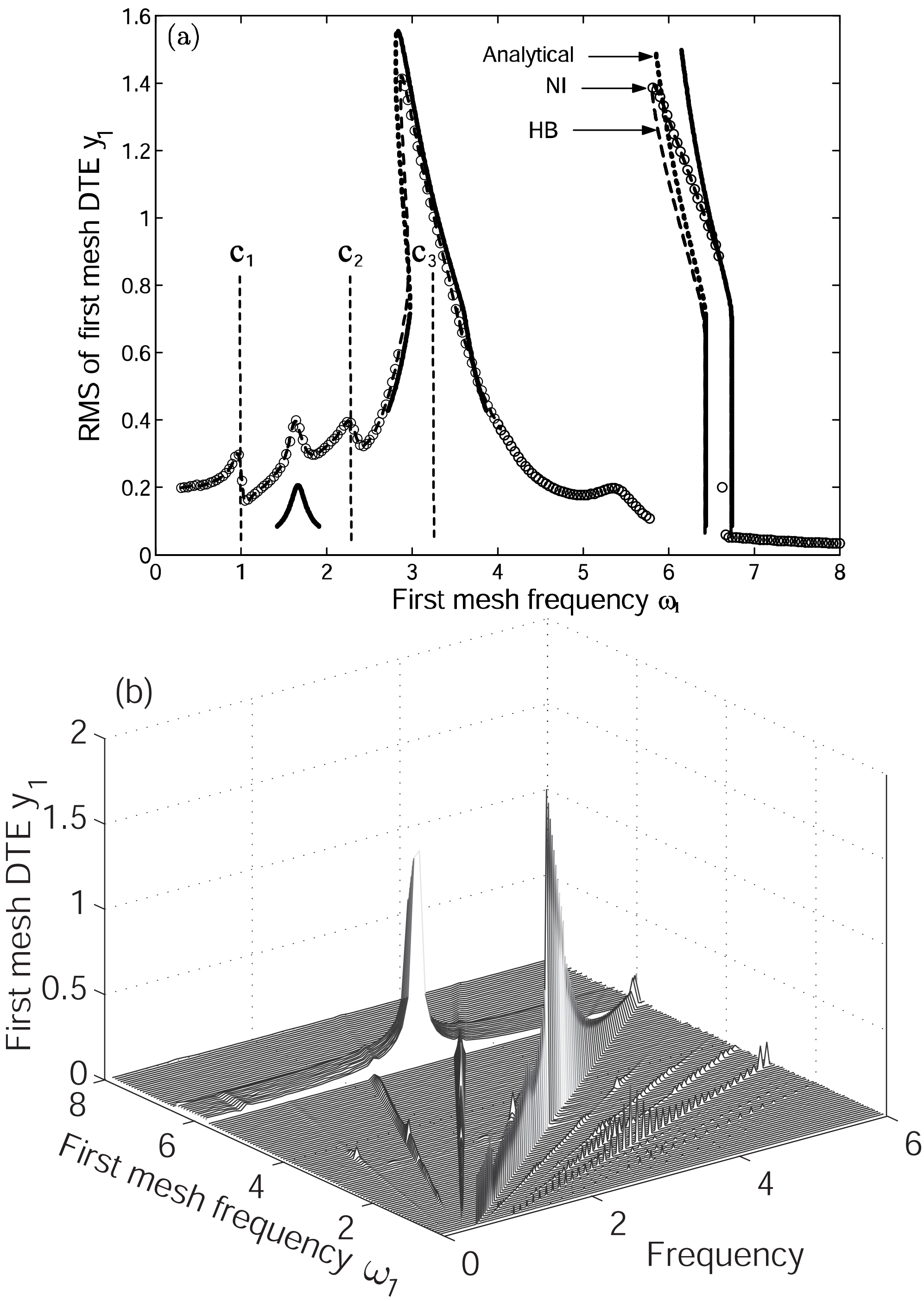

Figure 4.4: Comparison of RMS of the first mesh dynamic transmission error for ρ=3/5 and other parameters with default values of the second example system; (a) frequency response (——— stable perturbation; .... unstable perturbation; – – – harmonic balance; −○− numerical integration); (b) waterfall plot from numerical integration.

At subharmonic resonance, the harmonic balance method gives almost the same solutions as perturbation for the two linear branches (orthogonal to the frequency axis), but it indicates presence of a resonance peak, a bifurcation point where stable upper branch and unstable lower branch meet. The perturbation solution branches, however, do not converge to the resonance peak. The numerical integration cannot capture the two linear solution branches. It shows jump phenomena (for both up sweep and down sweep) at the two frequency boundaries in (4.26) and jump-down phenomenon (only presence for down sweep) at the peak.

Although the analytical expression (4.26) cannot directly predict the peak amplitude, it correlates the peak amplitude with the instability interval width predicted in (4.26). Figure 4.5 shows the correlation between instability interval width and peak amplitude for the subharmonic resonance near $\omega_1 = 2c_3$. The sensitivity of the subharmonic resonance on the contact ratio, mesh stiffness variation, and modal damping, are examined by harmonic balance method. The instability interval and peak amplitude have linear relation for contact ratio and mesh stiffness variation. A parabolic relation appears for modal damping. The peak amplitude and instability width decrease with increasing contact ratio, increasing modal damping, and decreasing mesh stiffness variation, respectively. The subharmonic resonance disappears at critical points (e.g., $\varepsilon = 0.225$). As shown in Figure 4.5, the distance between two adjacent data points increases when approaching the critical points, i.e., the three parameters become more sensitive on peak amplitude and instability interval.

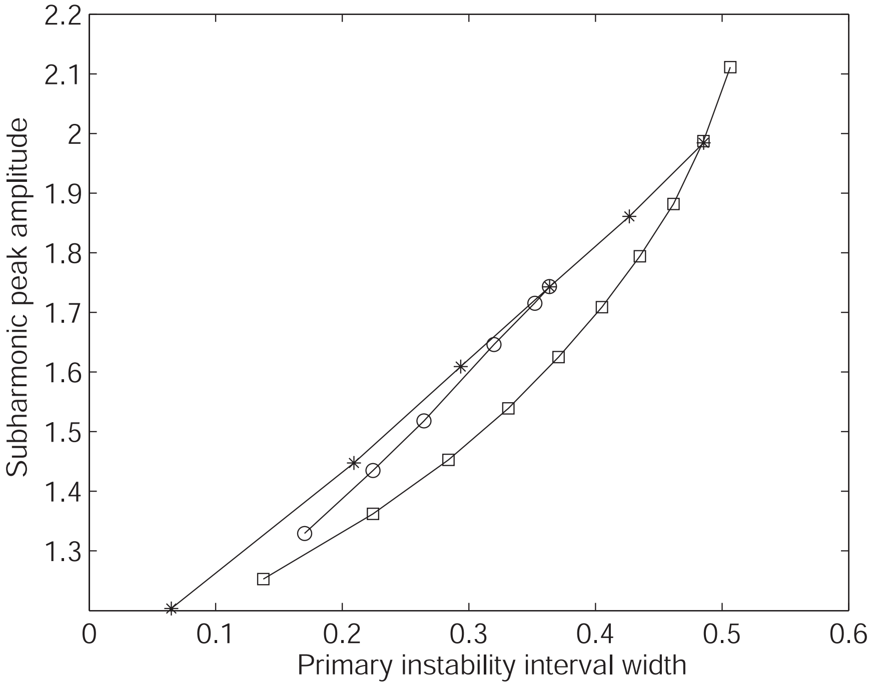

Figure 4.5: Correlation of peak amplitude and instability interval width for subharmonic resonance with $\omega_1 = 2c_3$, $\rho = 3/5$ and other parameters having default values of the second example system except for: □ $0.028 \le \zeta \le 0.037$, ε=0.35, * $0.225 \le \varepsilon \le 0.350$, ○ $1.50 \le \varsigma_1 \le 1.75$.

Figure 4.6 shows the comparison of y_2 RMS by the three methods. The two numerical methods (integration and harmonic balance) agrees well. Consistent with the vibration mode, the fundamental resonance of $\omega_2 \approx c_2$ (near $\omega_1 = c_2 / \rho = 3.9$) dominates in y_2 frequency response curve. The perturbation solution agrees well with numerical results at this resonance that shows classic jump phenomena. The other two nonlinear resonances ($\omega_1 = 3.29,\ 6.58$) are fundamental and subharmonic of mode 3 excited by mesh 1. Although these resonances are purely excited by mesh 1, they show up in y_2 response because of the vibration mode.

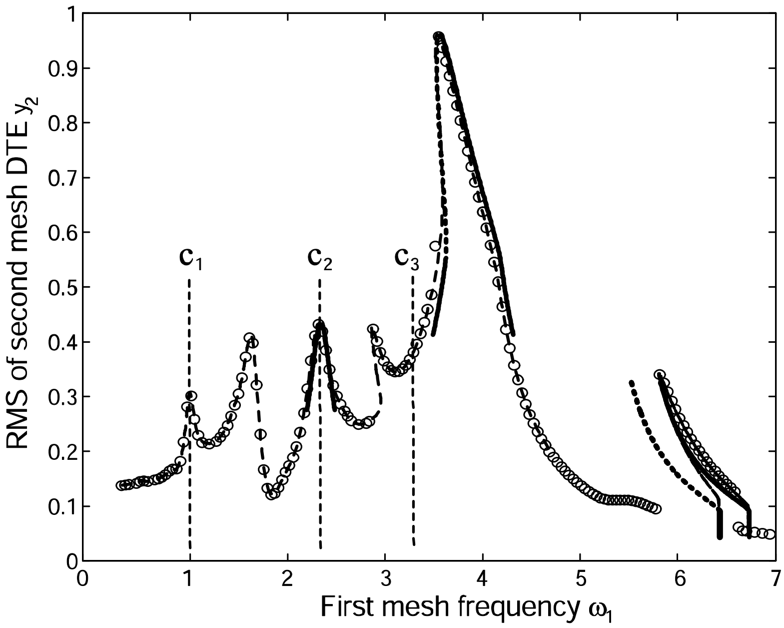

Figure 4.6: Comparison of RMS of the second mesh dynamic transmission error for ρ=3/5 and other parameters with default values of the second example system; (____ stable perturbation; .... unstable perturbation; _ _ _ harmonic balance; –○– numerical integration).

4.3.2.2 Comparisons of frequency response for $\rho = 1/2$

Figure 4.7 shows the comparison of y_1 RMS for perturbation and numerical integration methods. Nonlinear fundamental and subharmonic resonances are found near $\omega_1 = 3.29$ and $\omega_1 = 6.58$, respectively. The comparison at the fundamental resonance is good. The fundamental resonance near $\omega_1 = 3.29$ is excited by the first harmonic ($\tilde{\kappa}_{11}$) of mesh 1 and the second harmonic ($\tilde{\kappa}_{22}$) of mesh 2. There is a combination of subharmonic ($\tilde{\kappa}_{11}$ and $\tilde{\kappa}_{22}$) and fundamental ($\tilde{\kappa}_{21}$) resonances at $\omega_1 = 6.58$. The perturbation prediction on linear solution branches (dominated by the fundamental component in (4.28)) and instability interval (defined by the two points where linear branches change to nonlinear branches) agrees well with numerical integration. As discussed in (4.28), the linear solution branches are not parallel lines because of the fundamental resonance contribution from mesh 2. No jump down phenomenon occurs for up sweep in this case. The nonlinear solution branches of perturbation are still open and the resonant amplitude is correlated with the instability interval as similar to the discussion on Figure 4.4.

Summarizing, the perturbation solution of frequency response is obtained for counter-shaft gearsets. The numerical comparisons show that the closed-form expressions are effective to predict the nonlinear resonances. The expressions include most design parameters such as mesh phasing, contact ratio, mesh stiffness variations, damping, and vibration modes.

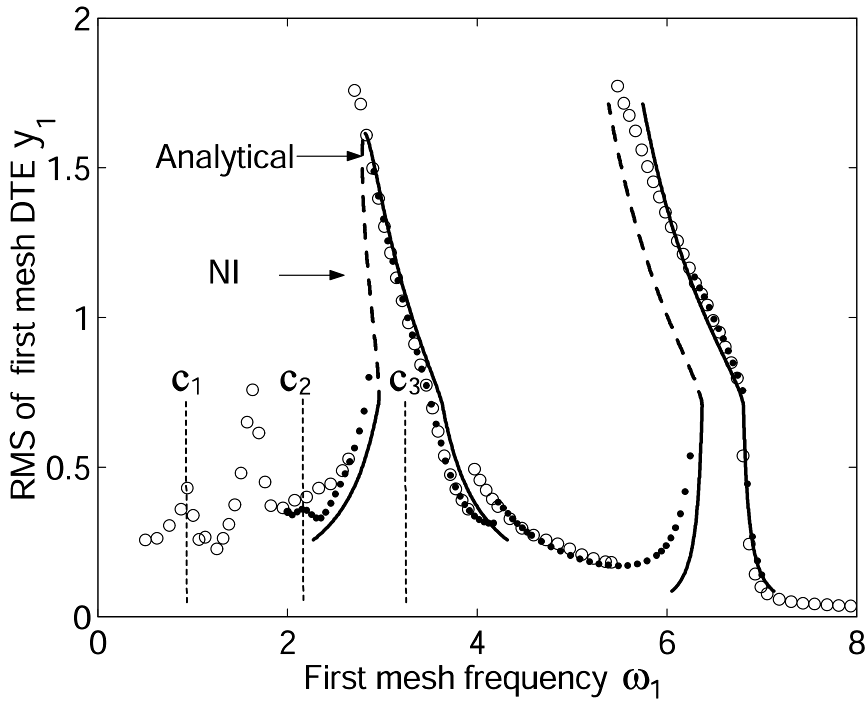

Figure 4.7: Comparison of RMS of the first mesh DTE for ρ=1/2 and other parameters with default values of the second example system (____ stable perturbation; _ _ unstable perturbation; ○ numerical integration sweep down; • numerical integration sweep up).

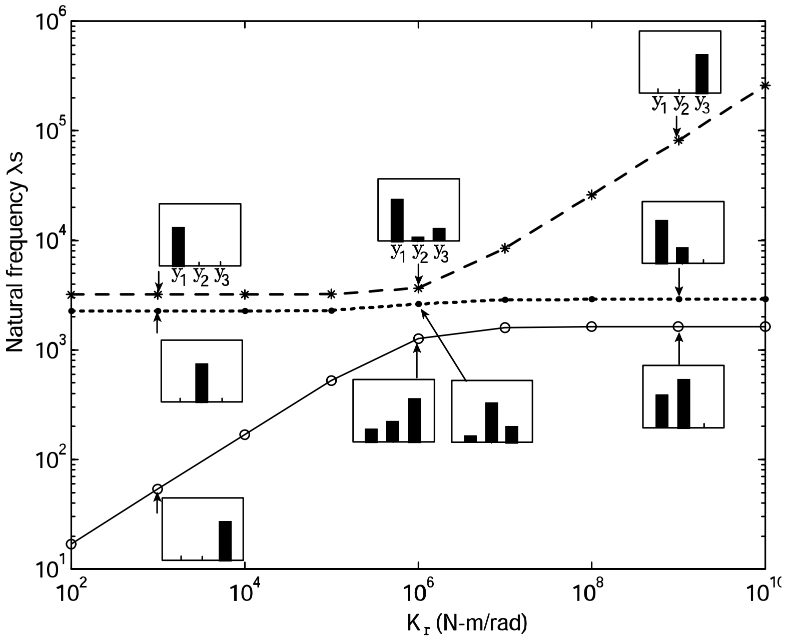

Figure 4.8: Sensitivity of vibration modes to stiffness of the middle shaft for the counter-shaft gear system in Table 4.1, λ_1, λ_2, and λ_3.

4.3.3 Dynamic Influences of Key Design Parameters

4.3.3.1 Impact of coupling shaft stiffness on vibration modes

The perturbation analysis shows that the shaft stiffness between the two middle gears is not explicitly included in the closed-form expressions. According to (4.3), the shaft stiffness, however, affects the vibration modes that explicitly participate in the perturbation solutions.

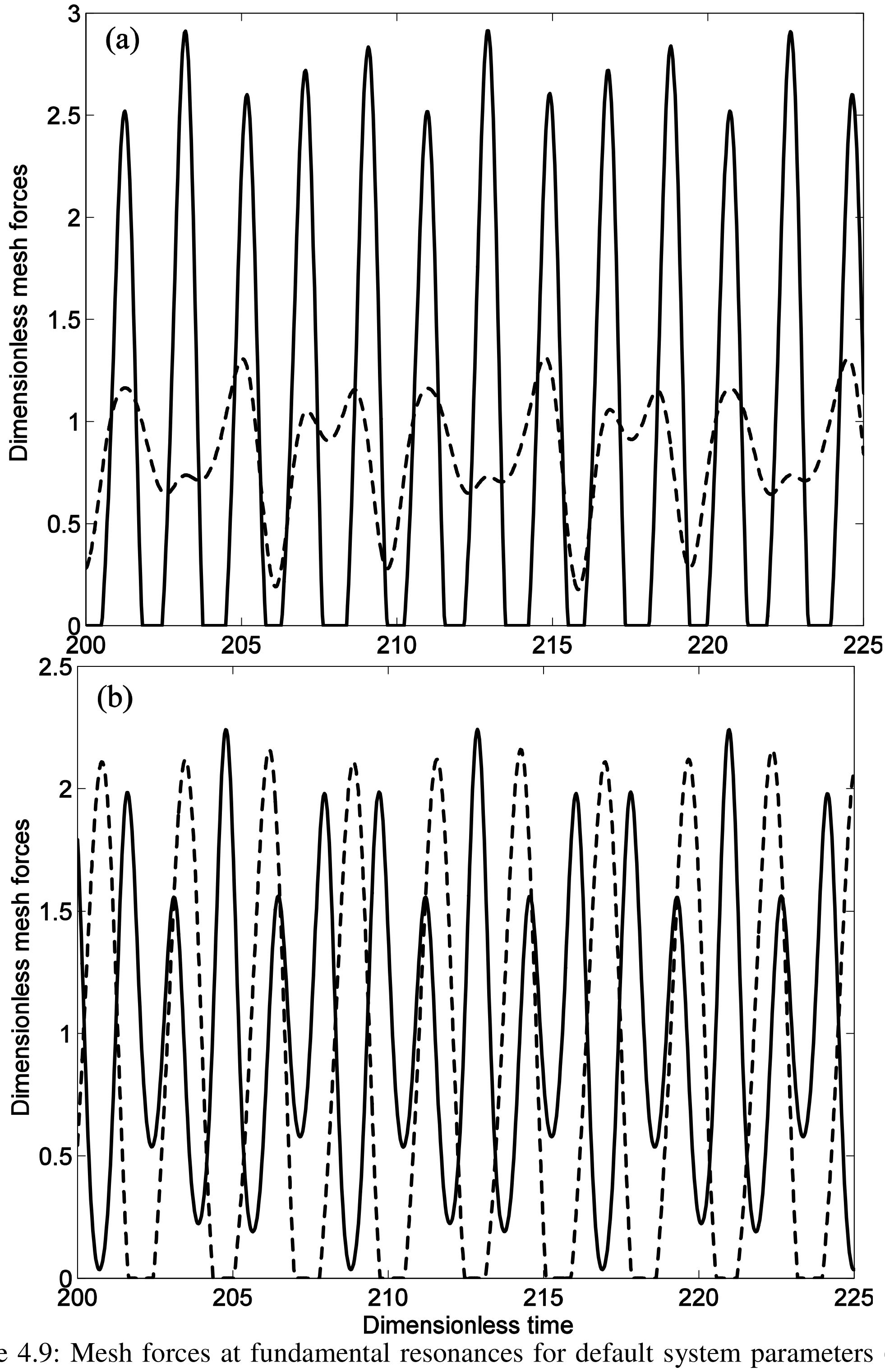

Figure 4.9: Mesh forces at fundamental resonances for default system parameters (—— first mesh; — — second mesh); (a) resonance at $\omega_1 \approx c_3$; (b) resonance at $\omega_2 \approx c_2$.

Figure 4.9 shows the sensitivity of vibration modes on the shaft stiffness for the example counter-shaft gear system in Table 4.1. The shaft stiffness has significant impact on vibration modes. A critical shaft stiffness (e.g., 1×10^{6} $N-m/rad$) separates two limit cases. For shaft stiffness much lower than the critical value, the three modes have decoupled y_3, y_2, and y_1, respectively. The two meshes act like two single mesh gear systems. For shaft stiffness much higher than the critical value, the modes change to two gear modes with two mesh deflection coupled and a shaft mode. For shaft stiffness around the critical value, coupled mesh motions and shaft rotations occur in all three modes. Thus, by tuning the shaft stiffness, one can change the mode properties and change the mesh interactions, if there is any. For instance, the shaft stiffness can affect v_{js}/v_{ls} to increase or decrease the mesh interaction in R_5 from (4.28).

4.3.3.2 Tooth separation

From (4.22) and (4.23), nonlinear solution (i.e., contact loss) occurs when peak amplitude is greater than the contact loss initiation amplitude α_j. For the third mode fundamental resonance, only the first mesh loses the contact as depicted in Figure 4.9a because $\alpha_1 < |R_3|/(\mu c_s) < \alpha_2$, but the initiation amplitude of the second mesh is higher than the peak amplitude and contact loss is not activated for the second mesh. Contact loss occurs for each mesh cycle (mesh 1) and there are five contact losses for each period of response. For the second mode fundamental resonance, $\alpha_2 < |R_3|/(\mu c_s) < \alpha_1$, which implies that only the second mesh loses contact as shown in Figure 4.9b. There are three contact losses for each response period.

4.3.3.3 Impact of mesh stiffness variations on resonant peak amplitude

To analytically study the second example system with, the rectangular mesh stiffnesses are defined by key analytical quantities as mean $\bar{k}_j$, variations ε_j, contact ratios ς_j, and mesh phasing ϕ. The impact of these quantities on the resonance peak are given by combining (4.5), (4.20), and (4.25)-(4.28) as

$$|R_3|^2 = \begin{cases} case\ 1: \dfrac{2v_{js}v_{ls}\varepsilon_j\varepsilon_l w_j w_l}{z\pi^2}\sin(\pi\varsigma_j)\sin(z\pi\varsigma_l)\cos\left(\pi(z\varsigma_l-\varsigma_j)-(z\phi_l-\phi_j)\right) \\ \qquad +\left(\dfrac{v_{js}\varepsilon_j w_j}{\pi}\right)^2\sin^2(\pi\varsigma_j)+\left(\dfrac{v_{ls}\varepsilon_l w_l}{z\pi}\right)^2\sin^2(z\pi\varsigma_l),\ \omega_l=\omega_j/z \\ case\ 2: \left(\dfrac{v_{js}\varepsilon_j w_j}{\pi}\right)^2\sin^2(\pi\varsigma_j),\ \omega_l=z\omega_j, z>2 \end{cases} \tag{4.32}$$

$$|R_4|^2 = \begin{cases} case\ 1: \dfrac{2v_{js}^2v_{ls}^2\varepsilon_j\varepsilon_l}{z\pi^2}\sin(\pi\varsigma_j)\sin(z\pi\varsigma_l)\cos\left(\pi(z\varsigma_l-\varsigma_j)-(z\phi_l-\phi_j)\right) \\ \qquad +\left(\dfrac{v_{js}^2\varepsilon_j}{\pi}\right)^2\sin^2(\pi\varsigma_j)+\left(\dfrac{v_{ls}^2\varepsilon_l}{z\pi}\right)^2\sin^2(z\pi\varsigma_l),\ \omega_l=\omega_j/z,\ z \text{ is odd} \\ case\ 2: \left(\dfrac{v_{js}^2\varepsilon_j}{\pi}\right)^2\sin^2(\pi\varsigma_j),\ \omega_l=z\omega_j,\ z>2 \end{cases} \tag{4.33}$$

$$\begin{aligned} |R_5|_{II}^2 &= \frac{2v_{js}v_{ls}^2\varepsilon_j\varepsilon_l w_j}{(\alpha_j^{(CL)})^2\pi^2}\sin(z\pi\varsigma_j)\sin(\pi\varsigma_l)\cos\left(\pi(\varsigma_l-z\varsigma_j)-(\phi_l-z\phi_j)\right) \\ &\quad +\left(\frac{v_{js}\varepsilon_j w_j}{z\pi\alpha_j^{(CL)}}\right)^2\sin^2(z\pi\varsigma_j)+\left(\frac{v_{ls}^2\varepsilon_l}{\pi}\right)^2\sin^2(\pi\varsigma_l),\ \omega_j\approx c_s/z, \omega_l=2z\omega_j \end{aligned} \tag{4.34}$$

where $w_j = \sum_{p=1}^{3}\left(v_{jp}F_p\right)$, $w_l = \sum_{p=1}^{3}\left(v_{lp}F_p\right)$, $\phi_1 = 0$, $\phi_2 = \phi$, $\omega_j \approx c_s$ in (4.32), $\omega_j \approx 2c_s$ in (4.33), and $\left|R_5\right|_{II}$ is the value at the bifurcation point. The peak amplitudes of fundamental and subharmonic resonances are determined by $\left|R_3\right|/(2\zeta c_s)$, $\sqrt{\left|R_4\right|^2 - 4\zeta^2 c_s^4}/c_s$ and $\sqrt{\left|R_5\right|_{II}^2 - 4\zeta^2 c_s^4}/c_s$, respectively. For the first case in (4.32) and (4.33) and the case in (4.34), the quantities of two mesh stiffness excitations are coupled together through vibration modes. The square of peak amplitude has quadratic form of ε_j. The quantities are decoupled in the third case, and the peak amplitude of fundamental resonance is a linear function of ε_j; the square of subharmonic peak amplitude is a parabolic function.

The impact of mesh stiffness variations ε_j on the peak amplitude of y_2 at the fundamental resonance $\omega_2 \approx c_2$ is examined on the second example system by numerical integration method.

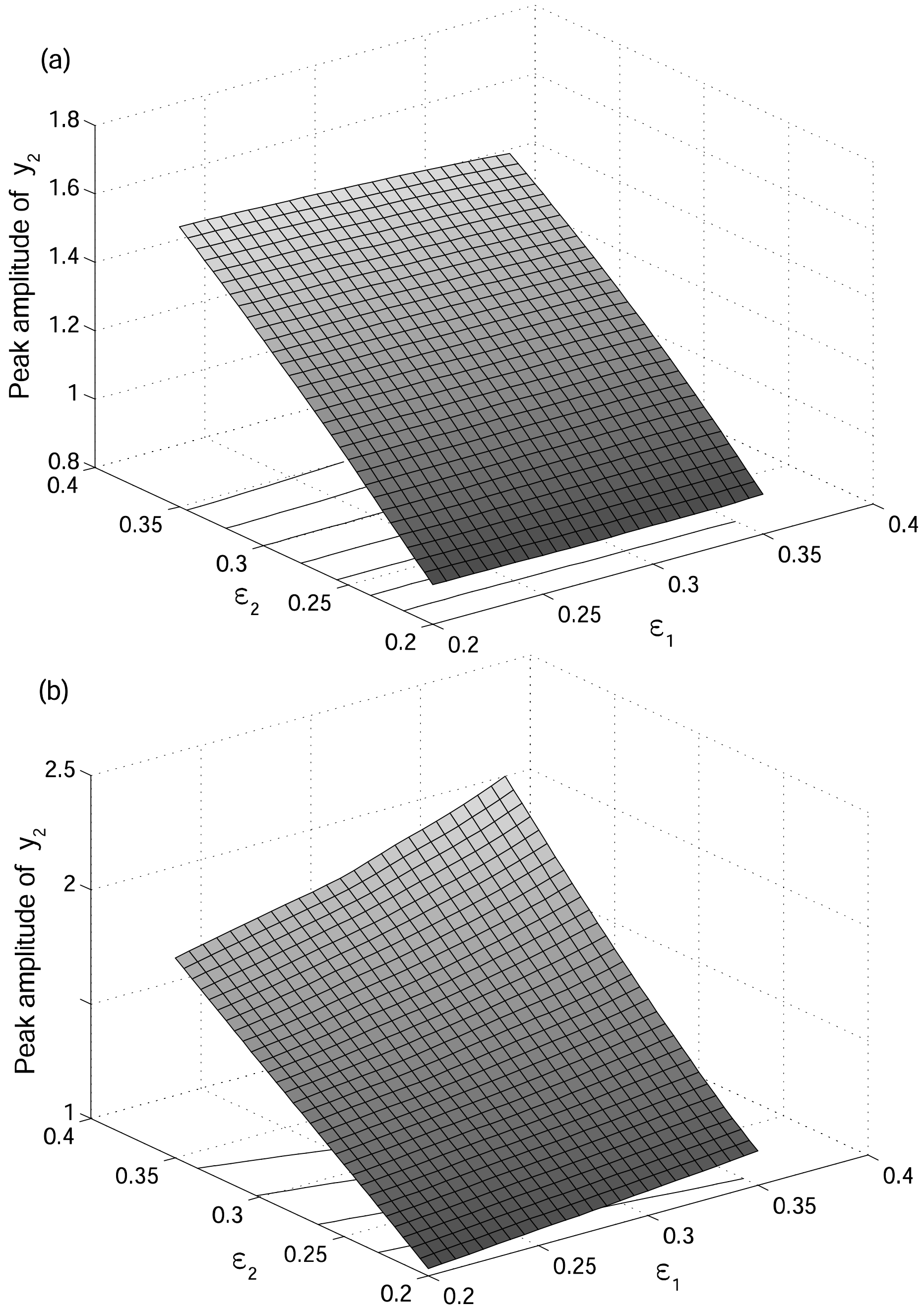

Figure 4.10: Impact of two mesh stiffness variations on the amplitude of the fundamental resonance for $\omega_2 \approx c_2$, ς_1=1.7, ς_2=1.6, ζ =3%, and $\phi = \pi$; (a) ρ =3/5; (b) ρ =1/2.

Figure 4.10a shows sensitivity of the peak amplitude on ε_j for $\rho = 3/5$. As predicted by case 2 of (4.32), the peak amplitude is linear function of ε_2 and not affected by ε_1. Figure 4.10b shows sensitivity of the peak amplitude on ε_j for $\rho = 1/2$. From case 1 of (4.32), the first harmonics of both mesh stiffnesses contribute to the resonance. For the example system, $w_1 w_2 > 0$, $v_{12} v_{22} < 0$, and $v_{13} v_{23} > 0$. Mode 2 is dominated by the second mesh deflection, i.e., $|v_{12}| < |v_{22}|$. With $\varsigma_1 = 1.7$, $\varsigma_2 = 1.6$, and $\phi = \pi$, case 1 of (4.32) is simplified as

$$|R_3|^2 = 0.29\left(v_{22} w_2 \varepsilon_2\right)^2 + 0.21\left(v_{12} w_1 \varepsilon_1\right)^2 + 0.48|v_{12} v_{22}| w_1 w_2 \varepsilon_1 \varepsilon_2 \tag{4.35}$$

The peak amplitude increases with $\varepsilon_{1,2}$. It is more sensitive to ε_2 than ε_1, i.e., the gradient along ε_2 axis is greater than the gradient along ε_1 axis in Figure 4.10b. Note that mesh phasing can change the interaction between two meshes. In two limit cases,

$$R_3 = \begin{cases} \left(\dfrac{v_{js}\varepsilon_j w_j}{\pi}\right)\sin\left(\pi\varsigma_j\right) + \left(\dfrac{v_{ls}\varepsilon_l w_l}{\pi}\right)\sin\left(\pi\varsigma_l\right), \ \mathit{if}\ \cos\left(\pi\left(c_l - c_j\right) - \left(\phi_l - \phi_j\right)\right) = 1 \\ \left(\dfrac{v_{js}\varepsilon_j w_j}{\pi}\right)\sin\left(\pi\varsigma_j\right) - \left(\dfrac{v_{ls}\varepsilon_l w_l}{\pi}\right)\sin\left(\pi\varsigma_l\right), \ \mathit{if}\ \cos\left(\pi\left(c_l - c_j\right) - \left(\phi_l - \phi_j\right)\right) = -1 \end{cases} \tag{4.36}$$

where two mesh contributions are added together or cancel to each other. The sign of vibration modes also affects the mesh interaction. Similar discussion can be made to the fundamental resonance ($\omega_1 \approx c_3$) that is dominated by the first mesh deflection. The first harmonic of mesh 1 and the second harmonic of mesh 2 contribute to excite the resonance. The peak amplitude is more sensitive to ε_1 than ε_2 for case 1 of (4.32).

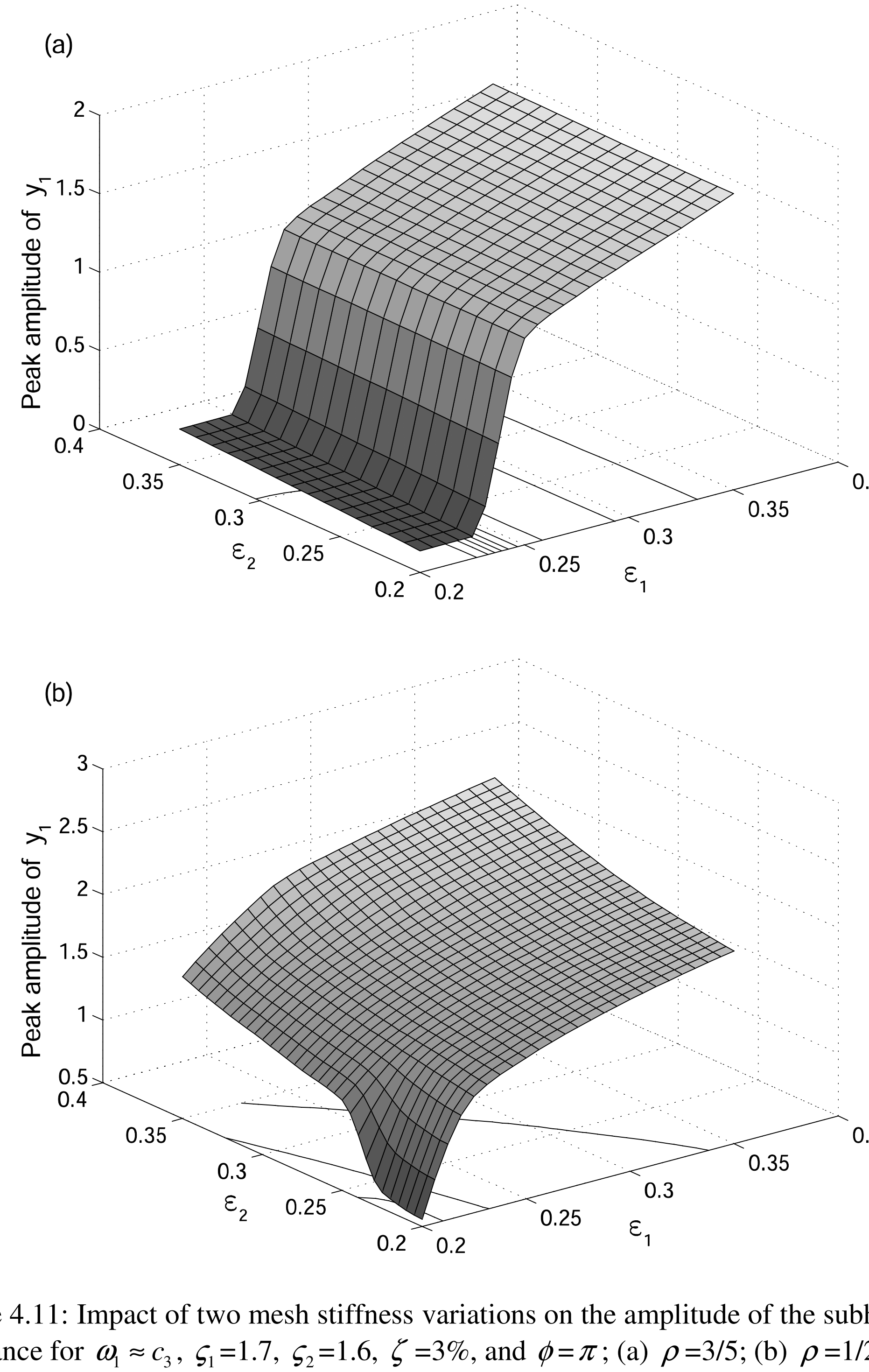

Figure 4.11: Impact of two mesh stiffness variations on the amplitude of the subharmonic resonance for $\omega_1 \approx c_3$, ς_1=1.7, ς_2=1.6, ζ =3%, and $\phi = \pi$; (a) ρ =3/5; (b) ρ =1/2.

The sensitivity of peak amplitude on ε_j for subharmonic resonance in case 2 of (4.33) is shown in Figure 4.11a. The amplitude is only affected by ε_1. The subharmonic disappears when ε_1<0.25. The amplitude linearly dependent on ε_1 when $\varepsilon_1 \geq 0.25$. The critical ε_1 for presence of subharmonic satisfies $|R_4| = 2\zeta c_s^2$ that gives

$$\varepsilon_1 = \frac{2\pi\zeta c_3^2}{v_{13}^2 \sin^2(\varsigma_1 \pi)} = 0.2459 \tag{4.37}$$

The sensitivity of peak amplitude on ε_j for subharmonic resonance in (4.34) ($z = 1$) is shown in Figure 4.11b. The amplitude is affected by both ε_1 and ε_2, and more sensitive to ε_1. The critical ε_1 for the presence of subharmonic is decreased to 0.225 due to the impact of ε_2. The critical ε_2 is 0.25. Again two mesh contributions could be added together or cancel to each other depending on mesh phasing. The constructive or destructive effects, however, do not depend on the sign of vibration modes, unlike the fundamental resonance.

4.3.3.4 Impact of Contact ratios on resonant peak amplitude

From (4.32) and (4.33), contact ratio contributes to the amplitude and phase of mesh stiffness harmonics. In case 2 of (4.32) and (4.33), the amplitude of resonance ($\omega_j \approx c_s$ or $2c_s$) varies with contact ratio j in sinusoidal forms, and the amplitude is independent of the contact ratio of the other mesh. The variation is qualitatively consistent with the expression in case 2 of (4.32). Minimum amplitude occurs for $\varsigma_j = 1$ and 2. As an example of case 1 of (4.32), the amplitude of the resonance

($\omega_1 \approx c_3$, $\rho = 1/2$) varying with two contact ratios are shown in Figure 4.12. With $\varepsilon_1 = \varepsilon_2 = 0.3$ and $\phi = \pi$, case 1 of (4.32) is simplified as

$$|R_3|^2 = 0.1\sin^2(\pi\varsigma_1) + 0.04\sin^2(2\pi\varsigma_2) + 0.07\sin(\pi\varsigma_1)\sin(2\pi\varsigma_2)\cos(\pi(2\varsigma_2 - \varsigma_1)) \quad (4.38)$$

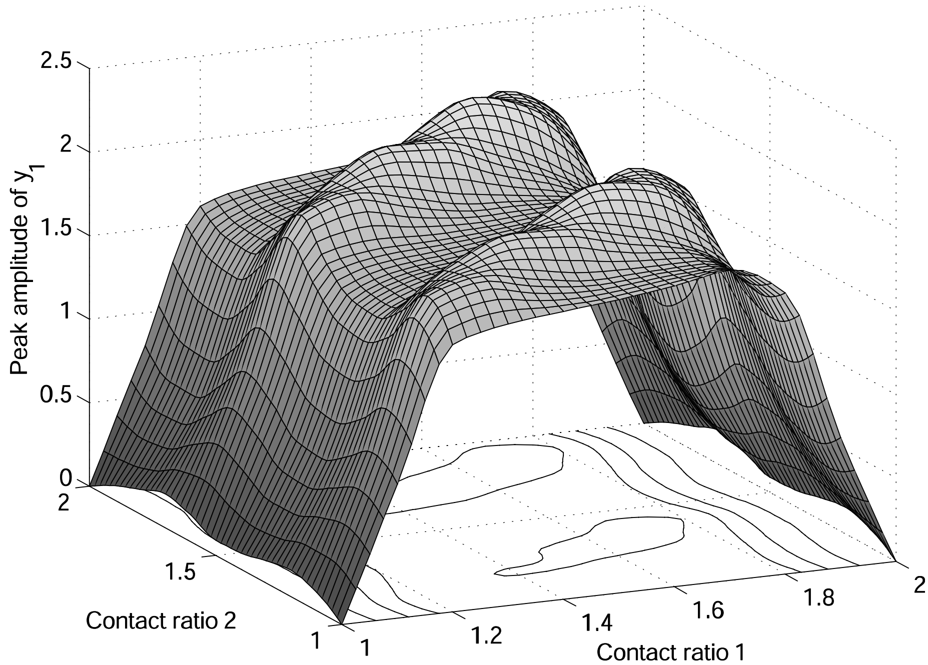

Figure 4.12: Impact of two contact ratios on the amplitude of the fundamental resonance for $\omega_1 \approx c_3$, ρ=1/2, $\varepsilon_1 = \varepsilon_2$=0.3, ζ =3%, and $\phi = \pi$.

The amplitude is affected by both contact ratios but more sensitive to ς_1 than ς_2. The amplitude changes with ς_1 in a similar way as $\sin(\pi\varsigma_1)$ (it is, however, not in an exact sinusoidal form due to impact of the other modes and higher harmonics), but it is modulated by the impact of ς_2 in a similar way as $\sin(2\pi\varsigma_2)$. For $\varsigma_1 = 1$ or 2, $|R_3|^2 = 0.04\sin^2(2\pi\varsigma_2)$. The amplitude in Figure 4.12 shows $\sin(2\pi\varsigma_2)$ wave form with maximum at $\varsigma_2 = 1.25$ and 1.75 and minimum at $\varsigma_2 = 1$ and 2. For $\varsigma_1 = 1.2$,

4.3.3.5 Impact of mesh phasing on resonant peak amplitude

One key parameter reflecting the interaction of multi-meshes is mesh phasing. For the first two cases in (4.32) and (4.33), mesh interactions occur. Figure 4.13 shows the impact of mesh phasing on the amplitudes of different resonances for $\rho = 1/2$ by numerical integration. The amplitude is dictated by $|R_3|$ in case 1 of (4.32). The phase angle $(2\pi\varsigma_2 - \pi\varsigma_1 - 2\phi)$ controls the interaction of the two mesh stiffness variations. By tuning mesh phasing ϕ, one can reduce or increase the amplitude of certain resonance. The waterfall plot of dynamic response y_2 shows that the mesh phasing has different impact on resonances. For the example system, the amplitude of mode 1 is minimized at $\phi = 0.75\pi$ ($v_{11}v_{21} < 0$ and $\cos(2\pi\varsigma_2 - \pi\varsigma_1 - 2\phi) = 1$) while the amplitude of mode 2 is maximized at $\phi = 0.75\pi$ ($v_{12}v_{22} > 0$).

On the other hand, two meshes do not interact to each other for case 2 in (4.32) and (4.33). For example, mesh phasing (non-dimensionlized by 2π) has no effect at the dynamic response for the example system with $\rho = 3/5$.

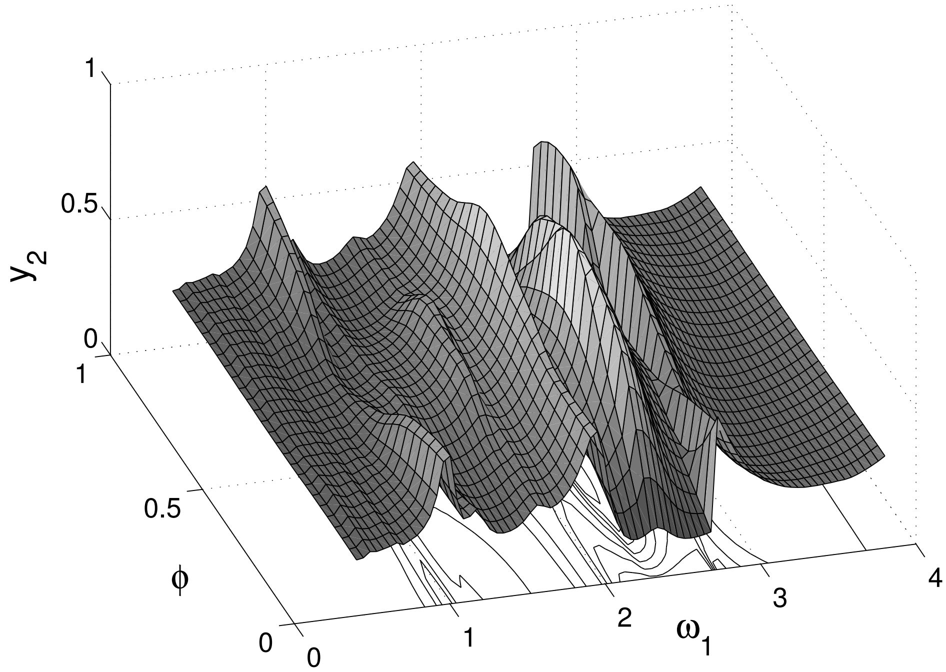

Figure 4.13: Impact of mesh phasing on the amplitude of response for ρ =1/2, $\varepsilon_1 = \varepsilon_2$=0.3, $\varsigma_1 = 1.7$, ς_2=1.6, and ζ =3%.

CHAPTER 5

IMPACT OF TOOTH FRICTION AND ITS BENDING EFFECT ON GEAR DYNAMICS

This chapter examines the influences of tooth friction on parametric instabilities and dynamic response of a single-mesh gear pair. A dynamic translational-rotational model is developed to consider a gear tooth bending effect from tooth friction together with other previously known contributions of tooth friction and mesh stiffness fluctuation. An iterative integration method and perturbation analysis examine parametric instabilities arising from these factors. The included effects of time-varying friction moments about the gear centers and friction-induced tooth bending are critical to parametric instabilities and dynamic response. The impacts of friction coefficient, bending effect, contact ratio, and modal damping on the stability boundaries and the nonlinear dynamic response are discussed.

5.1 Introduction

In the various treatments of the gear mesh characteristics in the numerous mathematical gear models found in the literature [21, 22, 91], most models neglect the dynamic contribution of tooth friction compared with mesh forces normal to the tooth surface. Parametric excitation from variable mesh stiffness and geometric deviations of tooth surfaces are usually treated as the dominant sources of gear vibration [10, 13, 19, 29]. Recently, tooth friction was demonstrated as an important factor in gear dynamics. Velex and Cahouet [92] analyze tooth friction in spur and helical gear dynamics. The comparison between simulated and measured bearing forces reveals the potentially significant contribution of tooth friction to gear vibration. The importance of tooth friction to structure-borne vibration of helical gear systems and to vibration reduction of gears with minimal static transmission error is discussed in [40, 41]. Vaishya and Houser [42] demonstrate the powerful influence of tooth friction on the vibro-acoustic performance of gears.

Due to the involute shape of gear teeth, the mesh contact undergoes rolling and sliding, resulting in sliding friction force normal to the line of action. Variable friction coefficients are applied in studies of gear wear and power efficiency. The coefficient of friction is a function of sliding velocity, surface roughness, lubrication film, contact load, temperature, etc. Theoretical friction coefficients are derived from elasto-hydrodynamic lubrication and tribology theory [93-95]. The experimental works in [42, 92, 96], however, show that a constant friction coefficient is acceptable for dynamic analysis. The measured dynamic friction loads show friction coefficients of approximately 0.04 to 0.06 [96]. Benedict and Kelley's empirical equation shows the coefficient of friction varies between 0.03 to 0.1 [97]. The value of 0.1 and even values as high as 0.2 are commonly used in gear dynamics [18, 43, 44, 47, 92].

The effects of tooth friction include moments about the gear centers from friction forces perpendicular to the line of action (affecting gear rotations), excitation of off-line-of-action gear translations, nonlinear dependence of friction on the sliding velocity, and energy dissipation. Iida et al. [98] examine time-varying tooth friction using a simplified dynamic model with friction as excitation and damping. Hochmann [99] focuses on the periodic external excitation from tooth friction while assuming constant mesh stiffness. Gunda and Singh [43] and Vaishya and Singh [18, 47] present dynamic rotational models. The sliding mechanism is formulated based on dynamic mesh force, and the friction term appears with time-varying parameters. Parametric excitation also results from variable mesh stiffness that causes instability and severe vibrations at certain mesh frequencies [19, 20, 31-33, 71]. Vaishya and Singh [18] apply Floquet theory to their dynamic rotational model to study parametric instabilities from variable mesh stiffness and tooth friction.

Previous works focus on models having only rotational degrees of freedom, where the only contributions from tooth friction are moments about the gear centers. Friction force, however, also affects gear tooth bending [100], which has not been previously examined for gear dynamics. This paper develops and analyzes a dynamic translational-rotational model admitting this additional contribution of tooth friction (bending effect) as well as gear translations. The model includes this friction bending effect combined with time-varying friction force orthogonal to the line of action, time-varying mesh stiffness, and contact loss nonlinearity. The friction bending effect is shown to be important for instability and dynamic response of gear mesh deflections. Parametric instabilities and quasi-periodic response due to friction and modal interactions are studied. An iterative numerical method based on Floquet-Liapunov theory and Peano-Baker series is proposed for stability analysis. This method is evaluated against a well-known numerical method. Furthermore, perturbation analysis is conducted to find approximate solutions that predict and explain the numerical parametric instabilities. The predicted instabilities occur in practical gears as resonance-like vibration near the mesh frequency and particular multiples of mesh frequency that are close to natural frequencies in combination. The large response triggers tooth separation nonlinearity that bounds the vibration. The effects of time-varying friction moment and friction bending effect are found to be critical for combination instabilities and certain single-mode instabilities. The impacts of friction coefficient, bending effect, contact ratio, and modal damping on stability boundaries are revealed. Finally, the bending effect of tooth friction on nonlinear dynamic response is discussed and validated by finite element (FE) results.

5.2 Tooth Bending Effect of Friction Force

The elastic deflection of a pair of loaded gear teeth consists of deflection of the tooth as a cantilever beam, gear body flexibility, and Hertzian contact compression. The normal contact force and tangential friction force both contribute to tooth bending. Tooth bending deflection for mesh force along the line of action is studied as a non-uniform cantilever beam in [100]. Extending that derivation to include friction perpendicular to the line of action gives the total deflection of a pair of loaded gear teeth as

$$W = \left(\frac{g_c \cos\varphi_c - g_s \sin\varphi_c}{EI} + \frac{1}{k_r} \right) N_{1,i} + \left(\frac{g_c \sin\varphi_c - g_s \cos\varphi_c}{EI} + \frac{1}{k_r} \right) f_{1,i} \qquad (4.39)$$

where $N_{1,i}$ and $f_{1,i}$ are contact and friction forces of tooth pair i, respectively; φ_c is the pressure angle at the current mesh position; EI denotes tooth bending rigidity; g_c and g_s are tooth geometric factors based on parameters defined in [100]; and k_r is the effective rotational stiffness of the gear flank as reduced from [100], which is assumed the same for both forces. Although the compliance for $N_{1,i}$ is softer than that for $f_{1,i}$, they are of the same order.

To demonstrate the significance of the friction bending effect, a pilot study static analysis is conducted on a pair of spur gears in Figure 5.1a. Gear 1 is loaded with torque T_1 and gear 2 is fixed. The equilibrium conditions yield the resultant contact and friction forces

$$N_1 = \sum_{i=1}^{z} N_{1,i} = \frac{T_1}{r_1 - \sum_{i=1}^{z} sgn(v_i)\mu_i l_i \alpha_i}$$
$$f_1 = \sum_{i=1}^{z} f_{1,i} = -N_1 \sum_{i=1}^{z} sgn(v_i)\mu_i \alpha_i \tag{4.40}$$

where $r_{1,2}$ denotes gear base radii; z is the number of tooth pairs in contact; v_i, μ_i and l_i are sliding velocities, friction coefficients and friction force moment arms (Figure 5.1b), respectively; and $\alpha_i = N_{1,i} / N_1$ are load sharing factors between the z tooth pairs. The contact force of tooth pair i is $\alpha_i N_1$ and the friction force is $\mu_i \alpha_i N_1$ according to Coulomb friction.

The friction moments about the gear centers depend on the position of the contact points. The moment arms of friction forces $f_{1,i}$ in Figure 5.1a are shown in Figure 5.2a. The difference between the two moment arms is a base pitch and $\rho_0 = r_1 \tan\varphi$, $\rho_1 = \rho_0 - 2\pi\gamma r_1$, and $\rho_2 = \rho_0 + 2\pi(c-1)r_1$, where φ is the pressure angle at the pitch point and c is the contact ratio. γ denotes the position in a mesh period where double-tooth contact starts.

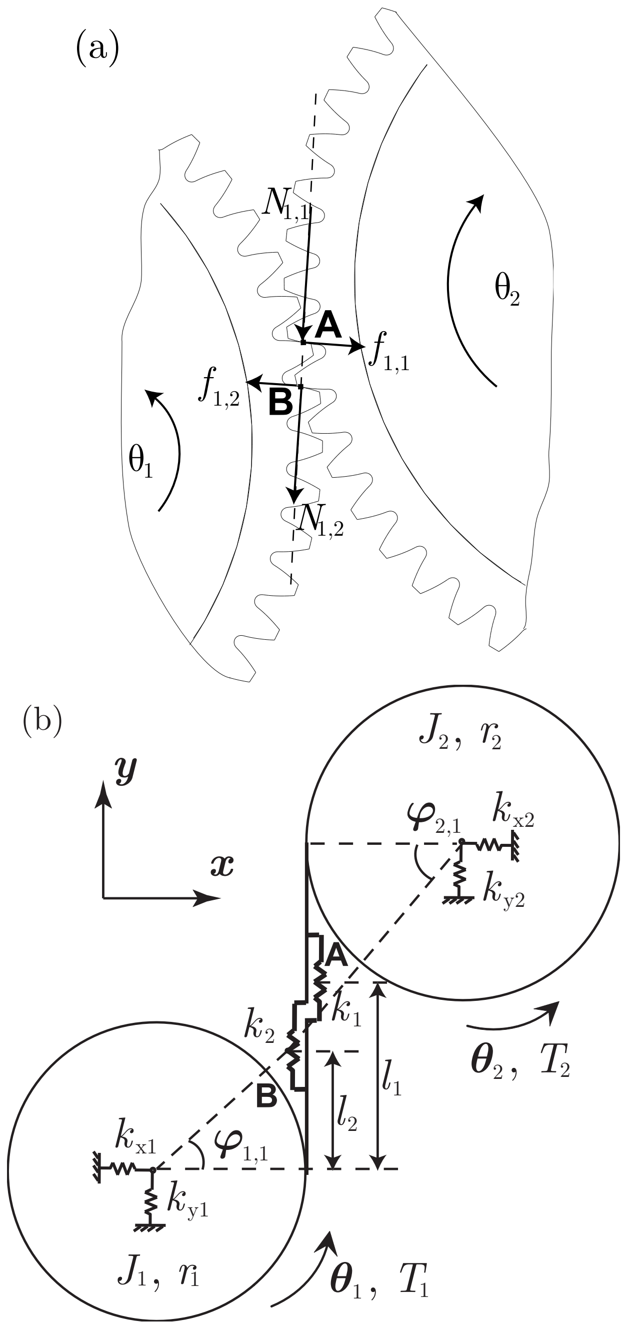

Figure 5.1: (a) Mesh forces. A and B are contact positions of the two tooth pairs; (b) Dynamic model of two gears with tooth friction.

Contact force variations results from the friction force. These variations *relative to the frictionless condition* are

$$\Delta N_1 = N_1 - \frac{T_1}{r_1} = N_1 \sum_{i=1}^{z} sgn(v_i) \mu_i \alpha_i l_i / r_1, \quad \Delta f_1 = -N_1 \sum_{i=1}^{z} sgn(v_i) \mu_i \alpha_i \qquad (4.41)$$

where N_1 is greater than the nominal contact force T_1 / r_1 when contact occurs in the approach region ($sgn(v_i) = 1$) where the sliding makes gear 1 approach gear 2. On the other hand, N_1 is smaller than the nominal force when contact occurs in the recess region ($sgn(v_i) = -1$) where the sliding acts to separate gear 1 from gear 2. In practice, $l_i / r_1 < 1$ implying $|\Delta N_1| < |\Delta f_1|$. From (4.39) and (4.41), mesh deflection variation due to tooth friction is $\Delta W = \Delta N_1 / k_m + \Delta f_1 / k_{fb}$, where k_m and k_{fb} are the mesh stiffness and friction bending stiffness, respectively, which are reciprocals of the compliances in (4.39). ΔW includes the impact of friction moments and the bending effect of friction forces. Note that the traditional analytical mesh deflection variation is $\Delta W = \Delta N_1 / k_m$, which only considers the moments of friction forces.

	Pinion	Gear
Number of teeth	38	55
Modulus (mm)	2.54	2.54
Base radius (mm)	45.35	65.64
Inertias I_i ($kg \cdot m^2$)	2.62e-3	3.27e-3
Mesh parameters	$\bar{k} = 2.98e8$ N/m, $T_1 = 100\,Nm$, $c = 1.4$ $\alpha = 0.6$, $\gamma = 0.28$	

Table 5.1: Parameters of example gears.

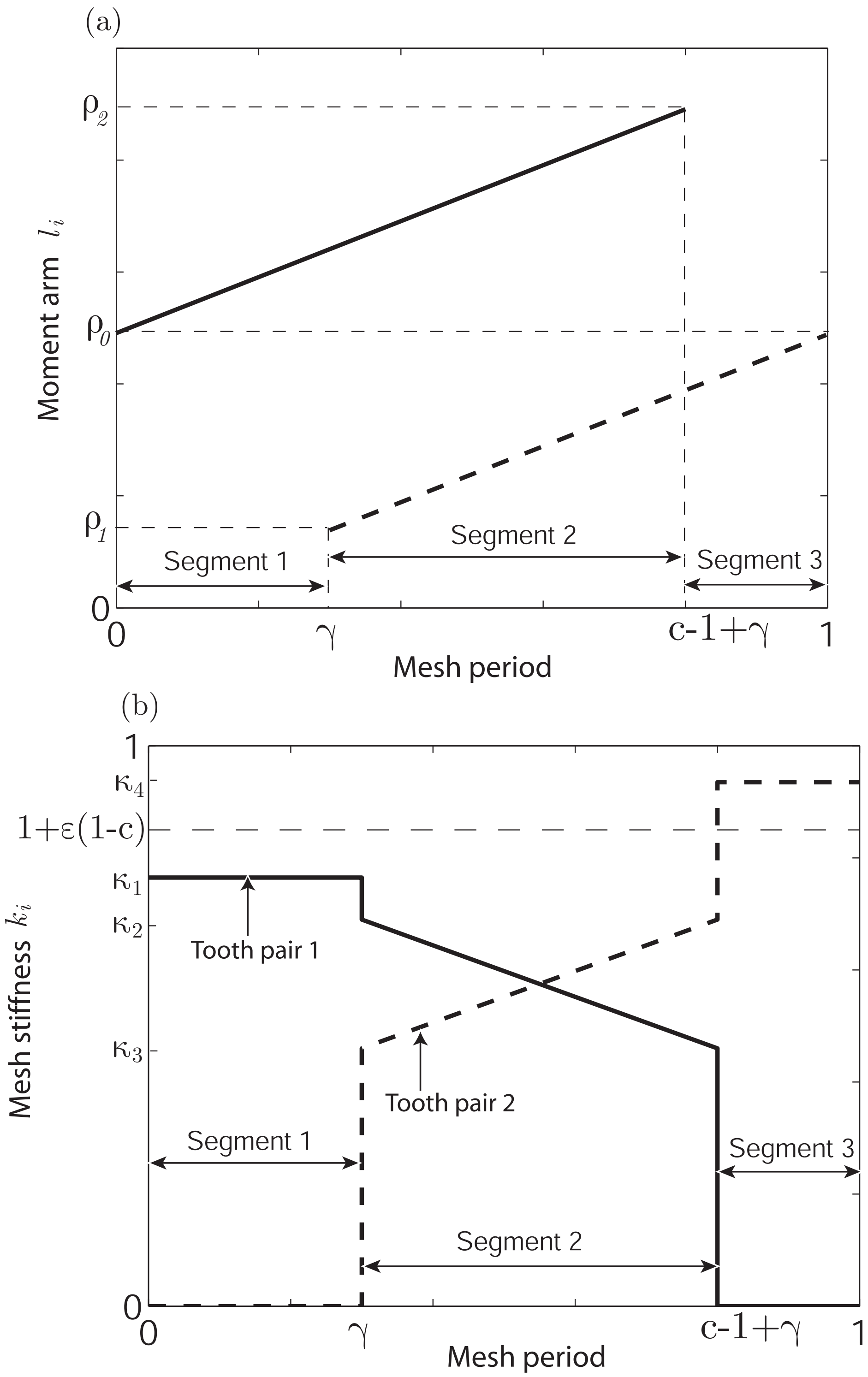

Figure 5.2: (a) Moment arms of two friction forces; (b) Mesh stiffnesses of gear tooth pairs including friction bending effect (—— the first tooth pair; – – the second pair).

A specialized finite element (FE) program is used to benchmark the analytical model. The FE model uses detailed contact analysis including Coulomb friction and careful tracking of the tooth contact kinematics. Its main features and validation against nonlinear gear vibration experiments are outlined in [5, 8, 88].

Variations of mesh deflection of the gear pair in Table 5.1 and $\mu_1 = \mu_2 = \mu = 0.1$ obtained by FE and analytical predictions are shown in Figure 5.3. Significant differences emerge from the friction bending effect. For a contact ratio less than two, there is a pair of gear teeth engaged from mesh period 0 (pitch point) to 0.84. Another gear pair starts contact from 0.1 to 1. For single-tooth contact in the recess region (mesh period $\in$ (0 0.1]), $\Delta N_1 = -\mu_1 l_1 N_1 / r_1 < 0$ such that $\Delta W \approx -2\,\mu m$ when the friction bending effect is neglected. The bending effect of friction force $\Delta f_1 = \mu_1 N_1 > 0$, however, increases the mesh deflection by about 0.5 μm. Combining the effects of friction force moment and bending, $\Delta W \approx -1.5\,\mu m$. The mesh deflection variation from the friction bending effect is 25% of the variation from the friction moment alone. For single-tooth contact in the approach region (mesh period $\in$ (0.84 1]), $\Delta N_1 = \mu_2 l_2 / r_1 N_1 > 0$ such that, without the friction bending effect, $\Delta W \approx 1.75\,\mu m$, which has smaller magnitude than in the recess region due to $l_1 > l_2$ (Figure 5.2a). The bending effect of friction force $\Delta f_1 = -\mu_2 N_1 < 0$ decreases the mesh deflection by about 0.5 μm, similar to the recess region because $|\Delta f_1|$ is the same for the recess and approach regions. Combining the effects of friction force moment and bending, $\Delta W \approx 1.25\,\mu m$. The mesh deflection variation from the friction bending effect is 28% of the variation from friction moment. Thus, the effect of friction force moment and bending are significant for mesh defection in the single-tooth contact region. Note that pure rolling occurs at the pitch point (mesh period=0) such that $\Delta N_1 = \Delta f_1 = 0$ and $\Delta W = 0$. The mesh deflection and friction force are discontinuous at the pitch point due to the discontinuity of sliding velocity direction. For the double-tooth region (mesh period $\in$ (0.1 0.84]), $\Delta N_1 = \left(\mu_2 \alpha_2 l_2 - \mu_1 \alpha_1 l_1\right) / r_1 N_1 \approx 0$ and $\Delta W \approx 0$. In addition, $\Delta f_1 = \left(\mu_1 \alpha_1 - \mu_2 \alpha_2\right) N_1 \approx 0$ due to the cancellation from two tooth pairs. Thus, the effect of friction force is negligible in this area. This may not be the case in dynamic analysis, however.

Summarizing, the contribution of tooth bending caused by friction to static mesh deflection is comparable to that from the friction force moment. The static analysis example shows that friction moments lower the STE in the recess region of single-tooth contact and increase the STE in the approach region of single-tooth contact. The friction bending effect, however, counteracts the STE variations arising from the friction moment in the static case. Thus, the combined effect of friction moment and friction bending on the STE variation (relative to the frictionless case) is destructive and so the individual effects are less evident in measured STE. As will be shown, the combined effect in the dynamic case is more complex, however, and can be destructive or constructive depending on the modal properties. The interaction between this friction bending effect and other time-varying parameters is important to the stability and dynamic response.

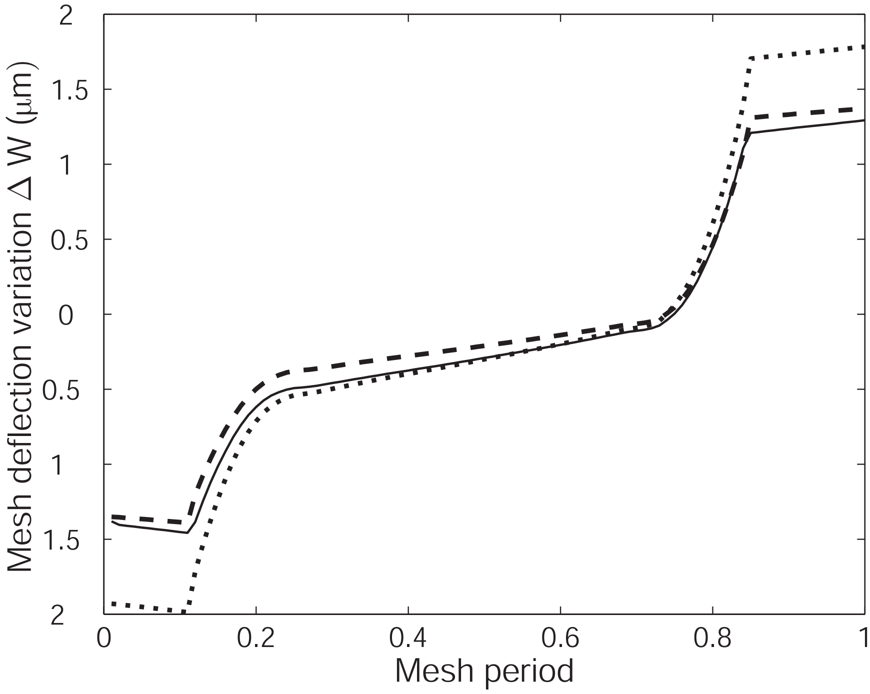

Figure 5.3: Mesh deflection variation comparisons for gears in Table 5.1 and $T_1 = 100$ N-m (___: FE μ =0.1; — —: analytical result with friction bending and μ =0.1; ...... : analytical result without friction bending and μ =0.1).

5.3 Mathematical Model

5.3.1 Modeling of Friction Bending Effect

For involute gear teeth, variation of mesh stiffness and tooth friction are the only excitations in this work. In contrast to existing gear models that treat gear meshes as one elastic element even when multiple tooth pairs are in contact, this study models each tooth pair as a separate elastic element, and they are connected in parallel. Although the number of tooth pairs in contact varies as the gears roll, by assigning zero mesh stiffness for the tooth pair out of contact there are always $Z = ceil(c)$ pairs of teeth in contact during a mesh period, where c is the contact ratio and $ceil(c)$ gives the smallest integer greater than c.

Mesh stiffness usually reflects the linear relation between normal load and mesh deflection. As discussed above, however, the bending effect of friction forces gives rise to pronounced impact on mesh deflection. In other words, applying the same normal load, the mesh deflections are different for friction and frictionless conditions. This contribution from friction bending can be included in an effective mesh stiffness. Substituting (4.40) into (4.39) and isolating $W / N_{1,i}$, the mesh stiffness of tooth pair i including the effect of friction bending is

$$\begin{aligned} k_i &= \frac{W}{N_{1,i}} = \tilde{k}_i \left[1 - sgn(v_i) \tilde{\beta} \mu_i \right]^{-1} \approx \tilde{k}_i \left[1 + sgn(v_i) \tilde{\beta} \mu_i \right] \\ \tilde{\beta} &= \frac{g_c \sin \varphi_c - g_s \cos \varphi_c + EI / k_r}{g_c \cos \varphi_c - g_s \sin \varphi_c + EI / k_r}, \quad \left| sgn(v_i) \tilde{\beta} \mu_i \right| \ll 1 \end{aligned} \tag{4.42}$$

where $\tilde{\beta}$ is the ratio of compliances of the two forces in (4.39), $\tilde{k}_i$ is the mesh stiffness without friction, and k_i is the effective mesh stiffness with friction. $\tilde{\beta}$ is less than 1 and varies periodically over a mesh cycle. The mean value of $\tilde{\beta}$ is used in this study.

From (4.42), the effective mesh stiffness is affected by the compliance ratio, friction coefficient and dynamic sliding velocity from nominal gear speed and gear vibration. The effect of the vibratory velocity, however, is negligible compared to the nominal velocity $\overline{v}_i = \Omega_1 r_1 (\tan \varphi_{1,i} - \tan \varphi_{2,i})$, where Ω_1 is the nominal rotation speed of the input gear and $\varphi_{z,i}$ is the pressure angle of tooth i of gear z [18, 47]. Low contact ratio gears ($c<2$) are considered in this study such that $Z=2$. For the mesh cycle shown in Figure 5.2, the pitch point is at zero, and the tooth pair in contact from mesh period 0 to $c-1+\gamma$, defined as the first tooth pair, is in the recess region ($sgn(v_1)<0$). The second tooth pair engages from γ to 1 and it is in the approach region ($sgn(v_2)>0$).

Defining $\bar{k}$ as the mean value of frictionless mesh stiffness and ε as the ratio of peak-peak to mean value of the mesh stiffness, the *frictionless* mesh stiffnesses are $\tilde{k}_1=\bar{k}[1+\varepsilon(1-c)]$ and $\tilde{k}_2=0$ for segment 1 (indicated in Figure 5.2b), and $\tilde{k}_1=0$ $\tilde{k}_2=\bar{k}[1+\varepsilon(1-c)]$ for segment 3. In segment 2, two tooth pairs share the gear load such that $\tilde{k}_1$ decreases linearly from $\alpha\bar{k}[1+\varepsilon(2-c)]$ to $(1-\alpha)\bar{k}[1+\varepsilon(2-c)]$ and $\tilde{k}_2$ increases from $(1-\alpha)\bar{k}[1+\varepsilon(2-c)]$ to $\alpha\bar{k}[1+\varepsilon(2-c)]$, where α is the load sharing factor at mesh period γ. α is approximated by the ratio of the static load of tooth pair 1 to the resultant tooth load, which is calculated by FE analysis. Note that $\tilde{k}_1+\tilde{k}_2=\bar{k}[1+\varepsilon(1-c)]$ for single-tooth contact and $\tilde{k}_1+\tilde{k}_2=\bar{k}[1+\varepsilon(2-c)]$ for double-tooth contact.

The quasi-static *frictional* mesh stiffnesses shown in Figure 5.2b are found by substituting the above $\tilde{k}_i$ into (4.42). The mesh stiffnesses normalized by $\bar{k}$ are

$$
\begin{aligned}
&\text{Segment 1: } k_1/\bar{k}=\kappa_1=(1-\beta)\left[1+\varepsilon(1-c)\right], \quad k_2=0 \\
&\text{Segment 2: } k_1/\bar{k} \text{ varies linearly from } \kappa_2 \text{ to } \kappa_3, k_2/\bar{k} \text{ varies linearly from } \kappa_3 \text{ to } \kappa_2 \\
&\qquad\qquad \kappa_2=\alpha(1-\beta)\left[1+\varepsilon(2-c)\right], \kappa_3=(1-\alpha)(1+\beta)\left[1+\varepsilon(2-c)\right] \\
&\text{Segment 3: } k_1=0, \quad k_2/\bar{k}=\kappa_4=(1+\beta)\left[1+\varepsilon(1-c)\right]
\end{aligned}
\tag{4.43}
$$

where $\beta = \tilde{\beta}\mu$ is the friction bending factor. The frictional mesh stiffnesses in segments 1 and 3 are reduced and increased by β, respectively, due to the friction bending effect. The mesh stiffnesses of high contact ratio gears ($c > 2$) can be treated in a similar way.

5.3.2 Dynamic Model of Gear Pair with Tooth Friction

Referring to Figure 5.1a, the dynamic normal forces $N_{z,i}$ and friction forces $f_{z,i}$ act at the mesh positions A and B. Elasticity of each tooth pair is captured by the variable mesh stiffnesses $k_{1,2}$ in Figure 5.1b. To visually emphasize the parallel connection of stiffnesses for the individual tooth pairs, each elastic mesh element is artificially shifted slightly in the x direction. The normal forces and mesh stiffnesses, however, are actually collinear along the line of action. The gear translations are constrained by bearings with lateral stiffnesses k_{xz} and k_{yz}. $J_{1,2}$ are polar moments of inertia. $\theta_{1,2}$ are vibratory gear rotations. T_1 and T_2 are the input torque and load, respectively. The 6-DOF equations of motion can be derived by Newtonian or Lagrangian methods. Dynamic transmission error (DTE) $u = r_1\theta_1 + r_2\theta_2$ is introduced to remove the rigid body mode. The governing equations in matrix form are

$$
\begin{aligned}
&\mathbf{M}\ddot{\mathbf{x}} + \mathbf{C}\dot{\mathbf{x}} + \left[\mathbf{L}(\mathbf{x}) + \mathbf{K}(\mathbf{x})\right]\mathbf{x} = \mathbf{F} \\
&\mathbf{M} = diag\left(\left[J_e, m_1, m_1, m_2, m_2\right]\right), \quad J_e = J_1 J_2 /(r_2^2 J_1 + r_1^2 J_2) \\
&\mathbf{X} = \left[u, x_1, y_1, x_2, y_2\right]^T, \quad \mathbf{F} = \left[T_1 / r_1, 0, 0, 0, 0\right]^T \\
&\mathbf{L} = \begin{bmatrix} L_m & 0 & L_m & 0 & -L_m \\ -L_\mu & 0 & -L_\mu & 0 & L_\mu \\ 0 & 0 & 0 & 0 & 0 \\ L_\mu & 0 & L_\mu & 0 & -L_\mu \\ 0 & 0 & 0 & 0 & 0 \end{bmatrix}, \mathbf{K} = \begin{bmatrix} k_m & 0 & k_m & 0 & -k_m \\ 0 & k_{x1} & 0 & 0 & 0 \\ k_m & 0 & k_m + k_{y1} & 0 & -k_m \\ 0 & 0 & 0 & k_{x2} & 0 \\ -k_m & 0 & -k_m & 0 & k_m + k_{y2} \end{bmatrix} \\
&L_m = \mu \sum_{i=1}^{Z} \left[\eta l_i / r_1 + (1-\eta)(D - l_i)/ r_2\right] sgn(v_i) \Gamma_i k_i \qquad (4.44) \\
&L_\mu = \mu \sum_{i=1}^{Z} sgn(v_i) \Gamma_i k_i \\
&v_i \approx \overline{v}_i = \Omega_1 r_1 (\tan\varphi_{1,i} - \tan\varphi_{2,i}) \\
&\Gamma_i = \tfrac{1}{2}\left[sgn(u + y_1 - y_2 - g_i) + sgn(u + y_1 - y_2 - g_i + B)\right] \\
&k_m = \sum_{i=1}^{Z} \Gamma_i k_i
\end{aligned}
$$

where L_m and L_μ include the contributions of tooth friction on rotations and off-line-of-action translations, respectively; $\eta = r_1^2 J_2 /(r_2^2 J_1 + r_1^2 J_2)$; $l_i = r_1 \tan\varphi_{1,i}$ are moment arms of the friction force $f_{1,i}$ with respect to the center of gear 1; $D = (r_1 + r_2)\tan\varphi$ is the length of the line of action; B is the gear backlash; the tooth separation function $\Gamma_i \in \{1, 0, -1\}$ determines the existence of drive-side contact (+1), contact loss (0) or backside contact (-1); and g_i is the tooth surface deviation, which is taken as zero in this study. The constant matrix **C** is determined from a modal damping ratio ζ whose fluctuation has no significant impact on parametric excitation [101].

The governing equation (4.44) is a group of nonlinear, time-varying (NTV) differential equations. Parametric excitations are included in $\mathbf{L}$ and $\mathbf{K}$ from the time-varying friction moment arms l_i and mesh stiffnesses k_i modified by the friction bending effect.

Substitution of $\bar{k}$ for k_m in $\mathbf{K}$ yields $\bar{\mathbf{K}}$. The eigenvalue problem for the linear time-invariant form of (4.44) averaged over a mesh cycle is $\bar{\mathbf{K}}\phi_n = \omega_n^{\ 2}\mathbf{M}\phi_n$ where $f_n = \omega_n/(2\pi)$ are natural frequencies. The normalized vibration modes are

$$\begin{aligned} &\phi_n = [\phi_{n1}, 0, \phi_{n3}, 0, \phi_{n5}]^T \quad n = 1,2,3 \\ &\phi_4 = [0, \phi_{n2}, 0, 0, 0]^T,\ \phi_5 = [0, 0, 0, \phi_{n4}, 0]^T \end{aligned} \tag{4.45}$$

where ϕ_{nr} are elements of the n^{th} vibration mode. Rotational modes ($n = 1,2,3$) have coupled motions of u, y_1, and y_2. Translational modes ($n = 4,5$) only have off-line-of-action translations x_1 and x_2.

To examine the parametric instabilities, we take $\Gamma_i = 1$ (contact loss occurs only after onset of large vibration). Equation (4.44) becomes a linear, time-varying (LTV) model with periodic, piecewise linear parametric excitations in a mesh period T. The mesh stiffnesses and moment arms vary in each of three segments in a period (Figure 5.2). Combining (4.43) and (4.44), the time-varying elements of $\mathbf{L}$ and $\mathbf{K}$ are as follows.

For segment 1 ($t_0 \le t < t_1$ where $t_0 = 0$ and $t_1 = \gamma T$)

$$\begin{aligned} &k_1 = \kappa_1 \bar{k} && k_m = (1-\beta)\left[1+\varepsilon(1-c)\right]\bar{k} \\ &k_2 = 0 && \Rightarrow L_\mu = \mu(1-\beta)\left[1+\varepsilon(1-c)\right]\bar{k} \\ &l_1 = \rho_0 + r_1\Omega t && L_m = L_{1,0} + L_{1,1}t \end{aligned} \tag{4.46}$$

For segment 2 ($t_1 \le t < t_2$ where $t_2 = (c+\gamma-1)T$)

$$\begin{aligned} k_1 &= \kappa_2 \bar{k} - (t-t_1)w \qquad & k_m &= \left(\kappa_2 + \kappa_3\right)\bar{k} \\ k_2 &= \kappa_3 \bar{k} + (t-t_1)w \Rightarrow & L_\mu &= \mu \bar{k}\left(\kappa_3 - \kappa_2\right) + 2(t-t_1)\mu w \\ l_1 &= \rho_1 + (t-t_1) r_1 \Omega & L_m &= L_{2,0} + (t-t_1)L_{2,1} + (t-t_1)^2 L_{2,2} \end{aligned} \tag{4.47}$$

For segment 3 ($t_2 \le t < t_3$ where $t_3 = T$)

$$\begin{aligned} k_1 &= 0 & k_m &= (1+\beta)\left[1+\varepsilon(1-c)\right]\bar{k} \\ k_2 &= \kappa_4 \bar{k} & \Rightarrow L_\mu &= \mu(1+\beta)\left[1+\varepsilon(1-c)\right]\bar{k} \\ l_1 &= \rho_2 + (t-t_2) r_1 \Omega \qquad & L_m &= L_{3,0} + (t-t_2)L_{3,1} \end{aligned} \tag{4.48}$$

where $w = (\kappa_2 - \kappa_3)/(t_3 - t_2)$, Ω is the mesh frequency, $L_{p+1,q}$ (segment index p =0,1,2) are coefficients that emerge from simplication of L_m (see Appendix A), and $\rho_{0,1,2}$ are defined previously in Figure 5.2b.

Substitution of (4.46)-(4.48) into (4.44) yields different matrices $\mathbf{L}$ and $\mathbf{K}$ for each segment. These matrices, however, have the common form

$$\begin{aligned} \mathbf{L} &= \mathbf{L}_a + \left(t-t_p\right)\mathbf{L}_b + \left(t-t_p\right)^2 \mathbf{L}_c \\ \mathbf{K} &= \mathbf{K}_a + \left(t-t_p\right)\mathbf{K}_b + \left(t-t_p\right)^2 \mathbf{K}_c \end{aligned} \qquad \text{for } 0 \le t < T \tag{4.49}$$

where $\mathbf{L}_{a,b,c}$ result from substitution of $L_{p+1,q}$ and L_μ into $\mathbf{L}$. $\mathbf{K}_{a,b,c}$ result from substitution of k_m into $\mathbf{K}$. $\mathbf{L}_{a,b,c}$ and $\mathbf{K}_{a,b,c}$ are different for each segment due to variations of mesh stiffnesses and moment arms. For the rectangular shape mesh stiffnesses used in this work, $\mathbf{K}_{b,c} = 0$ for all segments, but that is not true for general stiffness variations. Note $\mathbf{L}$ and $\mathbf{K}$ are periodic operators with period T .

With substitution of (4.49), (4.44) is recast into homogeneous state-space form as

$$\dot{\mathbf{y}} = \mathbf{G}(t)\mathbf{y} \quad \text{for } 0 \le t < T,$$
$$\mathbf{y} = [\mathbf{x}, \dot{\mathbf{x}}]^T, \mathbf{G} = \begin{pmatrix} \mathbf{0} & \mathbf{I} \\ -\mathbf{M}^{-1}(\mathbf{K}+\mathbf{L}) & -\mathbf{M}^{-1}\mathbf{C} \end{pmatrix} = \mathbf{G}_a + (t-t_p)\mathbf{G}_b + (t-t_p)^2\mathbf{G}_c \tag{4.50}$$

where $\mathbf{G}(t+T) = \mathbf{G}(t)$.

5.4 Parametric Instability

5.4.1 Calculation of the State Transition Matrix

According to Floquet-Liapunov theory [Richards, 1983 #27], the fundamental matrix $\mathbf{\Pi}(t)$ comprised of a complete set of fundamental solutions for (4.50) satisfies $\mathbf{\Pi}(t) = \mathbf{P}(t)e^{(t-t_0)\mathbf{Q}}$, where $\mathbf{P}(t)$ is a periodic function with period T, $\mathbf{Q}$ is a complex constant matrix, and t_0 is the initial time. After one period T,

$$\mathbf{\Pi}(t+T) = \mathbf{P}(t+T)e^{(t+T-t_0)\mathbf{Q}} = \mathbf{\Pi}(t)e^{\mathbf{Q}T} \tag{4.51}$$

where $e^{\mathbf{Q}T} = \mathbf{\Pi}^{-1}(t_0)\mathbf{\Pi}(t_0+T) = \mathbf{\Phi}(t_0+T, t_0)$ is the state transition matrix or monodromy matrix. The stability of fundamental solutions is determined by the eigenvalues λ_i of the state transition matrix: $|\lambda_i| < 1$ indicates stable solutions; $|\lambda_i| > 1$ indicates unstable; and $\lambda_i = 1^{1/m}$ for integer m means period-mT solutions.

As discussed above, the LTV model is expressed as three polynomial matrix forms associated with the three segments of one period defined previously. The state transition matrix of the system is obtained by the state transition matrices of the three segments

$$\mathbf{\Phi}(T,0) = \mathbf{\Phi}(t_1,0)\mathbf{\Phi}(t_2,t_1)\mathbf{\Phi}(T,t_2) \tag{4.52}$$

where $\mathbf{\Phi}(t_{p+1}, t_p) = \mathbf{\Pi}^{-1}(t_p)\mathbf{\Pi}(t_{p+1})$. The state transition matrix for any segment with

$t_p \le t < t_{p+1}$ is expanded using Peano-Baker series [102, 103] as

$$\begin{aligned}\mathbf{\Phi}(t_{p+1},t_p) = \mathbf{I} + \int_{t_p}^{t_{p+1}} \mathbf{G}(\tau_0 - t_p)d\tau_0 + \int_{t_p}^{t_{p+1}} \mathbf{G}(\tau_1 - t_p)\int_{t_p}^{\tau_1} \mathbf{G}(\tau_2 - t_p)d\tau_2 d\tau_1 + \\ \int_{t_p}^{t_{p+1}} \mathbf{G}(\tau_1 - t_p)\int_{t_p}^{\tau_1} \mathbf{G}(\tau_2 - t_p)\int_{t_p}^{\tau_2} \mathbf{G}(\tau_3 - t_p)d\tau_3 d\tau_2 d\tau_1 + \cdots\end{aligned} \tag{4.53}$$

Let $\tilde{\tau}_i = \tau_i - t_p$ such that,

$$\int_{t_p}^{t_{i-1}} \mathbf{G}(\tau_i - t_p)d\tau_i = \int_0^{t_{i-1}-t_p} \mathbf{G}(\tilde{\tau}_i)d\tilde{\tau}_i \Rightarrow \mathbf{\Phi}(t_{p+1},t_p) = \mathbf{\Phi}(h_p,0) \tag{4.54}$$

where $h_p = t_{p+1} - t_p$. Evaluation of the integrals in (4.53) and the polynomial form of $\mathbf{G}$ gives a recursive sequence for calculation of the state transition matrix as

$$\begin{aligned}
&\mathbf{\Phi}_P(h_p,0) = \mathbf{I} + \mathbf{T}_1(h_p) + \mathbf{T}_2(h_p) + \cdots + \mathbf{T}_n(h_p) + \cdots \\
&\mathbf{T}_1 = \sum_{i=1}^{3} \mathbf{T}_{1,i} = \mathbf{G}_0 h_p + \mathbf{G}_1 h_p^2/2 + \mathbf{G}_2 h_p^3/3 \\
&\mathbf{T}_n = \sum_{i=1}^{2n+1} \mathbf{T}_{n,i} \quad n \ge 2 \\
&\mathbf{T}_{n,1} = \frac{1}{n} h_p \mathbf{G}_0 \mathbf{T}_{n-1,1} \\
&\mathbf{T}_{n,2} = \frac{h_p}{n+1}\left(\mathbf{G}_0 \mathbf{T}_{n-1,2} + h_p \mathbf{G}_1 \mathbf{T}_{n-1,1}\right) \\
&\mathbf{T}_{n,i} = \frac{1}{n+i-1}\sum_{j=0}^{2} h_p^{j+1} \mathbf{G}_j \mathbf{T}_{n-1,i-j} \quad i = 3,4,\cdots 2n-1 \\
&\mathbf{T}_{n,2n} = \frac{h_p^2}{3n-1}\left(\mathbf{G}_1 \mathbf{T}_{n-1,2n-1} + h_p \mathbf{G}_2 \mathbf{T}_{n-1,2n-2}\right) \\
&\mathbf{T}_{n,2n+1} = \frac{1}{3n} h_p^3 \mathbf{G}_2 \mathbf{T}_{n-1,2n-1}
\end{aligned} \tag{4.55}$$

where $\mathbf{T}_n$ denotes the sequence of terms in (4.53).

For comparison, a numerical integration method [78-80] is applied. The time span h_p is discretized into m divisions, where Δ_i is the time step of division i ($t_i < t \le t_{i+1}$) and $\mathbf{C}_i$ is the mean value of $\mathbf{G}$ over a mesh cycle. Thus,

$$\begin{aligned}
&\mathbf{\Phi}_I(h_p,0)=\prod_{i=1}^{m}\left[I+\Delta_i\mathbf{C}_i+\tfrac{1}{2}\left(\Delta_i\mathbf{C}_i\right)^2+\cdots+\tfrac{1}{k!}\left(\Delta_i\mathbf{C}_i\right)^k+\cdots\right]\\
&\mathbf{C}_i=\frac{1}{\Delta_i}\int_{\Delta_i}\left(\mathbf{G}_0+\mathbf{G}_1\tau+\mathbf{G}_2\tau^2\right)d\tau=\mathbf{G}_0+\frac{t_{i+1}+t_i}{2}\mathbf{G}_1+\frac{t_{i+1}^3-t_i^3}{3\Delta_i}\mathbf{G}_2
\end{aligned} \tag{4.56}$$

The numerical integration method applies for arbitrary functions $\mathbf{G}$. The recursive process applies only to $\mathbf{G}$ having polynomial forms.

To validate the recursive process and compare performance against numerical integration, an example system is selected as

$$\ddot{x}+\left[a(t-nT)+b\right]x=0 \quad nT\le t<(n+1)T \tag{4.57}$$

The stiffness term is a periodic sawtooth function. The fundamental and state transition matrices are [104]

$$\mathbf{\Pi}(t)=\begin{bmatrix}\sqrt{at+b}J_{1/3}(\sigma) & \sqrt{at+b}J_{-1/3}(\sigma)\\ (at+b)J_{-2/3}(\sigma) & -(at+b)J_{2/3}(\sigma)\end{bmatrix},\quad \sigma=\frac{2(at+b)^{3/2}}{3a} \tag{4.58}$$

$$\mathbf{\Phi}_B(h_p,0)=\mathbf{\Pi}^{-1}(0)\mathbf{\Pi}(h_p) \tag{4.59}$$

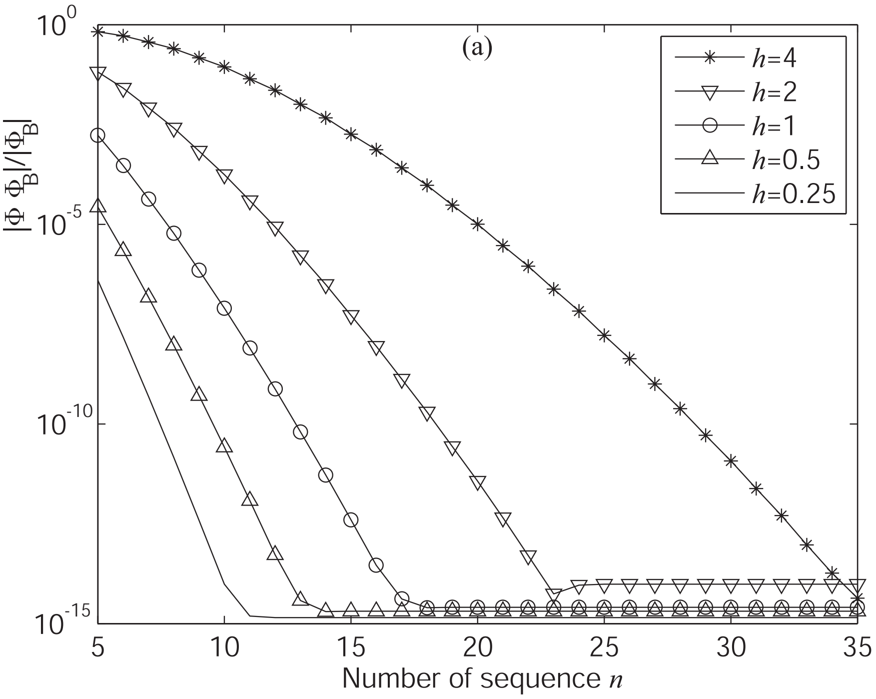

(a)

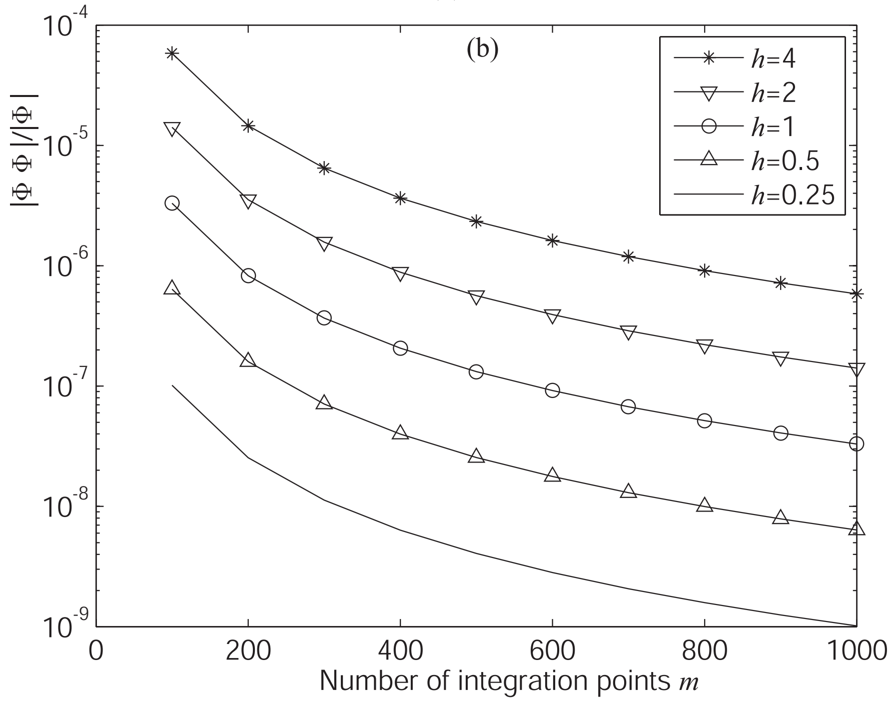

(b)

Figure 5.4: (a) Comparison of Peano-Baker series solution with analytical solution; (b) Comparison of the integration method with analytical solution (a=-1,b=-1).

The relative error of the recursive process with respect to the analytical solution is examined in Figure 5.4a. There is a critical value n_c for a given h_p above which the error is insensitive to n and the error is extremely small. The errors in the integration method shown in Figure 5.4b are higher than for the recursive process for comparable computation. Computation for the recursive process is slightly less than the integration method given $n = 20$, $m = 200$, and $h_p = 0.5$.

The recursive and numerical integration methods use Peano-Baker and exponential series expansions, respectively. Both have truncation errors. The truncation error of exponential series is smaller than Peano-Baker series for the same number of terms. The integration method, however, has additional discretization error. On the other hand, the computational demands of the recursive process increase significantly with the number of terms. In this study, the recursive process is more efficient than the integration method because a smaller number of terms provides the required accuracy. Overall, the recursive process has better accuracy and requires less computation than numerical integration for systems expanded as polynomial forms.

5.4.2 Perturbation Approximation

This study only considers small ratios of mesh stiffness variation to mean stiffness ($\varepsilon \ll 1$), small damping ($\zeta \ll 1$), and small coefficient of friction ($\mu \ll 1$). The nonlinear, time-varying terms in (4.44) for gear pairs with $c < 2$ are linearized in these quantities as

$$
\begin{aligned}
&k_m = k_1 + k_2 = \bar{k} + \varepsilon \tilde{K} \Rightarrow \tilde{K} = \left(k_1 + k_2 - \bar{k}\right) / \varepsilon \\
&L_\mu = \mu\left(k_2 - k_1\right) = \varepsilon \tilde{L}_\mu \Rightarrow \tilde{L}_\mu = g\left(k_2 - k_1\right) \\
&L_m = \varepsilon \frac{g}{r_1 r_2}\left\{k_2\left[\eta r_2 l_2 + r_1(1-\eta)(D - l_2)\right] - k_1\left[\eta r_2 l_1 + r_1(1-\eta)(D - l_1)\right]\right\} = \varepsilon \tilde{L}
\end{aligned} \tag{4.60}
$$

where $g = \mu / \varepsilon$ denotes the ratio of friction to mesh stiffness variation. $\tilde{K}$, $\tilde{L}_\mu$, $\tilde{L}$, and g are $O(1)$. These time-varying functions are expanded in Fourier series as

$$
\begin{aligned}
\tilde{L} &= g \sum_{s=1}^{\infty} \Lambda_s e^{is\Omega t} + c.c. \\
\tilde{L}_\mu &= g \sum_{s=1}^{\infty} \chi_s e^{is\Omega t} + c.c. \\
\tilde{K} &= \sum_{s=1}^{\infty} \Theta_s e^{is\Omega t} + c.c.
\end{aligned} \tag{4.61}
$$

where Λ_s, χ_s and Θ_s are known complex Fourier amplitudes. The symbol *c.c.* represents the complex conjugate of preceding terms.

The associated operators are $\mathbf{L} = \varepsilon \tilde{\mathbf{L}}$ and $\mathbf{K} = \bar{\mathbf{K}} + \varepsilon \tilde{\mathbf{K}}$, where $\tilde{\mathbf{L}}$, $\tilde{\mathbf{K}}$ are obtained from substitution of L_m, L_μ and k_m into $\mathbf{L}$ and $\mathbf{K}$. Let $\boldsymbol{\phi} = [\phi_n]$ be the modal matrix from (4.45). Applying the modal transformation $\mathbf{x} = \boldsymbol{\phi}\mathbf{u}$, (4.44) is recast into modal coordinates as

$$
\ddot{u}_n + 2\varepsilon \varsigma \omega_n \dot{u}_n + \omega_n^2 u_n + \varepsilon \sum_{r=1}^{5} \left(\phi_n^T \tilde{\mathbf{L}} \phi_r + \phi_n^T \tilde{\mathbf{K}} \phi_r\right) u_r = 0 \quad n = 1,2,3,4,5 \tag{4.62}
$$

where $\varsigma = \zeta / \varepsilon = O(1)$. Using (4.45), $\phi_n^T \tilde{\mathbf{L}} \phi_r$ and $\phi_n^T \tilde{\mathbf{K}} \phi_r$ are

$$
\begin{aligned}
&\phi_n^T \tilde{\mathbf{L}} \phi_r = \begin{cases} 0 & \text{if } r \geq 4 \\ D_{nr} \tilde{L} & \text{if } n, r < 4 \\ -D_{nr} \tilde{L}_\mu & \text{if } r < 4 \text{ and } n \geq 4 \end{cases} \\
&\phi_n^T \tilde{\mathbf{K}} \phi_r = \begin{cases} 0 & \text{if } r \geq 4 \text{ or } r < 4 \text{ and } n \geq 4 \\ E_{nr} \tilde{K} & \text{if } n, r < 4 \end{cases} \\
&D_{nr} = \phi_{n1}(\phi_{r1} + \phi_{r3} - \phi_{r5}) \\
&E_{nr} = (\phi_{n1} + \phi_{n3} - \phi_{n5})(\phi_{r1} + \phi_{r3} - \phi_{r5})
\end{aligned}
\tag{4.63}
$$

where $D_{nr} \in \mathbb{R}$ is asymmetric and $E_{nr} = E_{rn} \in \mathbb{R}$ is symmetric. E_{nr} is the product of the mesh deflections in modes n and r. D_{nr} is the product of rotational transmission error in mode n and mesh deflection in mode r. Substitution of (4.63) into (4.62) yields

$$
\ddot{u}_n + 2\varepsilon\varsigma\omega_n \dot{u}_n + \omega_n^2 u_n + \varepsilon \sum_{r=1}^{3} \left(D_{nr} \tilde{L} + E_{nr} \tilde{K} \right) u_r = 0 \quad n = 1, 2, 3 \tag{4.64}
$$

$$
\ddot{u}_n + 2\varepsilon\varsigma\omega_n \dot{u}_n + \omega_n^2 u_n - \varepsilon \sum_{r=1}^{3} D_{nr} \tilde{L}_\mu u_r = 0 \quad n = 4, 5 \tag{4.65}
$$

Observing the upper limit of the sum in (4.64), the rotation modes 1, 2 and 3 are coupled together in (4.64) through time-varying friction moments and mesh stiffness. Strong interactions between these modes may lead to combination instabilities. These rotation modes are decoupled from the translation modes 4 and 5 in (4.64). The translation modes, however, are impacted by rotation modes in (4.65), although no coupling exists between the two translation modes.

Applying the method of multiple scales, the solutions of (4.64) and (4.65) are expressed as

$$
u_n = u_{n,0}(t, \tau) + \varepsilon u_{n,1}(t, \tau) + \cdots \quad n = 1, 2, 3, 4, 5 \tag{4.66}
$$

where $\tau = \varepsilon t$. Substituting (4.66) into (4.64) and (4.65) and separating terms with the same power in ε yields

$$\ddot{u}_{n,0} + \omega_n^2 u_{n,0} = 0 \quad n = 1,2,3,4,5 \tag{4.67}$$

$$\ddot{u}_{n,1} + \omega_n^2 u_{n,1} = -2\frac{\partial^2 u_{n,0}}{\partial \tau \partial t} - 2\varsigma\omega_n \frac{\partial u_{n,0}}{\partial t} - \sum_{r=1}^{3}\left(D_{nr}\tilde{L} + E_{nr}\tilde{K}\right)u_{r,0} \quad n = 1,2,3 \tag{4.68}$$

$$\ddot{u}_{n,1} + \omega_n^2 u_{n,1} = -2\frac{\partial^2 u_{n,0}}{\partial \tau \partial t} - 2\varsigma\omega_n \frac{\partial u_{n,0}}{\partial t} + \sum_{r=1}^{3} D_{nr}\tilde{L}_{\mu} u_{r,0} \quad n = 4,5 \tag{4.69}$$

The general solutions of (4.67) are

$$u_{n,0} = A_n(\tau)e^{i\omega_n t} + c.c. \quad n = 1,2,3,4,5 \tag{4.70}$$

Substituting (4.61) and (4.70) into (4.68) yields

$$\begin{aligned} \ddot{u}_{n,1} + \omega_n^2 u_{n,1} &= -2i\omega_n e^{i\omega_n t}\frac{\partial A_n}{\partial \tau} - 2\varsigma\omega_n\left(i\omega_n\right)A_n e^{i\omega_n t} \\ -\sum_{r=1}^{3}\sum_{s=1}^{\infty}&\left(D_{nr} g\Lambda_s + E_{nr}\Theta_s\right)\left[A_r e^{i(s\Omega+\omega_r)t} + \bar{A}_r e^{i(s\Omega-\omega_r)t}\right] + c.c. \quad n = 1,2,3 \end{aligned} \tag{4.71}$$

where an overbar means the complex conjugate.

By letting $s\Omega = \omega_p + \omega_q + \varepsilon\sigma$ ($p, q \le 3$), where σ is a detuning parameter, two-mode ($p \ne q$) combination instabilities or single-mode ($p = q$) instabilities of rotation modes are examined. Elimination of secular terms leading to unbounded response in (4.71) requires

$$2i\omega_p \frac{\partial A_p}{\partial \tau} + 2i\varsigma\omega_p^2 A_p + \left(D_{pq} g\Lambda_s + E_{pq}\Theta_s\right)\bar{A}_q e^{i\sigma\tau} = 0 \tag{4.72}$$

$$2i\omega_q \frac{\partial A_q}{\partial \tau} + 2i\varsigma\omega_q^2 A_q + \left(D_{qp} g\Lambda_s + E_{qp}\Theta_s\right)\bar{A}_p e^{i\sigma\tau} = 0 \tag{4.73}$$

The solutions of (4.72) and (4.73) are

$$A_p = a_p e^{\lambda\tau} \quad A_q = a_q e^{(\bar{\lambda}+i\sigma)\tau} \tag{4.74}$$

where a_p, a_q are complex constants and λ are roots of the characteristic equation obtained from (4.72) and (4.73) such that

$$\begin{aligned}\lambda &= \frac{1}{2}\left\{-\varsigma(\omega_p+\omega_q)+i\sigma\pm\left[\varsigma^2(\omega_p-\omega_q)^2-\sigma^2+2i\varsigma\sigma(\omega_p-\omega_q)+\Psi\right]^{1/2}\right\} \\ \Psi &= \frac{1}{\omega_p\omega_q}\left(D_{pq}g\Lambda_s+E_{pq}\Theta_s\right)\left(D_{qp}g\bar{\Lambda}_s+E_{qp}\bar{\Theta}_s\right)\end{aligned} \tag{4.75}$$

The real parts of λ determine the stability of the solutions. Note Ψ is complex in general.

Combination instabilities of the difference type are examined by letting $s\Omega=\omega_p-\omega_q+\varepsilon\sigma$ $(\omega_p>\omega_q)$ where $p,q\le 3$. The λ analogous to (4.75) are

$$\lambda = \frac{1}{2}\left\{-\varsigma(\omega_p+\omega_q)+i\sigma\pm\left[\varsigma^2(\omega_p-\omega_q)^2-\sigma^2+2i\varsigma\sigma(\omega_p-\omega_q)-\Psi\right]^{1/2}\right\} \tag{4.76}$$

The interaction between rotation modes 1, 2 and 3 in (4.45) and translation modes 4 and 5 is examined by letting $s\Omega=\omega_p+\omega_q+\varepsilon\sigma$ ($p<4$, $q\ge 4$). The solvability conditions for (4.71) are

$$2i\omega_p\frac{\partial A_p}{\partial\tau}+2i\varsigma\omega_p^2A_p=0 \tag{4.77}$$

$$2i\omega_q\frac{\partial A_q}{\partial\tau}+2i\varsigma\omega_q^2A_q-gD_{qp}\chi_s\bar{A}_pe^{i\sigma\tau}=0 \tag{4.78}$$

The nontrivial solutions of (4.77) and (4.78) are

$$A_p = a_p e^{-i\varsigma\omega_p\tau} \quad A_q = a_q e^{i\left(\varsigma\omega_p+\sigma\right)\tau} \tag{4.79}$$

These solutions are always bounded, so there are no combination instabilities between a rotation mode and a translation mode. The same is true for combination instabilities between two translation modes, including for $p = q$. As a result, the following results address interactions between rotation modes 1, 2 and 3.

5.5 Results and Discussion

A single mesh gear pair with the nominal parameters $\bar{k} = 1.95\times 10^8 \ N/m$, $\alpha = 0.6$, $\gamma = 0.28$, $c = 1.5$, $\zeta = 0.001$, $\mu = 0.1$, and $\beta = 0.5\mu$ is examined from this point, where $\mu = 0.1$ is consistent with past studies on gear dynamics [47, 92, 105]. The dimensionless natural frequencies of the rotation modes are f_1 =1.55, f_2 =2.09, and f_3 =5.70. The natural frequencies of the translation modes are f_4 =1.85 and f_5 =2.34.

5.5.1 Parametric Instability from Variable Mesh Stiffness

Without friction ($\mu = g = 0$), the only parametric excitation is from the mesh stiffness. From (4.75) and (4.76) in the absence of damping ($\zeta = 0$),

$$\begin{aligned}
&\lambda = \frac{1}{2}\left(i\sigma \pm \sqrt{\Psi - \sigma^2}\right) \ \text{for} \ s\Omega = \omega_p + \omega_q + \varepsilon\sigma \\
&\lambda = \frac{1}{2}\left(i\sigma \pm \sqrt{-\Psi - \sigma^2}\right) \ \text{for} \ s\Omega = \omega_p - \omega_q + \varepsilon\sigma \qquad (4.80) \\
&\Psi = E_{pq}^2 \left|\Theta_s\right|^2 / (\omega_p \omega_q) > 0
\end{aligned}$$

The response for mesh frequencies near sum type instability regions is bounded ($\mathrm{Re}(\lambda) < 0$) when $\sigma^2 \geq \Psi$ and unbounded ($\mathrm{Re}(\lambda) > 0$) when $\sigma^2 < \Psi$. Thus, the instability boundaries are $s\Omega = \omega_p + \omega_q \pm \varepsilon \dfrac{\left|E_{pq}\Theta_s\right|}{\sqrt{\omega_p \omega_q}}$. From (4.76), difference type instabilities do not occur because $\mathrm{Re}(\lambda) = 0$ for them.

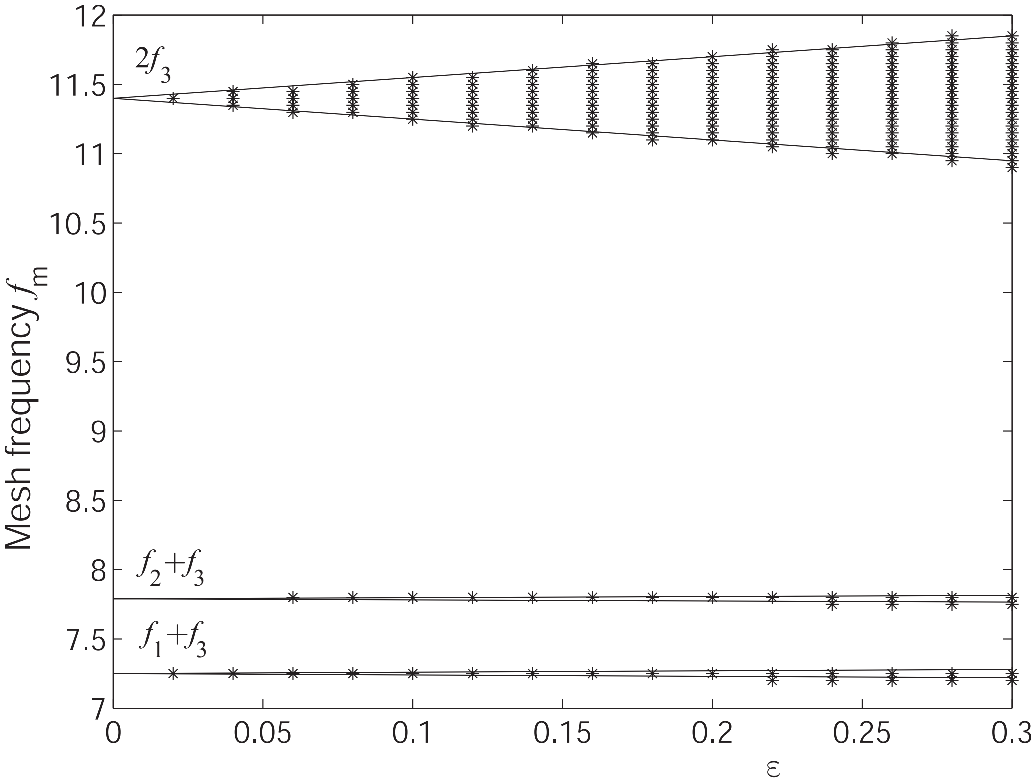

Figure 5.5: Instability boundaries for changing ε and $\mu = 0$, $\alpha = 0.6$, $\beta = 0$, $c = 1.5$, $\zeta = 0$, $\gamma = 0.28$ (*: recursive process; ___: perturbation).

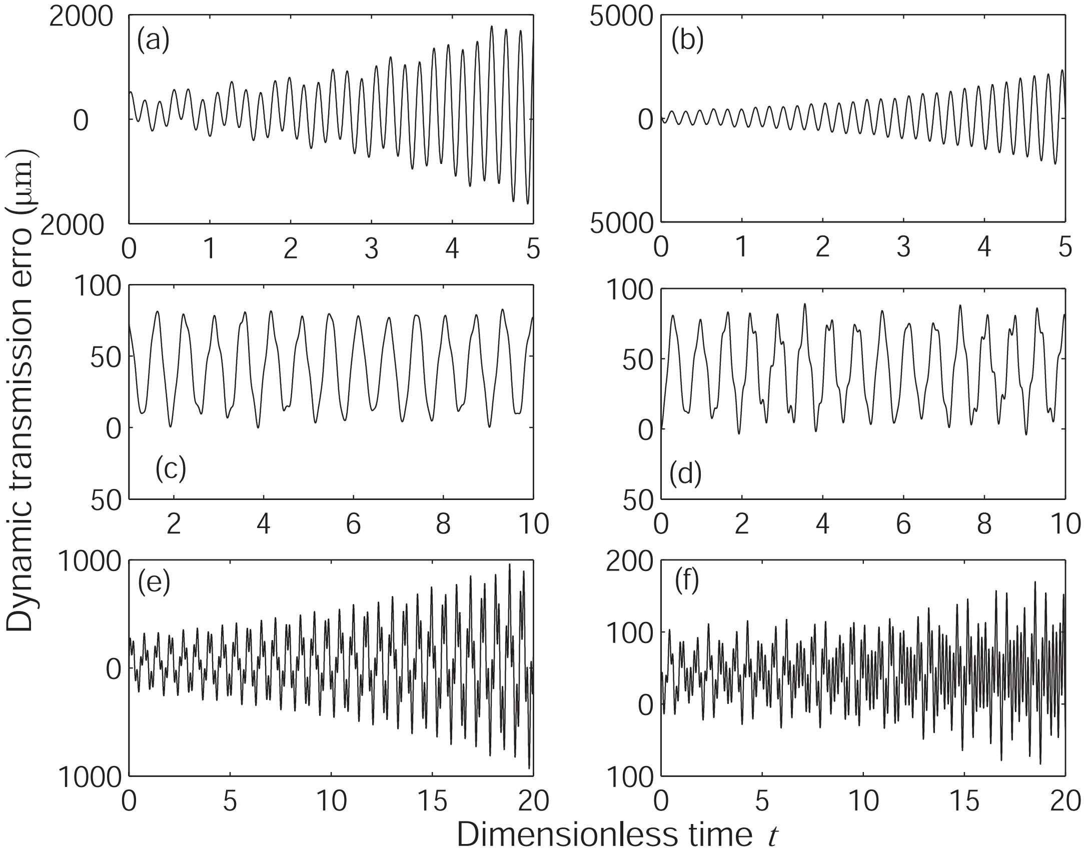

Figure 5.6: Dynamic response for mesh frequencies near the instability boundaries for $\varepsilon = 0.1$ and other parameters as in Figure 5.5; (a) $f_m = 11.2$; (b) $f_m = 11.6$; (c) $f_m = 11.1$; (d) $f_m = 11.7$; (e) $f_m = 7.25$; (f) $f_m = 7.79$.

The primary ($s = 1$) instability intervals for single-mode and sum type instabilities are shown in Figure 5.5 for perturbation analysis and the recursive process. These methods agree well even up to $\varepsilon = 0.3$. The largest parametric instability region occurs when mesh frequency is in the boundary of $\Omega = 2\omega_3 \pm \varepsilon \left| E_{33}\Theta_1 \right| / \omega_3$ because of the maximum mesh strain energy in mode 3, i.e., E_{33} is large. The two-mode instabilities $p = 1,\ q = 3$ and $p = 2,\ q = 3$ have much smaller instability regions because $\left| E_{13} \right| \ll \left| E_{33} \right|$ and $\left| E_{23} \right| \ll \left| E_{33} \right|$. With fixed $\varepsilon = 0.1$, the instability interval for primary single-mode instability is from f_m =11.2 to f_m =11.6, where $f_m = \Omega / 2\pi$. Figure 5.6 shows linear dynamic responses excited by six mesh frequencies near the instability interval obtained by numerical integration. The amplitudes increase exponentially for f_m = 11.2 and $f_m = 11.6$ in Figure 5.6a and Figure 5.6b. On the other hand, Figure 5.6c and Figure 5.6d show stable amplitudes for $f_m = 11.1$ and $f_m = 11.7$. The unstable responses at f_m=7.25 and f_m =7.79 for sum type instabilities are shown in Figure 5.6e and Figure 5.6f, respectively. Therefore, the instability boundary predictions by the recursive process and perturbation approximation agree well with numerical simulation.

5.5.2Effect of Tooth Friction on Parametric Instab

With friction and damping, the real parts of λ in (4.75) and (4.76) is derived as

$$\begin{aligned}
&\mathrm{Re}(\lambda) = \frac{1}{2}\left\{ -\varsigma\left(\omega_p + \omega_q\right) \pm \frac{\sqrt{2}}{2}\left[\left(A^2 + B^2\right)^{\frac{1}{2}} + A\right]^{\frac{1}{2}} \right\} \\
&A = \begin{cases} \varsigma^2(\omega_p - \omega_q)^2 - \sigma^2 + \Psi_R & \text{for } s\Omega = \omega_p + \omega_q + \varepsilon\sigma \\ \varsigma^2(\omega_p - \omega_q)^2 - \sigma^2 - \Psi_R & \text{for } s\Omega = \omega_p - \omega_q + \varepsilon\sigma \end{cases} \\
&B = \begin{cases} 2\varsigma\sigma(\omega_p - \omega_q) + \Psi_I & \text{for } s\Omega = \omega_p + \omega_q + \varepsilon\sigma \\ 2\varsigma\sigma(\omega_p - \omega_q) - \Psi_I & \text{for } s\Omega = \omega_p - \omega_q + \varepsilon\sigma \end{cases}
\end{aligned} \tag{4.81}$$

The stability boundaries ($\mathrm{Re}(\lambda) = 0$) are determined as $\left(A^2 + B^2\right)^{\frac{1}{2}} + A = 2\varsigma^2\left(\omega_p + \omega_q\right)^2$.

Manipulating this yields the boundaries of combination instability with friction as

$$
\begin{aligned}
s\Omega &= \omega_p + \omega_q + \frac{1}{8\zeta\omega_p\omega_q}\left[\left(\omega_p - \omega_q\right)\Psi_I \pm \left(\omega_p + \omega_q\right)\sqrt{\Psi_I^2 + 16\zeta^2\omega_p\omega_q(\Psi_R - 4\zeta^2\omega_p\omega_q)}\right] \\
s\Omega &= \omega_p - \omega_q + \frac{1}{8\zeta\omega_p\omega_q}\left[\left(\omega_q - \omega_p\right)\Psi_I \pm \left(\omega_p + \omega_q\right)\sqrt{\Psi_I^2 - 16\zeta^2\omega_p\omega_q(\Psi_R + 4\zeta^2\omega_p\omega_q)}\right] \\
\Psi_R &= \mathrm{Re}(\Psi) = \frac{1}{\omega_p\omega_q}\left[\varepsilon^2 E_{pq}^2\left|\Theta_s\right|^2 + \mu^2 D_{pq}D_{qp}\left|\Lambda_s\right|^2 + \mu\varepsilon E_{pq}(D_{pq} + D_{qp})\mathrm{Re}(\Lambda_s\bar{\Theta}_s)\right] \\
\Psi_I &= \mathrm{Im}(\Psi) = \frac{\mu\varepsilon}{\omega_p\omega_q}E_{pq}(D_{pq} - D_{qp})\mathrm{Im}(\Lambda_s\bar{\Theta}_s)
\end{aligned}
\tag{4.82}
$$

where $\omega_p > \omega_q$ and $\bar{\Theta}_s$ is the complex conjugate of Θ_s.

The effects of mesh stiffness variations and friction bending effect are incorporated in $\varepsilon\left|\Theta_s\right|$. The effects of friction moments are included in $\mu\left|\Lambda_s\right|$. The difference type instabilities, which are absent for $\mu = 0$, arise when $\mu \neq 0$. Each instability region occurs as a backbone (e.g., $\dfrac{\left(\omega_p - \omega_q\right)\Psi_I}{8\zeta\omega_p\omega_q}$ for sum type instability) and a symmetric deviation (the terms after $\pm$ in (4.82)). The backbones are linear functions of μ and ε whose slopes are determined by modal properties, mesh stiffness variations, and sliding friction. For the same two modes and the same s, the backbone slopes for the sum and difference type instabilities have equal magnitude and opposite sign. The backbone slopes for the sum type are negative; they are positive for the difference type. The deviations can be approximated as linear functions of μ and ε with Taylor expansion of the square roots.

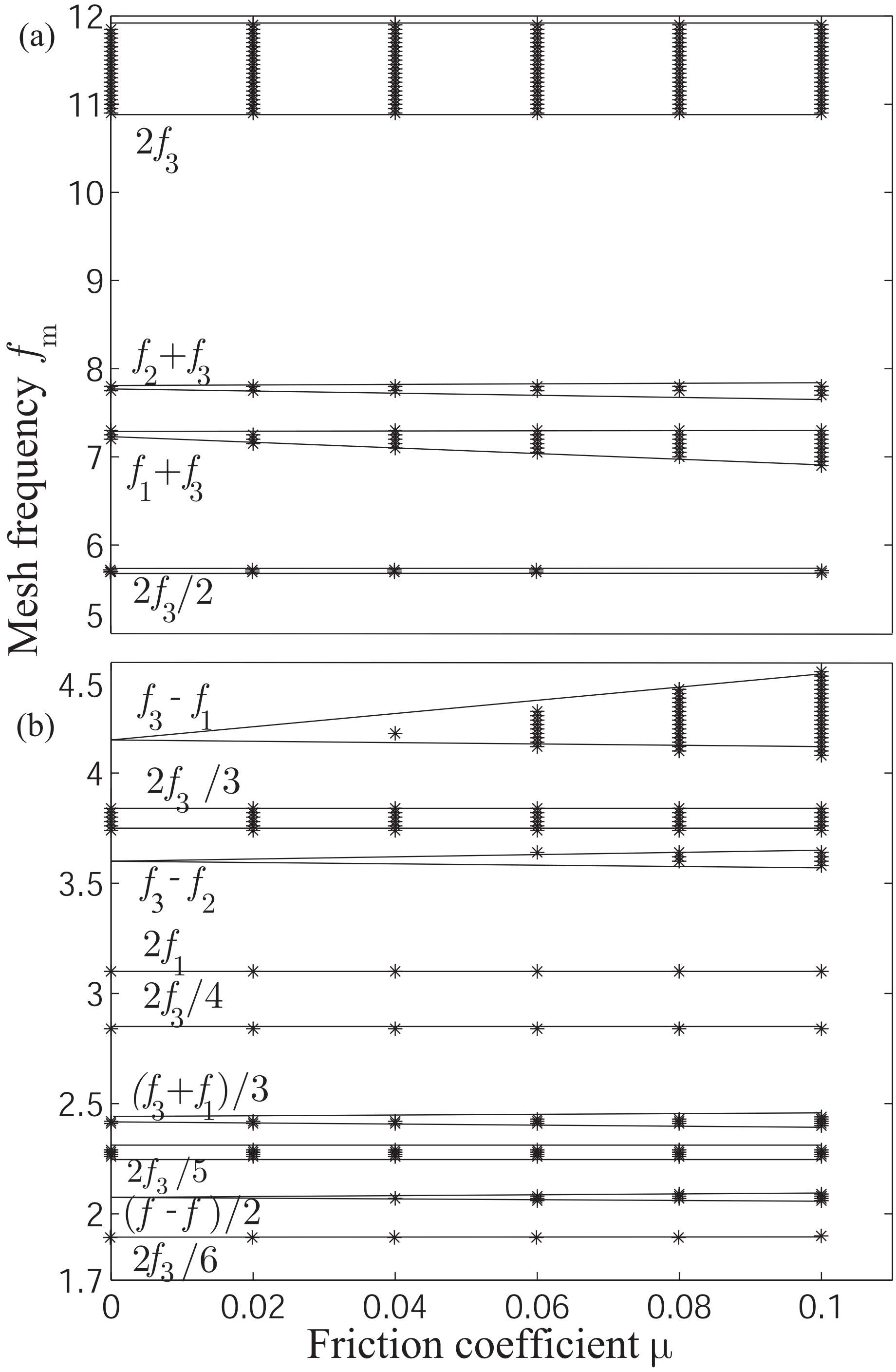

Figure 5.7: Instability boundaries for changing μ and $\alpha = 0.6$, $\beta = 0$, $\varepsilon = 0.3$, $c = 1.5$, $\zeta = 0.001$, $\gamma = 0.28$ (*: recursive process; ___: perturbation); (a) f_m from 1.7 to 4.5; (b) f_m from 5 to 12.

Figure 5.7 shows the instability boundaries varying with μ while the friction bending $\beta = 0$. Mesh frequency f_m varies from 1.7 to 12 covering most combination and single-mode instabilities. The perturbation solutions agree well with numerical solutions. For a combination instability to occur, the corresponding quantity inside the square root of (4.82) (call it Δ) must be positive. This quantity Δ, which also governs the width of the instability region, depends on strength of parametric excitation, friction, modal mesh strain energy (as captured by E_{pq} and D_{pq}), natural frequency, and damping. For fixed system parameters, the modal mesh strain energy dictates existence and width of a possible instability. For instance, sum type instability for modes 1, 2 does not occur because $\Delta = -1.6 \times 10^{-5} < 0$. Sum type instabilities involving modes 1, 3 and modes 2, 3 are present because $\Delta = 0.0014$ and $\Delta = 0.0009$, respectively, a result of the larger modal mesh strain energy in mode 3. The instability intervals for modes 1, 3 are larger than for modes 2, 3 for the same type of instability (sum or difference) because mode 1 has stronger mesh strain energy than mode 2. Note that in the absence of damping $\Delta > 0$ and instability always occurs. In essence, there is a critical mesh strain energy required to overcome the damping and create instability.

The sum type instability intervals (i.e., deviations) are larger than the difference type for the same two modes, as proved in Appendix B. The sum type instability occurs even when $\mu = 0$ and is more sensitive to μ and ε than the difference type. The widths of the two-mode instability boundaries (sum and difference types) increase almost linearly with μ.

For single-mode instabilities ($p = q$), $\Psi_I = 0$ and the instability boundaries simplify to

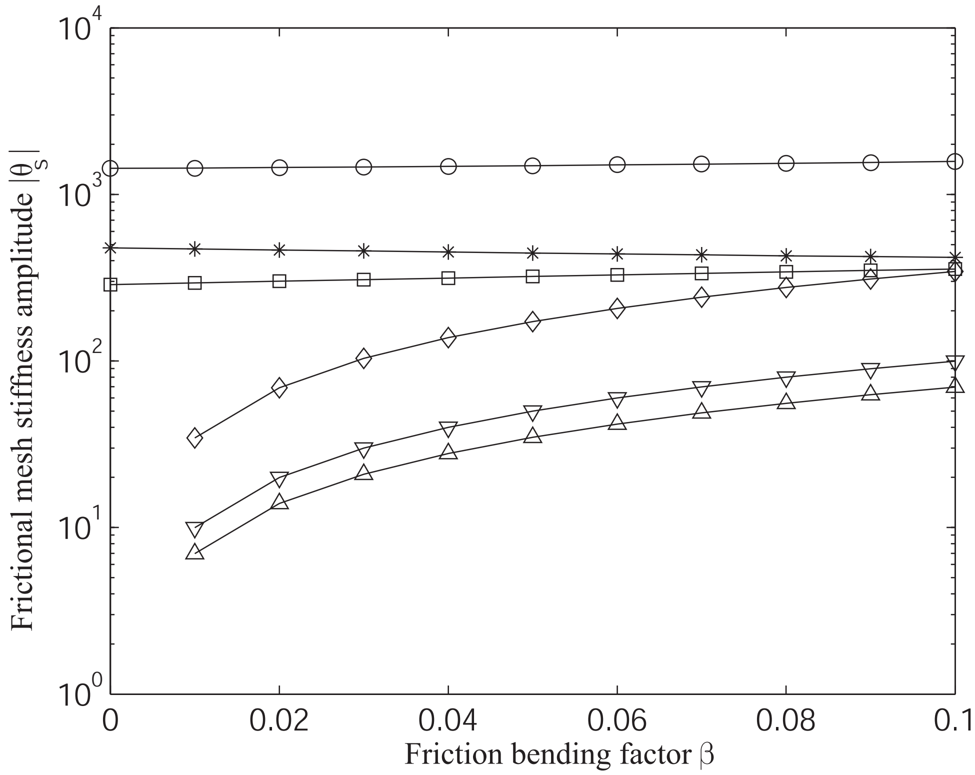

Figure 5.8: Effect of friction bending ratio β on mesh stiffness Fourier harmonics Θ_s for $\alpha = 0.6$, $\varepsilon = 0.3$, $c = 1.5$, $\gamma = 0.28$ (○: $s = 1$, ◊ : $s = 2$, * : $s = 3$, Δ : $s = 4$, □: $s = 5$, ∇ : $s = 6$).

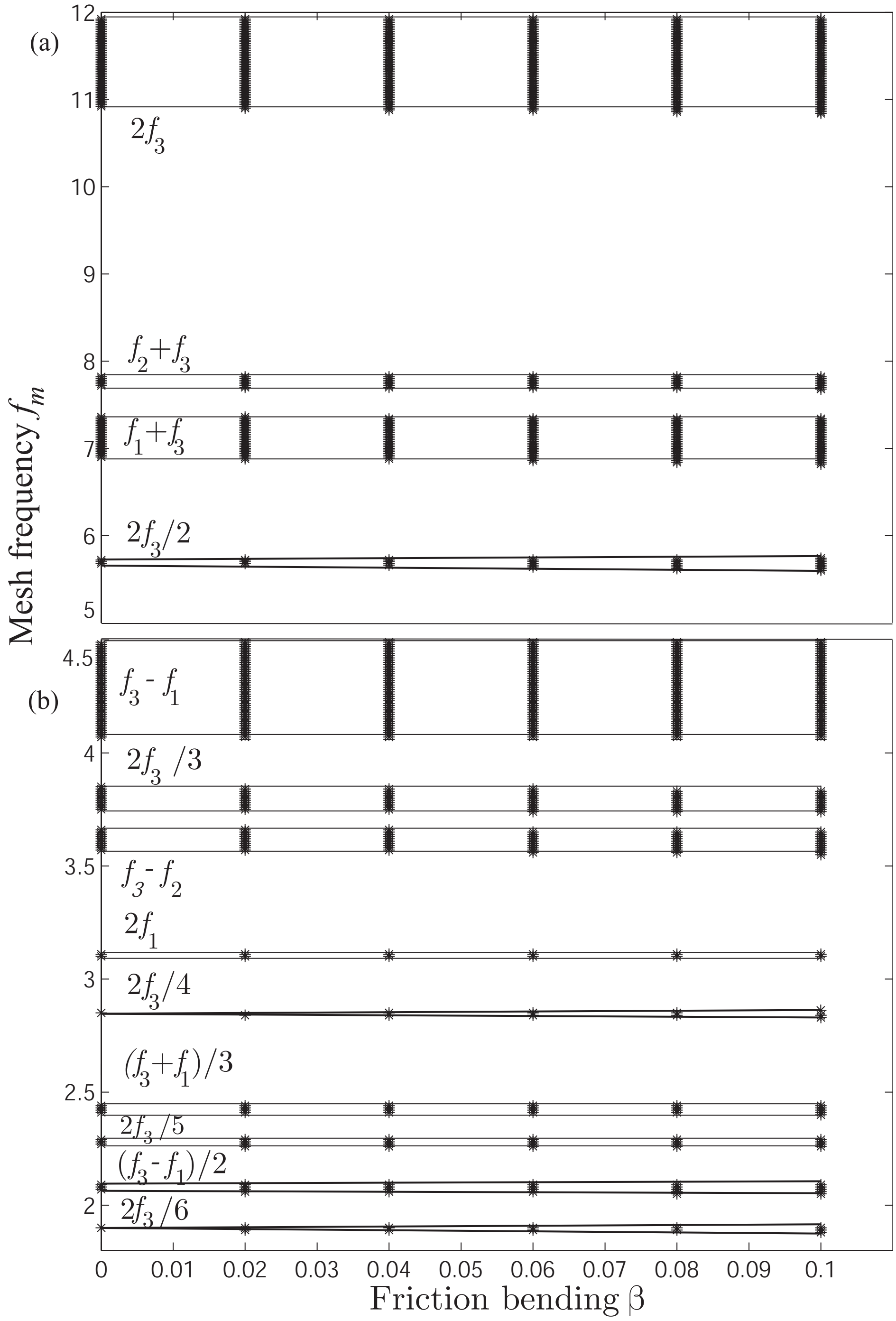

Figure 5.9: Instability boundaries for changing β and $\alpha = 0.6$, $\mu = 0.1$, $c = 1.5$, $\varepsilon = 0.3$, $\zeta = 0.001$, $\gamma = 0.28$ (*: recursive process; ___: perturbation); (a) f_m from 1.7 to 4.5; (b) f_m from 5 to 12.

$$s\Omega = 2\omega_p \pm \sqrt{\left|\varepsilon E_{pp}\Theta_s + \mu D_{pp}\Lambda_s\right|^2 / \omega_p^2 - 4\zeta^2\omega_p^2} \qquad (4.83)$$

The backbones vanish, in contrast to the two-mode instabilities. The instability intervals depend on $\varepsilon\Theta_s$ (mesh stiffness variation and friction bending) and $\mu\Lambda_s$ (friction moments). In practice, $\varepsilon > \mu$, $E_{pp} > D_{pp}$, and $|\Theta_s| > |\Lambda_s|$ due to the moment arm of friction l_i being less than the base radius. Thus, $|\varepsilon E_{pp}\Theta_s| \gg |\mu D_{pp}\Lambda_s|$ and the single-mode instabilities are sensitive to the friction bending effect and mesh stiffness variations while less sensitive to friction moments as evident in Figure 5.7. Because $|E_{33}| \gg |E_{11}| > |E_{22}|$, primary instabilities of modes 1 and 3 emerge in Figure 5.7, and the interval of mode 3 is much larger than that of mode 1. Higher order instabilities ($s = 1, 2, \cdots, 6$) also exist for mode 3. The intervals for odd order ($s = 1, 3, 5$) are larger than for even order ($s = 2, 4, 6$) because, for rectangular wave mesh stiffness, odd harmonics have higher magnitudes than even harmonics (Figure 5.8).

5.5.3 Effect of Friction Bending on Parametric Instability

The effects of friction bending ratio β on the mesh stiffness harmonics Θ_s are shown in Figure 5.8. Given $\varepsilon = 0.3$, $c = 1.5$, $\alpha = 0.6$ and $\gamma = 0.26$, the odd order harmonics are not sensitive to β while the even order harmonics are. As a result, the instability intervals with odd s are insensitive to β while those with even s are sensitive to β. As illustrated in Figure 5.9, the intervals with $s = 1, 3, 5$ are almost independent of β. The instabilities with $s = 2, 4, 6$, such as, $sf_m \approx 2f_3$ ($s = 2, 4, 6$) and $sf_m \approx f_3 - f_1$ ($s = 2$), however, change with β. The single-mode instabilities for $p = q = 3$ exist even for $s = 2, 4, 6$ because the third mode has the maximum mesh strain energy even though the $|\Theta_{2,4,6}|$ are much smaller than $|\Theta_1|$. For $p = q = 3$, the single-mode instability intervals with $s = 2, 4, 6$ are increased by the bending ratio β, while the intervals for $s = 4, 6$ are much smaller than for $s = 2$ (note different scales in two graphs) because $|\Theta_4| < |\Theta_6| < |\Theta_2|$ in Figure 5.8.

5.5.4 Effect of Contact Ratio on Parametric Instability

The contact ratio c affects both Λ_s and Θ_s (i.e., the harmonics of parametric excitation included in Ψ of (4.82)), so the impact of contact ratio on instability boundaries changes with tooth friction. Figure 5.10 shows the effect of contact ratio on single-mode and two-mode sum type instabilities with tooth friction and bending effect. The sum type instability boundaries without tooth friction are

$$\Omega = \omega_p + \omega_q \pm \frac{(\omega_p + \omega_q)}{2\omega_p \omega_q} \sqrt{\varepsilon^2 \left| E_{pq} \tilde{\Theta}_s \right|^2 - 4\zeta^2 \omega_p^2 \omega_q^2} \tag{4.84}$$

where the harmonics of frictionless mesh stiffness are

$$\tilde{\Theta}_s = \frac{\bar{k}}{s\pi} \sin s\pi(c-1) \left[\cos s\pi(c-1+2\gamma) + i \sin s\pi(c-1+2\gamma) \right] \tag{4.85}$$

Without tooth friction, the instability boundaries for varying contact ratio have sinusoidal profiles symmetric about $c = 1.5$ as $\left|\tilde{\Theta}_s\right| = \bar{k} \left| \sin s\pi(c-1) \right| / (s\pi)$, and the number of waves for each profile depends on s.

The instability boundaries with friction shown in Figure 5.10 are calculated by the perturbation and numerical recursive methods. The boundaries do not have sinusoidal profiles. The two-mode instabilities are determined by the complicated functions of Ψ_R and Ψ_I in (4.82) that are affected by the contact ratio c, friction moment μ, and friction bending β. The boundaries of two-mode instabilities are sensitive to μ, and the boundaries of single-mode instabilities for even s are sensitive to β. The sum type instability boundaries shown in Figure 5.10 are no longer symmetric about $c = 1.5$. The contact ratio having maximum boundary width is shifted to lower c due to tooth friction. The instability intervals with tooth friction are greater than those without friction because of the increased excitation. The secondary instability ($s = 2$) at f_3 occurs even for $c = 1$ due to the sensitivity to friction bending. The influence of contact ratio on the primary instability at $2f_3$ is minimal because that instability is insensitive to friction moment and bending effect as shown previously. The profile of the primary instability in Figure 5.10 is almost a symmetric sinusoidal profile even with friction.

Note that $c - 1 + \gamma \leq 1$ is required according to Figure 5.2. The analytical and numerical results for $c \geq 2 - \gamma = 1.85$ with the selected $\gamma = 0.15$ have no physical meaning.

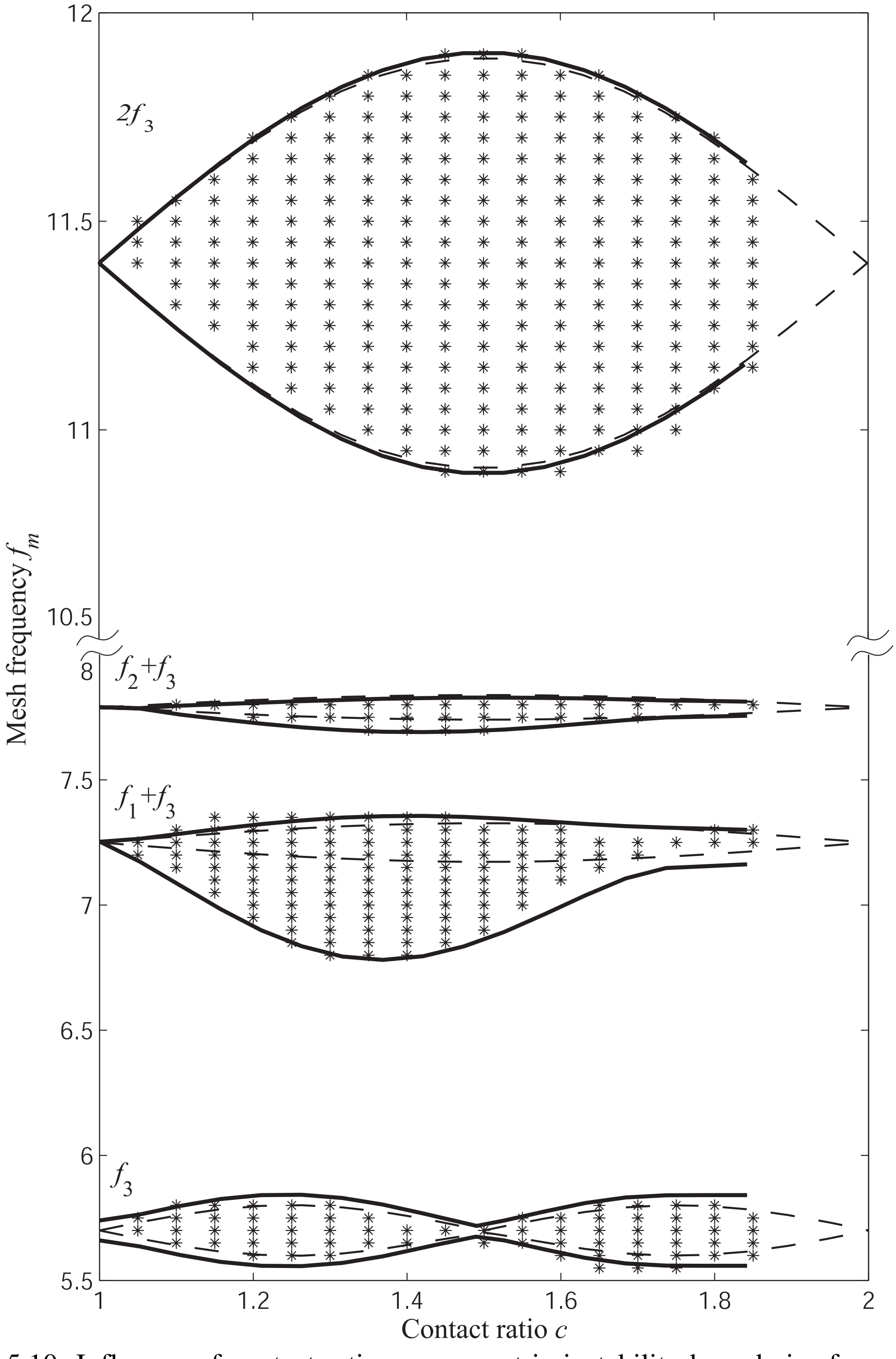

Figure 5.10: Influence of contact ratio on parametric instability boundaries for $\alpha = 0.6$, $\mu = 0.1$, $\beta = 0.05$, $\varepsilon = 0.3$, $\zeta = 0.001$, $\gamma = 0.05$ (- - - perturbation $\mu = 0$; —— perturbation $\mu = 0.1$; * numerical $\mu = 0.1$).

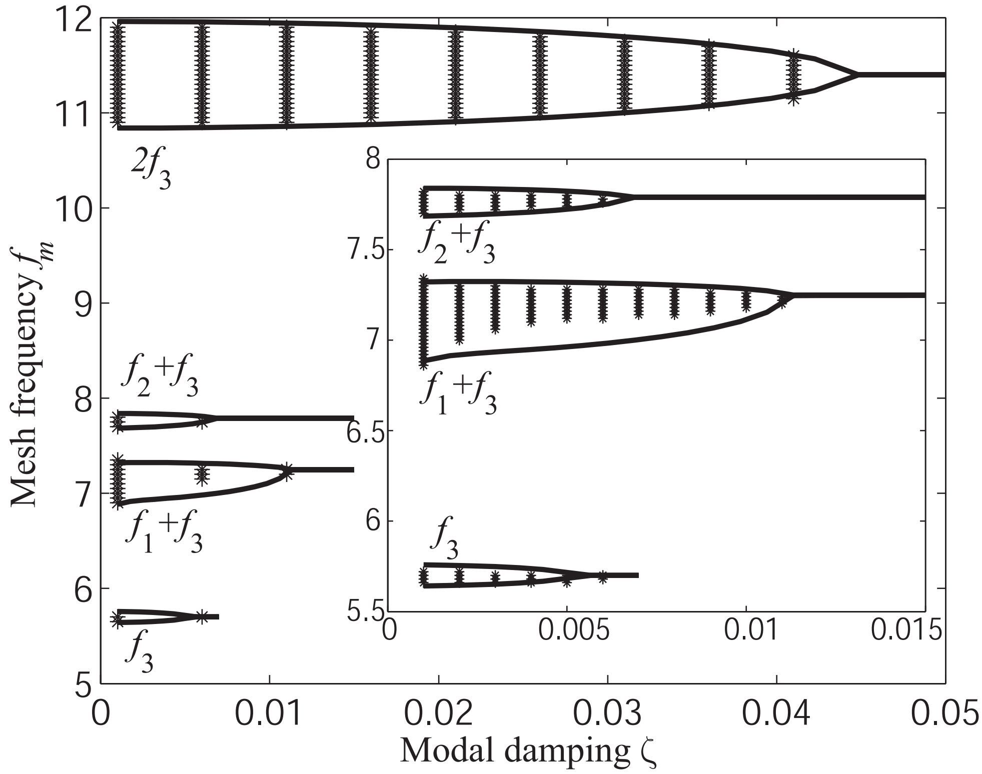

Figure 5.11: Impact of modal damping on instability boundaries for $\alpha = 0.6$, $\mu = 0.1$, $\beta = 0.05$, $\gamma = 0.28$, $c = 1.5$, $\varepsilon = 0.3$ (—— perturbation; * numerical method).

5.5.5 Effect of Modal Damping on Parametric Instability

From (4.82) and (4.83), the instability boundaries decrease with an increase in modal damping. Different types of instabilities have different critical damping where the unstable interval vanishes. Figure 5.11 shows the influence of damping on single-mode and two-mode combination instabilities. The perturbation and numerical solutions agree well. The primary single-mode instability has the biggest critical damping due to the strongest mesh strain energy in mode 3. The other instabilities decrease more rapidly than for the primary single-mode. The $f_1 + f_3$ combination instability has greater critical modal damping compared to the $f_2 + f_3$ combination due to the higher mesh strain energy of mode 1 than mode 2. The critical modal damping depends on tooth friction, mesh stiffness variation, and contact ratio.

5.5.6Influence of Tooth Friction on Dynamic Response

The parameters of two practical gears listed in Table 5.1 are used to generate finite element gear models. For comparison purposes, the realistic mesh stiffness variations over a mesh cycle calculated from the finite element model are used as the frictionless mesh stiffness in the analytical model. The mesh parameters are $\bar{k}$ =2.98e8 *N/m*, $T_1 = 100$ *N-m*, $\mu = 0.1$, $c = 1.4$, and $\zeta = 0.02$. The friction bending effect is inherently included in the finite element analysis. The bending factor β used in the analytical model is estimated from (4) where the deflection and load are calculated from FE static analysis.

The parametric instabilities for two-mode and single-mode combinations result in exponentially growing dynamic response, which eventually triggers nonlinear contact loss. The nonlinearity suppresses the growth of the amplitude and usually yields a steady periodic response. To study the sensitivity of nonlinear response on tooth friction and validate the proposed analytical model, numerical simulations of the nonlinear analytical model in (4.44) and the finite element model are compared in Figure 5.12a. Figure 5.12b shows the spectral details. Decreasing speed sweep analyses are conducted to cover the frequency range that includes the fundamental resonance of rotational mode 1 at $f_1 = 1835$ *Hz* and higher harmonic resonances of rotational mode 3 at $f_3 = 6924$ *Hz*. The RMS values of the dynamic transmission error u are calculated by

$$\left[\frac{1}{nT}\int_0^{nT}\left(u-\bar{u}\right)^2 dt\right]^{1/2} \tag{4.86}$$

where $\bar{u}$ is the mean value of u. The analytical models with and without friction bending effect agree well with the finite element model in Figure 5.12a for the resonances at 1731 Hz and 1835 Hz where the fourth harmonic excites mode 3 (Figure 5.12b) and the first harmonic excites mode 1, respectively. Tooth friction has negligible effect on these two single-mode resonances and in the off-resonant frequency ranges.

The finite element results reveal that tooth friction significantly excites the resonance at 2308 Hz where the third harmonic ($s=3$) excites mode 3 as shown in Figure 5.12b. The analytical model with friction bending effect shows a similar strong influence of tooth friction on this resonance. The analytical result for $\mu=0.1$ and $\beta=0$, which ignores the friction bending effect, cannot capture the strong impact of tooth friction on this resonance. This implies that the friction bending effect plays a key role in exciting this higher harmonic resonance. These findings confirm the conclusions from the stability analysis.

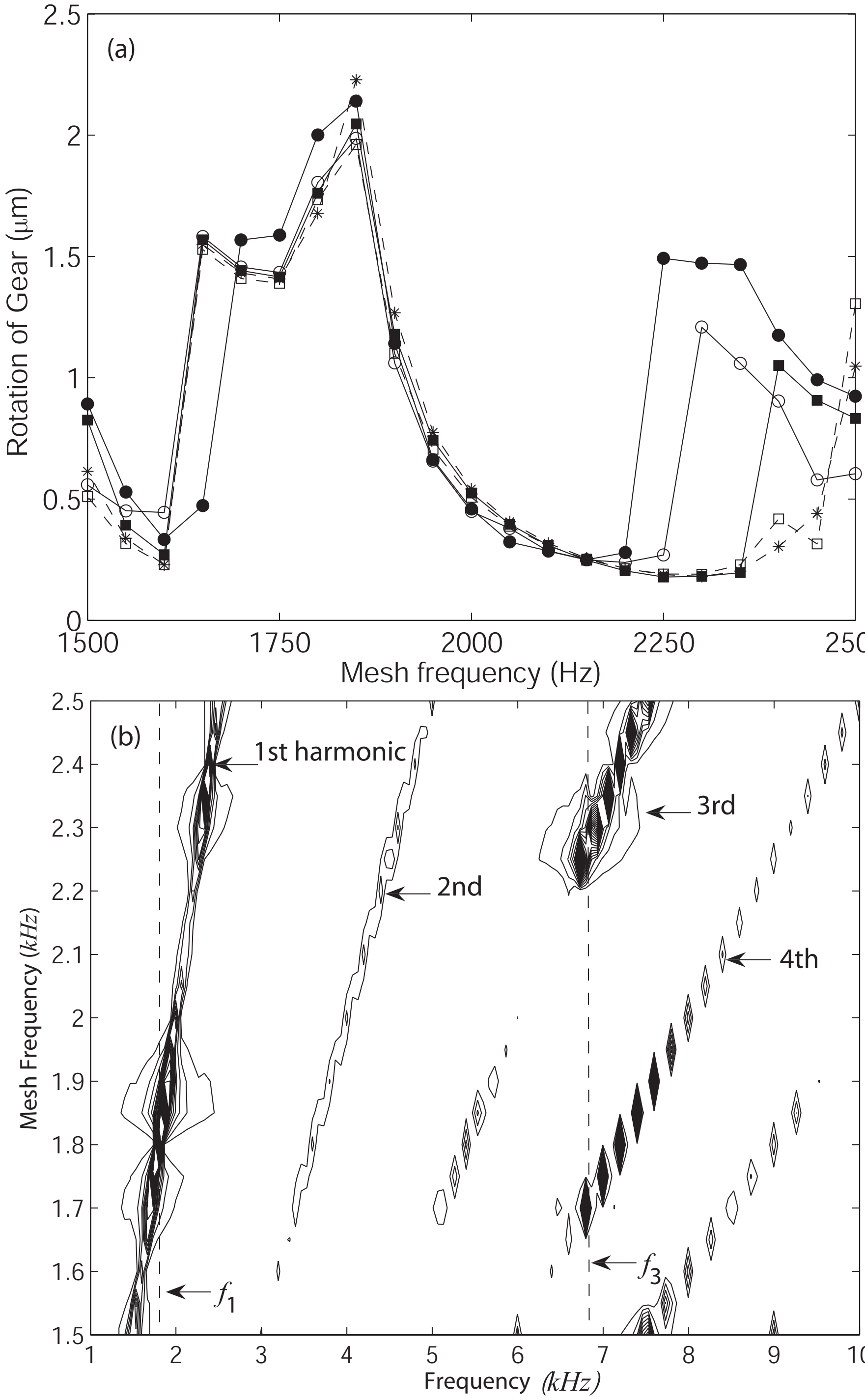

Figure 5.12: Speed sweep analysis for $\alpha = 0.6$, $\gamma = 0.28$, $c = 1.4$, $\varepsilon = 0.28$, $\zeta = 0.02$; (a) RMS comparisons (■: FE $\mu = 0$; □: analytical $\mu = 0$; ●: FE $\mu = 0.1$; ○: analytical $\mu = 0.1$, $\beta = 0.05$; *: analytical $\mu = 0.1$, $\beta = 0$); (b) FE Campbell diagram $\mu = 0.1$.

CHAPTER 6

SUMMARY AND FUTURE WORK

6.1 Summary

This work investigates, via analytical and numerical methods, nonlinear, parametrically excited dynamics for multi-mesh gear systems. The main results are summarized for each specific topic.

6.1.1 Dynamic Modeling and Analysis of Tooth Profile Modification for Multi-Mesh Gear

An analytical model of a multi-mesh spur gear train has been developed to study nonlinear gear dynamics due to time-varying mesh stiffness, profile modification, and contact loss. Dynamic response predictions of the proposed model are compared against two existing models and a FE benchmark across a range of frequencies. The main conclusions are:

1) The proposed model (Model-1) best agrees with the FE benchmark for dynamic predictions regardless of different loads, profile modifications, and bearings. The other models give poor predictions near gear speeds where a harmonic of mesh frequency drives resonance and resonances with the occurrence of contact loss.

2) The most important difference between Model-1 and the other two models are that Model-1 uses a dynamic contact analysis that admits contact loss between individual gear teeth when multiple tooth pairs are normally in contact (partial contact loss). Additionally, Model-1 includes the practical parametric excitation from changing mesh stiffnesses.

3) Optimized profile modification counteracts the mesh stiffness parametric resonance near fundamental frequency resonance ($\omega \approx \omega_m$), leading to linear response with low amplitude instead of the theoretically unbounded response and associated contact loss of parametric resonance without profile modification. Profile modification does not affect the parametric instability boundary for $\omega \approx 2\omega_m$, although it would affect the resulting nonlinear response.

4) Perturbation analysis of the linear time-varying model shows that profile modification for minimal STE depends only on the load and mesh stiffness of the single mesh. The optimal profile modification for minimal DTE is determined by mesh stiffness variations, contact ratios, mesh phasing, and the vibration modes. The profile modification for minimal STE does not necessarily lead to minimum DTE. Analytical and numerical results demonstrate that interactions between the

two meshes (through mesh phase and contact ratios, as two examples) must be considered in optimizing modifications for minimum DTE.

5) Mesh interaction studies on optimal profile modification for minimizing DTE shows: The mean and the first harmonic excitations of mesh stiffnesses and profile modifications of the two meshes are critical to the response amplitude; The DTE amplitudes as a function of two profile modification magnitudes form elliptical contours about the optimal profile modification; Mesh phasing affects the orientation and length of the elliptical axes and therefore the sensitivity of response to modifications that deviate from optimal; The contact ratios and modification lengths of the two meshes and the mesh phase interact with each other to affect dynamic response.

6.1.2 Nonlinear Dynamics of Idler Gear Systems

Parametric resonances and strong nonlinearity of idler gearsets are studied by perturbation analysis, and closed-form solutions for the frequency responses are given. The perturbation solutions are validated by numerical integration and harmonic balance method at fundamental, subharmonic and second-harmonic resonances. The maximum amplitudes and transition frequencies (onset of contact loss) are given as simple analytical expressions in terms of the harmonics of the mesh stiffnesses, mesh phase, contact ratios, modal damping and the vibration modes. The interactions among these parameters are important and unique to multi-mesh systems. The analytical solutions in terms of fundamental design quantities provide guidance to optimize these parameters for the reduction of vibration and noise. Main points include:

1) Parametric excitations from different meshes can cancel or add depending on the mesh phase. Mesh phase applies different effects (reduction or increase) on the same type of resonance for different modes, or on different types of resonance for the same mode. As an exception, the impact of mesh phase on the subharmonic resonance is independent of the mode.

2) Contact ratio not only interacts with mesh phase but affects the stiffness harmonics. Particular combinations of contact ratios can sharply reduce certain resonant amplitudes but increase other resonant amplitudes. High contact ratios are not always preferable in multi-mesh system because of the interaction between modes and mesh phase.

3) Dual-sided jump phenomenon and a wide range of resonant frequency occur at subharmonic resonances. The perturbation solution predicts the instability interval, indicating the existence of the subharmonic resonance and qualitatively showing the peak amplitude. The instability interval is highly sensitive to system parameters compared to other resonances.

4) The multiple meshes usually exhibit contact loss at different stages. The mesh contact losses can be either in-phase or out-phase depending on the vibration modes; which of these occurs determined analytically.

5) The second-harmonic excitation typically dominates when the mesh frequency is half of a natural frequency. Super-harmonic response dominates when the second-harmonic excitation of mesh stiffness is minimized.

6) The external torque does not qualitatively change the nonlinear behavior of the resonances. The amplitude of the response increases linearly with torque. Contact loss is not suppressed by high torque.

6.1.3 Nonlinear Dynamics of Counter-Shaft Gear Systems

Asymptotic solutions for frequency response of counter-shaft gear systems are found by perturbation method. The perturbation solutions are compared against numerical integration and semi-analytical harmonic balance method at fundamental, subharmonic and second harmonic resonances with varied system parameters. Some useful findings are

1) The perturbation solutions agree well with numerical results for nonlinear resonances except for subharmonic resonance peak. The analytical closed-form expressions capture nonlinear characteristics (peak amplitude, contact loss initiation, softening, and stability) and connect physical parameters to these features.

2) The interaction between two mesh stiffness excitations highly depends on the ratio of two mesh frequencies. No mesh interaction occurs when the ratio is not an integer or a reciprocal of an integer. Otherwise, mesh interaction is bound to happen, and how mesh interacts depends on the ratio, vibration modes, contact ratio, mesh stiffness variations, and mesh phasing.

3) Without mesh interaction, resonance peak amplitude linearly depends on the mesh stiffness variation, and is a function similar to sinusoidal form of the contact ratio. With mesh interaction, peak amplitude bilinearly depends on the two mesh stiffness variations, and is a function similar to sinusoidal forms for the two contact ratios.

Mesh phasing can change constructive/destructive action between the two mesh excitations.

4) For subharmonic resonance, the instability interval width is well correlated with the peak amplitude. The linear period-2 solution can be two branches orthogonal to frequency axis or two branches with finite slopes depending on how two meshes interact. Unlike fundamental resonance, the impact of mesh phasing is independent of the sign of the mode elements for subharmonic resonance.

6.1.4 Impact of Tooth Friction and Its Bending Effect on Gear Dynamics

A translational-rotational model with parametric excitations from variable mesh stiffness, tooth sliding friction moments, and a heretofore unexamined friction bending effect is established for a single-mesh gear pair. A numerical recursive method based on Floquet theory and a perturbation analysis examine the associated parametric instabilities and show strong agreement. The analytical expressions for instability boundaries reveal how key parameters impact the instabilities. The nonlinear responses from the analytical model and a FE benchmark also agree even when contact loss occurs.

1) Combination instabilities between a rotation mode and a translation mode or two translation modes cannot occur. Sum type and single mode instabilities can occur for both frictional and frictionless conditions. Difference type instabilities occur only when friction is present.

2) Two-mode combination instabilities are sensitive to the friction moment and bending effect. Single-mode instabilities are insensitive to the friction moment but

sensitive to the friction bending effect. The instability interval widths depend nearly linearly on mesh stiffness variations.

3) For the same type of instabilities, the instability intervals for different modes depend on the total mesh strain energy of the mode or the modes in combination. The mesh strain energy needs to be over a critical value to cause the instability. The sum type instability intervals are larger than for the difference type.

4) The effects of contact ratio on the instability intervals of two-mode combination and single-mode instabilities are altered significantly by the friction moments and the friction bending effect, respectively. The tooth friction destroys symmetry of the instability boundaries for varying contact ratio. The friction bending can cause instability even for integer contact ratios.

5) The proposed analytical model agrees with a FE benchmark for nonlinear response due to parametric instabilities, while the model without considering friction bending fails to predict the strong influence of tooth friction on certain parametric instabilities. The nonlinear dynamic analyses confirm that the friction bending effect can significantly alter the vibration.

6.2 Future Work

This study has been focusing on dynamic modeling and nonlinear dynamics analysis on mesh stiffness variations, and their interactions with profile modifications and tooth sliding frictions. On one hand, the study identifies some interesting problems that need further investigation, such as the aperiodic response in Figure 3.10 and nonlinear loop-like solution branch. On the other hand, this study builds solid foundation for expanding the model with new important features such as interactions between profile modifications and tooth sliding frictions, bearing nonlinearity, gyroscopic effects, and combination instability response excluded in the study.

6.2.1 Interactions between profile modifications and tooth frictions

Profile modifications are introduced to compensate mesh stiffness variations and reduce DTE for desired torques. Conversely, tooth sliding frictions might cause parametric instabilities that increase transmission errors as well as translations. In other words, there are interactions between dynamic effects of profile modifications and tooth frictions. It is found that profile tip relieves influence power losses due to tooth frictions because they modify normal loads and, consequently, the friction forces in the engagement and recess zones where sliding velocities are most important [106]. The effect of the profile modification on the dynamic transmission error has been analytically examined under the influence of frictional effects in [107]. The tip relief introduces an amplification in the off-line-of-action motions and forces due to an out of phase relationship between the normal load and friction forces. Three main questions remain open, and they are: How much can tooth frictions change the design of optimal profile modifications for maximum reduction of DTE? How do tooth frictions change profile modification designs? How to use profile modification to reduce dynamic responses induced by tooth friction instabilities?

Analytical models for profile modifications and tooth frictions, respectively, are established in this work. Combining these models, a new model including both effects is

$$\mathbf{M}\ddot{\mathbf{U}} + \mathbf{C}\dot{\mathbf{U}} + \left[\mathbf{K_b} + \mathbf{K_m}(\omega t, \mathbf{U}) + \mathbf{L}(\omega t, \mathbf{U}, \dot{\mathbf{U}})\right]\mathbf{U} - \mathbf{E}(\omega t, \mathbf{U}, \dot{\mathbf{U}}) = \mathbf{F_T} \tag{6.1}$$

where $\mathbf{K_b}$ the constant bearing stiffness matrix; $\mathbf{K_m}$ includes mesh stiffness variations and contact loss; $\mathbf{L}$ includes tooth sliding frictions; $\mathbf{E}$ includes profile modifications and tooth frictions; $\mathbf{U}$ comprises three degree-of-freedom (rotation about center axis and in-plane translations) for each gear body. An example for a gear pair in Figure 5.1 is

$$\mathbf{M} = diag\left(\left[J_1 / r_1^2, m_1, m_1, J_2 / r_2^2, m_2, m_2\right]\right)$$

$$\mathbf{X} = \left[u_1, x_1, y_1, u_2, x_2, y_2\right]^T, \quad \mathbf{F} = \left[T_1 / r_1, 0, 0, T_1 / r, 0, 0\right]^T$$

$$\mathbf{L} = \begin{bmatrix} L_{m1} & 0 & L_{m1} & L_{m1} & 0 & -L_{m1} \\ -L_{\mu} & 0 & -L_{\mu} & -L_{\mu} & 0 & L_{\mu} \\ 0 & 0 & 0 & 0 & 0 & 0 \\ L_{m2} & 0 & L_{m2} & L_{m2} & 0 & -L_{m2} \\ L_{\mu} & 0 & L_{\mu} & L_{\mu} & 0 & -L_{\mu} \\ 0 & 0 & 0 & 0 & 0 & 0 \end{bmatrix},$$

$$\mathbf{K}_m = \begin{bmatrix} \sum_{i=1}^{Z}\Gamma_i k_i & 0 & \sum_{i=1}^{Z}\Gamma_i k_i & \sum_{i=1}^{Z}\Gamma_i k_i & 0 & -\sum_{i=1}^{Z}\Gamma_i k_i \\ 0 & k_{x1} & 0 & 0 & 0 & 0 \\ \sum_{i=1}^{Z}\Gamma_i k_i & 0 & \sum_{i=1}^{Z}\Gamma_i k_i + k_{y1} & \sum_{i=1}^{Z}\Gamma_i k_i & 0 & -\sum_{i=1}^{Z}\Gamma_i k_i \\ \sum_{i=1}^{Z}\Gamma_i k_i & 0 & \sum_{i=1}^{Z}\Gamma_i k_i & \sum_{i=1}^{Z}\Gamma_i k_i & 0 & -\sum_{i=1}^{Z}\Gamma_i k_i \\ 0 & 0 & 0 & 0 & k_{x2} & 0 \\ -\sum_{i=1}^{Z}\Gamma_i k_i & 0 & -\sum_{i=1}^{Z}\Gamma_i k_i & -\sum_{i=1}^{Z}\Gamma_i k_i & 0 & \sum_{i=1}^{Z}\Gamma_i k_i + k_{y2} \end{bmatrix}$$

$$\mathbf{E} = \begin{bmatrix} \sum_{i=1}^{Z}\Gamma_i k_i g_i \left[1 + \mu sgn(v_i) l_i\right] / r_1 \\ \sum_{i=1}^{Z}\mu sgn(v_i)\Gamma_i k_i g_i \\ \sum_{i=1}^{Z}\Gamma_i k_i g_i \\ \sum_{i=1}^{Z}\Gamma_i k_i g_i \left[1 + \mu sgn(v_i) l_i\right] / r_2 \\ -\sum_{i=1}^{Z}\mu sgn(v_i)\Gamma_i k_i g_i \\ -\sum_{i=1}^{Z}\Gamma_i k_i g_i \end{bmatrix} \tag{6.2}$$

$$
\begin{aligned}
&L_{m1} = \mu \sum_{i=1}^{Z} \eta l_i sgn(v_i) \Gamma_i k_i / r_1; \quad L_{m2} = \mu \sum_{i=1}^{Z} (1-\eta)(D-l_i) sgn(v_i) \Gamma_i k_i / r_2 \\
&L_{\mu} = \mu \sum_{i=1}^{Z} sgn(v_i) \Gamma_i k_i; \quad v_i = \dot{x}_1 - \dot{x}_2 + \dot{u}_1 \tan \varphi_{1,i} - \dot{u}_2 \tan \varphi_{2,i} + \overline{v}_i \\
&\Gamma_i = \tfrac{1}{2} \left[sgn(u + y_1 - y_2 - g_i) + sgn(u + y_1 - y_2 - g_i + B) \right]
\end{aligned}
\tag{6.3}
$$

where all symbols are defined similar as (4.44).

Eqn. (6.1) are nonlinear, time-variant differential equations. Numerical methods, such as Numerical integration, harmonic balance, and AUTO package, can be applied to study response, forces, bifurcation, and frequency-amplitude relations. Finite element model can be considered to benchmark the analytical model. The realistic mesh stiffnesses and load sharing calculated from FE can be feed into the analytical model. The profile modifications obtained from (2.29) achieve minimum DTE for frictionless conditions and use in the frictional condition as well. The following analysis can be considered:

- Compare nonlinear response, normal forces, and friction forces with “optimal” profile modifications for frictionless case and frictional case.
- Examine the dynamic impact of tooth friction with optimal profile modification applied and compare this with no modification case

6.2.2 Nonlinear gear dynamics considering nonlinear bearing dynamics

Bearings are usually used in gear systems to overcome the speed difference between a rotating gear or shaft and its surrounding structure. A common ball bearing consists of a number of rolling elements and two rings (aka races), the inner and the outer ring. Ball bearings can be important generators of noise and vibrations in applications.

Due to the rotation of the lubricated contacts, the stiffness in the bearing is time dependent and generates parametric excitations. Clearance between rollers and raceways considering tolerance and thermal expansion leads to nonlinearity. Furthermore, vibrations are generated by geometrical imperfections on the individual bearing components. The imperfections are caused by irregularities during the manufacturing process, and although their amplitudes are on the nanometer scale, they can still produce significant vibrations in the application. The bearing flexibility excites gear translations that are coupled with gear rotations, and the vibration is passed from gears to surrounding structures via bearings, generating structure borne noises. Thus, bearing dynamics is potentially important for gear vibration and noise problems. Simplified linear bearing models, however, are mostly used in gear dynamics studies [5, 8, 20, 108, 109]. Constant resultant bearing stiffness is applied along each axis of the reference frame, and the bearing stiffness affects only the translational vibration modes in most gear dynamics studies. Contact outside the line of action and a time-varying working pressure angle resulting from bearing deflections is examined in [110].

More complex bearing models are established in studies of rotor dynamics and bearing dynamics. Nonlinear dynamics of rotor-bearing systems are investigated in [111], where a nonlinear bearing pedestal model is assumed which has a cubic nonlinear spring and linear damping characteristics. Dynamic models considering each roller elasticity and geometry between roller and raceways are found in[112-114]. The mathematical formulations account for tangential motions of rolling elements as well as inner and outer races with sources of nonlinearity such as Hertzian contact force and internal radial clearance resulting transition from no contact to contact state between rolling elements and races. With these detailed bearing models as a foundation, a bearing model with a balance in effectiveness and efficiency is proposed to study influence of bearing nonlinearity and parametric excitation on gear dynamics.

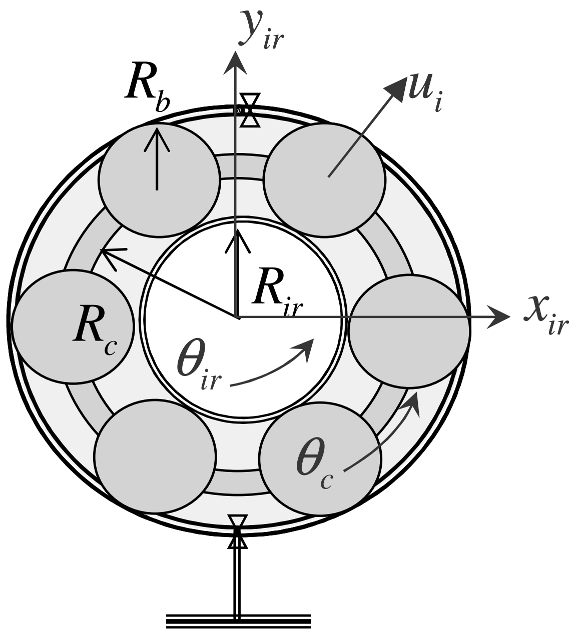

Figure 6.1: Schematic graph of a ball bearing model.

Figure 6.1 shows a ball bearing schematics. The contact load is assumed to be normal to the surfaces and only yields elastic deformation. The dimensions of the contact area are small compared to the radii of curvature of the contacting bodies. The deformations in the contact area are small compared to the dimensions of the contact area. Only pure roll is considered for rollers. The angular positions of rollers change with the carrier's rotation. Roll radial motion, cage rotation, and race rotation and translations are of the interest. Figure 6.2 shows a dynamic model for two gears and a bearing. Roller contacts and tooth contact are modeled as elastic elements. The contacts of roller-outer race and roller-inner race are two separated elastic elements. The engagement of tooth contact is decided by mesh deflection, and the engagement of roller contacts controlled by the distance (defined as mutual approach) between the roller center and the center of the race. The inner and outer races are considered as rigid bodies connected to the gear and external structure, respectively. From pure roll condition, the carrier rotation satisfies

$$\omega_c = \frac{\omega_1}{2}\left(1 - \frac{R_b \cos\alpha}{R_c}\right) \tag{6.4}$$

where ω_c and ω_1 are frequency of the carrier and driving gear; R_b and R_c are radii of the ball and the carrier; and α is the pressure angle of ball contact. Similar to mesh frequency, the ball pass frequency is $\omega_{bp} = Z(\omega_1 - \omega_c)$ where Z is the number of balls.

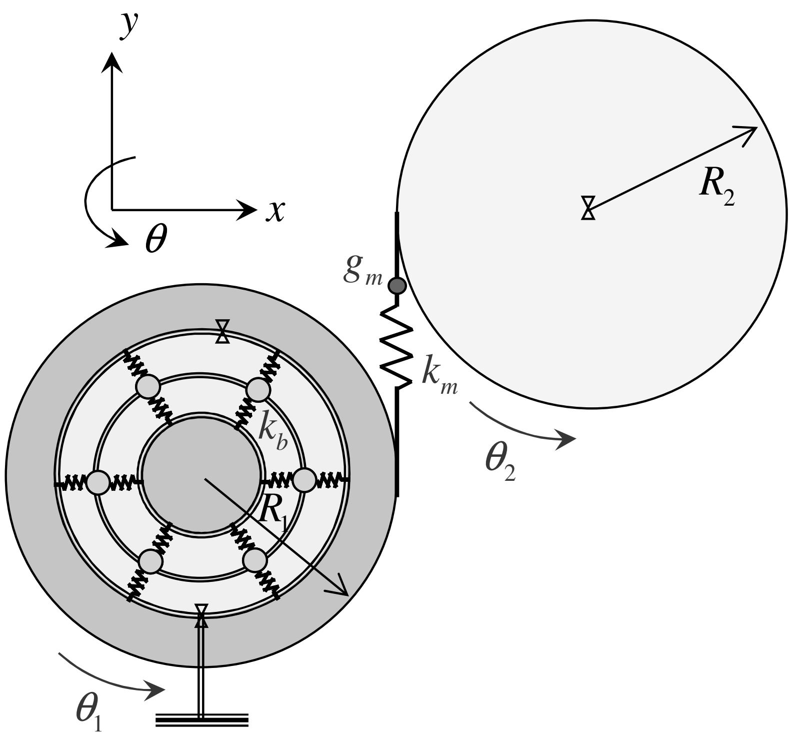

Figure 6.2: Dynamic model of two gears and a bearing.

The stiffness of two roller contacts can be approximated by Hertzain theory as

$$
\begin{aligned}
F &= \frac{\pi \varepsilon E'}{3\xi}\sqrt{\frac{2\eta R}{\xi}}\delta^n \quad \text{for a dry contact} \\
F &= \kappa_h \left(h_0 + \delta\right)^n \quad \text{for EHL condition}
\end{aligned}
\tag{6.5}
$$

where F is the contact force; δ is the mutual approach, i.e., elastic deformation; ε is the Ellipticity ratio; ξ and η are the elliptic integrals of the first and second kind; R is the curvature of radius; E' is the modulus of elasticity; κ_h is the coefficient of EHL contact; and h_0 is the lubrication film thickness. $n=\frac{3}{2}$ for balls and $n=\frac{10}{9}$ for cylindrical rollers.

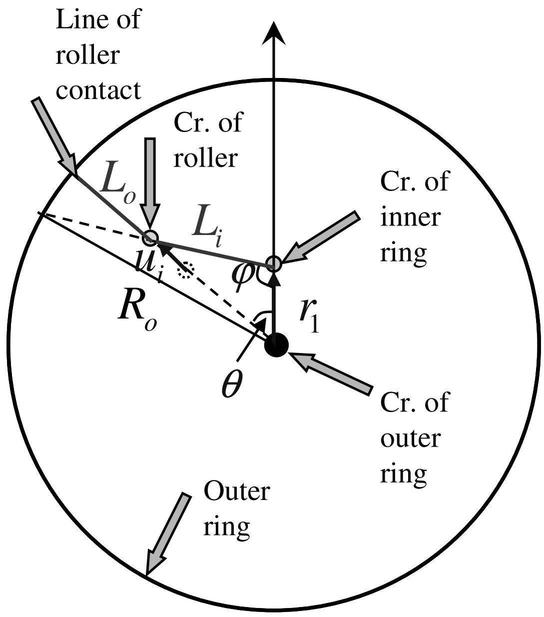

Figure 6.3: Calculation of mutual approaches.

Figure 6.3 depicts the analysis of mutual approach. From the geometry, the mutual approach is determined

$$
\begin{aligned}
&\delta_o = L_o - (R_b + R_{rc}/2) \\
&\delta_i = L_i - (R_c + R_{rc}/2) \\
&L_i = \left[r_1^2 + \left(u_i + R_c + R_b\right)^2 - r_1\left(u_i + R_c + R_b\right)\cos\theta \right]^{1/2} \\
&\approx R_c + u_i - x_1\cos\theta - y_1\sin\theta \\
&L_o = R_o - \left(u_i + R_c + R_b\right)
\end{aligned}
\tag{6.6}
$$

where δ_o and δ_i are mutual approaches of outer race-roller and inner race-roller contact; R_{rc} is the radial clearance; and $\theta = \int \omega_c dt$ is the angular position of roller.

Geometrical imperfections of bearings include waviness, roller diameter variation, carrier runout. The imperfections are modulated by ball pass frequency. Waviness cause variations in the contact loads. The wavelengths are much larger than the dimensions of the Hertzian contact areas, and the number of waves per circumference is denoted by the wave number. The waviness expanded by Fourier series as

$$
W(\theta) = \sum_{n=1}^{\infty} \frac{A}{n^s} \cos(n\theta + \varphi_n) \tag{6.7}
$$

The matrix form of equation of motion is

$$
\mathbf{M}\ddot{\mathbf{X}} + \mathbf{K}(\omega_m, \omega_{bp}, \mathbf{X})\mathbf{X} = \mathbf{F}(t) \tag{6.8}
$$

where $\mathbf{X} = \left[\{u_i\}, x_1, y_1, \Theta_1, y_2, \Theta_2\right]^T$ and $\mathbf{F}(t)$ includes bearing and gear tooth imperfections. (6.8) are nonlinear, time-varying differential equations including time-varying mesh stiffness, time-varying bearing stiffness, tooth separation, and bearing radial clearance and Hertzian contact nonlinearities. The following analysis is considered:

- Study the influences of bearing parametric excitation and nonlinearity on gear dynamics; identify the bigger impact factor.

- Examine rich nonlinear dynamics induced by bearing nonlinearities and the possible interaction between gear nonlinearity and bearing nonlinearities.
- Explore how to optimize bearing and gear parameters to reduce vibration and provide design guidance.

6.2.3 Investigation on aperiodic dynamic response for idler gear systems

The study in Figure 3.12 of Chapter 3 identifies aperieodic dynamic response when the mesh phase increases from 0 to $\pi/4$, the solutions for $\omega \approx 1$ change from period-T_m to period-$2T_m$ and then to chaos. Chaos occurs from $\omega = 0.65$ to $\omega = 0.84$ for $\phi = \pi/4$ as shown in Figure 3.11b. The solution for $\omega = 0.845$ is period-T_m, and that for $\omega = 0.840$ changes to period-$2T_m$. A further slight change to $\omega = 0.800$ yields chaos, as shown by the broadband spectrum in Figure 3.11b and the Poincare maps in Figure 3.12. A further study is needed to understand the parameters surrounding the onset of chaotic response and provide insight as to the character of chaotic behavior.

Investigators have used the term “strange attractor” to indicate bounded, non-periodic chaotic solutions of deterministic, nonlinear differential equations. According to Melnikov chaotic criterion [115], the strange attractor is related with the intersection of the stable and unstable orbits in the phase space. The nonlinear behavior of Duffing’s equation is experimentally and numerically studied in [116, 117]. A boundary was determined at which chaotic motion was first observed. It was found that the predicted chaos boundary from Melnikov force value was a good indicator of transient chaotic motion. Sustained chaotic motion occurs for significantly higher values of the forcing amplitude than that predicted by Melnikov criterion. This discrepancy is explained in [118] by harmonic balance and continuation method, through which stable and unstable solutions are found to be coexist for sustained chaos. Period-doubling cascade leads to the chaos. A criterion to predict bifurcation of homoclinic orbits in strongly nonlinear self-excited one-degree-of-freedom oscillator is presented in [119]. The Lindstedt–Poincaré perturbation method is combined formally with the Jacobian elliptic functions to determine an approximation of the limit cycles near homoclinicity. This criterion leads to the same results, formally and to leading order, as the standard Melnikov technique.

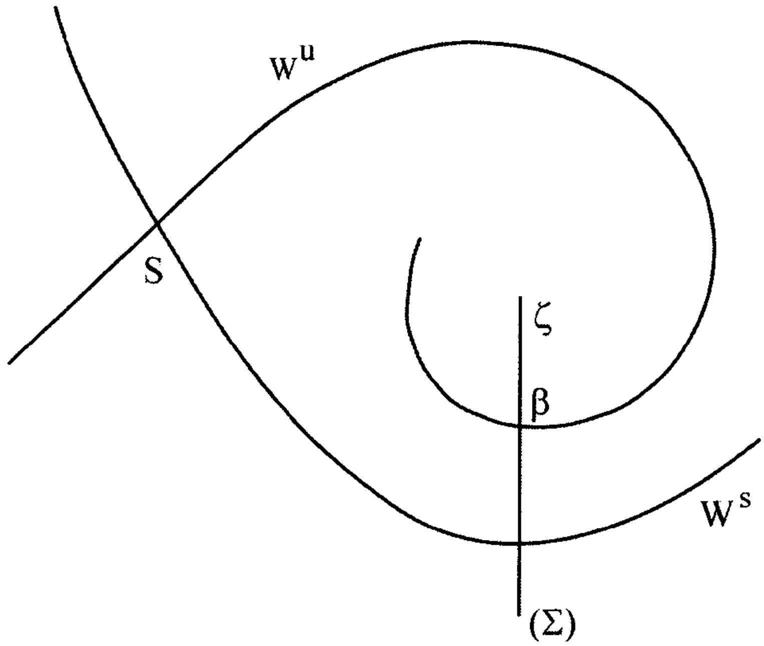

Figure 6.4: Homoclinic bifurcation according to Melnikov method.

The classical Melnikov method to predict a bifurcation in Figure 6.4 is based on the splitting function. To define this function one consider a one-dimensional local cross-section Σ to the stable manifold W^s. Define a coordinate ζ along Σ such that $\zeta = 0$ corresponds to the point of intersection with W^s. The splitting function $\beta = \zeta^u$ denotes the ζ value of the intersection of W^u with Σ (see Figure 1). Therefore, the condition for the homoclinic bifurcation is given by

$$\beta = \zeta^u = 0 \tag{6.9}$$

The solutions of (3.1) can be written in the form of a period$-mT$ solution. Using the harmonic balance and continuation method is discussed in Chapter 3, the solution of the equation of motion can be represented by the coefficients of the Fourier series as a function of the applied load, mesh frequency, and other system parameters. The above techniques yield both stable and unstable solution branches. The stability of the solutions is determined through the application of Floquet theory. Through these, one can trace bifurcation and period doubling cascade. The following analysis is considered:

- Apply harmonic balance and continuation method to study bifurcation and period doubling cascade and identify the route to chaos for the behavior in Figure 3.12 .
- Explore the application of Melnikov criterion and Lindstedt–Poincaré perturbation method to find the chaos prediction criterion for the phenomenon in Figure 3.12, and compare these with harmonic balance results.

6.2.4 Gyroscopic effect on gear dynamics

High speed rotating machinery such as turbomachinery, disk drives, rotor dynamics, and geared transmissions are employed extensively in industry for power generation and transmission. Dynamic response and stability for coupled disk-spindle systems has attracted much attention in previous research. Flowers and Wu investigate coupled disk-spindle dynamics for turbomachinery applications [120]. Parker investigates an elastic disk-spindle system with a rigid clamp by using the extended operator formulation [121]. Shen and Ku study the vibration of multiple elastic disks mounted on a rigid spindle supported by flexible bearings [122]. A rotating body on flexible bearings is a gyroscopic system. These systems exhibit rich eigenvalue and stability behavior including critical speeds, divergence, and flutter [123]. Huseyin [124, 125] and Parker [126] employ a perturbation method to predict the stability behaviors. The eigenvalue problem is reformulated in terms of λ^2 and ν^2, where λ is the eigenvalue and ν is the gyroscopic speed parameter. Concerning the dynamic response of the coupled vibration of geared rotor systems, Choi and Mau [12] investigate the lateral-torsional vibration of a geared rotor-bearing system using the transfer matrix method. For continuous systems, the presence of the skew-symmetric gyroscopic operator prevents analytical solution of the eigenvalue problem except for simple cases such as uniform rotating disks and axially moving strings.

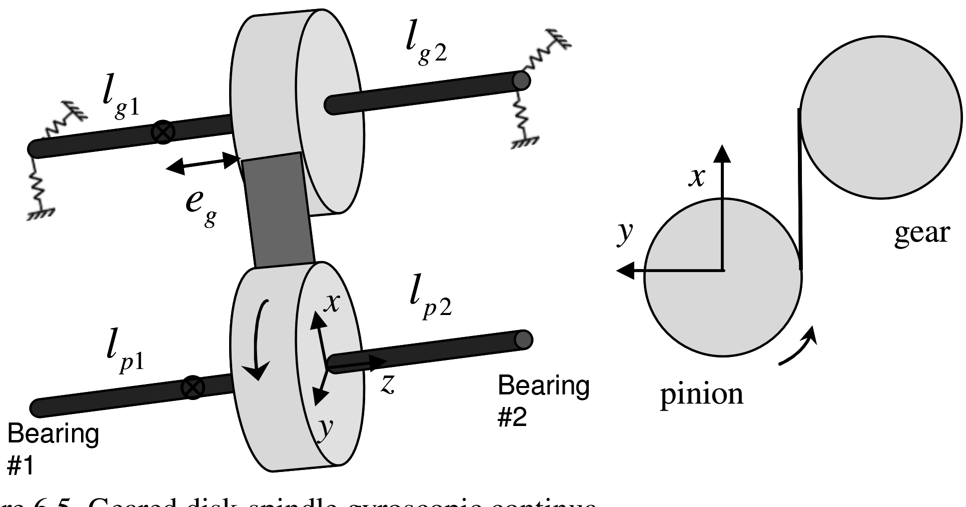

Figure 6.5 Geared disk-spindle gyroscopic continua

For typical problems of rotor-bearing systems, the lateral and rotational vibrations can be treated separately. For the geared rotor systems, however, past studies show that the coupling between translation and rotation should not be neglected [12]. Most gear models treating the parametric excitation and nonlinearity problems only deal with rigid shafts and gear bodies [22]. Few researchers address geared disk-spindle systems. The conjugate contact occurs along the common tangential line of two gear base circles, as illustrated by Figure 6.5. The contact actions couple the gear and shaft translation and rotation. The flexible bearings and mass eccentricity give rise to tilting and rocking motions that are further coupled with the translation motions. The flexibility of mating gear teeth and surface errors are the primary sources of rotational excitations.

A dynamic model for a planetary gearset and flexible bearings is

$$\mathbf{M\ddot{x}} + \Omega\mathbf{G\dot{x}} + (\mathbf{K} - \Omega^2\mathbf{\tilde{K}})\mathbf{x} = \mathbf{F} \tag{6.10}$$

where Ω is the speed of the spinning shaft, $\mathbf{M}$ and $\mathbf{K}$ are symmetric, $\mathbf{G}$ is the skew symmetric gyroscopic matrix, and $\mathbf{x}$ is an unknown vector including two transverse and two tilting motions of the rigid body. The roots of the characteristic equation satisfy $\det\left|-\omega^2\mathbf{M} + i\omega\mathbf{G} + \mathbf{K} - \Omega^2\mathbf{\tilde{K}}\right| = 0$. They appear in pairs ω_k, $-\omega_k$, $k=1,2, \ldots, N$ because of the symmetry of $\mathbf{M}$ and $\mathbf{K}$ and the skew-symmetry of $\mathbf{G}$. It follows that the characteristic polynomial expansion will be a function of ω^2. The system is stable if and only if all ω_k^2 are real and negative, i.e., all ω_k are purely imaginary.

The objective of this part is to extend this model to a planetary gear-shaft system and study the gear mesh problem with gyroscopic effects. The shaft is assumed to be a uniform Euler-Bernoulli beam and the gears are rigid bodies. The mesh action is modeled as a lumped spring. Eventually, a hybrid continuous-discrete model with nonlinearity, time-varying stiffness, and gyroscopic effects will be established. The system stability will be studied. One can use perturbation methods to investigate the gyroscopic effect on the stability, bifurcations, and critical speeds. Dynamic analysis will be conducted by using numerical simulations or the method of transfer matrix, and design guidance will be given for practical applications.

Appendix A Tooth Friction Excitation Coefficents

$$
\begin{aligned}
L_{1,0} &= -\mu\kappa_1\bar{k}\,\frac{\eta\rho_0 r_2 + r_1(1-\eta)(D-\rho_0)}{r_1 r_2} \\
L_{1,1} &= -\mu\kappa_1\bar{k}\,\Omega\frac{\eta r_2 - r_1(1-\eta)}{r_2}
\end{aligned}
\tag{A.1}
$$

$$
\begin{aligned}
L_{2,0} &= \frac{\mu\bar{k}}{r_1 r_2}\left\{r_1(1-\eta)\left[\kappa_3(D-\rho_1+2\pi r_1)-\kappa_2(D-\rho_1)\right]+r_2\eta\left[\kappa_3(\rho_1-2\pi r_1)-\kappa_2\rho_1\right]\right\} \\
L_{2,1} &= \frac{\mu\bar{k}\,\Omega}{r_2}\left[r_2\eta+r_1(1-\eta)\right](\kappa_3-\kappa_2)+\frac{2\mu w}{r_1 r_2}\left[r_2\eta(\rho_1-\pi r_1)+r_1(1-\eta)(D-\rho_1+\pi r_1)\right] \\
L_{2,2} &= \frac{2\mu w\Omega}{r_2}\left[(1\text{-}\eta)r_1-\eta r_2\right]
\end{aligned}
\tag{A.2}
$$

$$
\begin{aligned}
L_{3,0} &= \mu\kappa_4\bar{k}\,\frac{\eta\rho_2 r_2 + r_1(1-\eta)(D-\rho_2)}{r_1 r_2} \\
L_{3,1} &= \mu\kappa_4\bar{k}\,\Omega\frac{\eta r_2 - r_1(1-\eta)}{r_2}
\end{aligned}
\tag{A.3}
$$

Appendix B Proof of A Sum Type Instability

Examination of (4.82) shows that proving the deviation of a sum type instability is larger than for the difference type is achieved by showing $\Psi_R \geq 0$. To begin, consider the first component equation of the EVP $\bar{\mathbf{K}}\phi_p = \omega_p{}^2\mathbf{M}\phi_p$, which gives the following relations betweens the modal deflections

$$\phi_{p3} - \phi_{p5} = \frac{J_e\omega_p^2 - \bar{k}}{\bar{k}}\phi_{p1} \Rightarrow \phi_{p1}\left(\phi_{p1} + \phi_{p3} - \phi_{p5}\right) = \frac{J_e\omega_p^2}{\bar{k}}\phi_{p1}^2 > 0 \tag{B.1}$$

From (4.45), (4.63), and (B.1),

$$D_{pq}D_{qp} = \phi_{p1}\phi_{q1}\left(\phi_{p1} + \phi_{p3} - \phi_{p5}\right)\left(\phi_{q1} + \phi_{q3} - \phi_{q5}\right) = \left(\frac{J_e\omega_p\omega_q}{\bar{k}}\phi_{p1}\phi_{q1}\right)^2 > 0 \tag{B.2}$$

This implies D_{pq} and D_{qp} have the same sign. The following is for positive D_{pq} and D_{qp}, with straightforward modification for negative values. From $\left(D_{pq} - D_{qp}\right)^2 \geq 0$,,

$$\left|D_{pq} + D_{qp}\right| \geq 2\sqrt{D_{pq}D_{qp}} \tag{B.3}$$

The Fourier coefficients in (4.61) are expressed in real and imaginary parts as

$$\left.\begin{aligned}\Lambda_s &= \Lambda_R + i\Lambda_I \\ \Theta_s &= \Theta_R + i\Theta_I\end{aligned}\right\} \Rightarrow \mathrm{Re}\left(\Lambda_s\bar{\Theta}_s\right) = \Lambda_R\Theta_R + \Lambda_I\Theta_I \tag{B.4}$$

From (4.82), (B.3), and (B.4),

$$\Psi_R = \frac{1}{\omega_p \omega_q}\left(\Psi_{R1} + \Psi_{R2}\right) \tag{B.5}$$

$$\Psi_{R1} = \varepsilon^2 E_{pq}^2 \Theta_R^2 + \mu^2 D_{pq} D_{qp} \Lambda_R^2 + \mu\varepsilon E_{pq}(D_{pq} + D_{qp})\Lambda_R \Theta_R \geq \left(\varepsilon E_{pq}\Theta_R + \mu\sqrt{D_{pq}D_{qp}}\Lambda_R\right)^2 \geq 0$$
$$\Psi_{R2} = \varepsilon^2 E_{pq}^2 \Theta_I^2 + \mu^2 D_{pq} D_{qp} \Lambda_I^2 + \mu\varepsilon E_{pq}(D_{pq} + D_{qp})\Lambda_I \Theta_I \geq \left(\varepsilon E_{pq}\Theta_I + \mu\sqrt{D_{pq}D_{qp}}\Lambda_I\right)^2 \geq 0$$

(B.6)

Combination of (B.5) and (B.6) yields $\Psi_R \geq 0$.

REFERENCES

1. Houser, D.R., Bolze, V.M., and Graber, J.M. Static and Dynamic Transmission Error Measurements and Predictions for Spur and Helical Gear Sets. Proceedings of 7th ASME International Power Transmission and Gearing Conference. 1996: p. 365-372.

2. Gregory, R.W., Harris, S.L., and Munro, R.G. Dynamic Behavior of Spur Gears. Proceedings of Institue of Mechanical Engineers. 1963.178: p. 207-226.

3. Harris, S.L., Dynamic Loads on the Teeth of Spur Gears. Proceedings of Institue of Mechanical Engineers, 1958. 172: p. 87-112.

4. Kahraman, A. and Singh, R., Interactions between Time-Varying Mesh Stiffness and Clearance Non-Linear in a Geared System. Journal of Sound and Vibration, 1991. 146(1): p. 135-156.

5. Parker, R.G., Vijayakar, S.M., and Imajo, T., Nonlinear Dynamic Response of a Spur Gear Pair: Modeling and Experimental Comparisons. Journal of Sound and Vibration, 2000. 237(3): p. 435-455.

6. August, R. and Kasuba, R., Torsional Vibrations and Dynamic Loads in a Basic Planetary Gear System. Journal of Vibration, Acoustics, Stress, Reilability in Design, 1986. 108(3): p. 348-353.

7. Kahraman, A., Planetary Gear Train Dynamics. Journal of Mechanical Design, 1994. 116: p. 713-720.

8. Parker, R.G., Agashe, V., and Vijayakar, S.M., Dynamic Response of a Planetary Gear System Using a Finite Element/Contact Mechanics Model. Journal of Mechanical Design, 2000. 122(305-311).

9. Velex, P. and Flamand, L., Dynamic Response of Planetary Trains to Mesh Parametric Excitations. Journal of Mechanical Design, 1996. 118: p. 7-14.

10. Ozguven, H.N. and Houser, D.R., Dynamic Analysis of High-Speed Gears by Using Loaded Static Transmission Error. Journal of Sound and Vibration, 1988. 125(1): p. 71-83.

11. Kahraman, A., Dynamic Analysis of a Multi-Mesh Helical Gear Train. ASME Journal of Mechanical Design, 1994. 116(3): p. 706-712.

12. Choi, S.-T. and Mau, S.-Y., Dynamic Analysis of Geared Rotor-Bearing Systems by the Transfer Matrix Method. Journal of Mechanical Design, 2001. 123(4): p. 562-568.

13. Blankenship, G.W. and Kahraman, A., Steady State Forced Response of a Mechanical Oscillator with Combined Parametric Excitation and Clearance Type Non-Linearity. Journal of Sound and Vibration, 1995. 185(5): p. 743-765.

14. Kahraman, A. and Singh, R., Nonlinear Dynamics of a Spur Gear Pair. Journal of Sound and Vibration, 1990. 142(1): p. 49-75.

15. Litak, G. and Friswell, M.I., Vibrations in Gear Systems. Chaos, Solitons and Fractals, 2003. 16: p. 145-150.

16. Raghothama, A. and Narayanan, S., Bifurcation and Chaos in Geared Rotor Bearing System by Incremental Harmonic Balance Method. Journal of Sound and Vibration, 1999. 226(3): p. 469-492.

17. Theodossiades, S. and Natsiavas, S., Periodic and Chaotic Dynamics of Motor-Driven Gear-Pair Systems with Backlash. Chaos, Solitons and Fractals, 2001. 12: p. 2427-2440.

18. Vaishya, M. and Singh, R., Analysis of Periodically Varying Gear Mesh Systems with Coulomb Friction Using Floquet Theory. Journal of Sound and Vibration, 2001. 243(3): p. 525-545.

19. Lin, J. and Parker, R.G., Mesh Stiffness Variation Instabilities in Two-Stage Gear Systems. Journal of Vibration and Acoustics, 2002. 124(1): p. 68-76.

20. Lin, J. and Parker, R.G., Parametric Instability of Planetary Gears under Mesh Stiffness Variation. Journal of Sound and Vibration, 2002. 29(4): p. 411-429.

21. Blankenship, G.W. and Singh, R. A Comparative Study of Selected Gear Mesh Force Interface Dynamic Models. ASME 6th Power Transmission and Gearing Conference. 1992. Phoenix.

22. Ozguven, H.N. and Houser, D.R., Mathematical-Models Used in Gear Dynamics - a Review. Journal of Sound and Vibration, 1988. 121(3): p. 383-411.

23. Velex, P. and Maatar, M., A Mathematical-Model for Analyzing the Influence of Shape Deviations and Mounting Errors on Gear Dynamic Behavior. Journal of Sound and Vibration, 1996. 191(5): p. 629-660.

24. Al-shyyab, A. and Kahraman, A., Non-Linear Dynamic Analysis of a Multi-Mesh Gear Train Using Multi-Term Harmonic Balance Method: Sub-Harmonic Motions. Journal of Sound and Vibration, 2005. 279(1-2): p. 417-451.

25. Raclot, J.P. and Velex, P. Analysis of Dynamic Coupings in Two-Stage Geared Systems. Proceedings of the 1999 ASME Design Engineers Technical Conferences. 1999: p. 1-9.

26. Umezawa, K., Ajima, T., and Houjoh, H., Vibration of Three Axes Gear System. Bulletin of JSME, 1986. 29: p. 950-957.

27. Oswald, F.B., et al. Comparison of Analysis and Experiment for Gearbox Noise. Proceedings of the International Power Transmission and Gearing Conference. 1992: p. 675-679.

28. Jacobson, M.F., Singh, R., and Oswald, F.B. Acoustic Radiation Efficiency Models of a Simple Gearbox. Seventh International Power Transmission and Gearing Conference. 1996.

29. Kahraman, A. and Blankenship, G.W., Experiments on Nonlinear Dynamic Behavior of an Oscillator with Clearance and Periodically Time-Varying Parameters. Journal of Applied Mechanics, 1997. 64: p. 217-226.

30. Kahraman, A. and Blankenship, G.W. Gear Dynamics Experiments, Part-Iii: Effect of Involute Tip Relief. ASME Power Transmission and Gearing Conference. 1996. San Diego.

31. Bollinger, J.G. and Harker, R.J., Instability Potential of High Speed Gearing. Journal of the Industrial Mathematicas, 1967. 17: p. 39-55.

32. Tordion, G.V. and Gauvin, R., Dynamic Stability of a Two-Stage Gear Train under the Influence of Variable Meshing Stiffnesses. ASME Journal of Engineering Industry, 1977. 99: p. 785-791.

33. Benton, M. and Seireg, A., Factors Influencing Instability and Resonances in Geared Systems. Journal of Mechanical Design, 1981. 103: p. 372-378.

34. Natraj, C. and Whitman, A.M. Parameter Excitation Effects in Gear Dynamics. ASME Design Engineering Technical Conferences. 1997: p. DETC97/VIB-4018.

35. Vinayak, H. and Singh, R., Multi-Body Dynamics and Modal Analysis of Compliant Gear Bodies. Journal of Sound and Vibration, 1998. 210(2): p. 171-214.

36. Lin, J. and Parker, R.G., Analytical Characterization of the Unique Properties of Planetarty Gear Free Vibration. Journal of Vibration and Acoustics, 1999. 121: p.

316-321.

37. Theodossiades, S. and Natsiavas, S., Non-Linear Dynamics of Gear-Pair Systems with Periodic Stiffness and Backlash. Journal of Sound and Vibration, 2000. 229(2): p. 287-310.

38. Kahraman, A. and Blankenship, G.W., Effect of Involute Tip Relief on Dynamic Response of Spur Gear Pairs. Journal of Mechnical Design, 1999. 121: p. 313-315.

39. Oswald, F.B. and Townsend, D.P., Influence of Tooth Profile Modification on Spur Gear Dynamic Tooth Strain. The 31st Joint Propulsion Conference and Exhibit, 1995. San Diego.

40. Houser, D.R., Bolze, V.M., and Graber, J.M. Static and Dynamic Transmission Error Measurements and Predictions for Spur and Helical Gear Sets. Proceedings of 7th ASME International Power Transmission and Gearing Conference. 1996.San Diego: p. 365-372.

41. Borner, J. and Houser, D.R., Friction and Bending Moments on Gear Noise Excitations. SAE Transactions, 1996. 105(6): p. 1669-1676.

42. Vaishya, M. and Houser, D.R. Modeling and Analysis of Sliding Friction in Gear Dynamics. Proceedings of 8th ASME International Power Transmission Gearing Conference. 2000.Baltimore: p. 10.

43. Gunda, R. and Singh, R., Dynamic Analysis of Sliding Friction in a Gear Pair. ASME 2003 Design Engineering Technical Conferences and Computers and Information in Engineering Conference, 2003. Chicago, Illinois.

44. Lundvall, O., Stromberg, N., and Klarbring, A., A Flexible Multi-Body Approach for Frictional Contact in Spur Gears. Journal of Sound and Vibration, 2004. 278: p. 479-499.

45. Velex, P. and Sainsot, P., An Analytical Study of Tooth Friction Excitations in Errorless Spur and Helical Gears. Mechanism and Machine Theory, 2002. 37: p. 641-658.

46. Vaishya, M. and Singh, R., Strategies for Modeling Friction in Gear Dynamics. Journal of Mechanical Design, 2003. 125: p. 383-393.

47. Vaishya, M. and Singh, R., Sliding Friction-Induced Non-Linearity and Parametric Effects in Gear Dynamics. Journal of Sound and Vibration, 2001. 248(4): p. 671-694.

48. Gregory, R.W., Harris, S.L., and Munro, R.G. Dynamic Behavior of Spur Gears.

Proceedings of Institute of Mechanical Engineers. 1963.178: p. 207-226.

49. Vinayak, H., Singh, R., and Padmanabhan, C., Linear Dynamic Analysis of Multi-Mesh Transmissions Containing External, Rigid Gears. Journal of Sound and Vibration, 1995. 185(1): p. 1-32.

50. Raclot, J.P. and Velex, P., Simulation of the Dynamic Behavior of Single and Multi-Stage Geared Systems with Shape Deviations and Mounting Errors by Using a Spectral Method. Journal of Sound and Vibration, 1999. 220(5): p. 861-903.

51. Bahk, C.-J. and Parker, R.G., Nonlinear Dynamics of Planetary Gears with Equally Spaced Planets. ASME Journal of Vibration and Acoustics, 2007. Submitted.

52. Eritenel, T. and Parker, R.G., Effects of a Distributed Stiffness Model on the Dynamics of Helical Gears. Journal of Sound and Vibration, 2007. In Preparation.

53. Wu, X. and Parker, R.G., Parametric Instability of Planetary Geas Having Elastic Continuum Ring Gears. ASME Journal of Applied Mechanics, 2007. Submitted.

54. Huang, K.J. and Liu, T.S., Dynamic Analysis of a Spur Gear by the Dynamic Stiffness Method. Journal of Sound and Vibration, 2000. 234(2): p. 311-329.

55. Ambarisha, K.V. and Parker, R.G., Nonlinear Dynamics of Planetary Gears Using Analytical and Finite Element Models. Journal of Sound and Vibration, 2007. 302(3): p. 577-595.

56. Honda, S., Rotational Vibration of a Helical Gear Pair with Modified Tooth Surfaces (Modified Tooth Surface and Its Equivalent Tooth Profile). JSME Internaltional Journal, 1993. 36(1): p. 125-134.

57. Vijayakar, S.M., A Combined Surface Integral and Finite Element Solution for a Three-Dimensional Contact Problem. International Journal for Numerical Methods in Engineering, 1991. 31: p. 524-546.

58. Andersson, A. and Vedmar, L., A Dynamic Model to Determine Vibrations in Involute Helical Gears. Journal of Sound and Vibration, 2003. 260(2): p. 195-212.

59. Harris, S.L., Dynamic Loads on the Teeth of Spur Gears. Proceedings of Institute of Mechanical Engineers, 1958. 172: p. 87-112.

60. Oswald, F.B. and Townsend, D.P. Influence of Tooth Profile Modification on Spur Gear Dynamic Tooth Strain. The 31st Joint Propulsion Conference and Exhibit. 1995. San Diego.

61. Parker, R.G. and Lin, J., Mesh Phasing Relationships in Planetary and Epicyclic

Gears. ASME Journal of Mechanical Design, 2004. 126: p. 365-370.

62. Liu, G. and Parker, R.G., Nonlinear Dynamics of Idler Gear Systems. Nonlinear Dynamics, 2006. Submitted.

63. Velex, P. and Ajmi, M., On the Modelling of Excitations in Geared Systems by Transmission Errors. Journal of Sound and Vibration, 2006. 290: p. 882-909.

64. Zhu, F. and Parker, R.G., Non-Linear Dynamics of a One-Way Clutch in Belt-Pulley Systems. Journal of Sound and Vibration, 2005. 279: p. 285-308.

65. Meirovitch, L., Fundamentals of Vibrations. 2001, Boston: McGraw-Hill.

66. Nayfeh, A.H. and Mook, D.T., Nonlinear Oscillations. 1979, New York: John Wiley.

67. Liu, G. and Parker, R.G., The Impact of Tooth Friction and Its Bending Effect on Gear Dynamics. Journal of Sound and Vibration, 2007. Submitted.

68. A. Al-shyyab, A.K., Non-Linear Dynamic Analysis of a Multi-Mesh Gear Train Using Multi-Term Harmonic Balance Method: Sub-Harmonic Motions. Journal of Sound and Vibration, 2005. 279(1-2): p. 417-451.

69. Al-shyyab, A.K., Ahmet, Non-Linear Dynamic Analysis of a Multi-Mesh Gear Train Using Multi-Term Harmonic Balance Method: Period-One Motions. Journal of Sound and Vibration, 2005. 284(1-2): p. 151-172.

70. Ma, Q.K., Ahmet, Period-One Motions of a Mechanical Oscillator with Periodically Time-Varying, Piecewise-Nonlinear Stiffness. Journal of Sound and Vibration, 2005. 284(3-5): p. 893-914.

71. Nataraj, C. and Whitman, A.M. Parameter Excitation Effects in Gear Dynamics. ASME Design Engineering Technical Conferences. 1997. Sacramento, CA.

72. Ambarisha, K.V. and Parker, R.G., Nonlinear Planetary Gear Dynamics Using Analytical and Finite Element Models. Journal of Sound and Vibration, 2005. Submitted.

73. Parker, R.G., A Physical Explanation for the Effectiveness of Planet Phasing to Suppress Planetary Gear Vibration. Journal of Sound and Vibration, 2000. 236(4): p. 561-573.

74. Canchi, S.V. and Parker, R.G., Parametric Instability of a Circular Ring Subjected to Moving Springs. Journal of Sound and Vibration, 2006. 293(1-2): p. 360-379.

75. Padmanabhan, C. and Singh, R., Dynamics of a Piecewise Non-Linear System Subject to Dual Harmonic Excitation Using Parametric Continuation. Journal of Sound and Vibration, 1995. 184(5): p. 767-799.

76. Leung, A.Y.T. and Chui, S.K., Non-Linear Vibration of Coupled Duffing Oscillatos by an Improved Incremental Harmonic Balance Method. Journal of Sound and Vibration, 1995. 181(4): p. 619-633.

77. Kim, T.C. and Singh, R., Effect of Smoothening Functions on the Frequency Responses of an Oscillator with Clearance Non-Linearity. Journal of Sound and Vibration, 2003. 263(3): p. 665-678.

78. Hsu, C.S., Impulsive Parametric Excitation: Theory. Journal of Applied Mechanics, 1972. 39: p. 551-558.

79. Hsu, C.S. and Cheng, W.H., Applications of the Theory of Impulsive Parametric Excitation and New Treatments of General Parametric Excitation Problems. Journal of Applied Mechanics, 1973. 40: p. 78-86.

80. Friedmann, P., Hammond, C.E., and Woo, T., Efficient Numerical Treatment of Periodic Systems with Application to Stability Problems. International Journal for Numerical Methods in Engineering, 1977. 11: p. 1117-1136.

81. Blankenship, G.W. and Kahraman, A. Gear Dynamics Experiments, Part-I: Characterization of Forced Response. ASME Power Transmission and Gearing Conference. 1996.

82. Kahraman, A. and Singh, R., Interactions between Time-Varying Mesh Stiffness and Clearance Non-Linear in a Geared System. 1991.

83. Liu, G. and Parker, R.G., Dynamic Modeling and Analysis of Tooth Profile Modification for Multi-Mesh Gear Vibration. Journal of Mechanical Design, 2007. Submitted.

84. Vijayakar, S.M. and Houser, D.R., Contact Analysis of Gears Using a Combined Finite Element and Surface Integral Method. Gear Technology, 1993. July/August: p. 26-33.

85. Raclot, J.P. and Velex, P., Analysis of Dynamic Couplings in Two-Stage Geared Systems. Proceedings of the 1999 ASME Design Engineers Technical Conferences, 1999. Las Vegas, Nevada: p. 1-9.

86. Iwatsubo, T., Arii, S., and Kawai, R., The Coupled Lateral Torsional Vibration of a Geared Rotor System. I Mech E Conference Publications (Institution of Mechanical Engineers), 1984: p. 59-66.

87. Kahraman, A. and Blankenship, G.W., Interactions between Commensurate Parametric and Forcing Excitations in a System with Clearance. Journal of Sound and Vibration, 1996. 194(3): p. 317-336.

88. Kahraman, A., Kharazi, A.A., and Umrani, M., A Deformable Body Dynamic Analysis of Planetary Gears with Thin Rims. Journal of Sound and Vibration, 2003. 262: p. 752-768.

89. Kahraman, A. and Blankenship, G.W., Effect of Involute Contact Ratio of Spur Gear Dynamics. Journal of Mechanical Design, 1999. 121: p. 112-128.

90. Blankenship, G.W. and Kahraman, A. Gear Dynamics Experiments, Part-I: Characterization of Forced Response. ASME Power Transmission and Gearing Conference. 1996. San Diego.

91. Wang, J., Li, R., and Peng, X., Survey of Nonlinear Vibration of Gear Transmission Systems. ASME Applied Mechanics Review, 2003. 56(3): p. 309-329.

92. Velex, P. and Cahouet, V., Experimental and Numerical Investigations on the Influence of Tooth Friction in Spur and Helical Gear Dynamics. Journal of Mechanical Design, 2000. 122: p. 515-522.

93. Martin, K.F., A Review of Friction Predictions in Gear Teeth. Wear, 1978. 49: p. 201-238.

94. Kelley, B.W. and Lemanski, A.J., Lubrication of Involute Gearing. Proceedings of Institute of Mechanical Engineers, 1967. 182: p. 173-184.

95. Wu, S. and Cheng, H.S., A Friction Model of Partial-Ehl Contacts and Its Application to Power Loss in Spur Gears. Tribology Transactions, 1991. 34: p. 397-407.

96. Rebbechi, B., Oswald, F.B., and Townsend, D.P. Measurement of Gear Tooth Dynamic Friction. Proc. 7th ASME int. Power Transmission and Gearing Conf. 1996. San Diego.

97. He, S., Gunda, R., and Singh, R., Effect of Sliding Friction on the Dynamics of Spur Gear Pair with Realistic Time-Varying Stiffness. Journal of Sound and Vibration, 2007. 301: p. 927-949.

98. Iida, H., Tamura, A., and Yamada, Y., Vibrational Characteristics of Friction between Gear Teeth. Bulletin of JSME, 1985. 28: p. 1512-1519.

99. Hochmann, D. Friction Force Excitations in Spur and Helical Involute Parallel Axis Gearing. PhD Dissertation. The Ohio State University. 1997.

100. Lee, C., et al., Influence of Linear Profile Modification and Loading Conditions on the Dynamic Tooth Load and Stress of High-Contact-Ratio Spur Gears. Journal of Mechanical Design, 1991. 113: p. 473-480.

101. Butikov, E.I., Parametric Excitation of a Linear Oscillator. European Journal of Physics, 2004. 25: p. 535-554.

102. Barterls, R.E., A Time Integration Algorithm Based on the State Transition Matrix for Structures with Time Varying and Nonlinear Properties. Computers and Structures, 2003. 81: p. 349-357.

103. Kucharski, T., A Method for Dynamic Response Analysis of Time-Varying Discrete Systems. Computers and Structures, 2000. 76: p. 545-550.

104. Richards, J.A., Analysis of Periodically Time-Varying Systems. 1983, New York: Springer.

105. Vaishya, M. and Houser, D.R. Modeling and Analysis of Sliding Friction in Gear Dynamics. Proceedings of 8th ASME International Power Transansmission and Gearing Conference. 2000. Baltimore.

106. Diab, Y., Ville, F., and Velex, P., Prediction of Power Losses Due to Tooth Friction in Gears. Tribology Transactions, 2006. 49: p. 260-270.

107. He, S., Gunda, R., and Singh, R., Effect of Sliding Friction on the Dynamics of Spur Gear Pair with Realistic Time-Varying Stiffness. Journal of Sound and Vibration, 2007. 301: p. 927-949.

108. Kahraman, A. and Singh, R., Nonlinear Dynamics of a Geared Rotor-Bearing System with Multiple Clearances. Journal of Sound and Vibration, 1991. 144(3): p. 469-506.

109. Liu, G. and Parker, R.G., Dynamic Modeling and Simulation of Tooth Profile Modification of Multi-Mesh Gearsets. Journal of Sound and Vibration, 2007: p. In Preparation.

110. Vedmar, L. and Andersson, A., A Method to Determine Dynamic Loads on Spur Gear Teeth and on Bearings. Journal of Sound and Vibration, 2003. 267: p. 1065-1084.

111. Shabaneh, N. and Zu, J.W., Nonlinear Dynamic Analysis of a Rotor Shaft System with Viscoelastically Supported Bearings. Journal of Vibration and Acoustics, 2003. 125: p. 290-298.

112. Harsha, S.P., Nonlinear Dynamic Response of a Balanced Rotor Supported by

Rolling Element Bearings Due to Radial Interanal Clearance Effect. Machanism and machine theory, 2006. 41: p. 688-706.

113. Tiwari, M., Gupta, K., and Prakash, O., Effect of Radial Internal Clearance of a Ball Bearing on the Dynamics of a Balanced Horizontal Rotor. Journal of Sound and Vibration, 2000. 238(5): p. 723-756.

114. Wensing, J.A. On the Dynamics of Ball Bearings. PhD Dissertation. University of Twente. 1998.

115. Melnikov, V.K., On the Stability of the Center for Time Periodic Perturbations. Transactions of the Moscow Mathematical Society, 1963. 12: p. 1-57.

116. Dowell, E.H. and Pezeshki, C., On the Understanding of Chaos in Duffing's Equation Including a Comparison with Experiment. Journal of Applied Mechanics, 1986. 53: p. 5-9.

117. Moon, F.C. and Holmes, P.J., A Magnetoelastic Strange Attractor. Journal of Sound and Vibration, 1979. 12: p. 1-57.

118. Blair, K.B., Krousgrill, C.M., and Farris, T.N., Harmonic Balance and Continuation Techniques in the Dynamic Analysis of Duffing's Equation. Journal of Sound and Vibration, 1997. 202(5): p. 717-731.

119. Belhaq, M., Fiedler, B., and Lakrad, F., Homoclinic Connections in Strongly Self-Excited Nonlinear Oscillators: The Melnikov Function and the Elliptic Lindstedt–Poincaré Method. Nonlinear Dynamics, 2000. 23(1): p. 67-86.

120. Flowers, G.T. and F., W., Disk/Shaft Vibration Induced by Bearing Clearance Effects: Analysis and Experiment. Journal of Vibration and Acoustics, 1996. 118: p. 1395-1396.

121. Parker, R.G., Analytical Vibration of Spinning, Elastic Disk-Spindle Systems. Journal of Applied Mechanics, 1999. 66: p. 218-224.

122. Shen, I.Y. and Ku, C.-P.R., A Non-Classical Vibration Analysis of Multiple Rotating Disks/Spindle Assembly. Journal of Applied Mechanics, 1997. 64: p. 165-174.

123. Meirovitch, L., A Modal Analysis for the Response of Linear Gyroscopic Systems. Journal of Applied Mechanics, 1975. 42: p. 446-450.

124. Huseyin, K. and Plaut, R.H., Transverse Vibrations and Stability of Systems with Gyroscopic Forces. Journal of Structure Mechanics, 1974-1975. 3(2): p. 163-177.

125. Huseyin, K., Standard Forms of the Eigenvalue Problems Associated with Gyroscopic Systems. Journal of Sound and Vibration, 1976. 45: p. 29-37.

126. Parker, R.G., On the Eigenvalues and Critical Speed Stability of Gyroscopic Continua. Journal of Applied Mechanics, 1998. 65: p. 134-140.